# The impact of nitrogen chemistry in snow on atmospheric oxidising capacity in the polar boundary layer

Hoi Ga Chan

*A thesis submitted in fulfillment of the requirements for the degree of Doctor of Philosophy*

Department of Earth Sciences
Royal Holloway University of London

January 2018

# Declaration of Authorship

I, Hoi Ga Chan, hereby declare that this thesis and the work presented in it are entirely my own. I confirm that:

- This work was done wholly or mainly while in candidature for a research degree at this University.
- Where I have consulted the published work of others, this is always clearly attributed.
- Where the thesis is based on work done by myself jointly with others, I have made clear exactly what was done by others and what I have contributed myself.

Signed:

Date:

Royal Holloway University of London

# *Abstract*

Faculty Name
Department of Earth Sciences

Doctor of Philosophy

**The impact of nitrogen chemistry in snow on atmospheric oxidising capacity in the polar boundary layer**

by Hoi Ga Chan

Snow photochemical reactions drive production of chemical trace gases within snowpack, including nitrogen oxides ($NO_x$ = NO + $NO_2$), which are then released to the lower atmosphere. They were found to affect the oxidising capacity of the lower troposphere, especially in remote regions of high latitudes with low level of anthropogenic pollution, by altering concentration of ozone ($O_3$), a pollutant and green house gas, and hydroxyl radical (OH), responsible for the removal of many atmospheric pollutants including methane. However, the emission of $NO_x$ and its impact has not yet been quantified. Current air-snow coupled models are limited by poor understanding of interactions between air and ice and often require fitted parameters to match the model results with observations that limited their predictive capability.

Presented here is a new 1-D air-snow exchange model for nitrogen species to investigate snow as the source of $NO_x$ in the overlying atmosphere in Antarctica. Building on existing models, it includes heat and radiation transfer in snow, gas and solid phase diffusion, multi-phase chemistry and air-snow grain exchange of oxidised nitrogen species. The solar radiation transfer in snow is parameterised as an exponential decay with respect to depth to reduce computation cost. The impact of the exponential parameterisation on the photochemical production of $NO_x$ is evaluated by comparing the results with the outputs from a radiative transfer model - TUV (Lee-Taylor and Madronich, 2002). The study showed the exponential parameterisation of radiation of cold polar snowpack has no significant impacts on the estimation of photochemical production rate due to large solar zenith angles and the efficient light scattering environment of the snowpack. For other types of snowpack, such as melting or fresh snow, the overestimation in photochemical production at large solar zenith angles or underestimation at small solar zenith angles caused by the exponential parameterisation can be corrected by applying the solar zenith angle and chemical species dependent correction factor.

Two temperature dependent multi-phase air-snow grain exchange models were developed from physically based parameterisations, each based on different hypothesis on the interface between air and snow grain. The first model assumed at temperatures below a threshold temperature, $T_o$, the air-snow grain interface is pure ice and above $T_o$, a disordered interface (DI) emerges covering the entire surface of the snow grain, which is a similar approach taken by models previously developed. The other model assumed at temperatures below melting of ice, the air-snow grain interface is pure ice and liquid assumed to be co-existed with ice as micropocket at temperatures above the eutectic temperature. The models are validated with existing

Antarctic snow samples and atmospheric observations from a cold site on the Antarctica Plateau (Dome C, $75°06'\mathrm{S}, 123°33'\mathrm{E}$, 3233 $\mathrm{m}$ a.s.l.) and at a relatively warm site on the Antarctica coast (Halley, $75°35'\mathrm{S}, 26°39'\mathrm{E}$, 35 $\mathrm{m}$ a.s.l). The study showed the concentration of nitrate in surface snow is better described by the latter model, that it reproduced a good agreement with observations at both sites without requiring any tuning parameters whereas the first model only showed good agreement at Dome C but not at Halley. It is therefore suggested that in winter the air-snow exchange of nitrate is determined by non-equilibrium adsorption on ice and co-condensation coupled with diffusion to the bulk ice. In summer, the air-snow exchange of nitrate is dominated by solvation into liquid micropocket following Henry's law.

The 1-D air-snow model was developed based on an existing model framework and the newly developed temperature dependent multi-phase air-snow grain exchange models to estimate the flux of $NO_3^-$ to the overlying atmosphere and the distribution of $NO_x$ within the snowpack. The model predicted an average emission flux of $NO_2$, $F_{\mathrm{NO_2}}$, is $3 \times 10^{12}\ \mathrm{molecule\,m^{-2}\,s^{-1}}$ at Dome C, in late December.

# *Acknowledgements*

First of all I would like to thank my supervisors, Dr. Markus Frey and Prof. Martin King for their advice and helpful discussions, as well as being patient and give me a lot of encouragement. I have been lucky to have supervisors who responded to my questions and queries so promptly. I would also like to thank the members of the Atmospheric Chemistry group at the British Antarctic Survey, for their time and helpful suggestions to all my oral presentation practises. Thanks are also made to Dr. Maxim Lamare for his help on my computer problems and welcoming me when I visited RHUL. Thanks also to all my great office mates who have been sharing all the up and downs of my research.

Finally I would like to thanks my parents, sister and boyfriend for their constant moral and financial support. They have been so understanding throughout my PhD, especially towards the end when I was not able to spend much time with them.

I am grateful for the Natural Environment Research Council for funding this study, Royal Holloway Travel fund to allow me to attend a UNIS course in Svalbard and the IPSiS travel grants, provided me with the opportunity to attend IPSis Conference and Workshop in Svalbard.

# Contents

# List of Figures

# List of Tables

# Chapter 1

# Introduction

## 1.1 Importance of Snow Photochemistry

Nitrogen-containing trace gases, such as nitric oxide (NO), nitrogen dioxide ($NO_2$), nitric acid ($HNO_3$), dinitrogen pentoxide ($N_2O_5$), and nitrate radical ($NO_3$), play an important role in the chemistry of the atmosphere by altering the concentration of tropospheric ozone ($O_3$) and partition of hydroxyl radical (OH) and hydroperoxyl radical ($HO_2$). Tropospheric $O_3$ is one of the most important air pollutants in terms of impacts to human and plant health. It is also a greenhouse gas that changes the regional energy balance and climate via direct radiative forcing and indirectly by oxidising aerosols that has a strong radiative forcing (Fowler et al., 2008). Therefore, it is necessary to understand the natural tropospheric $O_3$ chemistry of the troposphere and predict the background tropospheric $O_3$ level. On the other hand, OH radical is known as the atmospheric cleaner which reacts with most trace species in the atmosphere, such as hydrocarbons, greenhouse gas methane and tropospheric ozone precursor $NO_2$.

Nitrogen oxides, $NO_x$ = NO + $NO_2$, in the troposphere are mainly from the downwelling from the stratosphere (Jacobson, 2005) or produced in the troposphere via lightning, biomass burning, or anthropogenic fossil fuel burning, where the nitrogen in the atmosphere or in the fuel get oxidised under high temperatures (Seinfeld and Pandis, 2012). The concentration of $NO_x$ were expected to be very low (few pptv) in remote boundary layer. The dominant source of $NO_x$ in the Antarctica proceeds mainly from downwelling from the stratosphere. In contrasts, due to the meteorology and atmospheric transport patterns in the Arctic the direct input of reactive nitrogen from the stratosphere is limited and $NO_x$ proceeds mainly through long-range transport from lower latitudes within the troposphere.

In the past, the snow and ice has been viewed as a sink of atmospheric species and measuring trace gases concentration at high latitudes was to improve understanding the chemistry of a clean background atmosphere. However, recent evidence has shown that sunlit snow can have a major influence

on the concentration of atmospheric oxidants in the overlying atmosphere by releasing reactive trace gases into the boundary layer due to photochemical reaction within the upper snowpack. A concentration of $NO_x$ that was 3 to >10 times higher than the ambient air concentration and with a diurnal variation was observed within the snow interstitial air (SIA) at Summit, Greenland (Honrath et al., 1999). The observation was explained by nitrate within the snow was photolysed to release $NO_x$ to SIA and to the overlying boundary layer. Other studies (e.g. Jones et al., 2000; Honrath et al., 2000; Jacobi et al., 2004; Davis et al., 2008) also confirmed that irradiate natural snow, from both high-latitude or mid-latitude, with light caused the release of $NO_x$. The impact of the snow photochemistry on atmospheric composition varies depending on the background concentration of radicals and the boundary layer height. For example, at the South Pole and Dome C, Antarctica, a large mixing ratio of $NO_x$, equaling those from the mid-latitudes had been observed (Davis et al., 2008; Frey et al., 2013) due to the shallow boundary layer that concentrated the $NO_x$ emitted from sunlit snowpack, and hence, the snow emission dominate the boundary layer chemistry. The isotopic composition of surface snow and aerosols (McCabe et al., 2007) as well as the ratio of organic to inorganic nitrate in Antarctica show a strong evidence for stratospheric source of nitrate in winter but a much stronger tropospheric signature in the summer, which is likely be recycled from photolysis of $NO_3^-$ within the near-surface snow.

The photolysis of snow nitrate can occur through the following pathways, with producing nitrogen dioxide ($NO_2$) as the major pathway (Grannas et al., 2007)

$$\mathrm{NO_3^- + hv(+H^+) \longrightarrow NO_2 + OH} \tag{R1}$$

and producing nitrite anion ($NO_2^-$) as the secondary pathway:

$$\mathrm{NO_3^- + hv \longrightarrow NO_2^- + O(^3P)} \tag{R2}$$

The photochemically produced $NO_2^-$ can further photolysed as follow:

$$\mathrm{NO_2^- + hv(+H^+) \longrightarrow NO + OH} \tag{R3}$$

The rate of the photolysis reaction is dependent on the amount of solar radiation available, the quantum yield and the absorption cross-section of the photolysed species (See Sect. 1.2.5 for details). The porous structure of the snowpack allows physical exchange of gases between the SIA and the overlying atmosphere, and therefore part of these photochemical produced NO

and $NO_2$ escape the snowpack to the atmosphere above.

As shown in Fig. 1.1, the gas-phase NO can be oxidised by ozone ($O_3$ via R4), hydroperoxyl radicals ($HO_2$ via R5) and peroxy radical ($RO_2$ via R6) to from $NO_2$, which can reacts with ground-state oxygen atom, O, via R7, and leads to a net destruction of $O_3$. The coupling reactions between $NO_x$, $O_3$, $HO_2$ and $RO_x$ can be described as follow (Eyring, 1962):

$$\mathrm{NO + O_3 \longrightarrow NO_2 + O_2} \tag{R4}$$

$$\mathrm{NO + HO_2 \longrightarrow NO_2 + {}^{\bullet}OH} \tag{R5}$$

$$\mathrm{NO + RO_2 \longrightarrow NO_2 + RO} \tag{R6}$$

$$\mathrm{NO_2 + O \longrightarrow NO + O_2} \tag{R7}$$

$$\tag{R8}$$

$$\mathrm{Net: O_3 + O \longrightarrow O_2 + O_2}$$

When sunlight is present, $NO_2$ can also undergo photolysis by sunlight to form back to NO and $O_3$, which competes with R7

$$\mathrm{NO_2 + hv \longrightarrow NO + O(^3P)} \tag{R9}$$

$$\mathrm{O(^3P) + O_2 \xrightarrow{M} O_3} \tag{R10}$$

The photolysis of $NO_2$ is one of the major sources for the in-situ production of $O_3$ in the troposphere other than the oxidation of volatile organic compounds (VOCs). Nonetheless, the interconversion between NO and $NO_2$ has a timescale of 5 $\mathrm{min}$ (Seinfeld and Pandis, 2012), which is a lot more rapid than the oxidation of VOCs (one to several hours).

The in-situ loss of tropospheric $O_3$ results mainly from photolysis of $O_3$ and the reaction with $HO_2$ radicals as

$$\mathrm{O_3 + hv \longrightarrow O_2 + O(^1D)} \tag{R11}$$

$$\mathrm{O_3 + HO_2 \longrightarrow OH + O_2} \tag{R12}$$

The $O_3$ destruction pathways, R11 & R12, each responsible for $\sim$ 40% of $O_3$ loss in the troposphere. In the presence of sunlight, in a particular region, the atmosphere is acting as a source of sink of tropospheric $O_3$ is depending on the local concentration of NO, $HO_2$, $RO_2$ and $O_3$. The local production and destruction of $O_3$ in the background troposphere can be estimated from

$$\mathrm{P_{O_3}} = (k_{R5}[\mathrm{HO_2}] + k_{R6}[\mathrm{RO_2}])[\mathrm{NO}]$$

$$\mathrm{L_{O_3}} = k_{R11}[\mathrm{O(1\,D)}][\mathrm{H_2O}] + k_{R12}[\mathrm{HO_2}][\mathrm{O_3}]$$

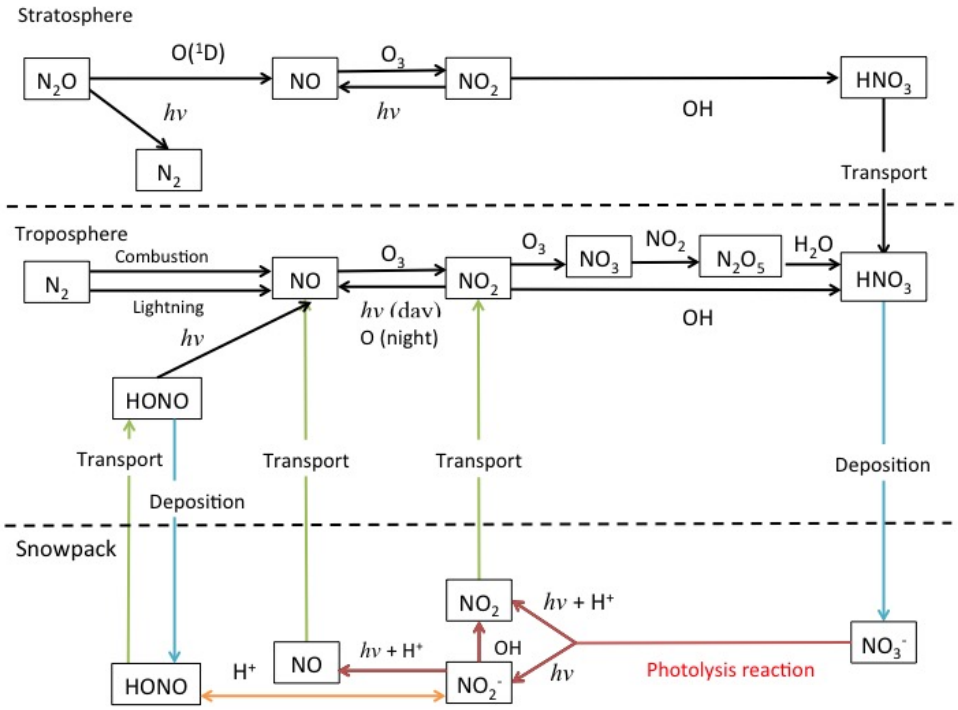


FIGURE 1.1: Nitrogen cycle in the atmosphere and in the snowpack.

The destruction of $O_3$ leads to production of OH radical, directly, through R12 and, indirectly, through the reaction between the excited singlet oxygen atom, $O(^1D)$, formed from the photolysis of $O_3$ (R11), and water molecule

$$O(^1D) + H_2O \longrightarrow OH + OH \tag{R13}$$

Besides the reactions with NO (R5) and $O_3$ (R12), the $HO_2$ radicals can react with itself to form hydrogen peroxide ($H_2O_2$), which can act as a temporary reservoir for $HO_x$ = OH + $HO_2$

$$HO_2 + HO_2 \longrightarrow H_2O_2 + O_2 \tag{R14}$$

$$H_2O_2 + \mathrm{hv} \longrightarrow OH + OH \tag{R15}$$

$$H_2O_2 + OH \longrightarrow HO_2 + H_2O \tag{R16}$$

Termination of the chain reactions of $NO_x$ (R4, R5, R6, R7 & R9) and $HO_x$ (R14, R15 & R16) occurs when OH reacts with NO or $NO_2$ to form nitrous acid (HONO) and nitric acid ($HNO_3$), respectively, as

$$NO + {}^{\bullet}OH \xrightarrow{M} HONO \tag{R17}$$

$$NO_2 + {}^{\bullet}OH \xrightarrow{M} HNO_3 \tag{R18}$$

During night time, no photolysis reactions can occur (R9) that almost all $NO_x$ is converted to $NO_2$ (R4, R5 & R6). The major removal path for $NO_2$ at night is its reaction with $O_3$ to form nitrate ($NO_3$) radical

$$NO_2 + O_3 \longrightarrow NO_3 + O_2 \tag{R19}$$

The concentration of $NO_3$ radicals during the day is very low (< 1 ppt, Seinfeld and Pandis, 2012 ) as it normally gets photolysed or react with NO and converted back to NO or $NO_2$. At night, the lack of solar radiation and low concentration of NO, the $NO_3$ radical reacts with $NO_2$ to produced $N_2O_5$, which can be hydrolysed to form $HNO_3$ as follow

$$NO_3 + NO_2 \overset{M}{\rightleftharpoons} N_2O_5 \tag{R20}$$

$$N_2O_5 + H_2O \longrightarrow 2\,HNO_3 \tag{R21}$$

Nitric acid is a very soluble gas which can be deposited to water vapour droplets to form acid rain or acid snow or it can react with sea salt aerosols and mineral dust.

In the polar region, where anthropogenic pollution is rare, the $NO_x$ emission from snow found to significantly influence the oxidising capacity in the lower atmosphere (Jones et al., 2008). Beine et al. (2002) measure midday $NO_x$ flux of 0-5 $\times 10^{12}$ $\mathrm{molecule\,m^{-2}s^{-1}}$ at Alert, Canadian Arctic between April and May 2000, Jones et al. (2000) observed a $NO_x$ flux of $\sim$3.2 $\times 10^6$ $\mathrm{molecule\,cm^{-2}s^{-1}}$ from near the center of a 10 $\mathrm{cm^3}$ snow cube held a meter above the ground at Neumayer, Antarctic. Chen et al. (2001) observed a high OH radical concentration at the South Pole corresponds to the rapid radical cycling driven by the emissions of $NO_x$ from snow, which the impact was enhanced by the low boundary layer height . Frey et al. (2015) also observed a net increase in $O_3$ production caused by the emission of $NO_x$ from snow at Dome C, Antarctica.

Furthermore, permanent ice sheets in the polar regions, mainly Greenland and Antarctica, preserve nitrogen compounds that are either deposited as nitrate aerosols and directly from gas phase $HNO_3$ onto the snow then compacted into ice or enclosed within air bubble as gas-phase nitrogen species, such as $N_2$ and $N_2O$, when snow and ice compressed with depth. The concentration of the nitrate in polar ice varies between 10-1000 $\mu\mathrm{gkg^{-1}}$ and the amount of nitrate preserved in the ice core depends on 1) amount of wet deposition, which linked to emission, strength and pathway of transport of nitrogen species from the source of origin to the deposition site; 2) the efficiency of dry deposition, which included adsorption and absorption on snow of gas-phase $HNO_3$ that formed by direct oxidation of $NO_2$ (R18) or via $NO_3$ radical

and $N_2O_5$ (R20 & R21) and nitrate aerosols; and 3) physical and chemical processes in the snowpack driving air-snow recycling of reactive nitrogen, which included the photolytic loss of nitrate from snow and gas species transport within and out of the snowpack.

Due the relatively short lifetime of $NO_x$, the nitrate records in polar ice has been using as an indictor of changing regional emission of $NO_x$, by assuming all the other factors listed above, such as deposition efficiency and post-depositional changes, do not contribute toward any variation in the preserved nitrate. However, these assumptions are probably only reasonable for a short-time scale, i.e. a century, when the climate conditions are relatively stable but not for long-time scale. Therefore, it is necessary to understand all these other factors in order to interpret the ice core record of nitrate for estimating the atmospheric composition in the past (Wolff et al., 2002; Wolff et al., 2008).

## 1.2 Current Understanding of Air-Snow Interaction of Trace Gases

The snow chemistry is still a relatively young study area that the interaction between air and snow is still not fully understood, such as the location of reactive species in snow and the physical exchange mechanism (Huthwelker et al., 2006). There are different possible locations where the reactive species might be located within the snow grain (BartelsRausch et al., 2014), such as on the surface of ice (Ch. 1.2.1), in the disordered interface (DI, Ch.1.2.2), in the liquid found at grooves between snow grains (Ch.1.2.3), or within the ice crystal (Ch. 1.2.4). The current measuring techniques can only measure the average uptake of ice but not identify each individual processes at different locations (Huthwelker et al., 2006). Improving the understandings of the location of reactive species is critical as it might have impacts on the rate of chemical reactions (See Sect.1.2.5) and the physical exchange (uptake and release) mechanism of chemical species between air and snow and its efficiency.

Metamorphism is the process responsible for the post-depositional physical evolution of snow, which changes the specific surface area (SSA, area per unit mass of snow) and modifies the shape and size of the snow grain. Metamorphism can occur at temperature below freezing, which often refers as the 'dry snow metamorphism' and mainly due to water vapour gradient (Colbeck, 1982). In general, there are two types of dry metamorphism, the 'equi-temperature' and 'temperature gradient' (Sommerfeld and LaChapelle, 1970). The 'equi-temperature' metamorphism happens when the temperature gradient is low ($<9\ ^{\circ}\mathrm{C\,m^{-1}}$) and the vapour transport is driven by the

differences in curvature between adjacent snow grains. The 'temperature gradient' metamorphism is the major drive of water vapour transport. The difference in temperature generates a water vapour flux within the snowpack, especially at the top meter of the snowpack where a strong temperature gradient can be found due to the diurnal cycle. The vapour flux causes condensation on parts of the snow grain and sublimation on other parts. Pinzer et al., 2012 found under a constant temperature gradient of 50 $^{\circ}\mathrm{C\,m^{-1}}$, up to 60% of the ice mass get redistributed per day. However, the redistribution of the reactive species under a temperature gradient is still not clear (Domine et al., 2008).

### 1.2.1 Air-Ice Interaction

At 190 K, ice is crystalline in the form of hexagonal type structure even to the outermost layer and water molecules arrange themselves in bilayer (Abbatt, 2003). The crystalline structure of the ice crystal at the surface will get more and more disordered as temperature increases towards melting and so the mobility of the surficial water molecules. Gas molecules can be adsorbed on the ice surface when the temperature is within the ice stability region. Adsorption is the adhesion of molecules to a surface which is the process that initiates the interaction between air and ice. The adsorbed molecules are physically accommodated into a weakly bound state, which might involve hydrogen bounds, charge transfer or Van der Waals interactions depending on the gas-molecules and the surface properties of the adsorbent. Under higher temperatures and/or low partial pressure of the strong acid, such as $HNO_3$ and HCl, the adsorption can be well described by single Langmuir adsorption isotherms which molecules can only adsorb on free surface adsorption site, S, and the adsorption can be irreversible thermally:

$$\mathrm{X\,(g) + S} \underset{k_{\mathrm{des}}}{\overset{k_{\mathrm{ads}}}{\rightleftharpoons}} \mathrm{XS} \tag{1.1}$$

where X(g) is a gas phase molecule, XS is the adsorbed molecule, $k_{ads}$ and $k_{des}$ are rate the adsorption and desorption respectively. The probability of adsorption when a molecule collides with a solid or liquid surface can be described by the surface accommodation coefficient (also known as the sticking probability), $\alpha$. The chance of a molecule being adsorbed increases as temperature decreases, the dependency of accommodation coefficient to temperature is as follow (Crowley et al., 2010):

$$\alpha = \frac{\exp\{\ln(\frac{\alpha_0}{1-\alpha_0})[-\frac{\Delta_{\mathrm{obs}}H}{R}(\frac{1}{T}-\frac{1}{T_f})]\}}{1-\exp\{\ln(\frac{\alpha_0}{1-\alpha_0})[-\frac{\Delta_{\mathrm{obs}}H}{R}(\frac{1}{T}-\frac{1}{T_f})]\}} \tag{1.2}$$

where $\alpha_0$ is the reference accommodation coefficient at reference temperature found by experiment, $T_f$ (K), $\Delta_{\text{obs}}H$ is the enthalpy of activation ($\text{J}\,\text{mol}^{-1}$), and $R$ is the molar gas constant ($\text{J}\,\text{K}^{-1}\,\text{mol}^{-1}$). The fraction of free adsorption site on the surface, $\theta$, is a function of surface concentration and the maximum number of available surface site per unit area, $N_{max}$ or as a function of the equilibrium constant for Langmuir adsorption, $K_{eq}$.

$$\theta = \frac{[\text{XS}]}{N_{max}} = \frac{K_{eq}[X(g)]}{1 + K_{eq}[X(g)]} \tag{1.3}$$

The value of Langmuir adsorption equilibrium, $K_{eq}$, can be found by laboratory experiments and is also the ratio of the rate constant of adsorption, $k_{ads}$, to the rate constant of desorption, $k_{des}$.

$$k_{ads} = \frac{\alpha v}{4}\frac{1}{N_{max}} \tag{1.4}$$

$$k_{des} = \frac{k_{ads}}{K_{eq}} \tag{1.5}$$

where $v$ is the mean molecular velocity.

On top of Langmuir adsorption of gas molecules on the surface of ice, molecules can be taken up to the ice when water molecules condense to the ice surface which called co-condensation. Condensation or sublimation of $H_2O$ is caused by the natural temperature gradients exist in snowpack which leads to significant fluxes of water vapour. Uptake of trace gases into growing ice occurs when the residence time on the surface is longer than the frequency of water molecules condensate on the surface.

### 1.2.2 Air-Disordered Interface Interaction

Molecular dynamics (MD) had been used to estimate the structure of water molecules on the surface of the ice using both classical and first-principles approaches. The MD approach shows the surface disorder, often referred as the breakup of the solid crystal structure of ice at the solid-air interface and deviates from the ideal hexagonal ice lattice (BartelsRausch et al., 2014), starts around 200 K The disorder at the surface increases and extends deeper into the ice crystal as temperature increases that the surface structure deviates from the bulk structure as temperature increases. The disordered surface layer is often referred as the disordered interface (DI), which is presented at the surface of a snow grain and acts as the interface between air and ice. However, the physical and chemical properties of the DI are still not well understood. One of the most used assumptions is that all or a fraction of the impurities are found in the DI (BartelsRausch et al., 2014).

Different laboratory methods had been used to quantify the disordered fraction of ice, i.e. estimate the thickness of the DI. The measurement techniques included atomic positioning, changes of refractive index, proton backscattering, and optical extinction coefficient (Table 1.1). In general, the thickness of the DI correlate positively with temperature but the average thickness of DI found within pure ice are ranging from 0.3 nm (monolayers of water molecule) to tens of nm down to a temperature of -80 °C. There are

TABLE 1.1: Experimental techniques for measuring surface disorder on ice (Huthwelker et al., 2006, and therein)

| Technique | Physical features | Thickness (nm) |
|---|---|---|
| AFM | Existence of a viscous surface layer on ice | 0.2-40 |
| Ellipsometry | Refractive index of the surface layer of ice is between those off water and ice | 1-20 |
| Infrared Spectrum | Attenuation of the ice surface is equal to the one measured at triplet point of water and gradually change to one measured of ice as temperature decreases | |
| NEXAFS | Photoelectron spectrum of ice surface slowly change from a water-like spectrum to ice-like spectrum as temperature decreases | 0.3-3 |
| NMR | Self-diffusion constant in the interfacial layer is between those of water and ice | |
| Proton Channelling | Larger vibrations of oxygen atoms in the near-surface region | 10-100 |
| Surface sensitive X-ray scattering | Direct evidence that surface layer is disordered | |
| Surface conductivity | High mobility of ice in the surface region | |

where AFM = Atomic force microscopy; NEXAFS = Near-edge X-ray absorption fine structures spectroscopy; NMR = Nuclear magnetic resonance;

three main reasons for this wide range of values, 1) the methods used were all based on examining different physical properties of the surface layer and some methods interact more with the surface than some other. 2) Limitation of the measuring techniques that the thickness cannot be observed directly that the reported values are average values over the entire probing area. 3) the preparation of the ice might have an impact on the orientation and deposition of the water molecules which have an impact on the optical properties of the ice. Moreover, studies have also found the thickness of the DI

increases with the presence of impurities, of which the impacts are impurity type and concentration dependent. For example, acetic acid induces a minor amount of $H_2O$ hydrating while nitrate and acetone only induced a small change to the structure of the ice surface and does not change the majority of the hydrogen-bonding network (Krepelova et al., 2010). However, the exact relationship between temperature, the type and quantity of impurities to the thickness of the DI is not yet established.

Recent laboratory study (Sazaki et al., 2012) had found that the disordered regions are heterogeneously distributed across the ice surface at near melting temperature. They have observed directly that round liquid-like droplets appear on the ice surface at -0.4 °C and thin liquid-like layer on ice from -0.2 °C. The distribution of the disordered regions at the lower temperature is still unknown. The most used assumption is that the disordered region is homogeneous and continuously spread across the surface of the ice. The partitioning between air and DI as well as the rate of reactions are often assumed to be same as those measured in liquid water as it is not yet feasible to measure the physical and chemical properties of the DI (Domine et al., 2008; BartelsRausch et al., 2014).

### 1.2.3 Air-Liquid Water Interaction

In the presence of impurities, liquid can co-exist with ice at subzero temperatures down to the eutectic temperature of that particular mixture (Atkins and Paula, 2010). The amount of liquid solution and the impurity concentration of the liquid solution can be found by the thermodynamic equilibrium phase diagram, which is a function of temperature and the total amount of impurities in the mixture. However, liquid water does not have a prefect wettability on ice that prevents the liquid spreading completely over the ice surface Domine et al. (2013b). The surface tension exerts, $\sigma_{surf}$, between the liquid water, ice and air causing a water droplet to form on the ice surface with a contact angle, $\theta$, between the ice surface and the tangent to the surface of liquid water at the liquid water-ice interface (Fig. 1.2). The contact angle, $\Theta$, of a water droplet in equilibrium with the ice surface is described by Youngś equation (Atkins and Paula, 2010)

$$\cos\theta = \frac{\sigma_{ai} - \sigma_{wi}}{\sigma_{aw}} \tag{1.6}$$

where $\sigma_{ai}, \sigma_{wi}$ and $\sigma_{aw}$ are the surface tension at the air-ice, water-ice and air-water interface. The value of $\sigma_{aw}$ is relatively easy to measure by deforming the liquid, which $\sigma_{aw}$ measured to be 75.7 $\mathrm{mJ\,m^{-2}}$ at 0°C (Hobbs, 1974). Measuring the surface tension of others are much more difficult but can be estimated from $\sigma_{aw}$, e.g. $\sigma_{wi} \simeq L_f \frac{\sigma_{aw}}{L_v}$, where $L_f$ and $L_v$ as the latent heats

of freezing and vapourisation of water respectively or $\sigma_{wi} \simeq \sigma_{ai} - \sigma_{aw}$. The values of $\sigma_{wi}$ estimated from various ways are ranging from 15-33 $\mathrm{mJ\,m^{-2}}$ at -40 °C and $\sigma_{ai}$ varied from 85-122 $\mathrm{mJ\,m^{-2}}$ at 0°C. From these measured and estimated surface tension value, the contact angle can be between 0.62-1.41° from Eq. 1.6, which suggests liquid water does not completely wet the solid ice surface.

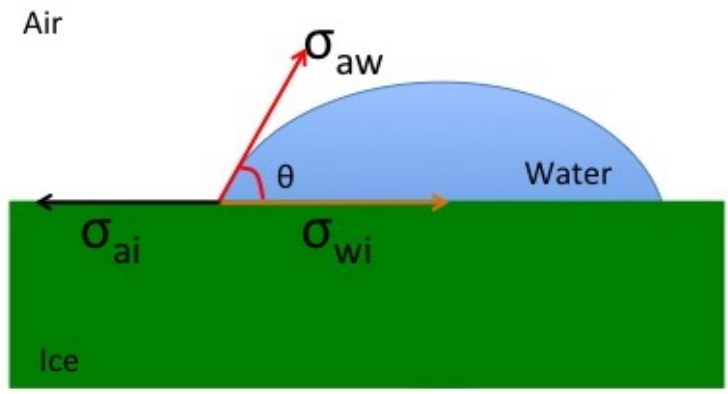


FIGURE 1.2: Drop of water on an ice surface with a contact angle, $\theta$.

The surface tension between liquid and ice causes liquid to form isolated patches on the ice surface. Ketcham and Hobbs (1969) observed visible amount of liquid water formed in grooves at grain boundaries, triple junctions (veins) and quadruple (nodes) before wetting the surface of the ice. Domine et al. (2013b) suggested that majority of the surface of the snow grain is ice which possibly adsorbed chemical species, and a small amount of true liquids coexist with ice but would be located in grooves at grain boundaries and triple junctions. Some studies suggested that the liquid presents at the grain boundaries could act as a diffusion short cuts for transport of trace elements within the snowpack (e.g. Aguzzi et al., 2003), that they found the diffusion of HCl and HBr were an order of magnitude faster in polycrystalline ice compared to single crystal ice. Nevertheless, the diffusion rate at the grain boundary is hard to identify with the current techniques.

### 1.2.4 Bulk Ice Diffusion

Solid solution can also be formed between the ice crystal and ice-soluble impurities, such as $HNO_3$, HCl and HCHO. Impurities might be incorporated into the ice crystal during cloud formations or diffused into the interior ice crystal structure when there is a concentration gradient across the outer layer of the snow grain and its centre (BartelsRausch et al., 2014). The molecular transport within the ice matrix can be described as stochastic transport which

is governed by Brownian motion (Huthwelker et al., 2006),

$$\frac{\partial n(x,t)}{\partial t} = -D\frac{\partial^2 n(x,t)}{\partial x^2} \tag{1.7}$$

where $n$ is the concentration of the impurities at a distance $x$ from the centre of the snow grain, $t$ is time and $D$ is the diffusion constant. The solid-phase diffusion constant and thermodynamic solubility in ice can be found by exposing single ice crystal to diluted trace gases under a well-controlled environment for a period of days to weeks. For $HNO_3$ the diffusion constant is in the $10^{-16}$ $\mathrm{m^2s^{-1}}$ order of magnitude at 253 K (Thibert et al., 1998). However, the measured diffusion constant in pure ice has a large variation that Thibert et al. (1998) suggested it is possible that there are two different diffusive processes in the ice; 1) diffusion through the signal crystal matrix which expected to be slow and 2) diffusion through grain boundaries, triple junctions and other crystal defects that expected to be quick as they are less ordered in comparison to the crystal lattice (Huthwelker et al., 2006). Therefore, due to numerous experimental artefacts, the measured solubility and diffusivity of impurities in ice might have a large error margin.

To summarise, snow grain is a multi-phase media of which impurities can be adsorbed onto the ice surface, formed solid solution with the bulk ice or dissolved into DI or micro-liquid pockets.

### 1.2.5 Photochemical Reactions

The production rate of $NO_2$ from the photolysis reaction of $NO_3^-$ (React. R1) can be written as follow:

$$\frac{\mathrm{d}[\mathrm{NO_2}]}{\mathrm{d}t} = J_{R1}\,[\mathrm{NO_3}^-] \tag{1.8}$$

where $\frac{\mathrm{d}[\mathrm{NO_2}]}{\mathrm{d}t}$ is the rate of change of $NO_2$ concentration with time corresponds to photolysis of nitrate, $[NO_3^-]$ is the concentration of nitrate, and $J_{R1}$ is the first-order photolysis rate constant of reaction R1. The photolysis rate constant, $J$, with a units of $\mathrm{s^{-1}}$ is a function of actinic flux ($I$), quantum yield ($\Phi$) and absorption cross section of the photolysed species ($\sigma$), which is defined as follow:

$$J(z,\theta,T) = \int_{\lambda_1}^{\lambda_2} I(\lambda,z,\theta)\Phi(\lambda,T)\sigma(\lambda,T)\mathrm{d}\lambda \tag{1.9}$$

where $z$ is the depth of the snowpack, $\theta$ is the solar zenith angle and $\lambda$ is the wavelength. The quantum yield for photolysis of nitrate in snow still remains a major uncertainty in current snow chemistry models. The measured

quantum yield of $NO_2$ from photolysis of nitrate in ice through reaction R1, $\Phi_{R1}$, ranges from 0.0028 (Chu and Anastasio, 2003) to 0.6 (Zhu et al., 2010) at -20°C depending on the experimental technique, i.e. preparation of the snow sample and the choice of product to be measured. For example, Chu and Anastasio (2003) prepared ice pellets by slow freezing sodium nitrate solution ($NaNO_3$) on a template, then illuminate it at wavelength above 290 nm, and measure the photochemically produced $^{\bullet}OH$. The quantum yield of $^{\bullet}OH$, $\Phi_{OH}$ from nitrate photolysis which was assumed to be equivalent to $\Phi_{R1}$. They found the $\Phi_{R1}$ is a function of pH and temperature, that it value decreases as pH or temperature decrease. The authors suggested that the small $\Phi_{R1}$ is likely due to a domain-specific effect known as the 'cage effect', which the initially formed photoproducts in liquid and ice are unable to escape as they are surrounded by water molecules. The collisions between the photoproducts and water molecules consumed the excess energy of the photoproducts that they often reform as the initial compound.

On the other hand, Zhu et al. (2010) adsorbs nitric acid ($HNO_3$) on the surface of the ice films, then irradiate it at wavelength 308 nm, and determine $\Phi_{R1}$ by measuring the photo-produced $NO_2$. The large $\Phi_{R1}$ is suggested to be as a result of the photolabile nitrate located on the surface of the ice film by surface adsorption, which is more likely to escape the ice. Therefore, the quantum yield from Chu and Anastasio (2003) probably account for cage effect while Zhu et al. (2010) study have little or no cage effect and that is the major reason for the large deviation in the value.

Measurements with natural snow samples by Meusinger et al. (2014) support the theory of nitrate reservoirs dependent quantum yield for nitrate photolysis reaction. Meusinger et al. (2014) measured the quantum yield for loss of nitrate, $\Phi_{R1+R2}$, the combined quantum yield of React. R1 and R2 plus the cage effect, by illuminating snow samples collected from the top $\sim$ 10 cm of the snowpack at Dome C, Antarctica, at 200 and 305 nm for a various period of time from 5 to 283 hours. The snow nitrate concentrations were measured prior and after the illumination. They observed the quantum yield for loss of nitrate decreases with irradiant exposure time, that $\Phi_{R1+R2}$ reduced from 0.44 at the beginning of the experiment to 0.003 after 283 hours of illumination. The irradiant exposure time dependent quantum yield was explained by the two different snow-photochemical domains, one of accessible photolabile and one of buried nitrate. The photolabile nitrate might correspond to adsorbed $HNO_3$ on the ice surface and resulted in a higher quantum yield as photoproducts can leave the snow easily. The buried nitrate might correspond to nitrate that surrounded by water molecules, such as solid solution of $HNO_3$ in ice, aqueous $HNO_3$ solution that coexist with solid solutions of

$HNO_3$ or in the disordered interface, that the cage effect inhibiting emission and enhanced reformation of nitrate. Meusinger et al. (2014) concluded that quantum yield for nitrate photolysis has a complex mechanism and should not be quantified as a single value.

### 1.2.6 Snow Budget of $NO_3^-$

The deposition of nitrate in snow is reversible of which the loss of nitrate from snow can be through chemical and physical processes. The chemical loss of nitrate corresponds to lose through nitrate photolysis while the physical loss is often referred to lost through evaporation and/or desorption. The relative importance of the physical and chemical loss of nitrate has been quantified by analysing the stable isotopic composition of nitrate and suggested that photolysis dominates nitrate loss from snowpacks (Frey et al., 2009), which is significant in dry regions such as the high East Antarctic Plateau (Rothlisberger et al., 2000; Frey et al., 2009; Erbland et al., 2013). A brief summary of the isotope approach is given below.

The stable isotopic ratios, $\delta$, of nitrate are expressed as $\delta^{15}\mathrm{N}$, $\delta^{17}\mathrm{O}$ and $\delta^{18}\mathrm{O}$, where $\delta = R_{\mathrm{spl}}/R_{\mathrm{ref}} - 1$, with $R_{\mathrm{spl}}$ and $R_{\mathrm{ref}}$ as the isotopic fractionation of the sample and reference, respectively, and $R$ denoting the isotope ratios: $^{15}\mathrm{N}/^{14}\mathrm{N}$, $^{17}\mathrm{O}/^{16}\mathrm{O}$, and $^{18}\mathrm{O}/^{16}\mathrm{O}$.

A common metric to analyse oxygen isotopes is the 'oxygen isotope anomaly', $\Delta^{17}\mathrm{O} = \delta^{17}\mathrm{O} - 0.52 \times \delta^{18}\mathrm{O}$. The relative importance of different formation pathways of atmospheric nitrate can be obtained from $\Delta^{17}\mathrm{O}$ analysis. As the atmospherically produced $O_3$ has a large positive $\Delta^{17}\mathrm{O}$ value while OH possesses lower $\Delta^{17}\mathrm{O}$ value, and the isotopic composition would be transferred to the atmospheric nitrate when they oxidise the nitrogen in the atmosphere. However, the post-depositional snow nitrate fractionation in $\Delta^{17}\mathrm{O}$ is minor compared to the signal residual from the tropospheric oxidation, it is hard to identify the post-depositional processes from $\Delta^{17}\mathrm{O}$ analysis.

Nonetheless, a $\delta^{15}\mathrm{N}$ value up to +399 ‰ have been observed in nitrate obtained from surface snow at Dome C, which is significantly higher than the $\delta^{15}\mathrm{N}$ value from non-polar atmospheric particulate nitrate ($\sim -10$ to $+10$‰, Erbland et al., 2013 and therein). The fractionation of post-depositional loss of nitrate can be quantified by the apparent fractionation constant, $^{15}\varepsilon_{\mathrm{app}}$, of which, a negative $^{15}\varepsilon_{\mathrm{app}}$ indicates enrichment of $^{15}\mathrm{N}$ (Blunier et al., 2005). Blunier et al. (2005) and Frey et al. (2009) observed a $^{15}\varepsilon_{\mathrm{app}}$ ranging from -49.8 to -71.0 ‰ at Dome C.

The apparent fractionation constant associated with nitrate photolysis, $^{15}\varepsilon_{\mathrm{pho}}$, is estimated to be negative with a max $^{15}\varepsilon_{\mathrm{pho}} = -48$‰ based on zero point energy shift model (Frey et al., 2009). And the apparent fractionation

constant associated with the physical loss of nitrate, $^{15}\varepsilon_{\text{phy}}$, is estimated to be only slightly negative (-3.6±1.1 ‰ at -10°$C$, Erbland et al., 2013), based on study of natural snow from Dome C carried under a controlled environment which does not take the effects such as temperature gradient and wind pumping into account. Despite the apparent fractional constant associated with the chemical, $^{15}\varepsilon_{\text{pho}}$, and physical, $^{15}\varepsilon_{\text{phy}}$, loss are both negative it is possible to determine the main loss process from $^{15}\varepsilon_{\text{app}}$ due to the large difference in magnitude.

## 1.3 Current Snow Chemistry Models

Snow chemistry box models have been developed to estimate the interaction between trace gases and snow located at the surface of the snowpack and the post-depositional exchange of snow chemistry. One-dimensional (1-D) air-snow models have been developed to predict the vertical distribution of different trace gases, such as formaldehyde (HCHO), hydrogen peroxide ($H_2O_2$), nitrogen oxides ($NO_x$) etc., within the SIA and the in snow concentration. Global chemical transport model had been ran with an idealised snowpack along with snow radiative transfer model to investigate the potential spatial variability in $NO_3^-$ concentration in snow, recycling and redistribution of reactive nitrogen across Antarctica and Greenland (Zatko et al., 2016a). Below is a brief summary of various snow chemistry models.

### 1.3.1 Box Models

McConnell et al. (1997) and Bock et al. (2016) both developed a box model to describe the exchange of chemical species between surface snow and the atmosphere above based on the interaction between air and ice. McConnell et al. (1997) model is to estimate concentration of hydrogen peroxide ($H_2O_2$) in the atmosphere from the concentration of $H_2O_2$ in the surface snow samples at the South Pole, Antarctica, so called the inversion model. They assumed the deposition of the atmospheric $H_2O_2$ on snow is via co-condensation with water vapour and that the uptake is reversible when the co-condensation are supersaturated with respect to the solid phase. The degassing of $H_2O_2$ from ice matrix from snow grain was described by a spherical diffusion model of individual snow grains and the snow-atmospheric partitioning coefficient, $K_D$. The value of $K_D$ was adjusted to fit the observed concentration of $H_2O_2$ in the atmosphere. The tuned snow-atmospheric partitioning coefficient, $K_D$, showed a similar relationship with temperature as the laboratory found values, yet, the model tuned value is an order of magnitude higher. Recent box model developed by Bock et al. (2016) is to investigate the physicochemical

processes of nitrate in the surface snow at Dome C, Antarctica and to predict the concentration of nitrate in surface snow from the concentration of nitric acid in the atmosphere above. They suggested the concentration of nitrate in the snow is driven by thermodynamic equilibrium solubility on the outer layer of the snow grain followed by solid-state diffusion in the winter whereas in the summer the uptake of nitrate acid is dominated by co-condensation of nitric acid and water vapour. The co-condensation related parameters were adjusted in Bock et al. (2016) model. In one of their configurations (configuration 2-BC2) an empirical relationship between the co-condensation concentration and the partial pressure of nitric acid and water vapour were used to fit the model results to the observation while in another configuration (configuration 2-BC3), they varied the complementary error function, which has a value between 0-1, to match the modelled results to the observations.

The two box snow chemistry models briefly introduced above are based on an air-ice interaction and both requires tuning parameters to fit the results to the observations, which limited the predictive capability of the models.

### 1.3.2 1-D Models

For 1-D transport model, the vertical distribution of trace gases within snowpack can be described by a general partial differential diffusion equation:

$$\frac{\partial[\mathrm{X}_g]}{\partial t} = \frac{\partial}{\partial z}\kappa\frac{\partial[\mathrm{X}_g]}{\partial z} + S_g \tag{1.10}$$

where $[\mathrm{X}_g]$ is the concentration of the trace gas, $t$ is time, $z$ is the depth of the snowpack, $\kappa$ is the diffusivity of the gas in snow (molecular diffusion and windpumping) and $S_g$ is the source term, which can be the net of chemical production and destruction and/or mass transfer from one phase to another. The source term in various previously developed snow-chemical models is listed in Table 1.2. Some of the models assumed an 'air-ice' interface between snow grains and surrounding air (Albert, 1996; McConnell et al., 1998; Hutterli and Rothlisberger, 1999) that the models included mass transfer into the ice phase while others assumed an 'air-DI' interface between snow grains and surrounding air (Liao and Tan, 2008; Thomas et al., 2011; Toyota et al., 2014; Murray et al., 2015) that they included mass transfer into the DI, chemical production and loss. All of these models have the required physical characteristics of the snowpack, such as the snow temperature, ventilation, solar radiation, and chemical reactions in snow estimated by separate established chemical kinetic models.

Albert (1996) model is more focus on how the of permeability of the snowpack can have an impact on the transport of chemical species. They compared model results with mass transport experiments with inert gases, which concluded permeability has a first-order effect on transport in the snow. Snow layers with high permeability can act as a channel for faster flow in the air. The 1-D model developed by McConnell et al. (1998) was based on the air-ice exchange box model of $H_2O_2$ by McConnell et al. (1997) as well as the value of partitioning coefficient, $K_D$, found in that study (from the same location) to estimate the deposition, uptake and release, and final preservation of $H_2O_2$ in snow. The model was driven by the concentration of $H_2O_2$ in the atmosphere and was validated against the concentration profile of $H_2O_2$ from the South Pole. They suggested that the $H_2O_2$ in surface snow is always out of equilibrium as the change of temperature and the change of concentration of atmospheric $H_2O_2$ is faster than the uptake capacity of snow. The vertical transport of formaldehyde, HCHO, in the snowpack was investigated by Hutterli and Rothlisberger (1999) and also based on air-ice interactions, which was assumed to be a combination of adsorption and partitioning between bulk phase (Table. 1.2). The model results were fitted to the observation collected at Summit, Greenland by adjusting the sorption parameters, including the mass transfer coefficient, $k_b$, and the partitioning coefficient $K_D$, that has a form related to temperature.

The production of nitrous acid, HONO, within the top 2.5 $\mathrm{m}$ of the snowpack and emission of HONO out of the snowpack were estimated by Liao and Tan (2008) with a 1-D air snow model that included chemical production and loss via photolysis of HONO and $NO_3^-$ respectively, and the interaction between air and snow grain only restricted to solvation in the DI (which is referred as QLL in their paper). In their model, a single value of the volume ratio of DI to snow and the pH of the snow were chosen arbitrarily and the surface layer was assumed to be a true liquid with Henry's law as the partitioning coefficient. The PHANTAS 1-D model developed by Toyota et al. (2014) is a multiphase transport and chemistry model to study the exchange of bromine ($Br_2$), ozone ($O_3$) and mercury (Hg) in Arctic snow on sea ice in the springtime. They assumed the DI (which is referred as liquid-like layer, LLL, in their paper) is covering the entire snow grain with bulk liquid properties and that all the condensed-phase reactants are located in the DI. The PHANTAS model also assumed the DI of the snow grains are interconnected that aqueous-phase diffusion is allowed through those inter-connecting DI along with the vertical transport in gas-phase (as in Eq. 1.10). However, as there are no observed or laboratory measured values for the diffusivity of DI, it was assumed to be 10% of those measured in bulk liquid, which is an

empirical fractionation. They concluded that the release of $Br_2$ to the atmosphere is dominated by the deposition of hypobromous acid (HOBr) from the atmosphere oxidised $Br^-$ on the snow grains which then converted to $Br_2$ via aqueous radical chemistry in the DI.

An other 1-D model - MISTRA-SNOW developed by Thomas et al. (2011) was used to estimate the emission of $NO_x$ and Br from snow to the overlying atmosphere at Summit, Greenland. The interface between air and snow was assumed to be air-DI (referred as LLL in the paper). The DI was assumed to have a fixed thickness of 10 nm and have a partitioning coefficient and rate of reactions same as those measured in liquid. In MISTRA-SNOW, it assumes only a fraction of the reactants are located in the DI, that are available to undergo photolysis reactions and transfer in and out of the snow grain. The fraction of the total nitrate, bromide and chloride found in the DI was used as an adjustable parameter to fit the results of the model to the observations. They estimated only 6% of the total nitrate is located in the DI while 100% of the total bromide and chloride is located in the DI. They have identified a few processes, such as the diurnal cycle, the contribution of windpumping to the emission flux, attenuation of actinic flux in the snowpack, and that play an important role in the boundary layer composition over sunlit snow. Murray et al. (2015) model share the same framework as in MISTRA-SNOW, except the diffusion equation (Eq. 1.10) is solved by a different numerical method and the thickness of the DI is adjusted online depending on the solute concentration and temperature.

### 1.3.3 Global Models

Zatko et al. (2016a) incorporates a parameterisation of $NO_3^-$ photolysis within an idealised snowpack into a global transport model (GEOS-Chem) to estimate the associated snow-sourced $NO_x$ flux and redistribution of reactive nitrogen across Antarctica and Greenland. The spatial patterns of $NO_x$ are determined by 1) the spatial patterns of liquid-absorbing impurity concentration in snow, which changes the penetration depth of radiation; 2) surface temperatures, which changes the quantum yields for $NO_3^-$ photolysis; and 3) the amount of 'photolabile' $NO_3^-$. The 'photolabile' $NO_3^-$ is referred to the dry deposited $NO_3^-$ originated from long range transport and stratosphere as well as downward recycled flux of $HNO_3$ while the wet deposited $NO_3^-$ are assumed to be embedded in the interior of the snow grain and has a negligible contribution to the $NO_x$ emission. The ratio between the concentration of dry deposited photolabile $NO_3^-$ and total $NO_3^-$ (dry + wet deposition) is adjusted in the model and that the major uncertainties in Zatko et al. (2016a) model are the quantum yield for $NO_3^-$ photolysis and the concentration of

photolabile $NO_3^-$. Their results also suggested the reactive nitrogen is recycled multiple times between air and snow across most of Antarctica, except near the coast. In Greenland, only central Greenland experience multiple recycling, as it is closer to pollution sources that the source of dry deposition is mainly via transport. For the same reason, the influenced by $NO_x$ emission from snow in the Greenland boundary layer is less as its proximity to pollution sources.

To summarise, all the previous developed snow-chemical models requires empirical parameterisations or tuning parameters, which are optimised with respect to a particular set of observations, to provide a match between the modelled results and observations due to the gaps in knowledge of both the physical and chemical interactions between the air and snow. These models help to improve the understanding of the interaction and exchange between air and snowpack, however, it might only be valid at a particular site and also have limited predictive capability.

## 1.4 Aims of the thesis

The aim of this PhD project is to improve the predictive capability of the snow chemistry model for the emission of nitrogen oxide, $NO_x$ from sunlit snow to the overlying atmosphere by investigating the physical interaction between air and snow. The framework of the new model is based on previous 1-D air-snow model, which includes important processes such as diffusion, advection in the snowpack generated by surface wind and topography, gas and condensed phase chemistry in the snowpack, but focus on the following: 1) the attenuation of solar actinic flux, which is the main driver of the production and emission of $NO_x$ from snow via photolysis of $NO_3^-$. As suggested by Thomas et al. (2011) that an accurate description of the actinic flux within the snowpack is required, it is necessary to access the impact of parameterisation solar radiation with Beer-Lambert law, which often adopted in snow chemistry or climate models, on the photochemical production of $NO_x$ in snow; 2) develop a new multi-phase air-snow exchange model to test the hypothesis by Domine et al. (2013b), which suggests majority of the surface of snow grain is ice and if real liquid co-existed with ice at the surface of the snow grain, the liquid is concentrated in grooves at grain boundaries rather than forming a continuous liquid layer cover the whole surface of the snow grain as suggested previously; This development is crucial as it is a new way of describing the interaction between air and snow and is important in terms of improving existing model and the knowledge of snow photochemistry. 3)

to access if the multi-phase air-snow exchange model would improved the estimation of $NO_x$ emission flux as well as the dynamics of $NO_x$ and $O_3$ within the snowpack at Antarctica.

TABLE 1.2: Summary of the source term, $S_g$, of the general 1-D mass transport equation Eq. 1.10 by various snow chemistry models.

| Model / Reference | $S_g$ | note |
|---|---|---|
| Albert, 1996 | $-k_f([\mathrm{X}_g] - \frac{[\mathrm{X}_i]}{K})$ | $k_f$ is the mass transfer coefficient and $K$ is the air-ice equilibrium partition coefficient |
| McConnell et al., 1998 | $-\frac{1}{K_D}\frac{\partial[X_i]}{\partial t}$ | $K_D$ is the air-ice partitioning coefficient and $\frac{\partial[X_i]}{\partial t}$ is the rate of diffusion into and out of modeled snow grains |
| Hutterli and Rothlisberger, 1999 | $-\frac{\theta_i}{\theta_a}k_b([\mathrm{X}_g]K_D - [\mathrm{X}_i])$ | $k_b$ is the mass transfer coefficient, where $k_b = k_{ba}e^{(-k_{bb}/kT)}$ and $K_D$ is the ice-air equilibrium partition coefficient, where $K_D = \frac{SSA}{\theta_i}K_{Da}\sqrt{T}e^{(K_{Db}/kT)}$) |
| Liao and Tan, 2008 | $P-D-k_{mt}\frac{LWC}{1-LWC}([\mathrm{X}_g] - \frac{[\mathrm{X_{DI}}]P_{air}}{H})$ | $P$ and $D$ are the chemical production and loss terms, $k_{mt}$ is the mass transfer coefficient, $LWC$ is the dimensionless liquid water content, $P_{air}$ is the air pressure and $H$ is the Henry's law constant, |
| Thomas et al., 2011 | $P-D-k_{mt}(\omega_1[\mathrm{X}_g] - \frac{[\mathrm{X_{DI}}]}{k_{\mathrm{H}}^{cc}})$ | $P$ and $D$ are the chemical production and loss terms, $k_{mt}$ is the mass transfer coefficient, $\omega_1$ is the dimensionless liquid water content ($\mathrm{m}^3_{\mathrm{aq}}/\mathrm{m}^3_{\mathrm{air}}$) of the snow LLL and $k_{\mathrm{H}}^{cc}$ is the dimensionless Henry's law constant, |
| Toyota et al., 2014 | $P_g - L_g[\mathrm{X}_g] - \frac{1-\phi}{\phi}k_{mt}([\mathrm{X}_g] - \frac{[\mathrm{X_{DI}}]}{K_{\mathrm{H}}RT})$ | $P_g$ and $L_g$ is the chemical production and lost terms in gas phase, $\phi$ is the porosity of the snowpack and $K_{\mathrm{H}}$ is the Henry's law conefficient |
| Murray et al., 2015 | $P-D-V_rk_{mt}([\mathrm{X}_g] - \frac{[\mathrm{X_{DI}}]}{K_{\mathrm{H}}})$ | $P$ and $D$ are the chemical production and loss terms, $V_r$ is the volumetric ratio of QLL to interstitial air, $k_{mt}$ is the mass transfer coefficient and $K_{\mathrm{H}}$ is the dimensionless Henry's law constant |

$[\mathrm{X}_g]$ is the concentration in the gas phase, $[\mathrm{X}_i]$ is the concentration in the ice phase, and $[\mathrm{X_{DI}}]$ is the concentration in the QLL

# Chapter 2

# Methods

## 2.1 Model Overview

To estimate the emission flux and vertical distribution of trace gases in the snowpack interstitial air, such as $NO_x$ and $O_3$, as well as the snow nitrate $NO_3^-$ profile in the near surface snow, a one-dimensional (1D) air-snow model is created. Building on an existing 1D model, the new model (Fig. 2.1) includes optical radiation and heat transfer in snow, windpumping, gas-phase diffusion, interfacial transfer of chemical species, solid-phase diffusion, and heterogeneous chemical reactions. The main focus of this work is on improving the description of the interaction between air and snow of $HNO_3$, and hence, improve the predictive capacity of air-snow model.

Each component of the 1D model is to be discussed in details in the following sections. In brief, the photolysis rate coefficient of a photochemical reaction, $J$, is a function of the actinic flux, $I$, the quantum yield of the photolysis reaction, $\Phi$, and the absorption cross-section of the photolysis species, $\sigma$ (Eq. 1.9). Therefore, the radiative-transfer (Ch.2.2) through the atmosphere and in snow is important for determining the actinic flux in snow and rate of photochemical reactions above and in snow ; Heat transfer (Ch.2.3) is required for estimating the temperature profile within snowpack, which has impacts on the rate of chemical reactions, rate of diffusion, condensation, and interfacial mass transfer ; Both gas-phase diffusion (Ch.2.4.1) and windpumping (Ch.2.4.2) responsible for the transport of trace gases in and out as well as up and down the snowpack ; The interfacial transfer is the interactions between air and ice and is referred as the mass transfer to and from the gas-phase and condensed-phase; The solid-phase diffusion is to describe the movement of species within the snow grain; and the model includes gas-phase chemistry in the atmosphere and both gas-phase and condensed-phase chemistry in the snowpack (Ch. 2.7.2).

The air-snow interaction model is validated with year long data set from

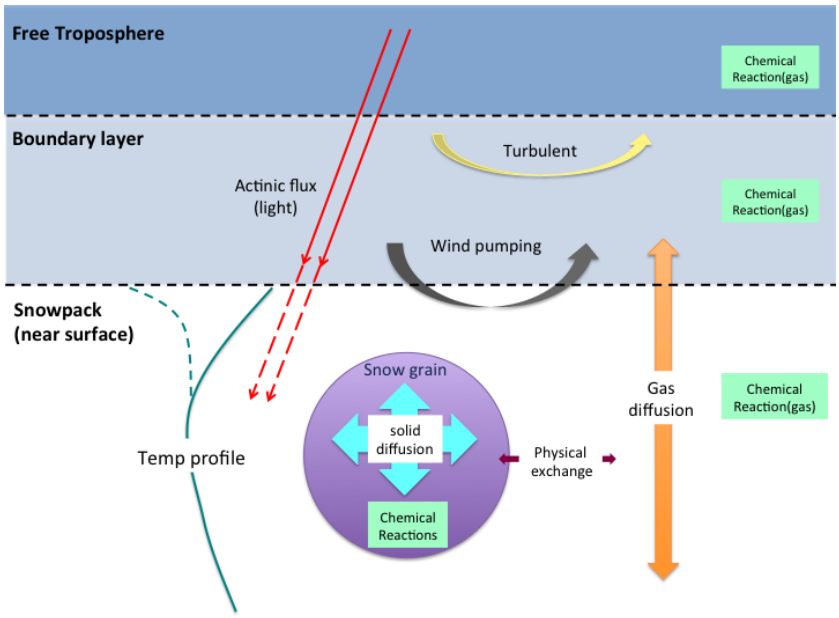


FIGURE 2.1: 1D air-snow exchange model schematic which included gas phase chemical reactions in the upper and lower troposphere and snowpack, attenuation of actinic flux, wind pumping and gas phase diffusion across the boundary layer and the surface of the snowpack, heat transfer within the snowpack, exchange between snow grain and SIA, ice phase chemical reactions and solid state diffusion within snow grain.

Halley, coastal Antarctica and Dome C, Antarctic Plateau (Ch.2.6.1). However, due to data availability the complete 1D model is validated with summer time data set from Dome C. The snowpack is limited to the photic zone, the depth where actinic flux can penetrate to and often defined as 3-4 times the $e$-folding depth. In Antarctica, where the temperature is low and has a relatively small influence from light absorbing impurities, the typical $e$-folding depth is around tens of $\mathrm{cm}$. Therefore, in this study, the working layer is limited to the top 1 $\mathrm{m}$ of the snowpack.

## 2.2 Radiative Transfer

Radiation is the propagation of photon, a quantum of electromagnetic energy that has no mass and no electric charge. Before the solar radiation reaches the ground, it might have been scattered, absorbed, or transmitted by air molecules, pollutants, water droplets or clouds when traveling through the atmosphere or by snow grain when propagating in the snowpack.

The probability of a photon being scattered or absorbed by a particle can

be represented by the scattering coefficient, $\kappa_{\text{scatt}}$, and the absorption coefficients, $\kappa_{\text{abs}}$, respectively. The sum of the absorption and scattering coefficient is known as the extinction coefficient, $\kappa_{\text{ext}} = \kappa_{\text{scatt}} + \kappa_{\text{abs}}$. The ratio of scattering to total extinction is known as the single scattering albedo, $\omega_0 = \kappa_{\text{scatt}}/\kappa_{\text{ext}}$. Here, we focus on the transfer of photons in the UV and visible wavelength as those wavelengths are the driving force for all tropospheric photochemical processes.

Scattering is the combined effects of reflection, refraction and diffraction. The angular distribution of radiation intensity scattered is related to the wavelength of the incident radiation, $\lambda$, and as well as the size of the particle, $D_p$, which can be expressed as the dimensionless size parameter, $\alpha_{scatt} = \frac{\pi D_p}{\lambda}$ and the angle deviated from the photon's original path after scattering is referred as the scattering angle, $\Theta$. Scattering can be approximated by geometric optics when the size of the particle is much larger compares to the wavelength of the radiation, i.e. $\alpha_{scatt} \gg 1$. When the particles are similar size to the wavelength of the radiation, i.e. a water droplet or a large aerosol particles in the air that the size parameter $\alpha_{scatt} \simeq 1$, the scattering of radiation is described by the Mie Theory (Fig. 2.2), where the scattering angle and intensity of the scattered radiation is found by a complex scattering phase functions. The distribution of the scattered intensity can be expressed by the asymmetry parameter, $g$, which is a function of the phase function. For $g = 1$, it indicates light scattered in the forward direction ($\Theta = 0°$), $g = -1$ for light scattered completely in the backward direction ($\Theta = 180°$).

Rayleigh scattering is to describe the scattering of radiation by particles with similar diameters as its wavelength (i.e. $\alpha_{scatt} \ll 1$) One of the characteristics of Rayleigh scattering is the radiation scatter symmetrically in the forward and backward direction. The intensity of the forward and backward scattered radiation are equal and at $\Theta = 90°$, the intensity of the radiation is half of the forward/back scatter. The Rayleigh scattering is the dominant regime of scattering in the atmosphere, of which the size of air and gas-phase molecules are much smaller than the wavelength of radiation.

The absorption spectra in the atmosphere are complex. In general, most of the incident radiation with wavelengths shorter than 290 $\text{nm}$ is absorbed by $O_2$ and $O_3$, the radiation with wavelengths between 300-800 $\text{nm}$ is weakly absorbed by the atmosphere, and from 800-2000 $\text{nm}$, the longwave radiation is moderately absorbed by water vapour in the atmosphere. In the Antarctica, the total ozone column has a strong seasonal variability due to the ozone hole that the ozone column has a minimum around spring (Chu and Anastasio, 2003). The depletion of ozone leads to an increase of short wavelength radiation reaching the ground. At the same time, at high latitude, there are also

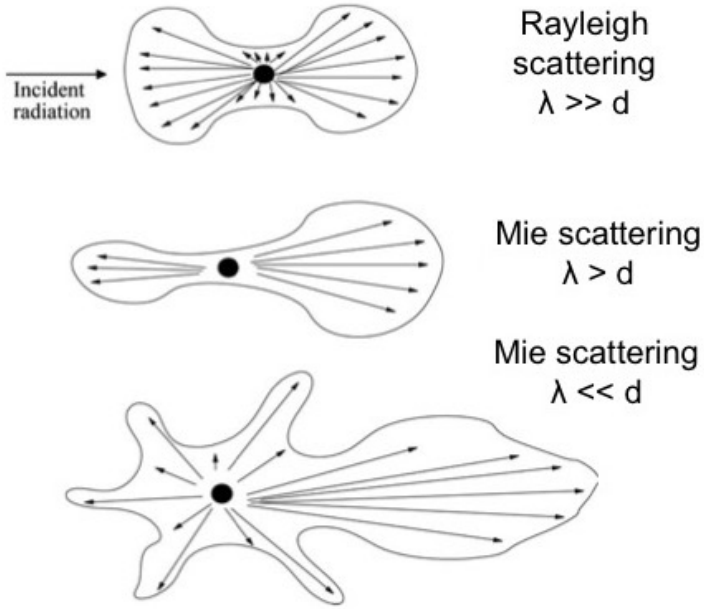


FIGURE 2.2: Scattering of incident radiation with a wavelength $\lambda$ by a particle with a diameter $d$. The angular distribution of radiation intensity scattered by a particle with a given refractive index is depends on both the wavelength of the incident radiation and the size of the particle. When the particle is much smaller than the wavelength of the incident radiation, the radiation would scatter symmetrically in the forward and backward direction, which is often referred as 'Rayleigh scattering'. When the particle is about the same size as the wavelength, the scattering and absorption of light can be computed by the 'Mie scattering' theory.

relatively less anthropogenic gases and particles, such as $CO_2$, $CH_4$, black carbon and nitrates, are suspending in the atmosphere compared to mid or low latitude. The suspended particles, depending on their size, absorption spectrum and location, can change the absorption and scattering in the atmosphere and hence changes the amount of radiation reaches the ground. The way the particles change the reflection and absorption of visible and infrared radiation can be described by the aerosol optical depth, AOD. An AOD less than 0.1 indicates clear sky with good visibility and higher the AOD implies less clear and hazier sky. The wavelength dependency of the AOD is described by the Angstrom exponent, Å, as follow

$$\frac{\mathrm{AOD}(\lambda)}{\mathrm{AOD}(\lambda_0)} = \left(\frac{\lambda}{\lambda_0}\right)^{\text{Å}} \tag{2.1}$$

where $\mathrm{AOD}(\lambda)$ is the AOD at wavelength $\lambda$ and $\mathrm{AOD}(\lambda_0)$ is the AOD at the reference wavelength $\lambda_0$.

For snow, the Mie Theory is applicable by assuming snow grains are spherical. The scattering coefficient of snow increases as the size of the snow grain decreases and the size of the snow grain is depending on the temperature and age of the snow. Smaller the snow grain implies a larger surface area per unit volume, hence, increase the chances of a photon 'meeting' an edge and gets scattered. Snow has a tendency to scatter radiation in the forward direction that it has a asymmetry parameter, $g = 0.886$ (Libois et al., 2014).

The absorption coefficient of snow depends on the combination of absorption by ice and by the impurities within the snow, such as Black Carbon (BC), dust, and HUmic LIke Substances (HULIS). The absorption in the

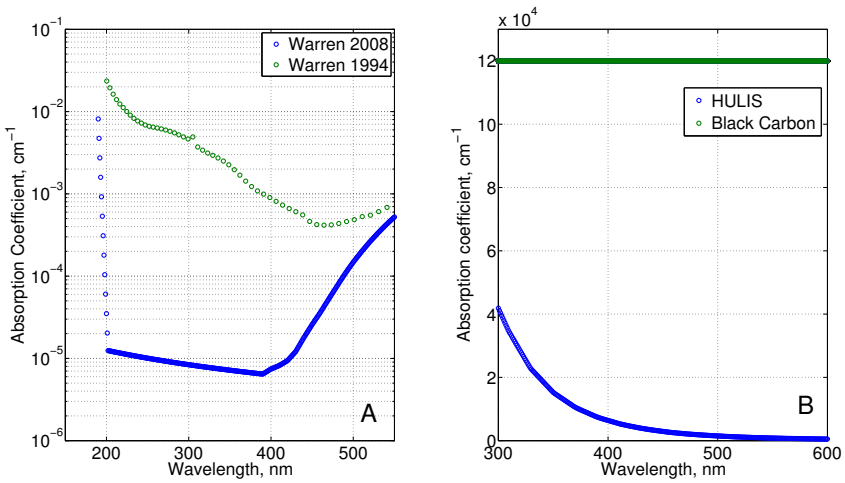


FIGURE 2.3: A) Absorption coefficient of pure ice as a function of wavelength $\lambda$, in $\mathrm{cm}^{-1}$ by Warren (1984) in Green and the revised compilation Warren and Brandt (2008) in Blue. B) Absorption coefficient of HULIS and Black carbon in $\mathrm{cm}^{-1}$.

near-UV and blue wavelengths of pure ice is really small (Fig. 2.3A, Warren and Brandt, 2008) and that is the reason for why glacier and borehole in snow appear blue as red preferentially absorbed. The wavelength dependency of the overall absorption coefficient of snow depends on the type and quantity of the impurities. For example, the absorption of HULIS decreases with wavelength while the absorption of BC is effectively independent of the wavelength while the absorption of HULIS decreases with wavelength Fig. 2.3B). The scattering coefficient of pure snow, in the near-UV and visible wavelengths, is much larger than the absorption coefficient that the single scattering albedo, $\omega_0$, is close to unity. The absorption increases as wavelength increase into the infrared region (Fig. 2.3A).

The attenuation of actinic flux through the atmosphere and within snowpack can be estimated by radiative transfer models. The Tropospheric Ultraviolet and Visible model-snow, TUV, developed by Lee-Taylor and Madronich

(2002) is one of the more advanced radiative transfer models which coupled the radiative transfer between the atmosphere and the snowpack, where the optical properties of the snowpack is defined by scattering, $\kappa_{\text{scatt}}$, and absorption coefficients, $\kappa_{\text{abs}}$, as well as the asymmetry factor, $g$.

The values of scattering, $\sigma_{\text{scatt}} = \kappa_{\text{scatt}}/\rho_{snow}$, and absorption cross-section, $\sigma_{\text{abs}} = \kappa_{\text{abs}}/\rho_{snow}$, which are the scattering and absorption coefficient adjusted by the snow density respectively, can be determined by TUV from the measured reflectance and $e$-folding depth, $z_e$, the depth at which incident radiation has been reduced to $1/e$ ($\sim 37\%$) of it initial value. A range of values of $\sigma_{\text{scatt}}$ and $\sigma_{\text{abs}}$ were used to calculate the irradiance at different depth in snow, which were then used to interpret a range of values of reflectance and $e$-folding depth. The values of $\sigma_{\text{scatt}}$ and $\sigma_{\text{abs}}$ of a particular snowpack can then be found by matching the modelled and measured reflectance and $e$-folding depth.

TUV version 4.4 was used in this study. A few edits regarding the absorption coefficient of pure ice by Warren and Brandt (2008), the quantum yield and adsorption cross-section of photochemical reactions of $NO_3^-$ (Chu and Anastasio, 2003), $NO_2^-$ (Chu and Anastasio, 2007) and $H_2O_2$ (Chu and Anastasio, 2005) at 258 K were added to the reaction list. The absorption peak of $NO_3^-$, $NO_2^-$ and $H_2O_2$ at sub-zero temperature are between 320 and 375 nm, therefore, it is important to adopt the most recent adsorption cross-section of pure ice of which the adsorption in the blue and near-ultraviolet (200 - 390 nm) are few orders of magnitude smaller than the previous estimation by Warren (1984) (Fig. 2.3A). The values of absorption coefficient of ice by Warren (1984) had to be revised, especially in for wavelengths between 250-600nm, as the attribution of scattering in ice in the UV and visible wavelengths has been underestimated in the laboratory measurements. The attenuation of radiation in the UV and visible wavelengths is dominated by scattering in ice, the revised values of absorption coefficient of ice by Warren and Brandt (2008) is comparable to the field measured values by Ackermann et al. (2006).

The computational cost of running a complete radiative transfer model on a global scale model is expensive that many snow photochemical models simplified the transmission of radiation in snow with Beer-Lambert law, which the actinic flux, $I$, as a function of depth, z, and the $e$-folding depth, $z_e$:

$$I(z) = I_0 e^{\frac{z-z_0}{z_e}} \tag{2.2}$$

where $I_0$ and $z_0$ are the actinic flux and depth at the reference depth, i.e. at the surface of the snowpack, z = 0. The $e$-folding depth parameterisation is simple and provide a good estimation of actinic flux profile in the asymptotic

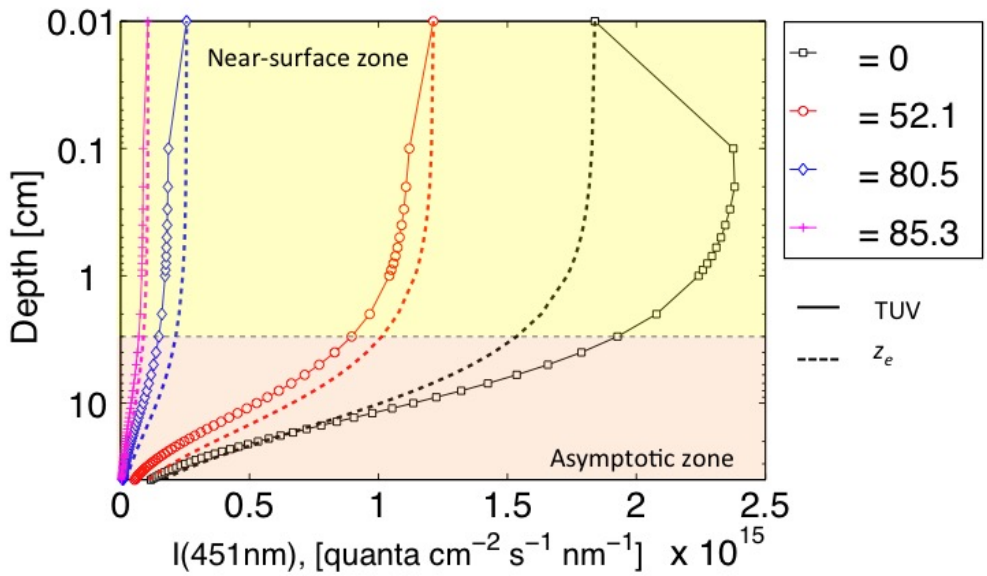


FIGURE 2.4: Modelled depth profile of actinic flux ($\lambda = 451\text{nm}$) in the upper snow, results from TUV in solid and results from Eq.2.2 in dashed line. In the 'near-surface zone', there is an enhancement at small solar zenith angle ($< 30°$) due to the conversion of direction radiation to diffuse radiation and rapid attenuation of actinic flux for large solar zenith angle ($> 80°$) as photons tends to scatter upwards and out of the snowpack.

zone, where the radiation is completely diffused and attenuate exponentially. However, it can lead to over or underestimation of actinic flux in the near surface zone (See Fig. 2.4) by neglecting the complex subsurface enhancement mechanism due to the combination of direct radiation is converting to diffusion radiation by scattering near the surface and upwelling radiation escaping the snowpack. A detail study on the difference between the radiative transfer model, TUV, and the $e$-folding depth parameterisation in estimating the actinic flux profile, and hence, photolysis rate coefficient, for different types of snowpack is presented in Ch. 3.

## 2.3 Heat Transfer in Snow

The transport of heat within the snowpack is driven by different physical processes, including 1) thermal conduction of heat through the network of interconnected snow crystal; 2) thermal conduction through the snow interstitial

air (SIA); 3) latent heat exchange through condensation and sublimation under the almost always exist temperature gradient in dry snow; and 4) thermal convection which driven by wind flowing over surface roughness. The combination of the first three processes can be expressed as the effective thermal conductivity, $k_{\text{eff}}$, which can be measured by inserting a heated needle probe into the snowpack and analysing the rate of dissipation of the heat pulses sent by the probe (Courville et al., 2007). Sturm and Benson (1997) also proposed a parameterisation of $k_{\text{eff}}$ for seasonal snow based on the density, $\rho_{snow}$, of the snowpack, however, the parameterisation is not applicable to polar snowpack (Domine et al., 2008). The thermal conductivity of air, $k_{air}$, is significantly lower than the thermal conductivity of ice, $k_{ice}$, at the temperatures found in the polar regions, for example, at -40 °C, $k_{air} = 0.021\text{Wm}^{-1}\text{K}^{-1}$ (Haynes, 2016) whereas $k_{ice} = 2.60\text{Wm}^{-1}\text{K}^{-1}$ of which the thermal conductivity of ice is calculated as $k_{ice} = 9.828e^{-0.0057T}$ (Paterson, 1994). The sensible heat fluxes are likely to be much larger than the latent heat fluxes due to the low temperatures found in Antarctica, especially at Dome C where the atmospheric moisture content is low (Gallée et al., 2015). Therefore, the thermal conductivity of the polar snowpack can be simplified as follow by only considering conduction through the snow crystal:

$$k_{snow} = k_{ice}\left(\frac{\rho_{snow}}{\rho_{ice}}\right)^{2-0.5\frac{\rho_{snow}}{\rho_{ice}}} \tag{2.3}$$

where $\rho_{snow}$ is the density of snowpack and $\rho_{ice}$ is the density of ice. This simplification agrees well with the observed effective thermal conductivity from East Antarctica near-surface snow, which $k_{\text{eff}}$ = 0.2-0.4 $\text{W m}^{-1}\,\text{K}^{-1}$ for density between 350-450 $\text{kg m}^{-2}$ (Courville et al., 2007).

Assuming there are no lateral heat transport, i.e. the horizontal temperature gradients are very small, no internal heat production and the snowpack is an semi-infinite medium, the heat transfer in snow can be expressed as

$$\frac{\partial T}{\partial t} = \frac{\partial}{\partial z}\left(\frac{k_{snow}}{\rho_{snow}\,c}\right)\frac{\partial T}{\partial z} \tag{2.4}$$

where $T$ is the temperature, $z$ is depth, $t$ is time, $c$ is the specific heat capacity, and $c\,(\text{J kg}^{-1}\,\text{K}^{-1}) = 152.2 + 7.122T$ (Paterson, 1994). The temperature profile within the snowpack is driven by the observed surface temperature of the snowpack, $T_{skin}$, and the initial temperature profile is estimated as follow (Paterson, 1994):

$$T(z,t) = A_t\, e^{(-z\sqrt{\frac{\omega}{2k_{snow}}})}\sin\left(\omega t - z\sqrt{\frac{\omega}{2k_{snow}}}\right) \tag{2.5}$$

where $A_t$ is the amplitude of the temperature change, $\omega$ is the frequency of the surface temperature change. Eq. 5.13 was solved by the Crank-Nicholson method described in Sect. 2.7.1 with a spin up time of 30 days. An example of the model output from the heat transfer model is shown in Fig. 2.5, where the normalised measured and modelled temperature, $\hat{T}$, is plotted at various depth. The normalised temperatures were plotted due to the difference in measuring techniques and they were not calibrated against each other. The skin temperatures, which used as the boundary condition for the temperature model, were measured with IR-sensor. Whereas the temperatures further down the snowpack were measured with thermocouples. Even the thermocouples were wrapped up in white teflon tape, it is likely to absorb light and created a positive bias.

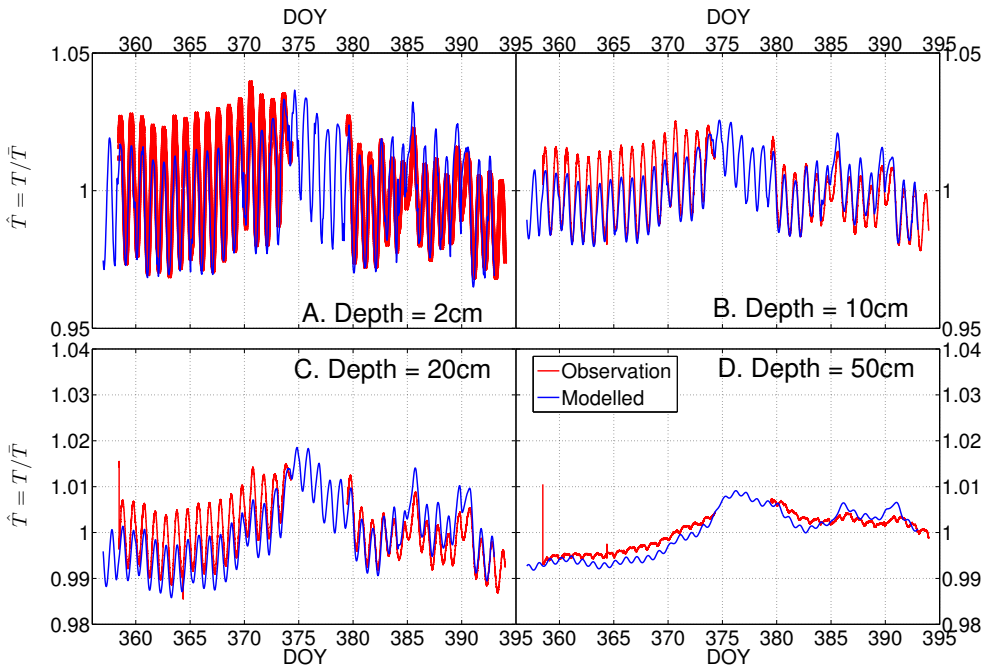


FIGURE 2.5: Normalised observed(red) and modelled (blue) temperatures, $\hat{T}$, at depth A) 2 cm, B) 10 cm, C) 20 cm and D) 50 cm at Dome C between 2009-2010 (Frey et al., 2013).

The major diurnal variation at different depths was captured, however, the mismatch might be caused by 1) positive bias of the thermocouples that absorb more sensible heat, especially during mid-day; 2) inaccurate thermal conductivity due to neglecting latent heat transport and lack of accurate density measurement of the snowpack. There were no density profile measurements were taken together with those temperature measurements and only a mean Dome C density profile (Gallet et al., 2011) were used when determining the thermal conductivity (Eq. 5.14). However, the spatial variation of

the snowpack stratigraphy can be large at Dome C (See Ch. 2.6.4) and an increase in snow density would increase the diffusion coefficient, hence, a more effective transport of heat; 3) the heat transport caused by convection were not taken into account, howver, it is suggested that the turbulent condition is only effective in the shallow layer (Pietroni et al., 2014). Furthermore, the wind speed at Dome C is generally low (average wind speed at 3.3 $\mathrm{m}$ above ground was ~2.5 $\mathrm{m\,s^{-1}}$ in December 2009- January 2010).

## 2.4 Macroscopic Mass Transport in Snowpack

The transport of chemical species can be separated into macroscopic and microscopic level. The macroscopic mass transfer is referred as the vertical transport of species from local atmosphere into the snow as well as the distribution of chemical species within the snow caused by both molecular diffusion (Ch.2.4.1) and windpumping (Ch.2.4.2).

### 2.4.1 Molecular Diffusion within Snow Interstitial Air

Molecular diffusion in snow interstitial air, SIA, play an important role in the transport of trace gases in polar snowpack despite being a relatively slow process, especially at sites with low wind speed (Albert and Shultz, 2002). The diffusivity of a gas molecule in air, $D_g$, can be parameterised by Jacobson (1999) as

$$D_g = \frac{5}{16\,A\,di^2\,\rho_{air}}\left(\frac{R\,T\,M_{air}}{2\pi}\frac{M_{\mathrm{HNO_3}}+M_{air}}{M_{\mathrm{gas}}}\right) \tag{2.6}$$

where $A$ is the Avogadro's number, $R$ is the universal constant, $\rho_{air}$ is the density of air, $M_{air}$ is the molecular weight of dry air, $M_{\mathrm{gas}}$ is the molecular weight of the gas molecule (e.g. $HNO_3$) and $d_i$ is the diameter of the gas molecule (the average diameter of a gas molecule is 4.5-5$\times 10^{-10}$ $\mathrm{m}$). The diffusivity can also be approximated using mean free path length and thermal velocity, $\nu$, as follow (Atkins and Paula, 2010)

$$D_g = \frac{1}{3}\frac{2\eta}{\rho_{air}\nu_{air}}\nu_{\mathrm{gas}} \tag{2.7}$$

where $\eta$ is the viscosity of air, $\nu_{air}$ and $\nu_{\mathrm{gas}}$ is the thermal velocity of the air and the targeted gas molecule. The thermal velocity is defined as $\nu = \sqrt{\frac{8\,R\,T}{\pi M}}$, where $M$ is the molecular mass of air or gas molecule.

To minimise the additional errors that might arise using parameterised diffusivity, here, we used the measured gas phase diffusivity by Tang et al. (2014). All the measurements were done at 296 $\mathrm{K}$ and assuming the temperature dependence can be described by Fuller's method the diffusion coefficient

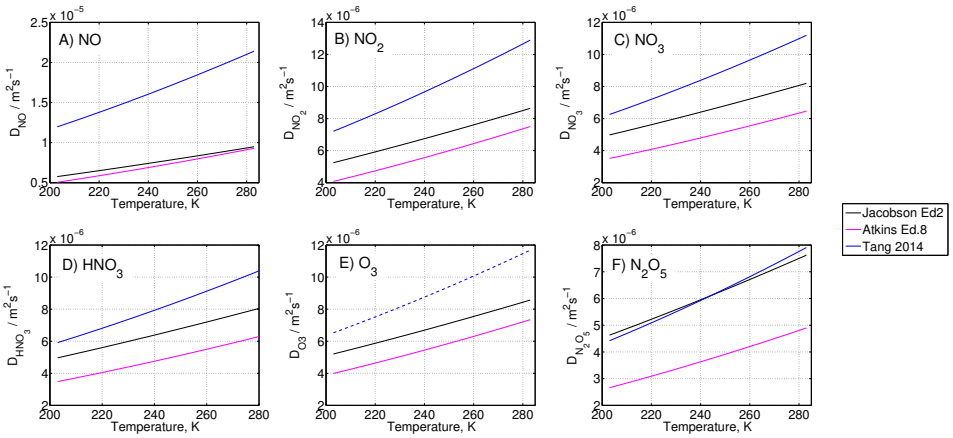


FIGURE 2.6: Comparison the different parameterisations of diffusivity in air as a function of temperature by Jacobson (1999) in black, Atkins and Paula (2010) in pink, Tang et al. (2014) in blue, and Ivanov et al. (2007) in dash line ($O_3$ only) for A) NO; B) $NO_2$; C) $NO_3$; D) $HNO_3$; E) $O_3$ and F) $N_2O_5$

at temperature $T$ can be expressed as

$$D_g(T) = D_g(296\mathrm{K}) \left(\frac{296}{T}\right)^{-1.75} \tag{2.8}$$

The diffusivity of $HNO_3$ in air is 87±7 $\mathrm{Torr\,cm^2\,s^{-1}}$, measured by using denuders at 296 K. The diffusivity of other gases used in this study, such as NO, $NO_2$, $NO_3$, and $N_2O_5$, were measured using flow tubes and have a values of 176±18, 106±37, 92±46, 65±33 $\mathrm{Torr\,cm^2\,s^{-1}}$ at 296 K respectively. Despite the importance of $O_3$ and $HO_2$ in the troposphere and stratosphere, there is no measurement of the diffusivity of $O_3$ and $HO_2$ in air (or $N_2$ / $O_2$) available. Therefore, an estimated value for the diffusivity of $O_3$ and $HO_2$ was used, which have a value of 96 and 107 $\mathrm{Torr\,cm^2\,s^{-1}}$ at 296 K, respectively. The parameterisations of diffusivity of different chemical species in air summarised in Fig. 2.6.

In snow, the molecules have to diffuse within the pore space of the porous snow, that the diffusivity of species in snow has to scaled by the tortuosity, $\tau$, of the snowpack. The tortuosity is often defined as the squared ratio of the minimum possible path length to the mean path length. Albert and Shultz (2002) found the tortuosity of the surface wind-packed snow is ~0.5. The diffusivity of a gas-phase species in snow due to molecular diffusion, $k_{\mathrm{diff}}$, is expressed as

$$k_{\mathrm{diff}} = \tau\, D_g \tag{2.9}$$

### 2.4.2 Windpumping

Windpumping is to describe the air flow in snow due to the pressure gradients exert over a snow surface, which has a major impact on dry deposition of chemical species from the atmosphere into the snow. The pressure gradients can be created by barometric pressure variations, wind turbulence and steady wind flow over topography (Waddington et al., 1996, therein). Barometric pressure variations are caused by synoptic weather systems of which the air pressure can change on the order of 5% over periods of a few days. A rise in air pressure would force air into the snowpack and a reduction in air pressure would draw air out. However, the air flow rate in snow and the aerosol deposition velocity due to the barometric changes are found to be negligible (Waddington et al., 1996, therein). The pressure changes due to wind turbulence are faster than the pressure changes due to barometric variation. Wind turbulence can increases the air flow in surface and particle deposition velocity by tenfold depending on the wind speed and the permeability of snow. However, for turbulent ventilation, the air masses are moves from the boundary layer, which is already depleted of aerosols and trace gases, into the snow that the dry deposition flux should still be very small.

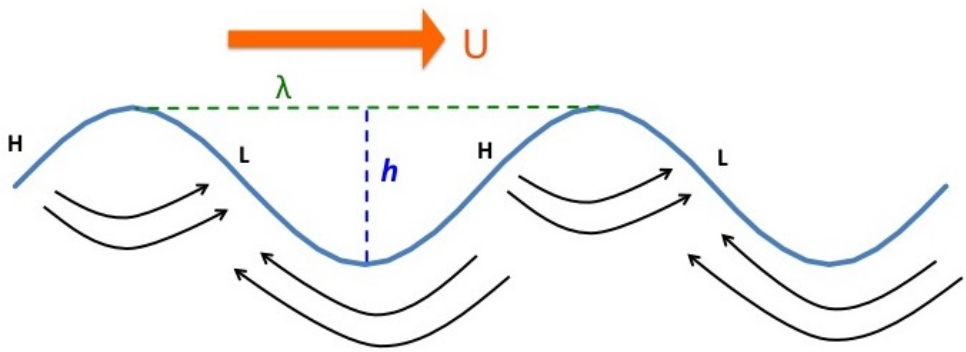


FIGURE 2.7: Pressure different induced by horizontal wind across topography bump.

Steady air flow within the snow is driven by horizontal wind flow over an uneven surface (Fig. 2.7). The dynamic wind pressure causes air pressure to build up on the upwind face of a topographic bump while the airfoil effect lowers the pressure on the lee side near the crest of the bump. The distribution of the pressure within snow is depending on the shape and orientation of the topographic bump. The pressure gradient across the surface created by the topography is found to be much bigger than the pressure gradient caused

by barometric pressure and turbulence. The maximum pressure different induced by steady flow over an uneven surface is given by

$$p_0 = C\,\rho_{air} U_{10}^2 \frac{h}{\lambda} \tag{2.10}$$

where $C$ is an empirical constant of proportionality ($C \approx 3$), $U$ is the wind speed at 10 $\mathrm{m}$ above ground, $h$ and $\lambda$ are the height and wavelength of the topography bump. The pressure induced by topography decreases with depth, and hence, the sub-surface air flux in the vertical direction, $Q_z$, is a function of the pressure induced at the surface, $p_0$, depth, $z$, permeability, $k_p$, of the snowpack, viscosity of air, $\mu$, induced pressure at the surface, $p_0$, and the windpumping $e$-folding depth, $\delta$.

$$\bar{Q_z}(z) = \frac{k_p}{\mu} \frac{p_0}{\pi^2} \frac{1}{\delta}\, e^{-\frac{z}{\delta}} \tag{2.11}$$

where the windpumping $e$-folding depth, $\delta$, is defined as follow

$$\delta = \frac{\alpha_{\mathrm{asp}}}{\sqrt{\alpha_{\mathrm{asp}}^2 + 1}} \frac{\lambda}{2\pi} \tag{2.12}$$

where $\alpha_{\mathrm{asp}}$ is the horizontal aspect ratio of the topographic bumps. The topographic bumps are elongated in the direction of the wind for $\alpha_{\mathrm{asp}} < 1$, and elongated across the wind for $\alpha_{\mathrm{asp}} > 1$. Substituting Eq. 2.10 and Eq. 2.12 to Eq. 2.11, the vertical air flux can be expressed as

$$\bar{Q_z}(z) = \frac{k_p}{\mu} \frac{6\rho_{air} U_{10}^2}{\pi} \frac{h}{\lambda} \frac{1}{\lambda} \frac{\sqrt{\alpha_{\mathrm{asp}}^2 + 1}}{\alpha_{\mathrm{asp}}}\, e^{-\frac{z}{\delta}} \tag{2.13}$$

The surface topography is the dominant driving force for air flow in the snow, therefore, air flow induced by barometric pressure and wind turbulence are neglected and only topography induced flow is taken account when determining the diffusivity due to windpumping, $k_{wp}$.

$$k_{wp} = \bar{Q_z}(z)\Delta z \tag{2.14}$$

where $\Delta z$ is the thickness of the snowpack. $k_{wp}$ has the highest value near the surface and that SIA at the top few $\mathrm{cm}$ would be well mixed by wind induced air fluxes when there is a strong wind. As mentioned earlier, the gas transport in snow is depending on the sum of both molecular diffusion and windpumping. The effective diffusion constant, $\kappa$, in the snowpack is the

sum of both contributing terms

$$\kappa = k_{\text{diff}} + k_{wp} = \tau D_g + \bar{Q}_z(z)\Delta z \tag{2.15}$$

This effective diffusion constant, $\kappa$, is a key parameter for determining the vertical temporal variation in concentrations of chemical species, details are listed in paper Ch.**??**.

## 2.5 Microscopic Mass Transport in Snowpack

The microscopic mass transfer is henceforth referred as the physical exchange of mass between snow grains and the surrounding air by surface adsorption, co-condensation and solvation in liquid micropocket as well as the solid-phase diffusion within snow grain. Details of how the different processes are linked are presented in Ch.4 Sect. 3, the focus of this section is to discuss the assumptions that made and the choice of parameterisations for liquid water content (Ch.2.5.1), non-Equilibrium Kinetics (Ch.2.5.3), surface adsorption (Ch.2.5.3) and co-condensation (Ch.2.5.4) used in the final air-snow interaction mode.

First, the assumption made about the shape and size of the snow grains, which is one of the key variables for quantifying the interaction between air and snow. The snow grain is simplified as a sphere with an effective radius, $R_{\text{eff}}$, which often define using the surface to volume ratio of the snow grain, i.e. the specific surface area, SSA, as follow (BartelsRausch et al., 2014)

$$R_{\text{eff}} = \frac{3}{\rho_{ice}\, SSA} \tag{2.16}$$

where $\rho_{ice}$ is the density of ice.

### 2.5.1 Liquid Water Content

Liquid solution co-exists with ice when the temperature is above the eutectic temperature of a particular $H_2O$-X mixture, where X is a chemical compound. The eutectic temperature of a complex solution is always lower than those of the simple solutions of the components. However, for simplicity, the eutectic temperature is selected based on the mixture most abundant ion. For example, at Dome C the major ion is $NO_3^-$ (Erbland et al., 2013, details in Ch.2.6.1) and so the eutectic temperature of the $HNO_3$-$H_2O$ system is used ($T_e$ = -42.5 °C, Fig. 2.8, Thibert et al., 1998 ). At Halley, NaCl is dominating the ionic composition and so the eutectic temperature of a NaCl-$H_2O$ mixture is used ($T_e$ = -21.2 °C, Fig. 2.9, Akinfiev et al., 2001).

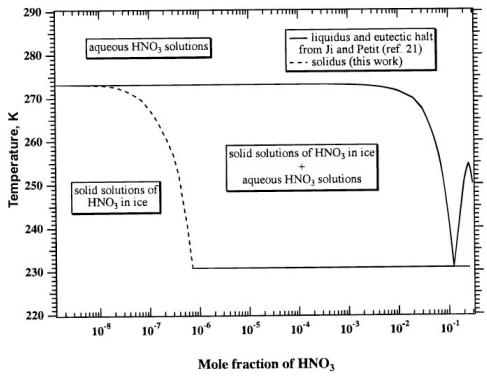


FIGURE 2.8: Reproduced by Thibert et al. (1998), Figure 5: The $HNO_3$-$H_2O$ equilibrium phase diagram at low $HNO_3$ mole fraction.

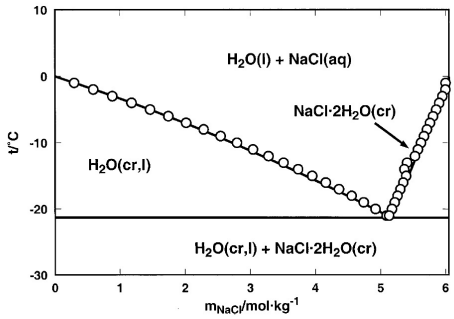


FIGURE 2.9: Reproduced by Akinfiev et al. (2001), Figure 8: The NaCl-$H_2O$ equilibrium phase diagram.

Above the eutectic temperature, the liquid water content, $\phi_{\mathrm{H_2O}}$, of an ice grain, at a given concentration of the total mixture and temperature can be derived from the phase diagram. However, in natural snow, the chemical composition is a lot more complex, i.e. it does not only contain only a single component. It is impossible to create a phase diagram for each combination of components, therefore, parameterisation by Cho et al. (2002) was applied for deriving the liquid water content.

$$\phi_{\mathrm{H_2O}}(T) = \frac{\overline{m}_{\mathrm{H_2O}} R T_f}{1000 \Delta H_f^0} \left( \frac{T}{T_f - T} \right) \Phi_{\mathrm{bulk}}^{\mathrm{aq}} \left[ \mathrm{Ion}_{\mathrm{tot(bulk)}} \right] \tag{2.17}$$

where $\phi_{\mathrm{H_2O}}(T)$ has units of $\mathrm{m}_{\mathrm{liquid}}^3\,\mathrm{m}_{\mathrm{ice}}^{-3}$, $\overline{m}_{\mathrm{H_2O}}$ is the molecular weight of water, $R$ is the ideal gas constant, $T_f$ is the freezing temperature of pure water in K, $\Delta H_f^0$ is the enthalpy of fusion in $\mathrm{J\,mol^{-1}}$, $\Phi_{\mathrm{bulk}}^{\mathrm{aq}}$ is the fraction of the total solute in the aqueous phase and $[\mathrm{Ion}_{\mathrm{tot,\,bulk}}]$ is the total ionic concentration in the melted sample. At Dome C, the total ionic concentration is simplified to be the sum of concentration of $H^+$ and $NO_3{}^-$ where as at Halley, the total ionic concentration is assumed to the sum of concentration of $H^+$, $Na^+$, $NO_3{}^-$ and $Cl^-$.

The liquid water fraction, $\phi_{\mathrm{H_2O}}$, calculated from Eq. 2.17 and the phase diagram of NaCl-$H_2O$, at various concentrations of NaCl is shown Fig. 2.10 as a function of temperature. The values of $\phi_{\mathrm{H_2O}}$ from both methods are comparable. However, note that there are uncertainties associated with Eq. 2.17 when applying to natural snow as the solute concentrations used in Cho

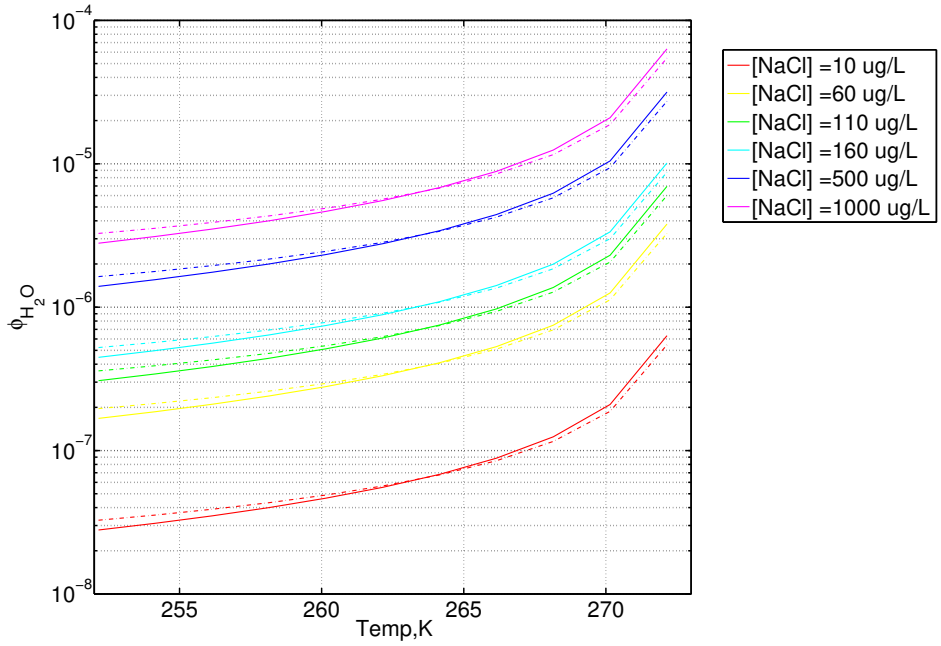


FIGURE 2.10: Liquid water fraction, $\phi_{H_2O}$, at various concentration of NaCl derived from Eq. 2.17 by Cho et al., 2002 (solid line) and by NaCl-$H_2O$ phase diagram (dashed line) as a function of temperature.

et al. (2002) experiments were orders of magnitude greater than natural snow and their ice samples were significantly smaller than natural snow crystal due to the fast freezing of very small amount of solution.

The chemical properties of the liquid water fraction are assumed to be same as the bulk liquid, of which the partitioning between air and the liquid water fraction is described by Henry's coefficient, $k_H$. By means, the liquid water fraction is assumed to have ideal behaviour. However, the concentration of solutes in the liquid water fraction is likely to be too large to be considered as an ideal dilute solution that the non-ideality should be taken into account. The non-ideal behaviour can be estimated using the activity coefficient, $\gamma$. For example, dissolution and dissociation of $HNO_3$ in liquid water involves the following reactions

$$\mathrm{HNO_3(g)} \rightleftharpoons \mathrm{HNO_3(aq)} \tag{R22}$$

$$\mathrm{HNO_3(aq)} \rightleftharpoons \mathrm{H^+(aq) + NO_3{}^-(aq)} \tag{R23}$$

$$\tag{R24}$$

$$\mathrm{Net: HNO_3(g)} \rightleftharpoons \mathrm{H^+(aq) + NO_3{}^-(aq)}$$

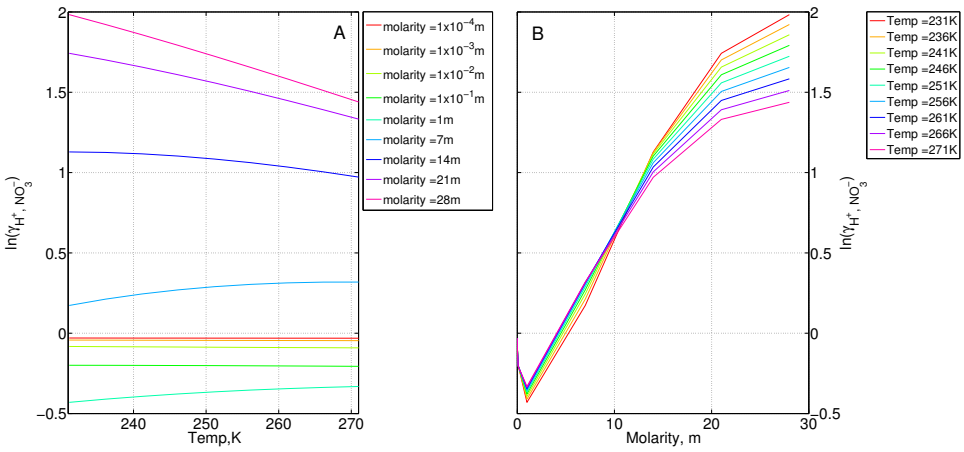


FIGURE 2.11: The mean mixed solute activity coefficient of $HNO_3$, $\gamma_{H^+,NO_3^-}$, as a function of, A) temperature; and B) molarity (Hamer and Wu, 1972).

the equilibrium coefficient of reaction R22 can be expressed as

$$\frac{\{HNO_3(aq)\}}{\{HNO_3(g)\}} = \frac{HNO_3(aq)}{HNO_3(g)} = \frac{m_{HNO_3(aq)}\gamma_{HNO_3(aq)}}{p_{HNO_3(g)}} = K_{eq,\text{dissolution}} \tag{2.18}$$

where $\{HNO_3(aq)\}$ & $\{HNO_3(g)\}$ is the activity of aqueous-phase and gas-phase $HNO_3$, $p_{HNO_3(g)}$ is the saturation vapour pressure of $HNO_3$, $m_{HNO_3(aq)}$ is the molality of $HNO_3$ in solution ($\mathrm{m}$, $\mathrm{moles}$ of solute per $\mathrm{kg}$ of solvent), $\gamma_{HNO_3(aq)}$ is the activity coefficient of dissolved but undissociated $HNO_3$ and $K_{eq}$ is the equilibrium constant. For a dilute solution, $\gamma_{HNO_3(aq)}$ = 1 and the $K_{eq}$ in Eq. 2.19 is referred as Henry's constant. Likewise, the equilibrium coefficient for the dissociation reaction R23 can be expressed as

$$\frac{\{H^+\}\{NO_3^-\}}{\{HNO_3(aq)\}} = \frac{m_{H^+}m_{NO_3^-}\gamma^2_{H^+,NO_3^-}}{m_{HNO_3(aq)}\gamma_{HNO_3(aq)}} = K_{eq,\text{dissociation}} \tag{2.19}$$

where $\gamma_{H^+,NO_3^-}$ is the mean mixed solute activity coefficient, $\gamma_{H^+,NO_3^-} = \gamma_{H^+}\gamma_{NO_3^-}$. The value of $\gamma_{H^+,NO_3^-}$ can be determined from theoretical parameterisation, i.e. the Pitzer's method (Fahidy, 1993), or measurements, i.e. by Hamer and Wu (1972). The limitation of the activity coefficient derived from the Pitzer's method is that it only accurate up to about 6 $\mathrm{m}$ whereas the measured data are accurate up to 28 $\mathrm{m}$. The temperature and molarity dependency of the mean mixed solute activity coefficient of $HNO_3$ measured by Hamer and Wu (1972) is shown in Fig. 2.11.

The overall equilibrium constant for the combined reactions of dissolution and dissociation is often referred as the effective Henry's constant, $K_{eq,\text{eff}}$,

which is the product of $K_{eq,\text{dissolution}}$ and $K_{eq,\text{dissociation}}$, such that

$$\frac{\{\mathrm{H}^+\}\{\mathrm{NO_3}^-\}}{\{\mathrm{HNO_3(g)}\}} = \frac{m_{\mathrm{H}^+} m_{\mathrm{NO_3}^-} \gamma^2_{\mathrm{H}^+,\mathrm{NO_3}^-}}{p_{\mathrm{HNO)_3(g)}}} = K_{eq,\text{eff}} \tag{2.20}$$

The measured data by Hamer and Wu (1972) are accurate up to 28 $\mathrm{m}$, it is still lower than the estimated molarity found in the liquid water fraction. Hence, it is not possible to quantify the uncertainties caused by assuming the liquid water content as an ideal diluted solution. For molality higher than ∼4-5 $\mathrm{m}$, the activity coefficient tends to increase with molarity and hence lower the equilibrium constant. Therefore, by assuming the liquid water content has an ideal behaviour, it is likely to overestimate the concentration in the aqueous-phase.

### 2.5.2 Non-Equilibrium Kinetics

The processes involved in the equilibrium of the gas-phase and the surface of a droplet (Fig. 2.12): 1) Gas-phase diffusion from far away (> $\mu\mathrm{m}$) from the droplet to the surface of the droplet, which is likely to be driven by turbulence and molecular diffusion; 2) Interfacial mass transport; and 3) Condensed-phase diffusion and chemical reactions; Under certain conditions that equilibrium might not be reached, for example, if the rate of reaction in the condensed-phase is faster than it can be replaced from the gas-phase so it will not come into thermodynamic equilibrium.

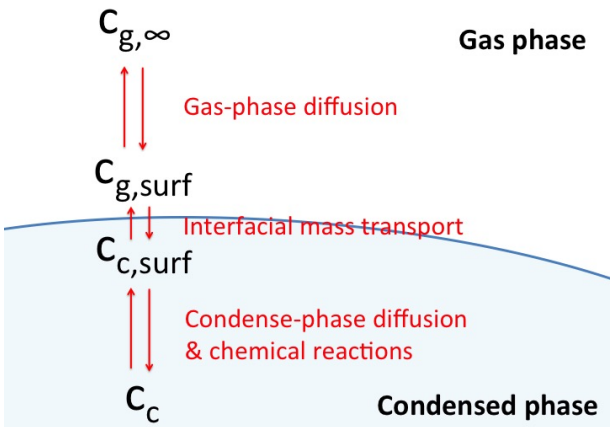


FIGURE 2.12: Processes involved in the equilibrium between gas-phase and condensed-phase, where $c_{g,\infty}$ is the gas-phase concentration in the SIA far away from the droplet, $c_{g,\text{surf}}$ is the gas-phase concentration at the surface (outside the droplet), $c_{c,\text{surf}}$ is the condensed-phase concentration at the surface (inside the droplet) and $c_c$ is the average condensed-phase concentration.

Transport of gas-phase species from the SIA to the surface of the droplet can be described using Fick's law as diffusion flux, $J_g$:

$$J_g = -D_g \frac{dc_g}{dx} \tag{2.21}$$

where $D_g$ is the gas-phase diffusivity, and $\frac{dc}{dx}$ is the concentration gradient at the droplet surface that $\frac{dc_g}{dx} = \frac{c_{g,\infty} - c_{g,\text{surf}}}{r}$ with $r$ as the radius of the droplet. The concentration change in the condense-phase can be expressed as

$$\frac{dc_c}{dt} = \frac{A\,J_g}{V} = -\frac{A}{V}\frac{D_g}{r}(c_{g,\infty} - c_{g,\text{surf}}) \tag{2.22}$$

where $A$ is the surface area of the droplet and $V$ is the volume of the droplet. The first-order rate coefficient for the gas-phase diffusion process can be defined as $k_{dg} = \frac{A}{V}\frac{D_g}{r}$ (Sander, 1999). For an example, a liquid droplet with a radius $r$ the gas-phase diffusion rate coefficient $k_{dg} = \frac{3D_g}{r^2}$.

The interfacial mass transport from gas-phase to condensed-phase can be expressed in terms of accommodation coefficient, $\alpha$. The flux through the phase boundary into the droplet, $J_b^{in}$, is defined as:

$$J_b^{in} = \frac{\alpha\bar{v}}{4} c_{g,\text{surf}} \tag{2.23}$$

where the subscript $b$ stands for 'boundary' and $\bar{v}$ is the mean molecular velocity. The opposite flux, $J_b^{out}$, through the phase boundary out of the droplet can be expressed in the similar form as Eq. 2.23 that $J_b^{out} = \frac{\alpha_a \bar{v_c}}{4} c_{a,\text{surf}}$, where $\bar{v_c}$ is the mean molecular velocity in condensed-phase and $\alpha_c$ is the condensed-phase accommodation coefficient. The net flux through the grain boundary, $J_b$, is the difference between the in and out flux.

$$J_b = J_b^{in} - J_b^{out} = \frac{\alpha\bar{v}}{4}\left(\frac{c_{c,\text{surf}}}{K} - c_{g,\text{surf}}\right) \tag{2.24}$$

where $K$ is the equilibrium constant, of which $K = c^{eq}_{c,\text{surf}}/c^{eq}_{g,\text{surf}}$. For example, for a gas-aqueous interface, the ratio of aqueous-phase concentration to gas-phase concentration at equilibrium can be described as $c^{eq}_{a,\text{surf}}/c^{eq}_{g,\text{surf}} = k_H^{cc}$, where $c_{a,\text{surf}}$ is the aqueous-phase concentration at the surface and $k_H^{cc}$ is the Henry's constant. For a gas-ice interface, the ratio between adsorbed concentration and gas-phase concentration at equilibrium can be described as $c^{eq}_{i,\text{surf}}/c^{eq}_{g,\text{surf}} = K_{eq}$, where $c_{i,\text{surf}}$ is the ice-phase concentration at the surface and $K_{eq}$ is the Langmuir adsorption equilibrium constant. The concentration change in the condensed phase due to interfacial mass transport can be expressed as:

$$\frac{dc_c}{dt} = -\frac{A\,J_b}{V} = \frac{A}{V}\frac{\alpha\bar{v}}{4}\left(c_{g,\text{surf}} - \frac{c_{c,\text{surf}}}{K}\right) \tag{2.25}$$

The first-order rate coefficient for the interfacial mass transport can then be defined as $k_i = \frac{A}{V}\frac{\alpha\bar{v}}{4}$. For an example, a liquid droplet with a radius $r$ the diffusion rate coefficient $k_i = \frac{3\alpha\bar{v}}{4r}$.

Assuming the fluxes of gas-phase diffusion, $J_g$, is equal to the interfacial mass transport, $J_b$, and the concentration of condensed-phase species, $c_c$, is homogeneous, i.e. $c_{c,\text{surf}} = c_c$, that the rate of change of concentration in the condensed phase can be expressed as (See App.A for deviation of the expression)

$$\frac{dc_c}{dt} = \frac{A}{V}\left(\frac{r}{D_g} + \frac{4}{\bar{v}\alpha}\right)^{-1}\left[c_{g,\infty} - \frac{c_c}{K}\right] \tag{2.26}$$

the term ' $\frac{A}{V}\left(\frac{r}{D_g} + \frac{4}{\bar{v}\alpha}\right)^{-1}$' is often referred as the mass transfer coefficient, $k_{mt}$, for a chemical species transfer from air to liquid/solid. The mass transfer coefficient for chemical into a liquid spherical droplet with radius $r$ would be $k_{mt} = (\frac{r^2}{3D_g} + \frac{4r}{3\bar{v}\alpha})$. Note that this derivation of $k_{mt}$ is often used for describing the mass transfer between air and DI in previously developed models (e.g. Liao and Tan, 2008; Thomas et al., 2011; Toyota et al., 2014; Murray et al., 2015, , as shown in Table. 1.2). In those models, the DI is assumed to be covering the entire surface of the snow grain, i.e. the DI has a surface area of $\sim 4\pi r^2$, however, the volume of the DI is only a fraction of the volume of the snow grain, i.e. $V_{DI} = \phi_{\text{H}_2\text{O}} V_{grain}$. Therefore, using a mass transfer coefficient of a liquid droplet is likely to be underestimated the mass transfer through the boundary as the flux is divided by the volume of the entire snow grain instead of the volume of DI.

### 2.5.3 Surface Adsorption on Ice

For the surface adsorption of $HNO_3$ on snow in Antarctica, it was assumed the surface of the snow grain and the surrounding air are not in equilibrium and is defined as

$$\frac{d[\text{HNO}_{3(\text{ads})}]}{dt} = k_{\text{ads}}\left([\text{HNO}_{3(g)}][\text{S}] - \frac{[\text{HNO}_{3(\text{ads})}]}{K_{\text{eq}}}\right) \tag{2.27}$$

where $[\text{HNO}_{3(\text{ads})}]$ is the surface concentration of $HNO_3$ on ice due to the net surface adsorption, [S] is the concentration of available surface site, and $K_{eq}$ is the Langmuir adsorption equilibrium constant. A non-equilibrium approach is taken as concentration of nitric acid in the atmosphere in Antarctica is below the concentration for saturating adsorption surface site (Ullerstam et al., 2005) and the constant sublimation and condensation of water vapour are likely to prevent the adsorption equilibrium being reached (details see paper Ch. 4, Sect. 3.1.1). Here, the choice of surface adsorption related parameters,

such as Langmuir adsorption equilibrium constant, $K_{eq}$, and the reference accommodation coefficient, $\alpha_0$, are discussed.

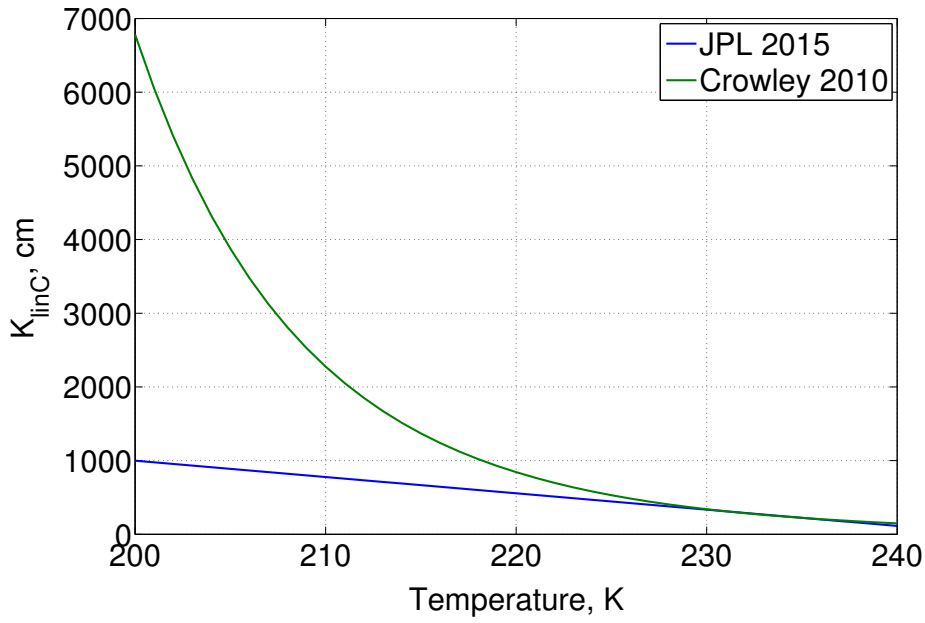


FIGURE 2.13: Partitioning coefficient of $HNO_3$ to an ice surface as a function of temperature by parameterisation recommended from Burkholder et al. (2015), in blue, and Crowley et al. (2010), in green.

Burkholder et al. (2015) and Crowley et al. (2010) recommended two different $K_{eq}$ parameterisations for $HNO_3$ adsorption on an ice surface (with units of $\mathrm{cm^3 molecule^{-1}}$) both valid for temperature between 214 to 240 K. Burkholder et al. (2015) suggested $K_{eq}$ for $HNO_3$ on ice is best described by a linear relation with temperature, as follow

$$K_{eq} = -8.2 \times 10^{-12} T + 2.01 \times 10^{-9} \tag{2.28}$$

whereas Crowley et al. (2010) suggested $K_{eq}$ for $HNO_3$ on ice is exponential to the inverse of temperature, as follows

$$K_{eq} = \frac{K_{linC}}{N_{max}} = \frac{7.5 \times 10^{-5} \exp(\frac{4585}{T})}{2.7 \times 10^{14}} \tag{2.29}$$

where $K_{linC}$ is the partitioning coefficient expressing in units of $\mathrm{cm}$ and $N_{max}$ is the maximum number of adsorption site. The $N_{max}$ parameterisation recommendation by Crowley et al. (2010) is used this study ($N_{max} = 2.7 \times 10^{14}$ $\mathrm{molecule\,cm^{-2}}$). The temperature dependence of the two different parameterisations of $K_{linC}$ is shown in Fig. 2.13. The recommendation from Crowley et al. (2010) is a lot more sensitive to temperature and has an unrealistically high

value at temperatures below the recommended temperature range (T<214 K). The winter temperature in Antarctica can be below 200 K, therefore, the parameterisation suggested by Burkholder et al. (2015) is more suitable for extending to temperature below the lowest recommended temperature .

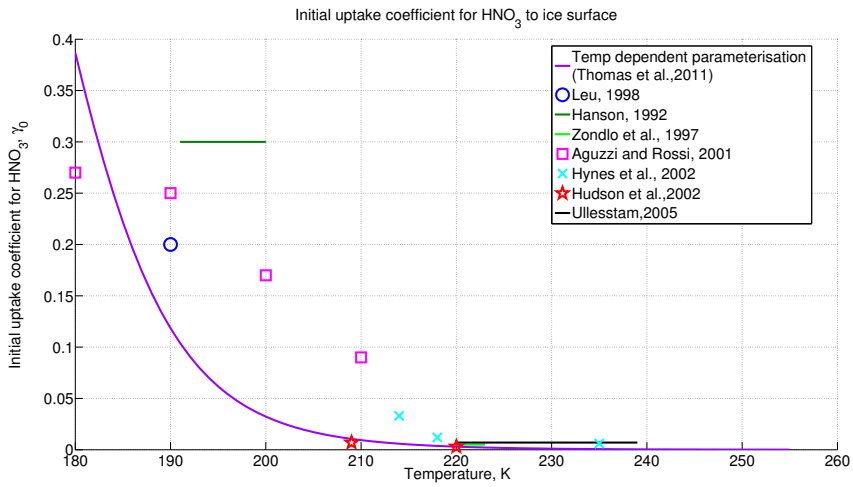


FIGURE 2.14: Initial uptake coefficient obtained from different laboratories and the parameterisation of accommodation coefficient used within this study.

The accommodation coefficient is a function of temperature as shown in Eq. 1.2. The reference accommodation coefficient, $\alpha_0$, can be interpreted from the initial uptake coefficient, $\gamma_0$, obtained by laboratory experiments, mainly by two different techniques - CWFT-MS and Knudsen cell. In this study, the value from Hudson et al. (2002) at 220 K is chosen to be the reference accommodation coefficient as their experiment was at carried at a temperature range close to the temperature that can be found in the lower atmosphere in the Antarctica. The temperature dependent accommodation coefficient (Thomas et al., 2011) used in this study matches reasonably well with the values found by various other studies (Fig. 2.14 in purple).

### 2.5.4 Co-condensation/ Sublimation

Co-condensation is the process of uptake of gas-phase species by ice surfaces undergoing growth by water vapour deposition. The contribution of co-condensation of nitrate to the overall concentration of nitrate at the grain surface depends on 1) the deposition efficiency of $HNO_3$ on growing ice, and/or 2) the rate of ice growth on the grain surface.

Domine et al. (1995) suggested the deposition of a gas $i$ along with water vapour on to the ice surface can be determined from the condensation

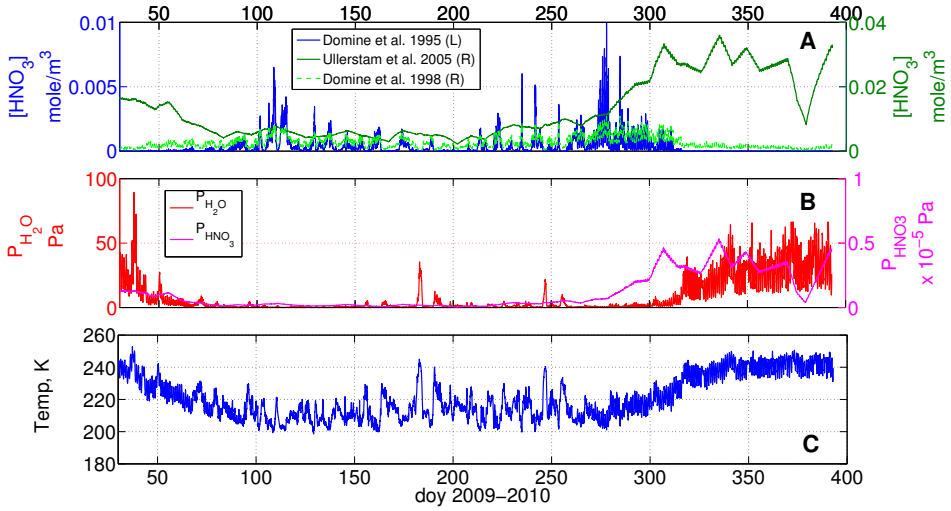


FIGURE 2.15: A) Compared the uptake of $HNO_3$ by growing ice surface via water vapour deposition on ice by Domine et al. (1995), Dominé and Thibert (1996), and Ullerstam and Abbatt (2005), in blue (left axis), dash green (right axis) and dark green (right axis), respectively for Dome C 2009-2010; B) The partial pressure of water vapour and $HNO_3$, in red (left axis) and orange (right axis), respectively at Dome C 2009-2010; C) The air temperature at Dome C 2009-2010.

kinetics as

$$X_i = \frac{P_i}{P_{\mathrm{H_2O}}} \frac{\alpha_i}{\alpha_{\mathrm{H_2O}}} \sqrt{\frac{M_{\mathrm{H_2O}}}{M_i}} \tag{2.30}$$

where $X_i$ is the mole fraction of $i$ in condensed-phase by condensation, $P_i$ and $P_{\mathrm{H_2O}}$ is the partial pressure of $i$ and water vapour respectively, $\alpha$ is the accommodation coefficient (Eq. 1.2), $M_i$ and $M_{\mathrm{H_2O}}$ is molar mass of $i$ and water vapour respectively. The solid-state diffusion is an important process for chemical species that has a high affinity for ice and high diffusion coefficient in ice, e.g. $D_{\mathrm{HNO_3}} \sim 10^{-10}\ \mathrm{cm^2\,s^{-1}}$ (Dominé and Thibert, 1996). Therefore, the incorporation mechanism of $HNO_3$ into ice by co-condensation can be determined by equilibrium solubility of gas in ice . The thermodynamic equilibrium solubility of $HNO_3$ in ice has been measured by Thibert et al. (1998) at nitric acid partial pressure between $10^{-4}$ and $10^{-3}$ Pa, at 238-258 K:

$$X_{\mathrm{HNO_3}} = 2.37 \times 10^{-12} e^{\left(\frac{3532.2}{T}\right)} P_{\mathrm{HNO_3}}^{1/2.3} \tag{2.31}$$

where $T$ is temperature in K. Ullerstam and Abbatt (2005) also found the mole fraction of $HNO_3$, which deposited onto the growing ice surface, is independent of the gas-phase water vapour partial pressure and only proportional to the gas-phase partial pressure of $HNO_3$ at nitric acid partial pressure between

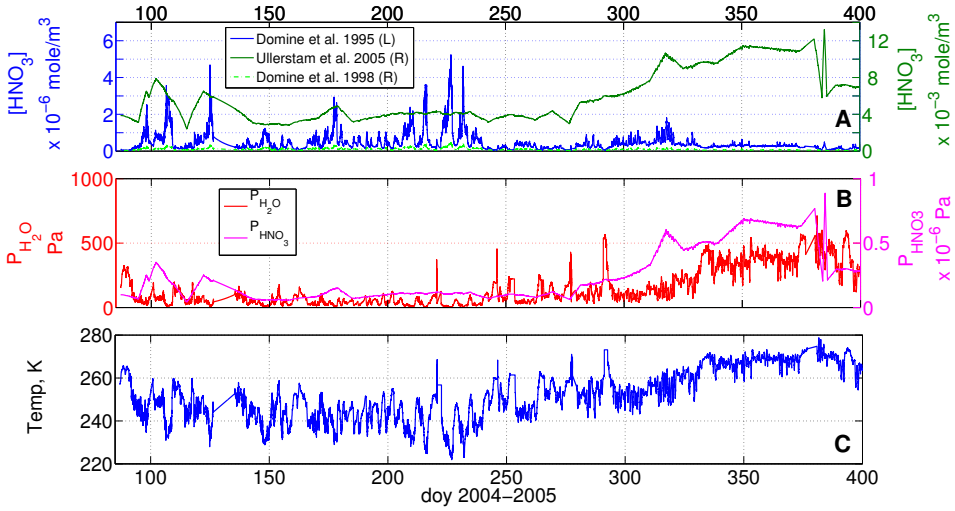


FIGURE 2.16: A) Compared the uptake of $HNO_3$ by growing ice surface via water vapour deposition on ice by Domine et al. (1995), Dominé and Thibert (1996), and Ullerstam and Abbatt (2005), in blue (left axis), dash green (right axis) and dark green (right axis), respectively for Halley 2004-2005; B) The partial pressure of water vapour and $HNO_3$, in red (left axis) and orange (right axis), respectively at Halley 2004-2005; C) The air temperature at Halley 2004-2005.

$10^{-7}$ and $10^{-6}$ hPa, at 214, 229 and 239 K:

$$log_{10}(X_{\mathrm{HNO_3}}) = 0.56 \times log_{10}(P_{\mathrm{HNO_3}}) - 3.2 \tag{2.32}$$

The comparison of the three parameterisations (Eq. 2.30, 2.31 and 2.32) for the concentration of nitrate in the co-condensation phase for data from Dome C 2009-2010 and Halley 2004-2005 are shown in Fig. 2.15 & 2.16 A. The concentrations estimated by the co-condensation kinetics Eq. 2.30 are 1-3 orders of magnitude lower than the equilibrium solubility (Eq. 2.31) and water vapour independent parameterisation (Eq. 2.32). In the summer, the mole fraction of $HNO_3$ calculated from co-condensation kinetics (Eq. 2.30) and the equilibrium solubility (Eq. 2.31) both shows an opposite trend to the water vapour independent parameterisation (Eq. 2.32), as shown in Fig. 2.15 & 2.16 A.

The co-condensation kinetic (Eq.2.30) is inversely proportional to the partial pressure of water vapour (Fig. 2.15 & 2.16 B), concurrently, the equilibrium solubility of $HNO_3$ (Eq.2.31) is inverse proportion to temperature (Fig. 2.15 & 2.16 C). In the summer, at both validation sites, the partial pressure of water vapour and temperature both increases as the partial pressure of $HNO_3$ increase. Therefore, the molar fraction of $HNO_3$ estimated from the

co-condensation kinetic (Eq. 2.30) and equilibrium solubility (Eq. 2.31) do not have the same trend as the observed partial pressure of $HNO_3$. In this study, the parameterisation by Ullerstam et al. (2005, Eq. 2.32) is used to determine the nitrate concentration in the condensed phase as 1) the range of nitric acid partial pressure and temperature used within their experiments were in the similar magnitude of what found in the polar regions ; 2) it is the most up-to-date published work; and 3) to avoid the uncertainties regarding to the partial pressure of water vapour and temperature on the deposition mechanism.

The growth rate of the snow grain is driven by the gradient of the water vapour density gradient between the ambient air, $\rho_{v,amb}$, and the surface of the snow grain, , $\rho_{v,s}$.

$$\frac{dm}{dt} = 4\pi r^2 D_{v,air} \frac{\rho_{v,amb} - \rho_{v,s}}{\Delta x} \tag{2.33}$$

where $\frac{dm}{dt}$ is the mass growth rate, $D_{v,air}$ is the diffusivity of water vapour in the air, $r$ is the radius of the grain and $\Delta x$ is the radial distance. The water vapour density gradient can be changed by the curvature of the particles by Kelvin's Law and/or temperature gradient (Flanner and Zender, 2006). Kelvin's Law stated the equilibrium vapour pressure over curved surfaces, $p_s$, exceeds that over planar surface, $p_{eq}$, the ratio of the two is given by

$$\frac{p_s}{p_{eq}} = \exp\left(\frac{2\gamma}{R_v T \rho_{ice} r}\right) \tag{2.34}$$

where $\gamma$ is the surface tension of ice against air, $R_v$ is the specific gas constant for vapour and $\rho_{ice}$ is the density of ice. The surface saturation ratio ($p_s/p_{eq}$) is only 1.021 and 1.002 for $r$ = 0.1 and 1 $\mu$m and the ratio is very close to 1 for $l$ larger than 10 $\mu$m. In general, the effective radius is larger than 20 $\mu$m thus the Kelvin curvature effect does not contribute significantly to the vapour density gradient except for the initial short timescale growth of fresh snow which has branch dendrites with sharp curvature. The vapour density gradient due to the curvature effect is neglected in this study for simplicity.

The temperature at a given depth within the snowpack can be derived from the heat transport model as shown Sect. 2.3 and the water vapour density can then be calculated as follow

$$\rho_v = \frac{P_{sat}\, RH}{100 R_v T} \tag{2.35}$$

where $P_{sat}$ is the saturated vapour pressure and $RH$ is the relative humidity. They are no known measurement of $RH$ inside the snowpack, however,

given the high density of solid surface, the SIA is assumed to be saturated. More details about how co-condensation linked with other processes can be found in Ch. 4 Sect. 3.1.1.

## 2.6 Model Validation

### 2.6.1 Study Sites: Dome C and Halley

Antarctica has an area of ∼14 million $\mathrm{km}^2$ and is surrounded by ocean and covered by a glacial ice sheet. Its remoteness and lack of local anthropogenic pollution that it can be considered as the most pristine location on earth. Data from a coastal (Halley) and high evaluation inland (Dome C) site were chosen to validate the model as they lie at a similar latitude ($\sim 75°S$, Fig. 2.17) and thus subject to similar diurnal variation, yet, they have a very different meteorological condition and chemical compositions in atmosphere and in snow.

Dome Concordia station at Dome C (Lat. 75°06′S, Long. 123°19′E, Evl. 3233 $\mathrm{m}$ a.s.l) is located on the East Antarctic Plateau and about 1100 $\mathrm{km}$ from the coast (Cap Prud'homme). As Dome C is located on top of a dome with no discernible slope, therefore, it does not experience the typical strong katabatic winds observed in Antarctica and has a very low precipitation rate. The local climate is dominated by temperature inversion and has a cold, clear and calm condition with an annual mean wind speed of 3 $\mathrm{m\,s^{-1}}$. The typical winter temperature is below -60 °C with a minimum temperature around -83 °C and, even in the summer, temperatures hardly rise above -25 °C (Gallée et al., 2015).

Halley Research Station (Lat. 75°35′S, Long. 36°39′W, Evl. 35 $\mathrm{m}$ a.s.l) is located at the coastal Antarctica on the Brunt Ice Shelf on the southeastern shore of the Weddell Sea. As Halley is located by the coast, it experiences moist maritime air masses originated both from over the Antarctic continent and from the Atlantic sector of the Southern Ocean, therefore Halley has a a relative high snow accumulation rate (480 $\mathrm{kg\,m^{-2}\,yr^{-1}}$) and humidity that generally close to saturation with respect to ice, or even slightly supersaturated and the monthly mean wind speed is between 5-8 $\mathrm{m\,s^{-1}}$. The typical winter temperature is below -20 °C with a minimum temperature around -55 °C, whereas in the summer, mean temperature are around -5 °C with rare occasion that rise above 0 °C (King et al., 2006).

The chemical composition of the surface snow is very different at the two study sites due to the different geographic location. At Dome C, the major ion is $NO_3^-$ whereas Halley is strongly influenced by sea salt aerosols that the ion composition is dominated by $Na^+$ and $Cl^-$ (Fig. 2.18).

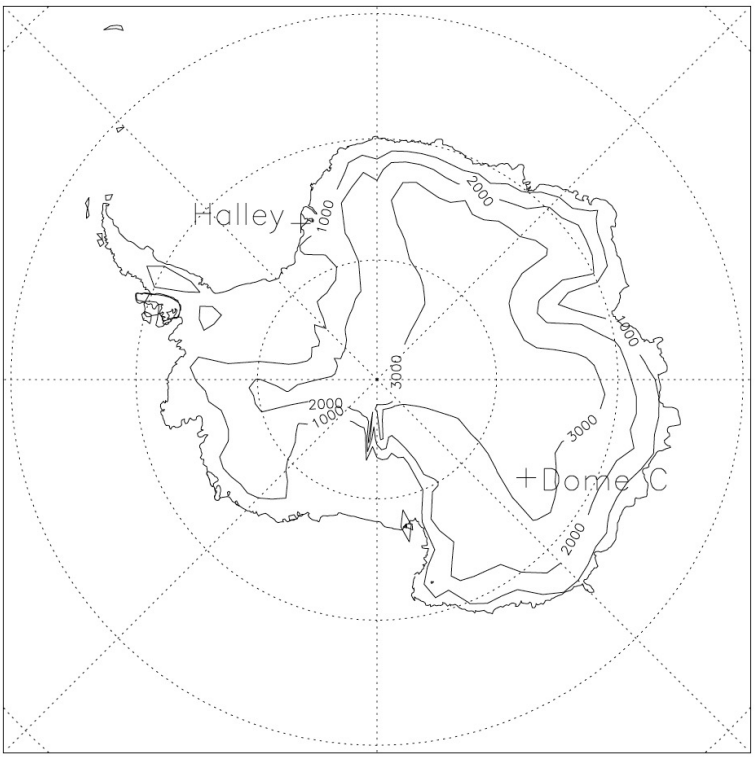


FIGURE 2.17: A map of Antarctica showing the location of Dome C and Halley (King et al., 2006). The topographic contours are at 1000 m interval and the latitude contours are at 10° interval.

### 2.6.2 Measurements of Atmospheric Nitrate

In general, the measuring techniques for atmospheric aerosols and gases concentration are based on passing air through an air sampler at a known flow rate then trapping the particles in the air by a filter or a cascade of filters. The particles on the filters are usually extracted into a known volume of extra pure water then analysed using ion chromatography (IC).

The collection efficiency of a particular particle can be affected by many factors such as flow rate, wall loss, particle bounce and nature of the filter (Fu et al., 2008). Air samplers with a high flow rate ( $> 600\ \mathrm{STP} - \mathrm{L\,min^{-1}}$) are referred as high volume air sampler (HVAS) and those with a lower flow rate ($\sim$ 20-30 $\mathrm{STP} - \mathrm{L\,min^{-1}}$) are referred as low volume air sampler (LVAS). The LVAS have a higher collection efficiency for particle size less than 10 $\mu\mathrm{m}$ compared to HVAS. For particles larger than 10 $\mu\mathrm{m}$ there is significant loss of particles via wall loss with the LVAS (Fu et al., 2008). For cascade filters, the LVAS can separate different-sized aerosols more accurately than the HVAS.

The two sets of data used in this study; 1) from CHABLIS campaign from January 2004-February 2005 at Halley (Jones et al., 2008) and 2) from January

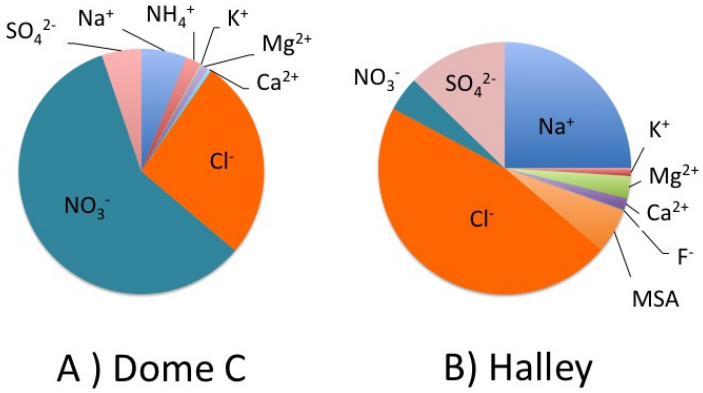


FIGURE 2.18: The major ions found in surface snow at A) Dome C, which dominated by $NO_3^-$ and $Cl^-$ (Udisti et al., 2004) and B) Halley, which the dominant ions are $Na^+$ and $Cl^-$ (Jones et al., 2008). Note that the $H^+$ ion is excluded from the chart.

2009 - January 2010 at Dome C (Erbland et al., 2013), use two different methods to measure nitrate in the atmosphere. During the CHABLIS campaign at Halley, gaseous nitrate acid ($HNO_3$) were measured with an annular Denuder System at weekly and daily resolution. The Annular Denuder System is one of the most commonly used techniques to collect acidic gases. Air was pumped through the denuder tubes that coated with sodium carbonate ($Na_2CO_3$) solution at a low flow rate. After a period of sampling time, the coating was risen with a known amount of Milli-Q water to extract $HNO_3$. The extracted solution was then analysed using ion chromatography (IC). In general, the removal efficiency of $HNO_3$ using $Na_2CO_3$ coating is over 70 % (Fitz, 2002). During this campaign, a second denuder was used to determine the artefact formation of nitrate which then uses for correcting the concentration of ambient $HNO_3$. The concentration of particulate nitrate ($p$-$NO_3^-$) was also measured by LVAS with a Zefluor (Teflon) filter at weekly, daily and 6-hourly sampling resolution. The Zefluor filter is a relatively inert filter which $HNO_3$ is likely lost by volatilisation and minimised retention of $HNO_3$. The advantage of the inert property of Zefluor/Teflon filter has minimised the error from atmospheric $HNO_3$ but at the same time it might underestimate due to dissociation of $p$-$NO_3^-$ to $HNO_3$, especially with low relative humidity and when atmospheric $H^+$ concentration is high. The $p$-$NO_3^-$ and other particulate matter were extracted from the filters by agitating in an ultrasound bath with extra pure water. The concentration of other major ions such as

$Na^+$, $Ca^{2+}$ were also measured alongside with $p$-$NO_3^-$ using an IC.

At Dome C, Erbland et al. (2013) measured the 'total atmospheric nitrate' (sum of $HNO_3$ and $p$-$NO_3^-$) using HVAS 4-stage cascade filter with glass fibre filters at 1-2 weekly resolution. Gaseous $HNO_3$ were collected via absorption into the glass fibre filter due its high alkalinity (Lodge, 1989) and adsorption on the other particulate matter collected on the filters (Appel et al., 1984; Erbland et al., 2013). The total nitrate was transferred from the filter into solution by centrifuging the filter into Milli-Q water then analysed using IC.

### 2.6.3 Measurements of Atmospheric $NO_x$

The atmospheric $NO_x$ was measured at Dome C from December 2009 to January 2010 (Frey et al., 2013). The $NO_x$ was detection by a 2-channel chemiluminescence detector (CLD), one with a photolytic converter (PLC) at 3 different level - 0.01, 1.00 and 4.00 $\mathrm{m}$ above ground. The technique measures the concentration of NO based on the reacting NO with excess $O_3$ to produced electronically excited $NO_2$, then measure the photons emitted by electronically excited $NO_2$ when it returns to the ground state. One of the CLD channels was to measure the ambient atmospheric NO concentration whereas the other channel with PLC is to measure the concentration of $NO_x$, where the $NO_2$ in the ambient air is converted to NO via photolysis. The difference in signal between the 2 channels was then used to calculate the concentration of $NO_2$ in the atmosphere.

The baseline, instrument sensitivity, detector artefacts and conversion efficiency needs to be measured regularly in order to convert the CLD signal into atmospheric mixing ratios. The baseline was measured every couple of minutes for all three inlets (height), where it was determined by measuring the ground state $NO_2$ after being excited. The baseline level for all three inlets was similar, except when the $NO_x$ concentrations between the inlets were very different. To correct the signal, baseline was subtracted from each individual specific inlet. The instrument sensitivity and artefacts were measured every 14 hours. The sensitivity to NO was determined by the standard addition to the sample air matrix of a 1 $\mathrm{ppmv}$ $NO/NO_2$ mixture. The artefacts of the detector were originated from surface reactions of $NO_x$ in inlets and reaction cells, which was determined by overflowing the instrument inlet with scrubbed ambient air. The conversion efficiency was found by addition of known mole-fraction of $NO_2$ and has an average of 0.30.

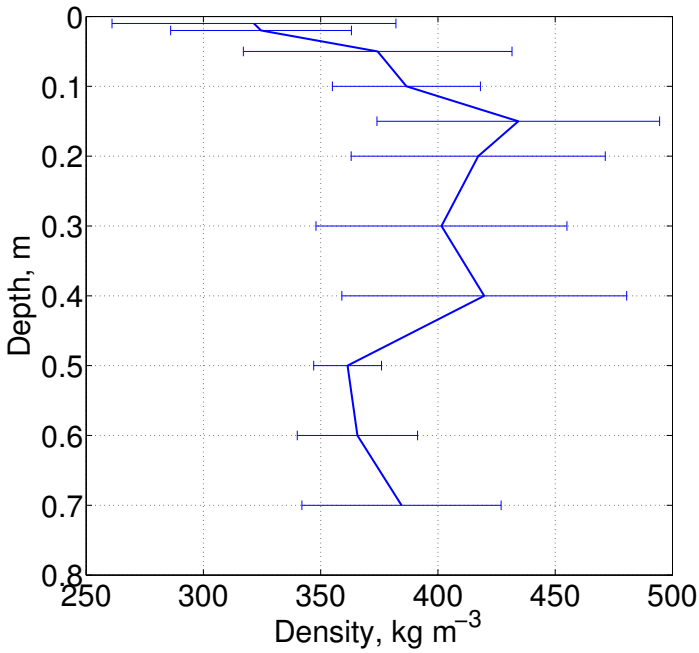


FIGURE 2.19: The mean (±standard deviation) density profile of 13 snow pits at Dome C (Gallet et al., 2011).

### 2.6.4 Measurements of Snow Physical Properties

Physical properties of snow, such as density ($\rho_{snow}$) of the snowpack and the snow surface area (SSA), controls on the vertical temperature profile, the capacity of the snow to accommodate chemical species and the transport of chemical species. Despite these crucial roles, the snow properties are not always being measured when snow samples were collected for chemical analysis due to time constraint or availability of equipment and labours. The density profile used for Dome C in this study was adopted from (Gallet et al., 2011). which a mean density profile was obtained by averaging 13 snow pits at Dome C between November 2008 to January 2009 (Fig. 2.19). Density was measured by weighing a known volume of snow samples for each stratified layer. The density at Dome C tends to increase from the surface to ~15 cm then followed by an essentially constant density. The spatial variation of the stratification is large, for example the snow pit C2 and C3 in (Gallet et al., 2011) were only 20 m apart but C2 has a thick layer of depth hoar between 37-70 cm depth while for the pit C3 have a faceted crystals or mixed-form crystals alternate at the same depth. The large spatial variation leads to the large error bar in the mean density profile.

The SSA values used in this study were interpolated from the 3-years time-series by Picard et al. (2016). They measured SSA of superficial snow at Dome C between 2012-2015 obtained by automatic spectral radiometer in

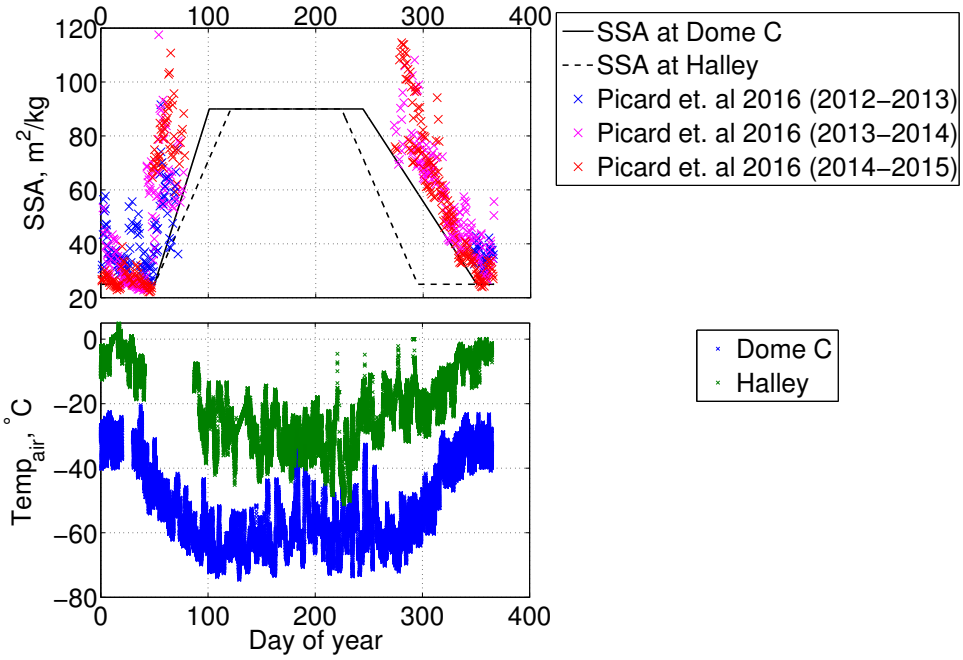


FIGURE 2.20: The specific surface area, SSA, at Dome C by Picard et al., 2016 in '**X**' and values used in this study in solid-line at Dome C, and dash-line at Halley, which are adjusted by the observed air temperature.

the visible/near infrared range. The seasonal variations of SSA at Dome C is significant that SSA in winter is 3-fold larger than the values in summer but the interannual variations are relatively small (Fig. 2.20).

### 2.6.5 Measurements of Snow Optical Properties

Optical properties of snowpack are also important as its determinate the rate of photochemical reactions in snow. The field measured values of $e$-folding depth and snow surface reflectance by France et al. (2011) at Dome C were used in this study. The optical properties of 14 snowpits all within 5 km were accessed. The $e$-folding depth was measured for each stratified snow layer that thicker than 25 cm with a custom-built 6 spectrometer (6 channels and fibre optics with a cosine corrector connected to individual spectrometers). Measurements were made by placing the probe horizontally into the shaded face of the snowpack at varying depths in a single stratigraphic layer and recorded the irradiance in the UV-Visible wavelength (320-700 nm). The spectrometers were calibrated by simultaneously measuring the intensity of the radiation above the snowpack and also measuring dark spectra, which were recorded in the field by capping the fibre optic probe. The $e$-folding depth of the soft (mixture of rounded grains and surface hoar) and hard (mixture of

faceted and rounded faceted grains) windpack snow are similar ($\sim 10$ cm), and these types of snow are often found in the top two layers of snowpack at Dome C. Often beneath the soft and hard windpack layer, below a depth of 20 cm, there is hoar like layer which consists of a mixture of faceted grains and depth hoar). The $e$-folding depth of the hoar like layer is roughly twice as much as the soft and hard windpack layer.

For the 1D model, where photochemistry was included as one of the processes, a single value of $e$-folding depth is used to estimate the photochemical reaction rate in the snowpack using Eq. 1.9 & 2.2 . This simplification was based on the assumption that at least 85% of the photochemically produced $NO_2$ are originated from the top 20 cm, which is in the soft and hard windpack layers (France et al., 2011).

## 2.7 Technical Tools

### 2.7.1 Finite Difference method - Crank-Nicolson Method

A general 1D diffusion equation is in the following form

$$\frac{\partial U}{\partial t} = \frac{\partial}{\partial x}\left(k(x,t)\frac{\partial U}{\partial x}\right) \tag{2.36}$$

The differential equation can be used to describe the transport of heat or mass. In this thesis, all the differential equation are solved by the Crank-Nicolson Method, which is a finite-difference method for solving partial differential equations. The Crank-Nicolson method is an implicit method and it is chosen for its stability and improved convergence (Press et al., 1996). To obtain an unconditional stability for the Crank-Nicolson method, the time and spatial dependent diffusion coefficient, $k(x,t)$, needs to be computed at the midpoint of each temporal subinterval. The Crank-Nicolson method can be numerically approximated as

$$\frac{U_i^{n+1} - U_i^n}{\Delta t} = \frac{k_i^{n+1/2}}{2}\left(\frac{U_{i+1}^{n+1} - 2U_i^{n+1} + U_{i-1}^{n+1}}{(\Delta x)^2} + \frac{U_{i+1}^n - 2U_i^n + U_{i-1}^n}{(\Delta x)^2}\right) \tag{2.37}$$

where $n$ is the $n^{th}$ time step, $i$ is the $i^{th}$ element of the spatial grid and $k_i^{n+1/2} = k(x_i, t_{n+1/2})$.

The system can be expressed in matrix form as

$$\begin{bmatrix} b_1 & c_1 & 0 & 0 & 0 & 0 \\ a_2 & b_2 & c_2 & 0 & 0 & 0 \\ 0 & a_3 & b_3 & c_3 & 0 & 0 \\ 0 & 0 & \ddots & \ddots & \ddots & 0 \\ 0 & 0 & 0 & a_{N-1} & b_{N-1} & c_{N-1} \\ 0 & 0 & 0 & 0 & a_N & b_N \end{bmatrix} \begin{bmatrix} U_1 \\ U_2 \\ U_3 \\ \vdots \\ U_{N-1} \\ U_N \end{bmatrix} = \begin{bmatrix} d_1 \\ d_2 \\ d_3 \\ \vdots \\ d_{N-1} \\ d_N \end{bmatrix} \tag{2.38}$$

where the coefficients are

$$\begin{aligned} a_i &= -d_i^{n+1/2}/(2\Delta x^2) && i = 2, 3, \ldots, N-1 \\ b_i &= (1/\Delta t) + (d_i^{n+1/2}/\Delta x^2) \\ c_i &= -d_i^{n+1/2}/(2\Delta x^2) \\ d_i &= a_i U_{i-1}^n + (1/\Delta t + a_i + c_i) U_i^n + c_i U_{i+1}^n \end{aligned}$$

For the Dirichlet boundary conditions, i.e. a fixed boundary condition

$$\begin{aligned} b_1 = 1, \quad c_1 = 0, \quad d_1 = U_0 \\ a_N = 0, \quad b_N = 1, \quad d_n = U_N \end{aligned}$$

For the Robin boundary conditions, also known as convective boundary condition, such that

$$\frac{\partial U}{\partial x} = g_0 \tag{2.39}$$

then the upper boundary coefficient would be as follow,

$$\begin{aligned} b_1 &= \tfrac{1}{\Delta t} + \tfrac{d_i^{n+1/2}}{\Delta x^2} \\ c_1 &= -\tfrac{d_i^{n+1/2}}{\Delta x^2} \\ d_1 &= \left( \tfrac{1}{\Delta t} - \tfrac{d_i^{n+1/2}}{\Delta x^2} \right) U_1^n + \tfrac{d_i^{n+1/2}}{\Delta x^2} U_2^n - \tfrac{2 d_i^{n+1/2}}{\Delta x} \tfrac{g_0^{n+1} + g_0^n}{2} \end{aligned}$$

### 2.7.2 ODE solver - KKP

Kinetic PreProcessor (KPP-2.2) is a software package for simulating the atmospheric chemical kinetics system by integrating sets of ordinary differential equations. KPP allow simulation of chemical kinetic systems in Fortran90 and Matlab. The Matlab version was adopted for quick implementation and analysis. Some of the complex reaction rates are parameterised by the Master Chemical Mechanism (MCM, http://mcm.leeds.ac.uk/MCM/) were added to the KPP's reaction rates file. The MCM's parameterisation for photolysis reactions are based on the typical photolysis rate coefficients that found at

low and mid-latitudes, where the amount of aerosol in the vertical column of the atmosphere is likely to be higher than polar region as well as having a much lower surface albedo. Therefore, the photolysis rate coefficients used within this study were attained offline with a radiative transfer model - TUV (Sect. 2.2). Lookup tables of surface photolysis rate coefficients for both gas and condense phase photolysis reactions were created with typical atmospheric and surface conditions, i.e. aerosol optical depth (AOD(500 $\mathrm{nm}$) = 0.015, Tomasi et al., 2007), and Ångstrom Exponent (Å = 1.60, Tomasi et al., 2007) surface albedo ($\omega_0$ = 0.95, France et al., 2011) and ozone column (200-400 $\mathrm{DU}$ with an interval of 50 $\mathrm{DU}$), found in the polar regions with a solar zenith angle resolution of 0.5°. A clear sky condition were assumed as the clouds cover at Dome C are generally low (King et al., 2006).

The solar zenith angle is calculated for each time step in KPP and the corresponding surface photolysis rate coefficients, $J(z_0)$, are obtained from the lookup table and interpolated to the input ozone column value. The photolysis rate coefficient of a particular layer in the snowpack, i.e. from depth $z_1$ to $z_2$, is represented by the depth-integrated photolysis rate coefficients, $v$.

$$v = J(z_0) \int_{z=z_1}^{z=z_2} e^{\frac{z-z_0}{z_e}} dz \tag{2.40}$$

where $z_0$ is at the surface, i.e. $z_0$ =0. Eq.2.40 are implemented using trapezoid rule as part of the ROOT_Rates.m file. Here is an example of determining the

depth-integrated photolysis rate coefficient of a condensed-phase reaction.

```
function [v] = Jsnow_c(React)
%-------------------------------------------------------
% Calculate depth-integrated photolysis rate coefficient of
% condense phase reaction between depth zu and zb
% Inputs :
% React = which reactions
%   2) NO3- -> NO2 + O- [T=258K]
%   3) NO3- -> NO2- + O(3P) [T=258K]
%   4) NO2- -> NO + O- [T=258K]
%   5) H2O2 -> 2OH [T=258K]
% Output
%   v = depth -integrated photolysis rate coefficient of
%   condensed phase in snowpack, [s^-1]
%-------------------------------------------------------
global Jg_lookup zu zb ze
  Jzu = Jg_lookup(React).*exp(-zu/ ze) ; %J at z = zu
  Jzb = Jg_lookup(React).*exp(-zb/ ze) ; %J at z = zb

  v = (zb-zu)*(Jzu+Jzb)/2; %trapezoidal rule.
return
```

The quantum yield adopted for the condense phase photolysis rate coefficients implicitly taken account the cage effect - make two chemical species from one, but these recombine to form the initial chemical before the products can escape cage. In practice, there is a need to convert the units of the photochemical products by multiplying the ratio of volume of ice/liquid to volume of air, i.e. $k_{air}^{H2O} = (m_{ice}^3 + m_{aq}^3)/m_{air}^3$. The following code are also implemented to KPP.

```
function [kH2O2g] = Caq2Cg(rho_snow, rho_water)
%-------------------------------------------------------
% This function to convert the units of the photochemical
% product from liquid concentration to gas concentration.
%   i.e.  d[NO2(c)]/dt = J [NO3-(c)]
%    units conversion : d[NO2(g)]/dt = kH2O2g [NO2(c)]
% Inputs :
%   rho_snow = density of snow, [kg m-3]
%   rho_water = density of water, [kg m-3]
% Output
%   kH2O2g = rate constant for the conversion
%   , [m^3_H2O m^-3_air s^-1]
%-------------------------------------------------------
global DT
  kH2O2g = (rho_snow./(rho_water - rho_snow))./DT;
return
```

# Chapter 3

# The impact of parameterising light penetration into snow on the photochemical production of $NO_x$ and OH radicals in snow

**Citation:**
**Chan, H. G.** , King, M. D. and Frey, M. M.: The impact of parameterising light penetration into snow on the photochemical production of $NO_x$ and OH radicals in snow, Atmos. Chem. Phys.,15, 7913-7927, doi:10.5194/acp-15-7913-2015, 2015.

**Author contributions:**
H.G.C. performed the radiative-transfer calculations, did the data analysis and result preparation.
M.D.K. oversaw the study and proof-read the paper.
M.M.F. oversaw the study and proof-read the paper.

**Note:**
1) Minor correction for P. 7919, Section 2.1, line 14. The correct sentence should be as follow:
"The model configuration in this study used 109 snowpack layers with 1 $\mathrm{mm}$ spacing in the top 1$\mathrm{cm}$ and 1 $\mathrm{cm}$ spacing for the rest of the 1 $\mathrm{m}$ snowpack".
2) Fig. 6 has been reproduced in Appendix B

Atmos. Chem. Phys., 15, 7913–7927, 2015
www.atmos-chem-phys.net/15/7913/2015/
doi:10.5194/acp-15-7913-2015


Atmospheric Chemistry and Physics
Open Access

# The impact of parameterising light penetration into snow on the photochemical production of $NO_x$ and OH radicals in snow

**H. G. Chan[1,2], M. D. King[2], and M. M. Frey[1]**

[1]British Antarctic Survey, Natural Environment Research Council, Cambridge, CB3 0ET, UK
[2]Department of Earth Sciences, Royal Holloway University of London, Egham, Surrey, TW20 0EX, UK

*Correspondence to:* H. G. Chan (hohan47@bas.ac.uk)

Received: 21 January 2015 – Published in Atmos. Chem. Phys. Discuss.: 23 March 2015
Revised: 23 June 2015 – Accepted: 3 July 2015 – Published: 17 July 2015

**Abstract.** Snow photochemical processes drive production of chemical trace gases in snowpacks, including nitrogen oxides ($NO_x = NO + NO_2$) and hydrogen oxide radical ($HO_x = OH + HO_2$), which are then released to the lower atmosphere. Coupled atmosphere–snow modelling of theses processes on global scales requires simple parameterisations of actinic flux in snow to reduce computational cost. The disagreement between a physical radiative-transfer (RT) method and a parameterisation based upon the *e*-folding depth of actinic flux in snow is evaluated. In particular, the photolysis of the nitrate anion ($NO_3^-$), the nitrite anion ($NO_2^-$) and hydrogen peroxide ($H_2O_2$) in snow and nitrogen dioxide ($NO_2$) in the snowpack interstitial air are considered.

The emission flux from the snowpack is estimated as the product of the depth-integrated photolysis rate coefficient, $v$, and the concentration of photolysis precursors in the snow. The depth-integrated photolysis rate coefficient is calculated (a) explicitly with an RT model (TUV), $v_{TUV}$, and (b) with a simple parameterisation based on *e*-folding depth, $v_{z_e}$. The metric for the evaluation is based upon the deviation of the ratio of the depth-integrated photolysis rate coefficient determined by the two methods, $\frac{v_{TUV}}{v_{z_e}}$, from unity. The ratio depends primarily on the position of the peak in the photolysis action spectrum of chemical species, solar zenith angle and physical properties of the snowpack, i.e. strong dependence on the light-scattering cross section and the mass ratio of light-absorbing impurity (i.e. black carbon and HULIS) with a weak dependence on density. For the photolysis of $NO_2$, the $NO_2^-$ anion, the $NO_3^-$ anion and $H_2O_2$ the ratio $\frac{v_{TUV}}{v_{z_e}}$ varies within the range of 0.82–1.35, 0.88–1.28, 0.93–1.27 and 0.91–1.28 respectively. The *e*-folding depth parameterisation underestimates for small solar zenith angles and overestimates at solar zenith angles around 60° compared to the RT method. A simple algorithm has been developed to improve the parameterisation which reduces the ratio $\frac{v_{TUV}}{v_{z_e}}$ to 0.97–1.02, 0.99–1.02, 0.99–1.03 and 0.98–1.06 for photolysis of $NO_2$, the $NO_2^-$ anion, the $NO_3^-$ anion and $H_2O_2$ respectively. The *e*-folding depth parameterisation may give acceptable results for the photolysis of the $NO_3^-$ anion and $H_2O_2$ in cold polar snow with large solar zenith angles, but it can be improved by a correction based on solar zenith angle and for cloudy skies.

## 1 Introduction

Field and laboratory experiments over the past 2 decades have provided evidence that photochemical reactions occurring within snow lead to the emission of various gaseous compounds from the snowpack (e.g. Jacobi et al., 2004; Jones et al., 2000; Beine et al., 2002, 2006; Dibb et al., 2002; Simpson et al., 2002) and production of radicals, e.g. hydroxyl radical (OH), within the snowpack (e.g. Mauldin et al., 2001; Chen et al., 2004; Sjostedt et al., 2005; France et al., 2011). The porous structure of snowpacks allows the exchange of gases and particles with the atmosphere. The exchange between snowpack and overlying atmosphere depends on dry and wet deposition, transport (including wind pumping and diffusion) and snow microphysics (e.g. Bartels-Rausch et al., 2014). Thus snow can act as both a source and a sink of atmospheric chemical species as summarised in Bartels-Rausch et al. (2014) and Grannas et al. (2007). Photochemistry in the snowpack needs to be fully understood because (1) emitted photolysis products play an impor-

tant role in determining the oxidising capacity of the lower atmosphere – e.g. concentration of $O_3$, $HO_x$, $H_2O_2$ – and (2) chemical preserved in ice cores, and potential palaeoclimate proxies, may be altered by reactions with OH radicals, photolysis or physical uptake and release (Wolff and Bales, 1996).

The photolytic lifetime of a chemical species in the snowpack is the reciprocal of the photolysis rate coefficient (also known as the photodissociation rate coefficient), $J$, which is dependent on the actinic flux (also known as spherical or point irradiance) in the snowpack, $I$, the quantum yield of the photolysis reaction, $\Phi$, and absorption cross section of the photolysing species, $\sigma$.

$$J(\theta, z, T) = \int \sigma(\lambda, T)\, \Phi(\lambda, T)\, I(\theta, z, \lambda)\, \mathrm{d}\lambda, \quad (1)$$

where $\theta$ is solar zenith angle, $z$ is the depth into the snowpack, $\lambda$ is the wavelength of the incident solar radiation and $T$ is the temperature of the snowpack.

Under clear-sky conditions, a homogeneous snowpack can be separated into two optical layers based on the propagation of actinic flux from the surface into the snow: the near-surface layer, i.e. the top few centimetres of the snowpack, where direct solar radiation is converted into diffuse radiation. Below the near-surface layer is the asymptotic zone, where all solar radiation is diffuse and will decrease exponentially with depth (Warren, 1982).

The relationship between actinic flux (and the photolysis rate coefficient) and depth is complex near the surface of the snowpack due to rapidly changing contributions from both direct and diffuse radiation. Enhancement or attenuation of actinic flux in the near-surface layer compared to above the snow is dependent on the solar zenith angle (Fig. 1 and Fig. 4 in Lee-Taylor and Madronich, 2002). Snowpack is a very scattering and low absorption environment for UV–visible photons with individual snow grains tending to forward-scatter photons (Warren, 1982). The enhancement in actinic flux compared to above the snow occurs for solar zenith angles $< 50°$. For solar zenith angles $\sim 50°$ actinic flux will decrease almost exponentially with depth (Wiscombe and Warren, 1980). For direct radiation from a low sun (large solar zenith angle, i.e. $> 50°$) there is a larger probability that the photons will be scattered upwards and out of the snowpack, leading to a rapid decrease in actinic flux with depth in the first few centimetres of the snowpack, i.e. decreasing faster than exponential (Warren, 1982).

In the asymptotic zone radiation is diffused, and provided that the snowpack is semi-infinite – i.e. the albedo of the surface underlying the snow does not affect the calculation of the actinic flux within the snowpack – the radiation decreases exponentially according to Beer–Lambert law (France et al., 2011, define semi-infinite as 3–4 $e$-folding depths).

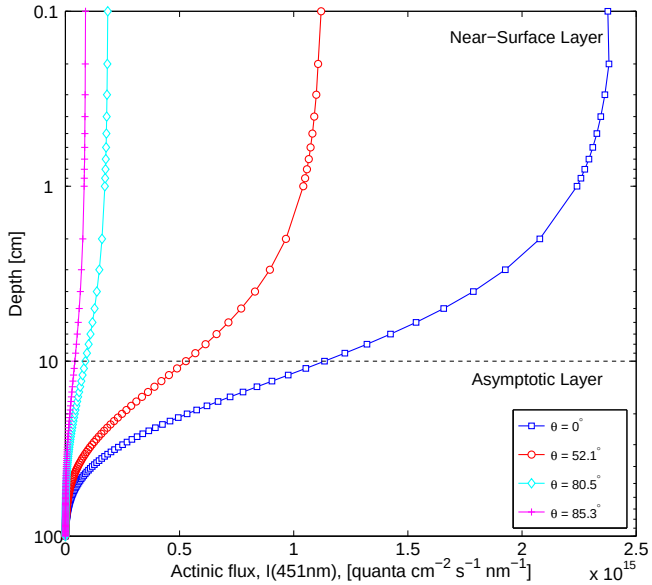


**Figure 1.** Depth profile within "cold polar snow" (base case: $\rho = 0.4\,\mathrm{g\,cm^{-3}}$, $[\mathrm{BC}] = 4\,\mathrm{ng(C)\,g^{-1}}$ and $\sigma_{\mathrm{scatt}} = 25\,\mathrm{m^2\,kg^{-1}}$) of actinic flux, $I$, at $\lambda = 451$ nm at different solar zenith angles $\theta$.

$$I(z, \lambda) = I_0\, e^{-\frac{z - z_0}{z_e(\lambda)}}, \quad (2)$$

where $I_0$ is the actinic flux at a reference depth $z_0$ within the asymptotic zone, and $z_e(\lambda)$ is the asymptotic $e$-folding depth at which $I$ has decayed to $1/e$, $\sim 37\,\%$ of its reference value, $I_0$.

Radiative-transfer (RT) models, such as the TUV-snow model (Lee-Taylor and Madronich, 2002), were developed to capture the non-exponential attenuation of radiation near the surface of the snowpack. However, running a radiative-transfer model is a time-consuming step within large-scale (e.g. 3-D) chemical transport models or global climate models, so photolysis rate coefficients in the snowpack, $J$, are often parameterised with $e$-folding depth (e.g. Thomas et al., 2011), i.e.

$$J_{z_e}(\theta, z) = J_0(\theta)\, e^{-\frac{z - z_0}{z_e(\lambda)}}, \quad (3)$$

where $J_{z_e}(\theta, z)$ is the parameterised photolysis rate coefficient at depth $z$; $J_0$ is the photolysis rate coefficient at the surface of the snowpack at solar zenith angle $\theta$; and $z_e$ is the $e$-folding depth of the snowpack. The aim of this paper is to investigate the accuracy of the $e$-folding depth parameterisation (Eq. 3) relative to a value of $J$ calculated using a physically explicit RT model and Eq. (1). The metric to compare the two models is the depth-integrated photolysis rate coefficient (also known as the transfer velocity; France et al., 2007), which may be considered approximately proportional to the flux of potential gaseous photo-produced compounds

**Table 1.** Reference for quantum yield, $\Phi$, used for Reactions (R1)–(R4) and (R7) and absorption cross section, $\sigma$, of the $NO_3^-$ anion, the $NO_2^-$ anion, $H_2O_2$, and $NO_2$.

| Reaction | Reference for $\Phi$ | Quantum yield, $\Phi$ at 258 K | Action spectrum peak $\lambda_{\text{act peak}}$, nm |
|---|---|---|---|
| R1 | Chu and Anastasio (2003) | 0.00338 | 321 |
| R2 | Warneck and Wurzinger (1988) | 0.00110 | 321 |
| R3 | Chu and Anastasio (2007) | 0.12066* | 345 |
| R4 | Gardner et al. (1987) | 0.97900 | 375 |
| R7 | Chu and Anastasio (2005) | 0.68300 | 321 |
| Species | Reference for $\sigma$ | | |
| $NO_3^-$ | Chu and Anastasio (2003) | | |
| $NO_2^-$ | Chu and Anastasio (2007) | | |
| $NO_2$ | DeMore et al. (1997) | | |
| $H_2O_2$ | Chu and Anastasio (2005) | | |

* Quantum yield at $\lambda = 345$ nm, the photochemical action spectrum peak of the $NO_2^-$ anion.

from the snowpack. The depth-integrated photolysis rate coefficient, $v$, is calculated (Simpson et al., 2002) as

$$v(\theta) = \int J(\theta, z)\,\mathrm{d}z. \tag{4}$$

The depth-integrated production rate of a chemical species $B$ from the photolysis of a chemical species $A$, $F_B(\theta)$, is the product of concentration of $A$, $[A]$, and the depth-integrated photolysis rate coefficient, $v_A$, assuming the concentration of $A$ is constant with depth.

$$F_B(\theta) = [A]\,v_A(\theta) \tag{5}$$

For example, the photolysis of the nitrate anion, $NO_3^-$, is important and has therefore been studied extensively in the past. It leads to emission of nitrogen oxides ($NO_x = NO + NO_2$) to the atmosphere. The following reactions summarise the main channels of $NO_x$ production from $NO_3^-$ photolysis in snowpack. The quantum yield and absorption cross section of all the chemical species used in this study are listed in Table 1.

$$NO_3^- + h\nu \rightarrow NO_2 + O^-, \quad \lambda_{\text{act peak}} = 321\,\text{nm}, \tag{R1}$$

$$NO_3^- + h\nu \rightarrow NO_2^- + O(^3P), \quad \lambda_{\text{act peak}} = 321\,\text{nm}, \tag{R2}$$

$$NO_2^- + h\nu \rightarrow NO + O^-, \quad \lambda_{\text{act peak}} = 345\,\text{nm}, \tag{R3}$$

where $h\nu$ represents a photon and $\lambda_{\text{act peak}}$ is the wavelength corresponding to the maximum in the action spectrum. Here the action spectrum is the spectral photolysis rate coefficient plotted as a function of wavelength. For example, the action spectrum shows that nitrate photolysis is most efficient at 321 nm. Snow is a porous medium in which gas-phase reactions can occur in the interstitial air. Gaseous nitrogen dioxide ($NO_2$) has a large quantum yield, and its action spectrum peak is in the UV-A wavelengths, around 375 nm. Long-wavelength UV light penetrates deeper into the snowpack than shorter-wavelength UV. Therefore, $NO_2$ photolyses within the snowpack and may produce ozone (Reactions R4 and R5).

$$NO_2 + h\nu \rightarrow NO + O(^3P), \quad \lambda_{\text{act peak}} = 375\,\text{nm}, \tag{R4}$$

$$O(^3P) + O_2 + M \rightarrow O_3 + M \tag{R5}$$

Studies have also demonstrated that photolysis of $NO_3^-$ and $NO_2^-$ in snow and ice contribute to the formation of OH radicals within the snowpack (Dubowski et al., 2001, 2002; Cotter et al., 2003; Chu and Anastasio, 2003; Anastasio and Chu, 2008) through reaction of oxygen radical anion ($O^-$) with water (Reaction R6).

$$O^- + H_2O \rightarrow OH + OH^- \tag{R6}$$

In the presence of oxygen, formation of the OH radical may create a radical-initiated oxidising medium allowing oxidation of organic chemicals to emit species such as formaldehyde, acetaldehyde or organic halogens to the lower atmosphere (McNeill et al., 2012). Another source of OH radicals in the snowpack is photolysis of hydrogen peroxide ($H_2O_2$) (Chu and Anastasio, 2005, 2007):

$$H_2O_2 + h\nu \rightarrow 2OH, \quad \lambda_{\text{act peak}} = 321\,\text{nm}. \tag{R7}$$

The ratio of the depth-integrated photolysis rate coefficients, $Q = \frac{v_{\text{TUV}}}{v_{z_e}}$, determined from the two methods – the RT model and $e$-folding depth parameterisation – were calculated for the photolysis of $NO_3^-$, $NO_2^-$, $NO_2$ and $H_2O_2$ in snow. Reactions rate coefficients for Reactions (R1)–(R4) and (R7) were determined for hypothetical snowpacks with different physical and optical properties and under different environmental conditions, e.g. total column ozone.

## 2 Modelling procedure

The hypothetical homogeneous snowpacks defined in this study were based on three different types of snow – cold polar, wind-packed and melting snow (Table 2, Marks and King, 2014). The snowpacks are assumed to be semi-infinite.

Sensitivity tests calculating $Q$ were run against the following parameters – base case: a typical cold polar snowpack; case 1: the density of the snowpack was varied; case 2: the scattering cross section was varied; case 3: the black carbon (BC) mass ratio was varied; case 4: the HUmid LIke Substances (HULIS) mass ratio was varied; case 5: the mass ratio with both BC and HULIS was varied; case 6: the asymmetry factor was varied; and case 7: the total column ozone was varied. Values for these parameters, listed in Table 3, were chosen based on previous field measurements made in various geographic locations and conditions (i.e. Grenfell et al., 1994; Beaglehole et al., 1998; King and Simpson, 2001; Fisher et al., 2005; France et al., 2010; Marks and King, 2014).

In case 1, snow densities were varied in the range observed typically in natural snowpack of 0.2–0.6 $\mathrm{g\,cm^{-3}}$ (Marks and King, 2014, and references therein).

In cases 2–5, the scattering cross section and mass ratio of light-absorbing impurities of the snowpack were varied – both of which have an impact on the propagation of actinic flux within the snowpack. The reciprocal of the $e$-folding depth, $z_e$, is the asymptotic flux extinction coefficient, $\kappa_{\mathrm{ext}}$, which is the sum of the scattering, $r_{\mathrm{scatt}}$, and absorption coefficients, $\mu$ (Lee-Taylor and Madronich, 2002). The scattering and absorption coefficients describe the attenuation per unit length, and both are density-dependent (Lee-Taylor and Madronich, 2002). For general use, the following scattering, $\sigma_{\mathrm{scatt}}$, and absorption, $\sigma_{\mathrm{abs}}$, cross sections are introduced:

$$\sigma_{\mathrm{ext}} = \sigma_{\mathrm{scatt}} + \sigma_{\mathrm{abs}}, \tag{6}$$

where $\sigma_{\mathrm{ext}} = \kappa_{\mathrm{ext}}/\rho$ is the extinction cross section, $\sigma_{\mathrm{scatt}} = r_{\mathrm{scatt}}/\rho$ is the scattering cross section of snow and $\sigma_{\mathrm{abs}} = \mu/\rho$ is the absorption cross section of snow and light-absorbing impurities. In case 2, values of $\sigma_{\mathrm{scatt}}$ were selected to cover a wide range of snow types (Table 2). The values of the scattering cross section are assumed to be independent of wavelength (Lee-Taylor and Madronich, 2002).

The absorption cross section of snowpack is due to wavelength-dependent absorption by ice, $\sigma_{\mathrm{abs}}^{\mathrm{ice}}$, and light-absorbing impurities, $\sigma^{+}$, such as black carbon and HULIS:

$$\sigma_{\mathrm{abs}} = \sigma_{\mathrm{abs}}^{\mathrm{ice}} + \sigma^{+}. \tag{7}$$

Warren et al. (2006) showed that BC can dominate the absorption in snow as it is a factor of $\sim 50$ more efficient absorber of light than mineral dust particles of the same mass. Thus in sensitivity test case 3, black carbon is considered to be the only light-absorbing impurity. For the work presented here the light-absorption cross section of black carbon, $\sigma_{\mathrm{BC}}^{+}$, is assumed to be wavelength-independent and equal to $\sim 10\,\mathrm{m^2\,g^{-1}}$ (France et al., 2010; Lee-Taylor and Madronich, 2002). To account for all pollution scenarios, from clean to dirty, the mass ratio of black carbon is varied from 4 to 128 $\mathrm{ng\,g^{-1}}$, to cover the concentration range typically measured in coastal (Beaglehole et al., 1998), Antarctica-near research stations (Zatko et al., 2013) or in midlatitude snow. Other common pollutants found in snow samples include HULIS, which represent an important fraction of biomass burning, biogenic and marine aerosol etc. (e.g. Voisin et al., 2012). HULIS absorb most effectively in the UV region of the solar spectrum, and the absorption cross section decreases towards the visible (Hoffer et al., 2006). Concentrations of HULIS measured in polar snow vary between 1 and 1000 $\mathrm{ng\,g^{-1}}$ and depend on the measurement method (Voisin et al., 2012; France et al., 2012), which is taken into account by the range of values used in case 4. In natural snow, it is rare that HULIS would be the only light-absorbing impurity within snow as shown in France et al. (2011) and France and King (2012); therefore, in case 5 a combination of both black carbon and HULIS were used and varied.

**Table 2.** Properties of snow type studied. Optical and physical properties are based on work by Marks and King (2014) and references therein.

| Snow type | $\rho$ $\mathrm{g\,cm^{-3}}$ | $\sigma_{\mathrm{scatt}}$ $\mathrm{cm^2\,kg^{-1}}$ |
|---|---|---|
| Cold polar snow | 0.2–0.6 | 15–25 |
| Wind-packed snow | 0.2–0.6 | 5–10 |
| Melting snow | 0.2–0.6 | 0.2–2 |

In case 6, the asymmetry factor, $g$, is the average cosine of the scattering angle and is a measure of the preferred scattering direction. Sensitivity tests were run with two different values of $g$ of 0.89 and 0.86 as discussed by Marks and King (2014) and Libois et al. (2014) respectively. Both selected values are close to 1, indicating light scattering by snow grains is dominated by forward scattering.

Within case 7, column ozone values were varied to cover the seasonal and spatial variability observed above the polar regions. The effect of column ozone on the depth-integrated photolysis rate coefficient ratio was explored as downwelling UV radiation is very sensitive to stratospheric ozone absorption and the attenuation is a strong function of wavelength. Typical value of column ozone in Antarctica (also the global average; Kroon et al., 2008) is about 300 DU but can be as low as 150 DU in the Antarctic $O_3$ hole (Kramarova et al., 2014). Column ozone generally increases from the tropics to midlatitudes. Therefore, there are three different values of total column ozone: 200, 300 and 400 DU.

**Table 3.** Optical properties of the snowpacks used. The bold numbers are to highlight the optical property that is varying in that particular case.

| | $\rho$ g cm$^{-3}$ | [BC] ng(C) g$^{-1}$ | $\sigma_{scatt}$ m$^2$ kg$^{-1}$ | $O_3$ col. DU | $g$ | $z_e$ * cm$^{-1}$ | Designation |
|---|---|---|---|---|---|---|---|
| Base case | 0.4 | 4.0 | 25 | 300 | 0.89 | 13.3 | BaseC |
| Case 1 | **0.2** | 4.0 | 25 | 300 | 0.89 | 25.2 | Den0.2 |
| Density of snowpack | **0.6** | 4.0 | 25 | 300 | 0.89 | 9.1 | Den0.6 |
| Case 2 | 0.4 | 4.0 | **2** | 300 | 0.89 | 35.3 | Scatt2 |
| Scattering cross section | 0.4 | 4.0 | **7** | 300 | 0.89 | 24.4 | Scatt7 |
| Case 3 | 0.4 | **0.18** | 25 | 300 | 0.89 | 36.9 | BC0.18 |
| Black carbon content | 0.4 | **32.0** | 25 | 300 | 0.89 | 4.9 | BC32 |
| | 0.4 | **128.0** | 25 | 300 | 0.89 | 2.5 | BC128 |
| Case 6, $g$ | 0.4 | 4.0 | 25 | 300 | **0.86** | 12.0 | g0.86 |
| Case 7 | 0.4 | 4.0 | 25 | **200** | 0.89 | 13.3 | $O_3$200 |
| Ozone column | 0.4 | 4.0 | 25 | **400** | 0.89 | 13.3 | $O_3$400 |
| | $\rho$ g cm$^{-3}$ | [HULIS] ng g$^{-1}$ | $\sigma_{scatt}$ m$^2$ kg$^{-1}$ | $O_3$ col. DU | $g$ | $z_e$ * cm$^{-1}$ | Designation |
| Case 4 | 0.4 | **1.0** | 25 | 300 | 0.89 | 36.9 | HULIS1 |
| HULIS content | 0.4 | **8.0** | 25 | 300 | 0.89 | 22.0 | HULIS8 |
| | 0.4 | **17.0** | 25 | 300 | 0.89 | 15.3 | HULIS17 |
| | 0.4 | **1000.0** | 25 | 300 | 0.89 | 2.06 | HU1000 |
| | 0.4 | **17.0** | **2** | 300 | 0.89 | 37.0 | HU17S2 |
| | 0.4 | **1000.0** | **2** | 300 | 0.89 | 7.3 | HU1000S2 |
| Case 5 | | [BC] + [HULIS] | | | | | |
| Combined | 0.4 | **0.6 + 8** | **7** | 300 | 0.89 | 30.6 | Comb |

* For cases 1–2 and 4–6, the reported $e$-folding depth, $z_e$, is the average of $e$-folding depth at 321, 345 and 375 nm. For cases 3 and 7, $z_e$ is the $e$-folding depth at 321 nm

### 2.1 RT method: radiative-transfer model, TUV

The attenuation of actinic flux with depth was calculated by a coupled atmosphere–snow radiative-transfer model, TUV 4.4, using an eight-stream DISORT (Discrete Ordinates Radiative Transfer Program for a Multi-Layered Plane-Parallel Medium) model (Lee-Taylor and Madronich, 2002). The model treats the snow as a weakly absorbing, very scattering homogenous layer with its optical properties described by the variables $g$, $\sigma_{scatt}$, and $\sigma_{abs}$. The snowpacks were modelled as described in detail in Lee-Taylor and Madronich (2002) except the absorption cross section of ice was updated to values given by Warren and Brandt (2008). The model configuration in this study used 110 snowpack layers with 1 mm spacing in the top 1 cm and 1 cm spacing for the rest of the 1 m snowpack, and 72 atmospheric layers with 1 m spacing for the first 10 m above snowpack surface then 10 m intervals until 100 m, 100 m interval up to 1 km, 1 km intervals up to 10 km and 2 km intervals up to 80 km, with no atmospheric loading of aerosol and assumed clear-sky conditions.

Values of the photolysis rate coefficient, $J$, for Reactions (R1)–(R4) and (R7) were calculated by TUV using Eq. (1). The absorption cross section of the chromophores in the ice phase are assumed to be the same as the aqueous phase and are listed with temperature-dependent quantum yields for reactions used in this study (Table 1). Photolysis rate coefficients calculated with the TUV are referred to as the "RT method".

### 2.2 $z_e$ method: $e$-folding depth

The $e$-folding depths, $z_e$, for the snowpacks described in Table 3 were calculated by fitting Eq. (2) to an actinic flux depth profile through snowpack obtained from TUV with a vertical resolution of 1 cm from 20 cm below the snowpack surface. At this depth, radiation is effectively diffuse and decays exponentially with depth (asymptotic zone). Field measurements of $e$-folding depth have been previously carried out over similar depths in the snowpack (e.g. France and King, 2012).

Values of $z_e$ were determined for three wavelengths ($\lambda =$ 321, 345 and 375 nm) and at seven different solar zenith angles (0, 36.9, 53.1, 66.4, 78.5, 80 and 90°). These wavelengths were chosen as they represent the peak of the pho-

tolysis action spectrum for each chemical species (Table 1). The photolysis rate coefficients were approximated by scaling the surface photolysis rate coefficient calculated by the RT method (TUV model) with the average $e$-folding depth, $z_e$, over seven solar zenith angles at a wavelength that is near the peak of the action spectrum of the chemical species (as shown in Eq. 3). For example in the case of $NO_3^-$ photolysis,

$$J_{z_e,NO_3^-}(\theta,z) = J_{NO_3^-}(\theta,z_0)\, e^{-\frac{z-z_0}{z_e(\lambda=321\,\mathrm{nm})}}, \quad (8)$$

where $J_{z_e,NO_3^-}(\theta,z)$ is the parameterised photolysis rate coefficient at depth $z$; $J_{NO_3^-}(\theta,z_0)$ is the photolysis rate coefficient of $NO_3^-$ at the surface obtained by the RT method (TUV model); and $z_e^{\lambda=321\,\mathrm{nm}}$ is the $e$-folding depth, $z_e$, at a wavelength of 321 nm. For clarity, this $e$-folding depth parameterisation is called the "$z_e$ method".

### 2.3 Ratio of depth-integrated photolysis rate coefficients

To determinate the accuracy of the $z_e$ method relative to the RT method, the ratio of depth-integrated photolysis rate coefficients, $Q$, was determined. The $Q$ ratio is defined as depth-integrated photolysis rate coefficient calculated with the RT method over the depth-integrated photolysis rate coefficients estimated by the $z_e$ method. For example, $Q$ in the case of $NO_2$ (Reaction R1) is given by

$$Q = \frac{v_{TUV,NO_2}}{v_{z_e,NO_2}} = \frac{\int J_{NO_3^-\to NO_2}(z)\,\mathrm{d}z}{J_{NO_3^-\to NO_2}(z_0)\int e^{-\frac{z-z_0}{z_e^{\lambda=321\,\mathrm{nm}}}}\,\mathrm{d}z}, \quad (9)$$

where $J_{z_e,NO_3^-\to NO_2}(z_0)$ is the photolysis rate coefficient for $NO_3^-$ photolysis at the surface of the snowpack. For Reactions (R3), (R4) and (R7), the surface photolysis rate coefficients were scaled, with $e^{\frac{-z-z_0}{z_e}}$ with $e$-folding depth at 345, 375 and 321 nm respectively for each depth $z$.

## 3 Results and discussion

The study evaluates the accuracy of parameterisation of photolysis rate coefficient to variation in solar zenith angle, different photolysis precursors, snowpack properties and total column ozone. Correction factors were also found for each different species to improve the performance of the $z_e$ method.

### 3.1 The response of $e$-folding depth to solar zenith angle and wavelength

Radiation in the asymptotic layer, i.e. below the first few centimetres of the snow surface (Fig. 1), decreases exponentially with depth as observed previously at various polar and non-polar sites (Warren and Wiscombe, 1980; Marks and King, 2014; Fisher et al., 2005; King and Simpson, 2001). Table 3 lists the average $e$-folding depth across seven solar zenith angles for all cases. For the base case, cases 1–3, 6 and 7, the $e$-folding depths listed are averaged not only across solar zenith angles but also across three wavelengths (321, 345 and 375 nm). There are no significant differences between the calculated $e$-folding depths, across different solar zenith angles or across the three wavelengths of which the variation coefficients are between 0.002 and 2 %. For snowpacks in cases 4 and 5, the $e$-folding depths were at a single wavelength (321 nm) only and the variation coefficients range from 0.007 to 0.16 %. Figure 2 shows how $e$-folding depth varies with wavelength and density, black carbon mass ratio, HULIS mass ratio or scattering cross section of the snowpack. At all wavelengths, the $e$-folding depth decreases with increasing snow density, and increasing the mass ratio of the black carbon increased the absorption of incident radiation. Absorption of HULIS is wavelength-dependent; i.e. increasing mass ratio of HULIS only increases absorption of UV and near-UV radiation. However, the absorption of the incident radiation in the visible wavelengths is independent of the mass ratio of HULIS. Increasing the scattering cross section also leads to a decrease in $e$-folding depth.

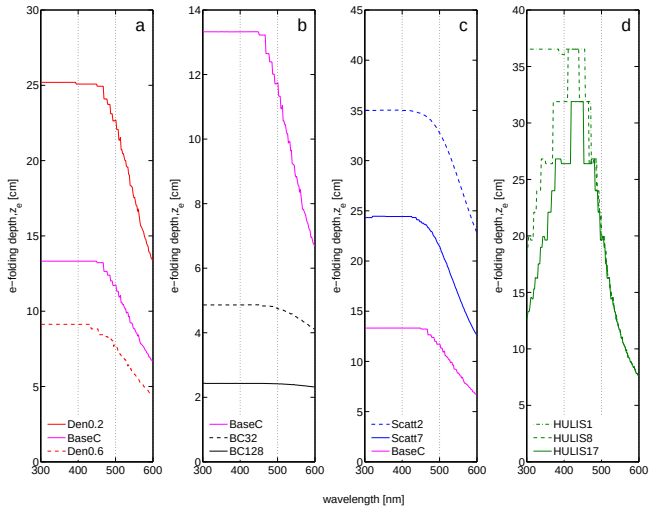


**Figure 2.** The $e$-folding depth, $z_e$, as a function of wavelength and dependence on **(a)** snow density, $\rho$ (case 1); **(b)** scattering cross section, $\sigma_{scatt}$ (case 2); **(c)** absorption due to black carbon, [BC] (case 3); **(d)** absorption due to HULIS, [HULIS] (case 4). Values of $e$-folding depth decrease as values of density, black carbon mass ratio and scattering cross section increase across wavelengths between 300 and 600 nm. For snowpacks containing black carbon as the only absorber other than ice, the change in $e$-folding depths are not sensitive to wavelength in the UV and near UV. However, for snowpacks containing e.g. HULIS the change in $e$-folding depth is sensitive to wavelength.

Scattering of photons typically occurs at the air–ice interface of a snow grain and absorption occurs within the snow grain. A denser snowpack implies more scattering or absorp-

tion events per unit length. A larger scattering cross section will typically reduce the path length of a photon through the snowpack and reduce the possibility for absorption by ice or light-absorbing impurities. Therefore, increases in density, light-absorbing impurities and scattering cross section result in a smaller $e$-folding depth.

### 3.2 Variation of $Q$, ratio of depth-integrated photolysis rate coefficients

Depth-integrated photolysis rate coefficients of the four chemical species considered ($NO_3^-$, $NO_2^-$, $H_2O_2$ and $NO_2$) were calculated by the RT method and the $z_e$ method. To evaluate the accuracy of the approximation by the $z_e$ method, the ratio $Q$ ($\frac{v_{TUV}}{v_{z_e}}$ using Eq. 9), is calculated and considered independently.

#### 3.2.1 Variation with solar zenith angle

When the solar zenith angle is between 0 and 37°, using the $z_e$ method leads to a depth-integrated photolysis rate coefficient ratio, $Q$, of up to 1.35 (Fig. 3). The underestimation of the $z_e$ method at small solar zenith angles is due to the enhancement of actinic flux compared to above the surface in the near-surface layer being considered in the RT method but being neglected in the $z_e$ method. For solar zenith angles around 50° and larger than 80° the value of $Q$ is close to unity, suggesting the $z_e$ method may be a good approximation for these solar zenith angles. Wiscombe and Warren (1980) suggested that solar illumination around a solar zenith angle of 50° was effectively the same as diffuse radiation, which deceases exponentially with depth from the snow surface. At large solar zenith angles (> 80°) there is little direct solar radiation relative to diffuse radiation illuminating the snowpack and the snowpack is effectively illuminated by diffuse radiation; thus the difference between the two methods is small. Between the solar zenith angles of ∼66 and 75°, i.e. minimum values of $Q$ in Fig. 3, the direct radiation entering the snowpack may be potentially scattered out of the snowpack due to the strong forward-scattering property of snow. Hence, the actinic flux attenuates at a quicker rate than the $e$-folding depth in the near-surface zone, and the $z_e$ method overestimates the intensity of solar radiation in the snowpack.

In reality, only high-altitude glaciers in the tropics, such as those found in the Himalayas or Andes, would experience the overhead sun or small solar zenith angles in the summer. In the polar regions, where snow emission can dominate boundary layer chemistry (e.g. Davis et al., 2004), solar zenith angles vary between 42.8° (Antarctic/Arctic Circle) and 66.5° (at the pole) at summer solstice and close to or greater than 90° during winter solstice for the Antarctic/Arctic Circle. Within this solar zenith angle range, the $z_e$ method is most likely to yield small overestimates of fluxes and photochemical production rate. However, small "effective" solar zenith angles can be achieved in sloping snow-covered terrain, as shown in Fig. 4. The effective solar zenith angle, $\theta_{eff}$, on a snow-covered slope is the difference between the solar zenith angle normal to a horizontal surface, $\theta_{dir}$, and the angle of the slope, $\phi$. Therefore, the $z_e$ method might lead to underestimation of depth-integrated production rates on snow-covered mountains.

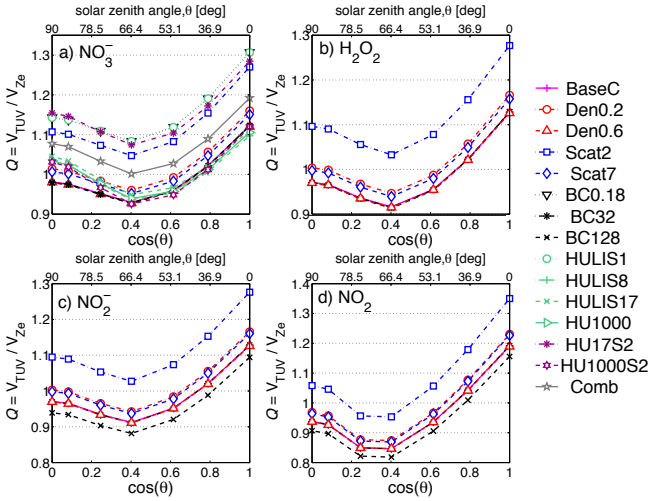


**Figure 3.** The ratio of depth-integrated photolysis rate coefficient, $Q = \frac{v_{TUV}}{v_{z_e}}$, for the two different methods as a function of solar zenith angle, $\theta$. **(a)** $NO_3^-$ anion; **(b)** $H_2O_2$; **(c)** $NO_2^-$ anion; **(d)** $NO_2$. Magenta: BaseC snowpack ($\rho = 0.4\,g\,cm^{-3}$, $[BC] = 4\,ng(C)\,g^{-1}$ and $\sigma_{scatt} = 25\,m^2\,kg^{-1}$).

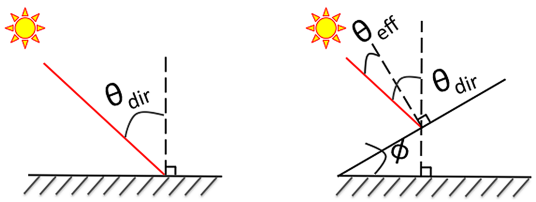


**Figure 4.** The effective solar zenith angle, $\theta_{eff}$, is the same as the solar zenith angle of direct solar radiation, $\theta_{dir}$, on a flat surface (left). However, on a surface that has an incline (right) the effective solar angle, $\theta_{eff}$, is the difference of the direct solar zenith angle and the angle of the surface, $\phi$, and typically smaller.

#### 3.2.2 Variation with chemical species and total column ozone

The value of the ratio $Q$ for the photolysis of the $NO_3^-$ anion and $H_2O_2$ is very similar in terms of its response to changing solar zenith angle (Fig. 3a and b). The maximum and minimum values of $Q$ are ∼1.27 (underestimation of solar radiation by the $z_e$ method), at direct overhead sun, and ∼0.92 (overestimation of solar radiation by the $z_e$ method), at solar zenith angles of ∼66–70°. The disagreement between the two methods for the photolysis of $NO_2^-$ is slightly larger,

with the ratio $Q$ ranging between 0.88–1.28 (Fig. 3c). The approximation with the $z_e$ method is the most inaccurate for the photolysis of $NO_2$ within snowpack interstitial air, having $Q$ values range between 0.82 and 1.35 (Fig. 3d).

The $NO_3^-$ anion and $H_2O_2$ have the peak of their action spectrum in the UV-B, while the $NO_2^-$ anion and $NO_2$ have a peak in near-UV and visible wavelengths respectively. Solar radiation in the UV region is less intense and more diffuse relative to the UV-A and visible radiation at the snow surface as (1) the ozone layer absorbs strongly in the UV-B and UV-C while relatively weakly in the UV-A and almost negligibly in the visible region and (2) the Rayleigh scattering of photons by air molecules increases as the wavelength decreases. The actinic flux attenuation profile with depth, in snow, of more diffused actinic flux can be better approximated by the $e$-folding depth; therefore, the $z_e$ method provides a better estimation of photolysis rate coefficient profile for $NO_3^-$ and $H_2O_2$ compared to $NO_2^-$ and $NO_2$.

The wavelength of the peak in the action spectrum of a chemical species also has an impact on its response to changes in column ozone concentration (case 7) in terms of photolysis rate coefficient. The surface photolysis rate coefficients for $NO_3^-$ and $H_2O_2$ are more sensitive to the changes in column ozone, due to their action spectrum peak in the UV-B region, compared to species that have their peak in UV-A, such as $NO_2^-$ and $NO_2$. The surface values of $J_{NO_3^-}$ (Fig. 5a) and $J_{H_2O_2}$ increased by $\sim 20\,\%$ when total ozone column decreased from 300 to 200 DU, while surface values of $J_{NO_2^-}$ and $J_{NO_2}$ (Fig. 5b) only increased by approximately 6 and 0.9 % respectively. When total ozone column increased from 300 to 400 DU, surface values of $J_{NO_3^-}$ and $J_{H_2O_2}$ dropped approximately by $\sim 14\,\%$, whereas surface values of $J_{NO_2^-}$ and $J_{NO_2}$ only decreased by $\sim 5$ and 0.6 % respectively.

Despite the value of the photolysis rate coefficient varying with values of different column ozone, especially for the $NO_3^-$ anion and $H_2O_2$, the propagation of radiation throughout the snowpack was not affected by the column ozone; i.e. the value of $Q$ was unchanged by changing the ozone column, and the $z_e$ method is not sensitive to ozone column values.

### 3.2.3 Variation with snow physical properties

Density (case 1), scattering cross section (case 2), light-absorbing impurities (cases 3–5) and asymmetry factor (case 6) were considered as the four varying physical properties of the snowpack in this study. Figure 3 highlights three results in terms of various physical properties of the snowpacks: Firstly, snow density has a small effect on the ability of the $z_e$ method to reproduce the results of RT method. Secondly, the $z_e$ method underestimates depth-integrated photolysis rate coefficients significantly for relatively clean snowpacks and snowpacks with low scattering cross section at small and large solar zenith angles. Thirdly, changes of $Q$

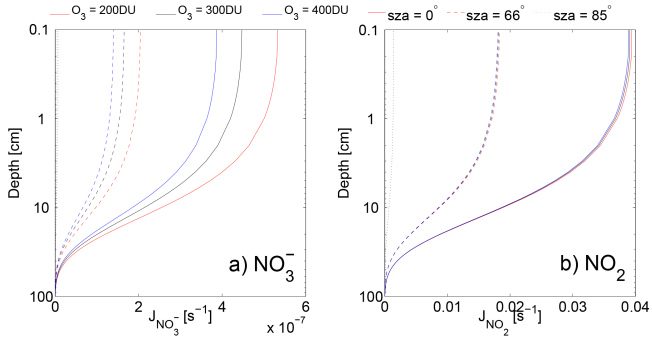


**Figure 5.** The effect of different column ozone amount on the photolysis rate coefficient of **(a)** $NO_3^-$ and **(b)** $NO_2$ at three selected solar zenith angles (0°, 66° and 85°).

with increasing mass ratio of light-absorbing impurities depend on the chemical species being photolysed. All three of these effects depend on either the ratio of direct to diffuse radiation in the top of the snowpack or the conversion of direct solar radiation to diffuse solar radiation in the near-surface layer of the snowpack.

With regard to the density of the snowpack, the photolysis rate coefficient maxima are at a deeper depth for snowpacks with lower density. That is, the path length of the photon is longer for less-dense snowpacks. However, for the range of density values found in natural snow (case 1, $\rho = 0.2$–$0.6\,\mathrm{g\,cm^{-3}}$) the difference in the $Q$ ratio is very small, of the order of $\sim 3.5\,\%$ (red symbols and lines in Fig. 3).

Scattering cross section of the snowpack: lower values of the scattering cross section imply longer path length of the photon between individual scattering events. Hence, the maximum photolysis rate coefficients tend to occur deeper into the snowpacks, as shown in blue in Fig. 6 (Scatt2, i.e. melting snow), compared with snowpacks that have a larger scattering cross section (magenta in Fig. 6, BaseC, i.e. cold polar snow). Thus for snowpacks with a small scattering cross section the agreement between the RT and $z_e$ methods is likely to be poor as the $z_e$ method will not capture the behaviour in the near-surface layer accurately.

Light-absorbing impurities in the snowpack: the propagation of actinic flux and the vertical variation of photolysis rate coefficient within snowpack is dominated by scattering when light-absorbing impurity contents are low and therefore the absorption properties of the impurity become unimportant, i.e. there is no difference between the value of $Q$ for snowpack BC0.18 and HULIS1 listed in Table 3. In case 3, absorption due to black carbon, the variation of $Q$ with solar zenith angle is approximately the same for the photolysis of $NO_3^-(\lambda \sim 321\,\mathrm{nm})$, $H_2O_2(\lambda \sim 321\,\mathrm{nm})$, $NO_2^-(\lambda \sim 345\,\mathrm{nm})$ and $NO_2(\lambda \sim 375\,\mathrm{nm})$. Except for heavily polluted snow, e.g. snowpack BC128 ($\rho = 0.4\,\mathrm{g\,cm^{-3}}$, $[\mathrm{BC}] = 128\,\mathrm{ng(C)\,g^{-1}}$ and $\sigma_{\mathrm{scatt}} = 25\,\mathrm{m^2\,kg^{-1}}$), the ratio $Q$ for photolysis of the $NO_2^-$ anion and $NO_2$ deviated from

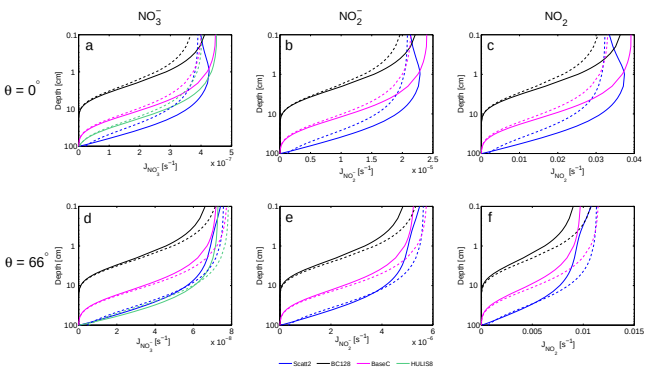


**Figure 6.** Photolysis rate coefficient for the $NO_3^-$ anion (**a** and **d**), the $NO_2^-$ anion (**b** and **e**) and $NO_2$ (**c** and **f**) computed by TUV (solid line) and $z_e$ method (dashed line) at two different solar zenith angles, $\theta$, at 0° (top row) and 66° (bottom row). Maximum and minimum depth-integrated photolysis rate coefficient ratio occurred at $\theta = 0°$ and $\theta = \sim 66°$ respectively. Blue is the "melting snow", Scatt2 ($\rho = 0.4\,\mathrm{g\,cm^{-3}}$, $[\mathrm{BC}] = 4\,\mathrm{ng(C)\,g^{-1}}$ and $\sigma_{\mathrm{scatt}} = 2\,\mathrm{m^2\,kg^{-1}}$); black is the "heavily black carbon polluted snow", BC128 ($\rho = 0.4\,\mathrm{g\,cm^{-3}}$, $[\mathrm{BC}] = 128\,\mathrm{ng(C)\,g^{-1}}$ and $\sigma_{\mathrm{scatt}} = 25\,\mathrm{m^2\,kg^{-1}}$); magenta is the "BaseC snow" BaseC ($\rho = 0.4\,\mathrm{g\,cm^{-3}}$, $[\mathrm{BC}] = 4\,\mathrm{ng(C)\,g^{-1}}$ and $\sigma_{\mathrm{scatt}} = 25\,\mathrm{m^2\,kg^{-1}}$); and green is the "HULIS-polluted snow", HULIS8 ($\rho = 0.4\,\mathrm{g\,cm^{-3}}$, $[\mathrm{HULIS}] = 8\,\mathrm{ng\,g^{-1}}$ and $\sigma_{\mathrm{scatt}} = 25\,\mathrm{m^2\,kg^{-1}}$). Surface (depth = 0 cm) values of photolysis rate coefficient from the "RT method" and "$z_e$ method" are the same (see Eq. 8 for calculation of $J_{\mathrm{TUV}}$).

snowpacks with lower black carbon mass ratio slightly (∼ 3 and ∼ 3.5 % respectively). In Fig. 6, black lines representing the extreme polluted case – BC128 – the photolysis rate coefficient calculated by the two methods matches at around 2 cm depth for the $NO_3^-$ anion, but ∼ 4 and ∼ 5 cm for the $NO_2^-$ and $NO_2$ respectively. The latter two compounds have the peak of their action spectrum at larger wavelengths relative to the $NO_3^-$ anion and $H_2O_2$ as discussed in Sect. 3.2.2. The ratio of direct to diffuse incident solar radiation in the snowpack increases with wavelength around 300–400 nm and will increase the difference between the photolysis rate coefficient depth profile calculated by the $z_e$ and RT methods especially in the top few centimetres of the snowpack.

In case 4, the absorption due to HULIS is considerable. A mass ratio of $100\,\mathrm{ng\,g^{-1}}$ of HULIS in the snowpack will reduce the photolysis of $NO_3^-$ anion and $H_2O_2$ much more than the photolysis of $NO_2^-$ and $NO_2$ as HULIS absorption cross section increases with decreasing wavelengths. The absorption cross section due to 1, 8, 17 and $1000\,\mathrm{ng\,g^{-1}}$ of HULIS is respectively equivalent to 0.18, 1.4, 3.0 and $177\,\mathrm{ng(C)\,g^{-1}}$ of black carbon at 321 nm, but only equivalent to 0.11, 0.87, 1.85 and $109\,\mathrm{ng(C)\,g^{-1}}$ of black carbon at 345 nm and 0.06, 0.50, 1.05 and $62.0\,\mathrm{ng(C)\,g^{-1}}$ of black carbon at 375 nm. If the light-absorption by impurities in a snowpack is dominated by black carbon, then the value of $e$-folding depth in the UV-B and UV-A will be similar. However, if the light-absorption in the snow is dominated by HULIS (or even dust), then strictly a different $e$-folding depth is needed for each wavelength that is characteristic of the photolysis of the species of interest.

Asymmetry factor of the snowpack: Libois et al. (2014) recently suggested that the value of the asymmetry parameter, $g$, should be $g = 0.86$ due to non-spherical grains observed in the laboratory and in the field in Antarctica and the French Alps. The $e$-folding depth is sensitive to the value of the asymmetry factor as shown by Libois et al. (2013). Reducing the asymmetry factor from 0.89 to 0.86 reduces the tendency of photons being forward-scattered, and hence the $e$-folding depth is reduced by ∼ 11 %. The reduction in photolysis rate coefficient is also ∼ 11 %. Nevertheless, there are no significant relative differences between the RT and $z_e$ methods for changing $g$. The parameterisation with $e$-folding depth generated a similar approximation of photolysis rate coefficient for either of the two $g$ values. The other properties of the snowpacks were unchanged.

### 3.3 Parameterisation correction

The difference in the depth-integrated photolysis rate coefficient, $v$, between the $z_e$ method and RT method can be minimised by applying a correction factor, $C(\theta)$, as a function of the solar zenith angle. The correction factor, $C(\theta)$, was computed by fitting a quadratic equation to the plot of depth-integrated photolysis rate coefficient ratio, $Q$ (Eq. 9), of each reaction as a function of solar zenith angle. The fitting is categorised into two types of snow – (1) wind pack and cold polar snow, and (2) melting and clean snow. Formulation of the correction factor, $C$, is shown in Eq. (10), and the coefficients $(a, b, c)$ of the quadratic equation are listed in Tables 4 and 5 for "wind pack and cold polar" and "melting and clean" snow respectively. The depth-integrated photolysis rate coefficient approximated by the $z_e$ method at a particular solar zenith angle can then be corrected by multiplying by the correction factor, $C(\theta)$, at that particular solar zenith angle as shown in Eq. (11).

$$C(\theta) = a\cos^2(\theta) + b\cos(\theta) + c, \tag{10}$$

$$v_{z_e}^{\mathrm{Corr}}(\theta) = C(\theta)\, v_{z_e}(\theta), \tag{11}$$

where $C(\theta)$ is the correction factor at a particular solar zenith angle; $a$, $b$, $c$ are the coefficient of the quadric equation; $v_{z_e}$ is the depth-integrated photolysis rate coefficients approximated by the $z_e$ method; and $v_{z_e}^{\mathrm{Corr}}$ is the corrected depth-integrated photolysis rate coefficient $v_{z_e}$.

For snowpacks with a large $e$-folding depth, i.e. > 30 cm – for example either having a small scattering cross section or containing a small amount of light-absorbing impurities – it is suggested to apply correction factors for "melting and clean snow" when solar zenith angles are smaller than 50° and larger than 80° to reduce the error by 10–30 %. For snowpacks that have an $e$-folding depth smaller than 30 cm, the

**Table 4.** Parameterisation correction for "cold polar and coastal" snowpacks. Values of the correlation coefficient were calculated for two different snowpacks (BaseC, HULIS8 and Comb) with and without applying the correction factors.

| | | | | BaseC | | HULIS8 | | Comb | |
|---|---|---|---|---|---|---|---|---|---|
| Species | $a$ | $b$ | $c$ | $R^2$, $v_{z_e}$ | $R^2$, $v_{z_e}^{\mathrm{Corr}}$ | $R^2$, $v_{z_e}$ | $R^2$, $v_{z_e}^{\mathrm{Corr}}$ | $R^2$, $v_{z_e}$ | $R^2$, $v_{z_e}^{\mathrm{Corr}}$ |
| $NO_3^-$ | 0.452 | −0.320 | 1.000 | 0.9788 | 0.9996 | 0.9862 | 0.9971 | 0.9468 | 0.9927 |
| $H_2O_2$ | 0.485 | −0.334 | 0.989 | 0.9758 | 0.9998 | | | | |
| $NO_2^-$ | 0.494 | −0.345 | 0.980 | 0.9749 | 1.0000 | | | | |
| $NO_2$ | 0.758 | −0.495 | 0.941 | 0.9435 | 0.9995 | | | | |

**Table 5.** Parameterisation correction for "melting and clean" snowpack. Values of the correlation coefficient were calculated for two different snowpacks (Scatt2, HULIS1 and Comb) with and without applying the correction factors.

| | | | | Scatt2 | | HULIS1 | | Comb | |
|---|---|---|---|---|---|---|---|---|---|
| Species | $a$ | $b$ | $c$ | $R^2$, $v_{z_e}$ | $R^2$, $v_{z_e}^{\mathrm{Corr}}$ | $R^2$, $v_{z_e}$ | $R^2$, $v_{z_e}^{\mathrm{Corr}}$ | $R^2$, $v_{z_e}$ | $R^2$, $v_{z_e}^{\mathrm{Corr}}$ |
| $NO_3^-$ | 0.523 | −0.384 | 1.146 | 0.9004 | 0.9996 | 0.8742 | 0.9991 | 0.9481 | 0.9833 |
| $H_2O_2$ | 0.550 | −0.378 | 1.107 | 0.8503 | 0.9934 | | | | |
| $NO_2^-$ | 0.565 | −0.394 | 1.106 | 0.8883 | 1.0000 | | | | |
| $NO_2$ | 0.868 | −0.565 | 1.062 | 0.8352 | 0.9995 | | | | |

"wind pack and cold polar snow" correction factors should be applied when the solar zenith angles are small than 30° or between 60 and 70°. This could reduce the error by up to 15 %.

The correction was evaluated by comparing the depth-integrated photolysis rate coefficients computed by the RT method, $v_{\mathrm{TUV}}$, to depth-integrated photolysis rate coefficient approximated by the $z_e$ method, $v_{z_e}$, and the corrected depth-integrated photolysis rate coefficient by the $z_e$ method, $v_{z_e}^{\mathrm{Corr}}$, for all four species at 20 different solar zenith angles of snowpack BaseC (Table 3) using wind pack and cold polar snowpack correction factors, and results are shown in Fig. 7. For evaluating the melting and clean snowpack correction factors, snowpack Scatt2 (Table 3) was used, and results are shown in Fig. 8. The corrections factors for the $NO_3^-$ photolysis rate coefficient were also tested against snowpacks HULIS1, HULIS8 and Comb (Table3).

The correlation between $v_{z_e}$ and $v_{z_e}^{\mathrm{Corr}}$ with $v_{\mathrm{TUV}}$ is described by the square of correlation coefficients, $R^2$, listed in Tables 4 and 5 correction factors for wind pack and cold polar, and melting and clean snowpacks respectively. The approximation of depth-integrated photolysis rate coefficient has improved significantly with the correction factor, especially for (1) the melting and clean snowpack, (2) photolysis of the $NO_2^-$ anion and (3) $NO_2$ at small solar zenith angles.

There are many factors that might have an impact on the disagreement between the two methods not taken into account in this study. Cloudy skies are not taken into account. However, clouds convert direct radiation into diffuse radiation. Under a very thickly clouded sky all radiation reaching the ground will be diffused and the decay of actinic flux within the snowpack would be exponential. Therefore, on a cloudy day the $z_e$ method would provide a very good approximation of actinic flux profile and photolysis rate coefficient within snowpack even without correction. Other assumptions have also been made on snowpack properties, i.e. assuming homogeneous single-layer snowpack, black carbon or HULIS as the only absorber other than ice and constant vertical chemical concentration profile. Geographic location and weather conditions may have a major influence on the number of layers within snowpack and the distribution of their physical and optical properties. Last, but not least, field observations on the Antarctic Plateau (Frey et al., 2009; France et al., 2011) show there is a much higher nitrate anion concentration in the top few centimetres of the snowpack, the region of the snowpack where the solar radiation attenuation is often non-exponential, than deeper into the snowpack, causing a potentially larger error estimating depth-integrated production rates from the $z_e$ method.

## 4 Conclusions

The parameterisation of snowpack actinic flux based on the $e$-folding depth – the $z_e$ method, which approximates the actinic flux profile by an exponential function – may lead to under/overestimation of depth-integrated photolysis rate coefficients compared to the RT (radiative transfer) method. The deviation depends on the chemical species, solar zenith angle and properties of the snowpack. The $z_e$ method is most likely to provide a poor estimation of depth-integrated photolysis rate under four conditions: (1) solar zenith angle or effective solar zenith angle being small ($\theta$ <37°); (2) the chemical species of interest having an action spectrum peak near or in the visible wavelength, such as $NO_2^-$ and $NO_2$; (3) melting

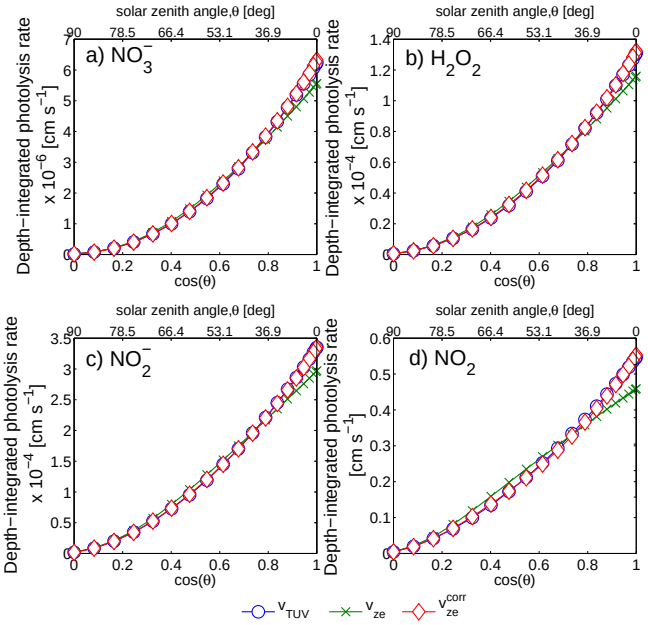


**Figure 7.** Depth-integrated photolysis rate coefficient at various solar zenith angle for different species within snowpack BaseC ($\rho = 0.4\,\mathrm{g\,cm^{-3}}$, $[\mathrm{BC}] = 4\,\mathrm{ng(C)\,g^{-1}}$ and $\sigma_{\mathrm{scatt}} = 25\,\mathrm{m^2\,kg^{-1}}$). **(a)** Depth-integrated photolysis rate coefficient of the $NO_3^-$ anion; **(b)** depth-integrated photolysis rate coefficient of $H_2O_2$; **(c)** depth-integrated photolysis rate coefficient of the $NO_2^-$ anion; **(d)** depth-integrated photolysis rate coefficient of $NO_2$; blue circle – $v_{\mathrm{TUV}}$, computed by TUV; green cross – $v_{z_e}$, calculated by the $e$-folding depth method; pink diamond – $v_{z_e}^{\mathrm{Corr}}$, corrected $v_{z_e}$ by coefficients listed in Table 4.

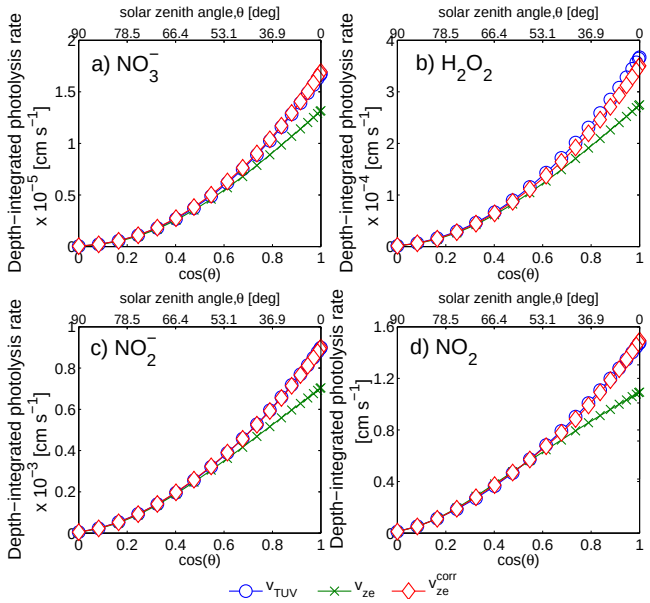


**Figure 8.** Depth-integrated photolysis rate coefficient at various solar zenith angle for different species within snowpack Scatt2 ($\rho = 0.4\,\mathrm{g\,cm^{-3}}$, $[\mathrm{BC}] = 4\,\mathrm{ng(C)\,g^{-1}}$ and $\sigma_{\mathrm{scatt}} = 2\,\mathrm{m^2\,kg^{-1}}$). **(a)** Depth-integrated photolysis rate coefficient of the $NO_3^-$ anion; **(b)** depth-integrated photolysis rate coefficient of $H_2O_2$; **(c)** depth-integrated photolysis rate coefficient of the $NO_2^-$ anion; **(d)** depth-integrated photolysis rate coefficient of $NO_2$; blue circle – $v_{\mathrm{TUV}}$, computed by TUV; green cross – $v_{z_e}$, calculated by the $e$-folding depth method; red diamond – $v_{z_e}^{\mathrm{Corr}}$, corrected $v_{z_e}$ by coefficients listed in Table 5.

snowpack, which has a small value of scattering cross section; and (4) clean snowpack, which has a small absorption cross section due to low impurity content.

The discrepancy between the $z_e$ and RT methods can be improved by applying the correction factors, $C(\theta)$, especially for melting and clean snowpack (i.e. snowpacks have an $e$-folding depth larger than ∼30 cm), for which the ratio of depth-integrated photolysis rate coefficient between the two methods, $Q$, has reduced from 0.82–1.35 to 0.97–1.02 for photolysis of $NO_2$, from 0.88–1.28 to 0.99–1.02 for photolysis of the $NO_2^-$ anion, from 0.93–1.27 to 0.99–1.03 for photolysis of the $NO_3^-$ anion and from 0.91–1.28 to 0.98–1.06 for $H_2O_2$. In the polar regions, solar zenith angles larger than 42.8° are the norm; the simple $z_e$ method provides an acceptable estimation (10–16 % underestimation compared to radiative transfer model). However, if the site of interest is a tropical glacier, low-latitude, slope snowpack or have a small effective solar zenith angle ($\theta < 37°$) and is moderately to heavily polluted (e.g. $e$-folding depth smaller than 30 cm), then correction factors, $C$, from Tables 4 should be applied to reduce error up to 15 %. Correction factors, $C$, listed in Table 5 should be applied when the snowpack is clean, wet or melting (e.g. $e$-folding depth larger than 31 cm) to reduce the difference by up to 30 %.

The values of $e$-folding depth used in some of the previous modelling studies were broadly based on field measurements (Thomas et al., 2011; Simpson et al., 2002). Recently research groups have started to develop new algorithms to estimate optical properties of snowpack, such as grain size and mass ratio of pollutants, from satellite measurements (Zege et al., 2011; Malinka, 2014; Khokanovsky, 2015). These measurements and algorithms can be integrated into large-scale chemical transport models in the future to estimate $e$-folding depth and photolysis rate coefficient for wide inaccessible areas.

An important approximation of the $e$-folding depth ($z_e$) method is that snowpack is optically thick, i.e. assuming the snowpacks are semi-infinite. For shallow snowpacks the exact RT method should be used. It is unlikely a robust simple parameterisation could be developed to correct the $z_e$ method for shallow snowpacks over a range of light-absorbing snowpack, solar zenith angles and underlying terrains for the thin snowpack, i.e. soil or sea ice. For shallow snowpacks (< 2–3 $e$-folding depths) the RT method is recommended.

## Appendix A

**Table A1.** Notation.

| | | |
|---|---|---|
| $\sigma$ | Absorption cross section of chemical species | $cm^2\,molecule^{-1}$ |
| $\sigma_{ice}$ | Absorption cross section of ice | $cm^2\,kg^{-1}$ |
| $\mu_{abs}$ | Absorption coefficient | $m^{-1}$ |
| $\sigma^+$ | Absorption cross section per mass of impurities | $cm^2\,kg^{-1}$ |
| $I$ | Actinic flux | $quanta\,cm^{-2}\,s^{-1}\,nm^{-1}$ |
| $z_e$ | Asymptotic $e$-folding depth | cm |
| $g$ | Asymmetry factor | dimensionless |
| $c$ | Correction factor for depth-integrated photolysis rate coefficient | dimensionless |
| $\rho$ | Density of snowpack | $g\,cm^{-3}$ |
| $\kappa_{ext}$ | Extinction coefficient | $m^{-1}$ |
| $\sigma_{ext}$ | Extinction cross section | $m^2\,kg^{-1}$ |
| $J$ | Photolysis rate constant | $s^{-1}$ |
| $F$ | Photochemical production rate | $\mu mol\,cm^{-2}\,s^{-1}$ |
| $\Phi$ | Quantum yield | dimensionless |
| $Q$ | Quotient, ratio of depth-integrated photolysis rate coefficient | dimensionless |
| $r_{scatt}$ | Scattering coefficient | $m^{-1}$ |
| $\sigma_{scatt}$ | Scattering cross section | $m^2\,kg^{-1}$ |
| $\theta$ | Solar zenith angle | degree |
| $\sigma_{abs}$ | Total absorption cross section | $cm^2\,kg^{-1}$ |
| $v$ | depth-integrated photolysis rate coefficient | $cm\,s^{-1}$ |
| $\lambda$ | Wavelength | nm |

*Acknowledgements.* H. G. Chan is funded by the Natural Environment Research Council through Doctoral Studentship NE/L501633/1.

Edited by: T. Bartels-Rausch

## References

Anastasio, C. and Chuand, L.: Formation of hydroxyl radical from the photolysis of frozen hydrogen peroxide, J. Phys. Chem. A, 112, 2747–2748, doi:10.1021/jp800491n, 2008.

Bartels-Rausch, T., Jacobi, H.-W., Kahan, T. F., Thomas, J. L., Thomson, E. S., Abbatt, J. P. D., Ammann, M., Blackford, J. R., Bluhm, H., Boxe, C., Domine, F., Frey, M. M., Gladich, I., Guzmán, M. I., Heger, D., Huthwelker, Th., Klán, P., Kuhs, W. F., Kuo, M. H., Maus, S., Moussa, S. G., McNeill, V. F., Newberg, J. T., Pettersson, J. B. C., Roeselová, M., and Sodeau, J. R.: A review of air-ice chemical and physical interactions (AICI): liquids, quasi-liquids, and solids in snow, Atmos. Chem. Phys., 14, 1587–1633, doi:10.5194/acp-14-1587-2014, 2014.

Beaglehole, D., Ramanathan, B., and Rumberg, J.: The UV to IR transmittance of Antarctic snow, J. Geophys. Res.-Atmos., 103, 8849–8857, doi:10.1029/97JD03604, 1998.

Beine, H. J., Dominé, F., Simpson, W., Honrath, R. E., Sparapani, R., Zhou, X., and King, M.: Snow-pile and chamber experiments during the Polar Sunrise Experiment "Alert 2000": exploration of nitrogen chemistry, Atmos. Environ., 36, 2707–2719, doi:10.1016/S1352-2310(02)00120-6, 2002.

Beine, H. J., Amoroso, A., Dominé, F., King, M. D., Nardino, M., Ianniello, A., and France, J. L.: Surprisingly small HONO emissions from snow surfaces at Browning Pass, Antarctica, Atmos. Chem. Phys., 6, 2569–2580, doi:10.5194/acp-6-2569-2006, 2006.

Chen, G., Davis, D., Crawford, J., Hutterli, L., Huey, L., Slusher, D., Mauldin, L., Eisele, F., Tanner, D., Dibb, J., Buhr, M., McConnell, J., Lefer, B., Shetter, R., Blake, D., Song, C., Lombardi, K., and Arnoldy, J.: A reassessment of $HO_x$ South Pole chemistry based on observations recorded during ISCAT 2000, Atmos. Environ., 38, 5451–5461, 2004.

Chu, L. and Anastasio, C.: Quantum yields of hydroxyl radical and nitrogen dioxide from the photolysis of nitrate on ice, J. Phys. Chem. A, 107, 9594–9602, doi:10.1021/jp0349132, 2003.

Chu, L. and Anastasio, C.: Formation of hydroxyl radical from the photolysis of frozen hydrogen peroxide, J. Phys. Chem. A, 109, 6264–6271, doi:10.1021/jp051415f, 2005.

Chu, L., and Anastasio, C.: Temperature and wavelength dependence of nitrite photolysis in frozen and aqueous solutions, Environ. Sci. Technol., 41, 3626–3632, doi:10.1021/es062731q, 2007.

Cotter, E. S. N., Jones, A. E., Wolff, E. W., and Bauguitte, S. J.-B.: What controls photochemical NO and $NO_2$ production from Antarctic snow? Laboratory investigation assessing the wavelength and temperature dependence, J. Geophys. Res.-Atmos., 108, 4147 , doi:10.1029/2002JD002602, 2003.

Davis, D., Chen, G., Buhr, M., Crawford, J., Lenschow, D., Lefer, B., Shetter, R., Eisele, F., Mauldin, L., and Hogan, A.: South Pole chemistry: an assessment of factors controlling variability and absolute levels, Atmos. Environ., 38, 5375–5388, 2004.

DeMore, W. B., C. J. Howard, D. M. G., Kolb, C. E., Hampson, R. F., and Molina, M. J.: Chemical Kinetics and Photochemical Data for Use in Stratospheric Modeling, JPL Publication 97–4, National Aeronautics and Space Administration, Jet Propulsion Laboratory, Pasadena, California, USA, 1997.

Dibb, J. E., Arsenault, M., Peterson, M. C., and Honrath, R. E.: Fast nitrogen oxide photochemistry in Summit, Greenland snow, Atmos. Environ., 36, 2501–2511, 2002.

Dubowski, Y., Colussi, A. J., and Hoffmann, M. R.: Nitrogen dioxide release in the 302 nm band photolysis of spray-frozen aqueous nitrate solutions. Atmospheric implications, J. Phys. Chem. A, 105, 4928–4932, doi:10.1021/jp0042009, 2001.

Dubowski, Y., Colussi, A. J., Boxe, C., and Hoffmann, M. R.: Monotonic increase of nitrite yields in the photolysis of nitrate in ice and water between 238 and 294 K, J. Phys. Chem. A, 106, 6967–6971, doi:10.1021/jp0142942, 2002.

Fisher, F. N., King, M. D., and Lee-Taylor, J.: Extinction of UV-visible radiation in wet midlatitude (maritime) snow: implications for increased $NO_x$ emission, J. Geophys. Res.-Atmos., 110, D21301, doi:10.1029/2005JD005963, 2005.

France, J. and King, M.: The effect of measurement geometry on recording solar radiation attenuation in snowpack (*e*-folding depth) using fibre-optic probes, J. Glaciol., 58, 417–418, doi:10.3189/2012JoG11J227, 2012.

France, J., King, M., and Lee-Taylor, J.: Hydroxyl (OH) radical production rates in snowpacks from photolysis of hydrogen peroxide ($H_2O_2$) and nitrate ($NO_3^-$), Atmos. Environ., 41, 5502–5509, doi:10.1016/j.atmosenv.2007.03.056, 2007.

France, J., King, M., and Lee-Taylor, J.: The importance of considering depth-resolved photochemistry in snow: a radiative-transfer study of $NO_2$ and OH production in Ny-alesund (Svalbard) snowpacks, J. Glaciol., 56, 655–663, doi:10.3189/002214310793146250, 2010.

France, J. L., King, M. D., Frey, M. M., Erbland, J., Picard, G., Preunkert, S., MacArthur, A., and Savarino, J.: Snow optical properties at Dome C (Concordia), Antarctica; implications for snow emissions and snow chemistry of reactive nitrogen, Atmos. Chem. Phys., 11, 9787–9801, doi:10.5194/acp-11-9787-2011, 2011.

France, J. L., Reay, H. J., King, M. D., Voisin, D., Jacobi, H. W., Domine, F., Beine, H., Anastasio, C., MacArthur, A., and Lee-Taylor, J.: Hydroxyl radical and $NO_x$ production rates, black carbon concentrations and light-absorbing impurities in snow from field measurements of light penetration and nadir reflectivity of onshore and offshore coastal Alaskan snow, J. Geophys. Res.-Atmos., 117, D00R12, doi:10.1029/2011JD016639, 2012.

Frey, M. M., Savarino, J., Morin, S., Erbland, J., and Martins, J. M. F.: Photolysis imprint in the nitrate stable isotope signal in snow and atmosphere of East Antarctica and implications for reactive nitrogen cycling, Atmos. Chem. Phys., 9, 8681–8696, doi:10.5194/acp-9-8681-2009, 2009.

Gardner, E. P., Sperry, P. D., and Calvert, J. G.: Primary quantum yields of $NO_2$ photodissociation, J. Geophys. Res.-Atmos., 92, 6642–6652, doi:10.1029/JD092iD06p06642, 1987.

Grannas, A. M., Jones, A. E., Dibb, J., Ammann, M., Anastasio, C., Beine, H. J., Bergin, M., Bottenheim, J., Boxe, C. S., Carver, G., Chen, G., Crawford, J. H., Dominé, F., Frey, M. M., Guzmán,

M. I., Heard, D. E., Helmig, D., Hoffmann, M. R., Honrath, R. E., Huey, L. G., Hutterli, M., Jacobi, H. W., Klán, P., Lefer, B., McConnell, J., Plane, J., Sander, R., Savarino, J., Shepson, P. B., Simpson, W. R., Sodeau, J. R., von Glasow, R., Weller, R., Wolff, E. W., and Zhu, T.: An overview of snow photochemistry: evidence, mechanisms and impacts, Atmos. Chem. Phys., 7, 4329–4373, doi:10.5194/acp-7-4329-2007, 2007.

Grenfell, T. C., Warren, S. G., and Mullen, P. C.: Reflection of solar radiation by the Antarctic snow surface at ultraviolet, visible, and near-infrared wavelengths, J. Geophys. Res.-Atmos., 99, 18669–18684, doi:10.1029/94JD01484, 1994.

Hoffer, A., Gelencsér, A., Guyon, P., Kiss, G., Schmid, O., Frank, G. P., Artaxo, P., and Andreae, M. O.: Optical properties of humic-like substances (HULIS) in biomass-burning aerosols, Atmos. Chem. Phys., 6, 3563–3570, doi:10.5194/acp-6-3563-2006, 2006.

Jacobi, H.-W., Bales, R. C., Honrath, R. E., Peterson, M. C., Dibb, J. E., Swanson, A. L., and Albert, M. R.: Reactive trace gases measured in the interstitial air of surface snow at Summit, Greenland, Atmos. Environ., 38, 1687–1697, doi:10.1016/j.atmosenv.2004.01.004,2004.

Jones, A. E., Weller, R., Wolff, E. W., and Jacobi, H. W.: Speciation and rate of photochemical NO and $NO_2$ production in Antarctic snow, Geophys. Res. Lett., 27, 345–348, doi:10.1029/1999GL010885, 2000.

Khokanovsky, A. A.: Remote Sensing of the Cryosphere, Ch4 Remote sensing of snow albedo, grain size, and pollution from space, 48–72, John Wiley & Sons, Ltd, Chichester, UK, doi:10.1002/9781118368909.ch4, 2015.

King, M. D. and Simpson, W. R.: Extinction of UV radiation in Arctic snow at Alert, Canada (82° N), J. Geophys. Res.-Atmos., 106, 12499–12507, doi:10.1029/2001JD900006, 2001.

Kroon, M., Veefkind, J. P., Sneep, M., McPeters, R. D., Bhartia, P. K., and Levelt, P. F.: Comparing OMI-TOMS and OMI-DOAS total ozone column data, J. Geophys. Res.-Atmos., 113, D16S28, doi:10.1029/2007JD008798, 2008.

Kramarova, N. A., Nash, E. R., Newman, P. A., Bhartia, P. K., McPeters, R. D., Rault, D. F., Seftor, C. J., Xu, P. Q., and Labow, G. J.: Measuring the Antarctic ozone hole with the new Ozone Mapping and Profiler Suite (OMPS), Atmos. Chem. Phys., 14, 2353–2361, doi:10.5194/acp-14-2353-2014, 2014.

Lee-Taylor, J. and Madronich, S.: Calculation of actinic fluxes with a coupled atmosphere–snow radiative transfer model, J. Geophys. Res., 107, 4796, doi:10.1029/2002JD002084, 2002.

Libois, Q., Picard, G., France, J. L., Arnaud, L., Dumont, M., Carmagnola, C. M., and King, M. D.: Influence of grain shape on light penetration in snow, The Cryosphere, 7, 1803–1818, doi:10.5194/tc-7-1803-2013, 2013.

Libois, Q., Picard, G., Dumont, M., Arnaud, L., Sergent, C., Pougatch, E., Sudul, M., and Vial, D.: Experimental determination of the absorption enhancement parameter of snow, J. Glaciol., 60, 714–724, 2014.

Malinka, A. V.: Light scattering in porous materials: Geometrical optics and stereological approach, J. Quant. Spectrosc. Radiat. Transfer, 141, 14–23, doi:http://dx.doi.org/10.1016/j.jqsrt.2014.02.022, 2014.

Marks, A. A. and King, M. D.: The effect of snow/sea ice type on the response of albedo and light penetration depth (*e*-folding depth) to increasing black carbon, The Cryosphere, 8, 1625–1638, doi:10.5194/tc-8-1625-2014, 2014.

Mauldin, R. L., Eisele, F. L., Tanner, D. J., Kosciuch, E., Shetter, R., Lefer, B., Hall, S. R., Nowak, J. B., Buhr, M., Chen, G., Wang, P., and Davis, D.: Measurements of OH, $H_2SO_4$, and MSA at the South Pole during ISCAT, Geophys. Res. Lett., 28, 3629–3632, doi:10.1029/2000GL012711, 2001.

McNeill, V. F., Grannas, A. M., Abbatt, J. P. D., Ammann, M., Ariya, P., Bartels-Rausch, T., Domine, F., Donaldson, D. J., Guzman, M. I., Heger, D., Kahan, T. F., Klán, P., Masclin, S., Toubin, C., and Voisin, D.: Organics in environmental ices: sources, chemistry, and impacts, Atmos. Chem. Phys., 12, 9653–9678, doi:10.5194/acp-12-9653-2012, 2012.

Simpson, W. R., King, M. D., Beine, H. J., Honrath, R. E., and Zhou, X.: Radiation-transfer modeling of snow-pack photochemical processes during ALERT 2000, Atmos. Environ., 36, 2663–2670, doi:10.1016/S1352-2310(02)00124-3, 2002.

Sjostedt, S. J., Huey, L. G., Tanner, D. J., Peischl, J., Chen, G., Dibb, J. E., Lefer, B., Hutterli, M. A., Beyersdorf, A. J., Blake, N. J., and Blake, D. R.: Peroxy and hydroxyl radical measurements during the spring 2004 Summit Field Campaign, American Geophysical Union, Fall Meeting 2005, abstract #A24A-02, 2005AGUFM.A24A..02S, 5–9 December 2005, San Francisco, CA, USA, 2005.

Thomas, J. L., Stutz, J., Lefer, B., Huey, L. G., Toyota, K., Dibb, J. E., and von Glasow, R.: Modeling chemistry in and above snow at Summit, Greenland – Part 1: Model description and results, Atmos. Chem. Phys., 11, 4899–4914, doi:10.5194/acp-11-4899-2011, 2011.

Voisin, D., Jaffrezo, J.-L., Houdier, S., Barret, M., Cozic, J., King, M. D., France, J. L., Reay, H. J., Grannas, A., Kos, G., Ariya, P. A., Beine, H. J., and Domine, F.: Carbonaceous species and humic like substances (HULIS) in Arctic snowpack during OASIS field campaign in Barrow, J. Geophys. Res.-Atmos., 117, D00R19, doi:10.1029/2011JD016612, 2012.

Warneck, P. and Wurzinger, C.: Product quantum yields for the 305-nm photodecomposition of nitrate in aqueous solution, J. Phys. Chem., 92, 6278–6283, doi:10.1021/j100333a022, 1988.

Warren, S. G.: Optical properties of snow, Rev. Geophys., 20, 67–89, doi:10.1029/RG020i001p00067, 1982.

Warren, S. G. and Brandt, R. E.: Optical constants of ice from the ultraviolet to the microwave: a revised compilation, J. Geophys. Res.-Atmos., 113, D14220, doi:10.1029/2007JD009744, 2008.

Warren, S. G. and Wiscombe, W. J.: A model for the spectral albedo of snow. II: Snow containing atmospheric aerosols, J. Atmos. Sci., 37, 2734–2745, doi:10.1175/1520-0469(1980), 1980.

Warren, S. G., Brandt, R. E., and Grenfell, T. C.: Visible and near-ultraviolet absorption spectrum of ice from transmission of solar radiation into snow, Appl. Optics, 45, 5320–5334, doi:10.1364/AO.45.005320, 2006.

Wiscombe, W. J. and Warren, S. G.: A model for the spectral albedo of snow. I: Pure snow, J. Atmos. Sci., 37, 2712–2733, doi:10.1175/1520-0469(1980)037<2712:AMFTSA>2.0.CO;2, 1980.

Wolff, E. W. and Bales, R. C.: Chemical Exchange Between the Atmosphere and Polar Snow, NATO ASI Series, 43, Springer, Berlin, Heidelberg, Germany, 1996.

Zatko, M. C., Grenfell, T. C., Alexander, B., Doherty, S. J., Thomas, J. L., and Yang, X.: The influence of snow grain size and im-

purities on the vertical profiles of actinic flux and associated $NO_x$ emissions on the Antarctic and Greenland ice sheets, Atmos. Chem. Phys., 13, 3547–3567, doi:10.5194/acp-13-3547-2013, 2013.

Zege, E. P., Katsev, I. L., Malinka, A. V., Prikhach, A. S., Heygster, G., and Wiebe, H.: Algorithm for retrieval of the effective snow grain size and pollution amount from satellite measurements, Remote Sens. Environ., 115, 2674–2685, doi:10.1016/j.rse.2011.06.001, 2011.

# Chapter 4

# Modeling the Physical Multi-Phase Interactions of $HNO_3$ Between Snow and Air on the Antarctic Plateau (Dome C) and coast (Halley)

**Citation:**
**Chan, H. G.** , Frey, M. M. and King, M. D.: Modeling the Physical Multi-Phase Interactions of $HNO_3$ Between Snow and Air on the Antarctic Plateau (Dome C) and coast (Halley), Atmos. Chem. Phys. Discuss, doi:10.5194/acp-2016-1069.

**Author contributions:**
H.G.C. developed the multi-phase interaction models , did the data analysis and result preparation.
M.M.F. oversaw the study and proof-read the paper.
M.D.K. oversaw the study and proof-read the paper.

Manuscript prepared for Atmos. Chem. Phys.
with version 2014/09/16 7.15 Copernicus papers of the LaTeX class copernicus.cls.
Date: 20 December 2017

# Modeling the Physical Multi-Phase Interactions of $HNO_3$ Between Snow and Air on the Antarctic Plateau (Dome C) and coast (Halley)

Hoi Ga Chan[1,2], Markus M. Frey[1], and Martin D. King[2]

[1]British Antarctic Survey, Natural Environment Research Council, Cambridge, CB3 0ET,UK
[2]Department of Earth Sciences, Royal Holloway University of London, Egham, Surrey, TW20 0EX, UK

*Correspondence to:* Markus M. Frey
(maey@bas.ac.uk)

**Abstract.** Emissions of nitrogen oxide ($NO_x$ = $NO$ + $NO_2$) from the photolysis of nitrate ($NO_3^-$) in snow affect the oxidising capacity of the lower troposphere especially in remote regions, of high latitudes with little pollution. Current air-snow exchange models are limited by poor understanding of processes and often require unphysical tuning parameters. Here, two multi-phase models were developed from physically-based parameterisations to describe the interaction of nitrate between the surface layer of the snowpack and the overlying atmosphere. The first model is similar to previous approaches and assumes that below a threshold temperature, $T_o$, the air-snow grain interface is pure ice and above $T_o$, a disordered interface (DI) emerges covering the entire grain surface. The second model assumes that air-ice interactions dominate over all temperatures below melting of ice and that any liquid present above the eutectic temperature is concentrated in micropockets. The models are used to predict the nitrate in surface snow constrained by year-round observations of mixing ratios of nitric acid in air at a cold site on the Antarctic Plateau (Dome C, $75°06'S, 123°33'E$, 3233 $m$ a.s.l.) and at a relatively warm site on the Antarctic coast (Halley, $75°35'S, 26°39'E$, 35 $m$ a.s.l). The first model agrees reasonably well with observations at Dome C ($C_v(RMSE)$ = 1.34), but performs poorly at Halley ($C_v(RMSE)$ = 89.28) while the second model reproduces with good agreement observations at both sites ($C_v(RMSE)$ = 0.84 at both sites). It is therefore suggested that in winter air-snow interactions of nitrate are determined by non-equilibrium surface adsorption and co-condensation on ice coupled with solid-state diffusion inside the grain, similar to Bock et al. (2016). In summer, however, the air-snow exchange of nitrate is mainly driven by solvation into liquid micropockets following Henry's law with contributions to total surface snow $NO_3^-$ concentrations of 75% and 80% at Dome C and Halley respectively. It is also found that the liquid volume of the snow grain and air-micropocket partitioning of $HNO_3$ are sensitive to both the total solute concentration of

mineral ions within the snow and pH of the snow. The second model provides an alternative method to predict nitrate concentration in the surface snow layer which is applicable over the entire range of environmental conditions typical for Antarctica and forms a basis for a future full 1D snowpack model as well as parameterisations in regional or global atmospheric chemistry models.

## 1 Introduction

Emissions of nitrogen oxides, $NO_x$ = NO + $NO_2$, from snow to the overlying air as a result of photolysis of the nitrate anion, $NO_3^-$, within snow have been observed in polar (Jones et al., 2001; Beine et al., 2002) and midlatitude regions (Honrath et al., 2000). They were found to have a significant impact on the oxidising capacity of the atmospheric boundary layer, especially in remote areas, such as the polar regions, where anthropogenic pollution is small (Grannas et al., 2007). The cycling of $NO$ and $NO_2$ in the troposphere alters the concentration of tropospheric ozone, $O_3$, partitioning of hydroxy radicals, $HO_x$, and organic peroxy radicals, $RO_x$. Tropospheric ozone is a pollutant and a greenhouse gas, and changes in the concentration can impact the regional energy balance and therefore climate (Fowler et al., 2008). Conversely, $HO_x$ radicals are responsible for removal of many atmospheric pollutants (e.g. Gligorovski et al., 2015), such as the greenhouse gas methane, and $RO_x$ radicals play an important role in the oxidation of volatile organic compounds (VOCs). Furthermore, $NO_x$ emission from $NO_3^-$ in snow imply post-depositional loss of $NO_3^-$, which complicates the interpretation of $NO_3^-$ measured in polar ice cores (Wolff et al., 2008; France et al., 2011).

The exchange of nitric acid, $HNO_3$, between the atmosphere or snow interstitial air and snow grains is complex, and is controlled by chemical and physical processes. The relative contribution of photochemical and physical processes has been a matter of debate (Röthlisberger et al., 2000). Isotopic studies have shown that photolysis of $NO_3^-$ is the dominating loss process of $NO_3^-$ in snow (Frey et al., 2009; Erbland et al., 2013). Based on a typical photolysis rate coefficient of nitrate, $J_{NO_3^-} \approx 1 \times 10^{-7}\ s^{-1}$ (at the surface in Dome C at a solar zenith angle of 52°, France et al., 2011), the characteristic time for nitrate photolysis is $\sim 10^7$ s. Thus, the characteristic time of nitrate photolysis is much larger compared to other physical processes near the snowpack surface, such as grain surface adsorption and solid-state diffusion (Table 1). At the top few mm of snowpack, hereafter called the skin layer and the focus region of snowpack in this paper, the physical uptake of nitrate is much quicker than the photochemical loss due to the availability of nitric acid at the snowpack surface. Therefore, it is assumed that the photochemical processes are negligible, and only physical processes are considered. The skin layer is defined as the top 4 mm of the snowpack, which is the depth of which the surface snow nitrate samples were collected at Dome C (Sect. 4.1).

The snow grain and the air around it form together a complex multiphase interface (Bartels-Rausch et al., 2014). Gaseous $HNO_3$ can be taken up by different reservoirs in snow, for example the molecule can 1) adsorb on the ice surface; 2) diffuse into the ice crystal and form solid solution;

3) co-condense to the growing ice or 4) dissolve into the liquid solution located in grain boundaries, grooves at triple junctions or quadruple points.

Air-snow models have been developed to predict the exchange of trace gases between the snowpack and the overlying atmosphere and the greatest challenge faced currently is the model description of the air-snow grain interface. One group of models assume a disordered interface, DI, at the snow grain surface with liquid-like properties (e.g. Boxe and Saiz-Lopez, 2008; Thomas et al., 2011; Toyota et al., 2014; Murray et al., 2015). The DI is defined as a thin layer on the surface of the snow grain and is assumed to have the following characteristics; 1) DI reaction and partition rate constants are similar to those in the aqueous phase, e.g. Henry's Law coefficients are used to describe the partitioning between air and the DI; 2) DI thickness of pure ice ranges from <1 to $\sim$100 nm based on observations (Bartels-Rausch et al., 2014) but is often set to an arbitrary value, e.g. 10 $\mathrm{nm}$ (Thomas et al., 2011; Murray et al., 2015); and 3) all (Toyota et al., 2014) or a fraction (Thomas et al., 2011; Murray et al., 2015) of the total solutes are located in the DI.

Another group of models assumes the interface between snow grain and surrounding air to be ice (e.g. Hutterli et al., 2003; Bock et al., 2016). The distribution of hydrogen peroxide, $\mathrm{H_2O_2}$, and formaldehyde, $\mathrm{HCHO}$, within the snowpack has been estimated using a physical air-snow and firn transfer model which included temperature driven 'Air-Ice' uptake and release (Hutterli et al., 2003; McConnell et al., 1998). The bulk concentration of $\mathrm{H_2O_2}$ is determined by solid-state diffusion of $\mathrm{H_2O_2}$ in ice while the bulk concentration of $\mathrm{HCHO}$ is determined by linear isotherm adsorption of $\mathrm{HCHO}$ on ice. A physical exchange model has been developed by Bock et al. (2016) to describe the concentration of $\mathrm{NO_3^-}$ in the skin layer at Dome C, East Antarctic Plateau. Bock et al. (2016) proposed that the skin layer snow nitrate concentration at Dome C is determined by thermodynamic equilibrium ice solubility on the grain surface followed by solid-state diffusion during winter. During summer the large increase in $\mathrm{NO_3^-}$ concentration in the skin layer snow is mainly attributed to co-condensation of $\mathrm{HNO_3}$ and $\mathrm{H_2O}$. However, Bock et al. (2016) model implies no loss of $\mathrm{NO_3^-}$ due to sublimation, a process that has been suggested to be important in surface snow dynamics (Röthlisberger et al., 2000).

Both types of models require tuning parameters used to fit the model output to a chosen set of observations. Some of these parameters do have a physical meaning yet the tuned values may not, for example the fraction of solute in the DI (Thomas et al., 2011) or the ion partitioning coefficients (Hutterli and Röthlisberger, 1999). Whereas some may not have a strict physical meaning, for example the co-condensation related parameters were adjusted in Bock et al. (2016) model, one of their configurations (configuration 2-BC2), total snow nitrate concentration contributed by co-condensation, which is the simultaneous condensation of water vapour and trace gases at the air-ice interface, has an empirical relationship with the partial pressure of nitric acid and water vapour while in another configuration (configuration 2-BC3) they varied the complementary error function when calculating the contribution from co-condensation to match the modelled results to the observations.

Any 'tuning' of a model to a specific set of observations may affect the confidence in model runs under different conditions or scenarios.

The aim of this paper is to develop a physical exchange model based on physical parameterisations and experimental data to describe the exchange of nitrate between the atmosphere and the skin layer of snow and minimising the number of tuning parameters. It is a first step towards a full snowpack model that would include deeper snow and other processes, such as wind pumping, molecular diffusion, and photochemistry. Two temperature dependent, multi-phase models (Model 1 and Model 2), are developed to evaluate two different concepts to describe the interaction of nitrate between air and snow.

Model 1 is based on the hypothesis of the existence of a DI covering the entire snow grain above a threshold temperature, $T_o$ (Sect. 3.1). Below $T_o$, the interface between snow grain and air is assumed to be 'Air-Ice', and the concentration of $\mathrm{NO_3^-}$ at the grain boundary is determined by non-equilibrium surface adsorption and co-condensation coupled with solid-state diffusion into the grain. Above $T_o$, the interface is assumed to be 'Air-DI' of which the $\mathrm{NO_3^-}$ concentration is defined by non-equilibrium solvation into the DI based on Henry's Law coefficient. This is similar to the approach taken by other models (e.g. Thomas et al., 2011; Toyota et al., 2014).

Model 2 is based on the hypothesis of Cho et al. (2002), that liquid co-exists with ice above eutectic temperature, $T_e$. The liquid forms micropockets and is assumed to be located in grooves at grain boundaries or triple junctions due to the limited wettability of ice (Domine et al., 2013). Therefore, at all temperatures below melting the major interface between air and snow grain is assumed to be pure ice and the concentration of $\mathrm{NO_3^-}$ in ice is defined by non-equilibrium surface adsorption and co-condensation followed by solid-sate diffusion within the grain. Above $T_e$, the partitioning of $\mathrm{HNO_3}$ to the liquid micropockets is described by Henry's Law (Sect. 3.2).

The models are validated with available observations from two sites in Antarctica that have very different atmospheric composition, temperatures and humidities: Dome C on the East Antarctic Plateau and Halley in coastal Antarctica.

## 2 Current Understanding of Physical Air-Snow Processes

Below we briefly review the current understanding of physical air-snow processes, which are relevant to nitrate. A more comprehensive discussion can be found in a recent review paper (Bartels-Rausch et al., 2014).

### 2.1 Surface Adsorption at the Air-Ice Interface

The probability of a gas molecule being adsorbed on a clean ice surface can be described by the dimensionless surface accommodation coefficient, $\alpha$ (Crowley et al., 2010). The adsorbed molecule can then be desorbed thermally or it can be dissociated and diffuse into the bulk and form a solid

solution (Abbatt, 1997; Huthwelker et al., 2004; Cox et al., 2005). At a low partial pressure of $HNO_3$, the adsorption of $HNO_3$ on an ice surface can be described by the single-site Langmuir adsorption (Ullerstam et al., 2005b):

$$HNO_{3,(g)} + S \underset{k_{des}}{\overset{k_{ads}}{\rightleftharpoons}} HNO_{3,(ads)} \tag{R1}$$

where $HNO_{3,(g)}$ and $HNO_{3,(ads)}$ are the gas-phase and surface adsorbed nitric acid, and $S$ is the surface site for adsorption. The concentration of surface sites, [S], i.e. number of site available per unit volume of air, is defined as follow:

$$[S] = (1-\theta)\, N_{max} \frac{A_{ice}}{V_{air}} \tag{1}$$

Here, $\theta$ is the fraction of surface sites being occupied, $N_{max}$ is the maximum number of surface sites with a unit of $\mathrm{molecule\,m_{ice}^{-2}}$, $A_{ice}$ is the surface area of ice per unit volume of snowpack with a unit of $\mathrm{m_{ice}^{2}\,m_{snowpack}^{-3}}$, and $V_{air}$ is the volume of air per unit volume of snowpack with a unit of $\mathrm{m_{air}^{3}\,m_{snowpack}^{-3}}$. Note that [S] has units of $\mathrm{molecule\,m^{-3}}$. The adsorption coefficient, $k_{ads}$ ,and desorption coefficient, $k_{des}$, in R1 are defined as

$$k_{ads} = \frac{\alpha \overline{v}}{4} \frac{1}{N_{max}} \tag{2}$$

$$k_{des} = \frac{k_{ads}}{K_{eq}} \tag{3}$$

Note that $k_{ads}$ has a unit of $\mathrm{m^3\,molecule^{-1}\,s^{-1}}$ while the unit of $k_{des}$ is $\mathrm{s^{-1}}$, $\overline{v}$ is the average gas-phase molecular speed and $K_{eq}$ is the equilibrium constant for Langmuir adsorption on ice with a unit of $\mathrm{m^3\,molecule^{-1}}$. The value of $K_{eq}$ for $HNO_3$ is inversely correlated with temperature because the scavenging efficiency of $HNO_3$ due to adsorption increases as temperature decreases. The parameterisations and values for the above variables used in this study are listed in Table A1. The value of the accommodation coefficient, $\alpha$, is the same as the experimental initial uptake coefficient, $\gamma_0$, if the time resolution of the laboratory experiments is high enough (Crowley et al., 2010). Fig. A1 shows the experimental initial uptake coefficients, $\gamma_0$, by various studies as a function of temperature. A comparison of different parameterisations of $K_{eq}$ is shown in Fig. A2.

### 2.2 Solid-State Diffusion

Due to its solubility and diffusivity, $HNO_3$ can form a solid solution in ice. The solid-state diffusion in natural snow was found to be an important process for understanding the partitioning of highly soluble gases, including $HNO_3$, between the atmosphere and snow (Bartels-Rausch et al., 2014). Thibert et al. (1998) derived a solid-state diffusion coefficient, $k_{diff}$, and a thermodynamic solubility of $HNO_3$ in ice from sets of $HNO_3$ concentration diffusion profiles obtained by exposing single ice crystal to diluted $HNO_3$ at different temperatures for a period of days to weeks. However, Thibert et al. (1998) did not present the kinetics of $HNO_3$ uptake on ice and hence a characteristic time for equilibrium between air and ice could not be established. A diffusion-like behaviour has

been observed from flow-tube studies for trace gas uptake onto ice (e.g. Abbatt, 1997; Huthwelker et al., 2004; Cox et al., 2005) suggesting the solid-state diffusion of nitrate molecules can occur concurrently with surface adsorption (R1), such that

$$\mathrm{HNO_{3,\,(ads)}} \overset{k_{\mathrm{diff}}}{\rightleftarrows} \mathrm{HNO_{3,\,(ice)}} \tag{R2}$$

where $\mathrm{HNO_{3,\,(ice)}}$ is the nitric acid incorporated into the ice matrix.

### 2.3 Coexistence of Liquid Solution with Ice

Liquid aqueous solution coexists with ice in the presence of soluble impurities, such as sea salt and acids. The liquid exist down to the eutectic temperature defined by the composition and solubility of the impurities in the ice. Cho et al. (2002) parameterised the liquid water fraction, $\phi_{\mathrm{H_2O}}(T)$, as a function of total ionic concentration of impurities, $\mathrm{Ion_{tot}}$,and temperature as follows:

$$\phi_{\mathrm{H_2O}}(T) = \frac{\overline{m}_{\mathrm{H_2O}} R T_f}{1000 \Delta H_f^0} \left( \frac{T}{T_f - T} \right) \Phi_{\mathrm{bulk}}^{\mathrm{aq}} \left[\mathrm{Ion_{tot\,(bulk)}}\right] \tag{4}$$

where $\phi_{\mathrm{H_2O}}(T)$ has a units of $\mathrm{m_{liquid}^3\,m_{liquid+solid}^{-3}}$, $\overline{m}_{\mathrm{H_2O}}$ is the molecular weight of water, $R$ is the ideal gas constant, $T_f$ is the freezing temperature of pure water in K, $\Delta H_f^0$ is the enthalpy of fusion in $\mathrm{J\,mol^{-1}}$, $\Phi_{\mathrm{bulk}}^{\mathrm{aq}}$ is the fraction of the total solute in the aqueous phase and $[\mathrm{Ion_{tot,\,bulk}}]$ is the total ionic concentration in the melted sample. There are different hypothesises regarding the location of the liquid solution. Most studies assume the liquid solution forms a thin layer covering the whole grain surface (e.g. Kuo et al., 2011) while Domine et al. (2013) suggested the liquid is located in grooves at grain boundaries and triple junctions. The arguments of the latter study were 1) the ionic concentration is so low in natural snow that only a small amount of liquid can be formed; and 2) the wettability of ice by liquid water is imperfect, preventing the liquid drop from spreading out across the entire solid surface. The volume of liquid is small relative to the ice grain and if spread uniformly across the ice grain the thickness would be less than the diameter of the $\mathrm{H_2O}$ molecule which is unrealistic.

The partitioning of atmospheric acidic gases between air and the liquid fraction of snow can be described by Henry's law using the effective dimensionless Henry's law coefficient, $k_{\mathrm{H}}^{\mathrm{eff}}$, (Sander, 1999)

$$k_{\mathrm{H}}^{\mathrm{eff}} = k_{\mathrm{H}}^{\mathrm{cc}} \frac{\mathrm{K_a}}{[\mathrm{H}_{(\mathrm{aq})}^{+}]} \tag{5}$$

where $k_{\mathrm{H}}^{\mathrm{cc}}$ is the dimensionless temperature dependent Henry's Law coefficient (App. A), $\mathrm{K_a}$ is the acid dissociation constant and $[\mathrm{H}_{(\mathrm{aq})}^{+}]$ is the concentration of hydrogen ions. Fig. A3 shows the temperature and pH dependence of $k_{\mathrm{H}}^{\mathrm{eff}}$. At a given temperature, $k_{\mathrm{H}}^{\mathrm{eff}}$ increases by an order of magnitude between pH 5 and 6.5 (Fig. A3 A), the typical range of pH in natural snow (Udisti et al., 2004). While at a given pH, $k_{\mathrm{H}}^{\mathrm{eff}}$ decreases by 2 orders of magnitude between -40°$C$ and 0°$C$ (Fig. A3 B). Note that the range of pH measured by Udisti et al. (2004) is the pH of the melted sample,

which might be different from the pH of the liquid fraction of the snow grain not observable by current measurement techniques.

## 3 Modelling Approach

The aim of this paper is to focus on the physical exchange mechanisms of $HNO_3$ between air and snow to predict the concentration of nitrate in the skin layer of the snowpack, as a first step towards a full snowpack model. The two models are constrained by the observed atmospheric concentration of $HNO_3$, air temperature, skin layer temperature, atmospheric pressure and humidity. The loss or gain in the atmospheric $HNO_3$ due to the mass exchange between air and snow are included implicitly by constraining the models with the observed atmospheric concentration of $HNO_3$. The following assumptions were made in both Model 1 & 2: 1) the concentration of $HNO_3$ in snow interstitial air is the same as in the overlying atmosphere justified by a short characteristic time scale for gas-phase diffusion of $\sim 1$ s (Table 1); 2) the physical properties of the skin layer are homogeneous and include density and specific surface area (SSA); and 3) the snow grain is assumed to be a radially symmetrical sphere with an effective radius, $R_{\mathrm{eff}}$, which is estimated from the SSA as the follows:

$$R_{\mathrm{eff}} = \frac{3}{\rho_{\mathrm{ice}}\,\mathrm{SSA}} \tag{6}$$

where $\rho_{\mathrm{ice}}$ is the density of ice. Snow metamorphism and resulting changes in snow grain size are not modeled explicitly, but are approximated instead by prescribing temporal changes in SSA. Here an annual cycle of SSA is included based on observations at Dome C (Picard et al., 2016), ranging from 25 $\mathrm{m^2kg^{-1}}$ in summer to 90 $\mathrm{m^2kg^{-1}}$ in the winter (details in Sect. 4.3 and Fig. A4a), and yielding a $R_{\mathrm{eff}}$ of $\sim$130 µm in summer, which gradually reduces to $\sim$ 30 µm in winter (Fig. A4b). Modeled co-condensation (Eq. 9 & 10) does not change model snow grain size, since the involved ice volumes are relatively small compared to the volume of the snow grain. The model set up implies also that the snow grain size remains constant during each model time step of $\Delta t$ = 10 $\mathrm{min}$.

For the calculation of solid-state diffusion the snow grain is divided into $N$ concentric shells of equal thickness. To optimise model performance and computational cost, the number of concentric shells is fixed to $N$ = 85, yielding a model shell thickness $\Delta r$ of $\sim$ 1.5 µm in summer and $\sim$ 0.5 µm in winter due to seasonal change in grain size. $\Delta r$ remains at all times smaller than the minimum typical length-scale, <$x$>, a molecule diffuses over a finite time, $\Delta t$, and described by the root-mean square displacement, <$x$> = $\sqrt{6\,\Delta t\,k_{\mathrm{diff}}}$. Minimum typical length-scales occur in winter when air temperatures are lowest, and for a modeling time step, $\Delta t$ = 10 $\mathrm{min}$, they range between 1.5 µm at Dome C and 5.5 µm at Halley.

### 3.1 Model 1 - Surface Adsorption/Solvation & Solid Diffusion

In Model 1, the uptake of $HNO_3$ is treated as a two-step process consisting of interfacial mass transport across the air-snow grain boundary and subsequent diffusion into the bulk, a similar approach as

taken by Bock et al. (2016). Below a threshold temperature, $T_o$, the snow grain boundary is assumed to be 'Air-Ice' and the concentration of the outermost model shell is determined by the combination of adsorption and co-condensation on ice (details in Sect. 3.1.1 & Fig. 1a). Above $T_o$, the air-snow grain boundary is assumed to be 'Air-DI', and the concentration of the outermost model shell is determined by solvation governed by Henry's law into the disordered interface, DI, (Details in Sect. 3.1.2 & Fig. 1b).

The threshold temperature, $T_o$, is a value based on lab experiments. The temperature at which a disordered interface is detected on pure ice varies between 238 and 270 K depending on the measurement technique (Domine et al., 2013 and references therein). Here, $T_o$, is set to 238 K, the lower end of the range. Model uncertainties due to the uncertainties in $T_o$ are evaluated in a sensitivity study further below (Sect. 6.5).

The physical properties of the DI are still poorly known, and currently there are no physical parameterisations available to estimate DI thickness, partitioning coefficients or diffusivities. Hence, for the DI in Model 1 the following four assumptions are made: 1) the partitioning between air and the DI follows Henry's law, similar to previous models (e.g.Thomas et al., 2011 & Toyota et al., 2014); 2) the model geometry described above implies that the DI, i.e. the outermost model shell of the snow grain, follows the seasonal cycle of snow grain specific surface area and has a thickness of 1.5 µm in summer decreasing to 0.5 µm in winter. A seasonal cycle is qualitatively consistent with laboratory measurements, which show that DI thickness increases with temperature (Bartels-Rausch et al., 2014). But the absolute model values are larger than previous lab measurements on pure ice, which range from the thickness of a monolayer of water (0.3 nm) to ∼100 nm, depending on the measurement technique (e.g. Bartels-Rausch et al., 2014), or values adopted in previous model studies (range 10-30 nm) (e.g. Thomas et al., 2011, Toyota et al., 2014, Murray et al., 2015). However, DI thickness is also sensitive to the type and concentration of impurities, and generally increases with ion concentration (e.g. Dash et al., 2006; Bartels-Rausch et al., 2014); 3) the DI is interacting with the bulk ice, i.e. solvated nitrate ions diffuse into the interior of the snow grain and the mass transport is determined by the solid-state diffusion coefficient of ice, $k_{\mathrm{diff}}$ and the concentration gradient across the snow grain; and 4) the solid-state concentration of nitrate in the bulk is limited by the thermodynamic equilibrium solubility of ice (e.g. by Thibert et al., 1998 as shown in Eq. 19), except the outermost model shell of the snow grain.

#### 3.1.1 $T \leq 238$ K: Non-Equilibrium Surface Adsorption & Co-condensation

At a temperature below $T_o$ = 238 K the interface between air and snow grain is assumed to be pure ice. The concentration of nitrate at the grain boundary, $[\mathrm{HNO_{3\,(surf)}}]$, is determined by a combination of non-equilibrium kinetic adsorption and co-condensation:

$$[\mathrm{HNO_{3\,(surf)}}] = [\mathrm{HNO_{3\,(ads)}}] + [\mathrm{HNO_{3\,(cc)}}] \qquad \text{if} \quad T \leq 238\mathrm{K} \tag{7}$$

where $[\mathrm{HNO_{3\,(ads)}}]$ is the concentration contributed by the sum of surface adsorption and desorption and $[\mathrm{HNO_{3\,(cc)}}]$ is the concentration contributed by co-condensation or co-sublimation. This configuration but without the contribution by co-condensation is referred to as 'Model 1 - BCice', where 'BC' stands for boundary condition. The net rate of adsorption can be described as $\frac{d[\mathrm{HNO_{3\,(ads)}}]}{dt} = k_{\mathrm{ads}}[\mathrm{HNO_{3\,(g)}}]\,[\mathrm{S}] - k_{\mathrm{des}}[\mathrm{HNO_{3\,(ads)}}]$. Substituting $k_{\mathrm{des}}$ with Eq. (3), the net adsorption rate is expressed as

$$\frac{d[\mathrm{HNO_{3\,(ads)}}]}{dt} = k_{\mathrm{ads}}\left([\mathrm{HNO_{3\,(g)}}]\,[\mathrm{S}] - \frac{[\mathrm{HNO_{3\,(ads)}}]}{K_{\mathrm{eq}}}\right) \tag{8}$$

Ullerstam et al. (2005b) have shown that for partial pressures of $\mathrm{HNO_3}$ lower than $10^{-5}$ Pa the ice surface is not entirely covered with $\mathrm{HNO_3}$, and therefore, undersaturated. The annual average atmospheric partial pressure of $\mathrm{HNO_3}$ recorded at Dome C is $\sim 10^{-6}$ Pa (Traversi et al., 2014) and is $\sim 10^{-7}$ Pa at Halley (Jones et al., 2008), hence, the ice surface is unlikely to be saturated with $\mathrm{HNO_3}$. A non-equilibrium kinetic approach is taken instead of an equilibrium adsorption as natural snowpacks are constantly undergoing sublimation and condensation of $\mathrm{H_2O}$, especially in the skin layer, due to temperature gradients present over a range of timescales from a fraction of seconds to days and seasons (Bartels-Rausch et al., 2014). Pinzer et al. (2012) observed that up to 60% of the total ice mass was redistributed under a constant temperature gradient of 50 $\mathrm{K\,m^{-1}}$ over a 12 $\mathrm{hour}$ period. Field observations (Frey et al., 2013) and the results from a heat transfer model (Hutterli et al., 2003) at Dome C in summer show temperature gradients of 71 $\mathrm{K\,m^{-1}}$ across the top 2 $\mathrm{cm}$ and 130 $\mathrm{K\,m^{-1}}$ across the top 4 $\mathrm{mm}$ of the snowpack, respectively. At Halley, the modelled summer temperature gradient in the top $\mathrm{cm}$ of snow is about 41 $\mathrm{K\,m^{-1}}$. Therefore, the dynamic $\mathrm{H_2O}$ exchange and redistribution at the snow grain surface prevent the equilibrium of adsorption from being reached and require a kinetic approach.

The temperature gradient and relative humidity gradient between the surface of the snowpack and the skin layer create a gradient in water vapour pressure, which drives condensation or sublimation of ice, depending on the sign of the gradient. Uptake of $\mathrm{HNO_3}$ molecules to growing ice is known as co-condensation. The surface concentration of $\mathrm{NO_3^-}$ contributed by co-condensation or co-sublimation, $[\mathrm{HNO_{3\,(cc)}}]$, is given by

$$[\mathrm{HNO_{3(cc)}}] = X_{\mathrm{HNO_3}}\,\frac{\rho_{ice}\,N_A}{\overline{m}_{\mathrm{H_2O}}}\,\frac{\Delta t}{\mathrm{V_{grain}}}\,\frac{d\mathrm{V}}{dt} \tag{9}$$

where $\mathrm{X_{HNO_3}}$ is the mole fraction of $\mathrm{HNO_3}$ condensed along with water vapour ($\mathrm{X_{HNO_3}} = 10^{-3.2}\,P_{\mathrm{HNO_3}}^{0.56}$, Ullerstam and Abbatt, 2005a), $\rho_{ice}$ is the density of ice (in $\mathrm{kg\,m^{-3}}$), and $N_A$ is Avogadro's constant ($6.022 \times 10^{23}$ $\mathrm{molecule\,mol^{-1}}$). The rate of volume change of snow grain, $\frac{dV}{dt}$, is specified by the growth law described by Flanner and Zender (2006)

$$\frac{d\mathrm{V}}{dt} = \frac{4\,\pi\,\mathrm{R_{eff}^2}}{\rho_{ice}}\,D_v\left(\frac{d\,\rho_v}{d\,x}\right)_{x=r} \tag{10}$$

where $\mathrm{D}_v$ is the diffusivity of water vapour in air and $\frac{d\rho_v}{dx}$ is the local water vapour density gradient, i.e. between air away from the snow grain and the air near the grain surface. However, to the author's

knowledge there are no observations reported and the calculation of water vapour density at these microscopic scales is computational costly as it would require 3-D modelling of the metamorphism of the snow grain. For simplicity, the macroscopic (few $\mathrm{mm}$) water vapour gradient across the skin layer was used to estimate the rate of volume change of snow grain due to condensation or sublimation, i.e. $\left(\frac{d\rho_v}{dx}\right)_{x=r}$ in Eq. 10 is replaced by $\left(\frac{d\rho_v}{dz}\right)_{z=4\mathrm{mm}}$. The water vapour density, $\rho_v$, can be calculated as follows:

$$\rho_v = \frac{P_{sat}\,\mathrm{RH}}{100\,R_v\,T} \tag{11}$$

where $P_{sat}$ is the saturated vapour pressure (Pa), RH is the relative humidity (%), $R_v$ is the gas constant ($\mathrm{J\,kg^{-1}\,K^{-1}}$) and $T$ is temperature (K). There are no measurements of fine resolution of vertical snow profile of RH and temperature available, therefore, RH within the snowpack was assumed to be 100% and the temperature of the skin layer is estimated using a heat transfer temperature model based on the heat diffusion equation (Hutterli et al., 2003):

$$\frac{\partial T}{\partial t} = \frac{\partial}{\partial z} k_w(z) \frac{\partial T}{\partial z} \tag{12}$$

where $T$ is the temperature, $t$ is time, $k_w$ is the thermal conductivity (App. A, Table A1) of snowpack and $z$ is the depth.

#### 3.1.2 $T > 238$ K: Non-Equilibrium Solvation

At temperatures above $T_o$ = 238 K the interface between air and the entire surface of the snow grain is assumed to be a DI.

$$[\mathrm{HNO_{3\,(surf)}}] = [\mathrm{HNO_{3\,(DI)}}] \qquad \text{if} \quad T > 238\mathrm{K} \tag{13}$$

The DI is also assumed to be out of equilibrium with the surrounding air as the exchange of water molecules at the surface of the snow grain is expected to be rapid that the surface is redistributed before equilibrium is reached (Details in Sect. 3.1.1). The concentration of the DI is then defined by the following equation:

$$\frac{d[\mathrm{HNO_{3\,(DI)}}]}{dt} = k_{\mathrm{mt}} \left( [\mathrm{HNO_{3\,(g)}}] - \frac{[\mathrm{HNO_{3\,(DI)}}]}{k_{\mathrm{H}}^{\mathrm{eff}}} \right) \tag{14}$$

The mass-transfer coefficient, $k_{\mathrm{mt}}$, is defined as $k_{\mathrm{mt}} = \left( \frac{\mathrm{R_{eff}}^2}{3\,D_g} + \frac{4\,\mathrm{R_{eff}}}{3\,\overline{v}\,\alpha} \right)^{-1}$, where $D_g$ is the gas-phase diffusivity (Sander, 1999). Note that in this model the concentration of the DI is used as the outermost boundary condition for solid-state diffusion within the grain (See Sect. 3.1.3) and the transfer of $\mathrm{NO_3^-}$ into the bulk is limited by the concentration gradient across the snow grain, the maximum solubility and diffusivity of ice.

#### 3.1.3 Solid-State Diffusion

The concentration gradient between the grain boundary and its centre drives solid state diffusion of nitrate within the bulk ice. The $\mathrm{NO_3^-}$ concentration profile within the snow grain can be found by

solving the following partial differential equation

$$\frac{\partial[\mathrm{NO}_3^-](n)}{\partial t} = k_{\mathrm{diff}} \left( \frac{2}{n} \frac{\partial[\mathrm{NO}_3^-](n)}{\partial n} + \frac{\partial^2[\mathrm{NO}_3^-](n)}{\partial n^2} \right) \tag{15}$$

where $[\mathrm{NO}_3^-](n)$ is the nitrate concentration in the $n^{th}$ concentric model shell, with $n = 0, 1, 2, \ldots, N$ and $k_{\mathrm{diff}}$ is the solid-state diffusion coefficient, which is assumed to be homogeneous across the snow grain. By substituting $U(n\Delta r) = \frac{n\Delta r}{R_{\mathrm{eff}}}[\mathrm{NO}_3^-](n)$, Eq. 15 can be re-written as

$$\frac{\partial U(n\Delta r)}{\partial t} = k_{\mathrm{diff}} \left( \frac{\partial^2 U(n\Delta r)}{\partial n^2} \right) \tag{16}$$

where $U(n\Delta r)$ is the concentration at distance $n\Delta r$ from the centre of the snow grain, with $N\Delta r = R_{\mathrm{eff}}$. The nitrate concentration at the centre is set to $U(0) = 0$ and at the grain boundary $U(N\Delta r) = [\mathrm{HNO}_{3\,(\mathrm{surf})}]$, which is defined by surface adsorption and co-condensation at temperatures below $T_o$ (Eq. 7) or by solvation into the DI at temperature above $T_o$ (Eq. 13).

The diffusion equation is solved with the Crank-Nicolson scheme (Press et al., 1996) and the bulk concentration of $\mathrm{NO}_3^-$ in the ice grain, $[\mathrm{NO}_{3\,(\mathrm{bulk})}^-]$, is the sum of the number of $\mathrm{NO}_3^-$ molecules in each shell divided by the volume of the whole grain, expressed as

$$[\mathrm{NO}_{3\,(\mathrm{bulk})}^-] = \frac{\sum[\mathrm{NO}_3^-](n)\,V(n)}{\sum V(n)} = \frac{\sum[\mathrm{NO}_3^-](n)\,V(n)}{V_{\mathrm{grain}}} \tag{17}$$

where $V(n)$ is the volume of the $n^{\mathrm{th}}$ layer of the concentric shell, $\sum V(n)$ is the total volume of the grain, $V_{\mathrm{grain}}$, and the concentration of nitrate in the $n^{\mathrm{th}}$ layer can be determined by re-substituting $U$ that $[\mathrm{NO}_3^-](n) = \frac{R_{\mathrm{eff}}}{n\Delta r} U(n\Delta r)$.

### 3.2 Model 2 - Non-Equilibrium Kinetic Adsorption & Solid Diffusion and Equilibrium Air - Liquid Micropocket

Model 2 is based on the hypothesis that the major air-snow grain interface is pure ice at all temperatures below melting temperature, $T_m$, and that liquid coexists with ice when the temperature is above the eutectic temperature, $T_e$ (Fig. 2). The liquid solution is assumed to be located in grooves at grain boundaries or triple junctions between grains and in the form of micropockets. This assumption implies that the grain surface area being covered by liquid solution is negligible. The bulk concentration of $\mathrm{NO}_3^-$ in Model 2 is defined as follows:

$$[\mathrm{NO}_{3\,(\mathrm{bulk})}^-] = \begin{cases} \frac{\sum[\mathrm{NO}_3^-](n)\,V(n)}{V_{\mathrm{grain}}} & \text{if} \quad T < T_e. \\ \frac{\sum[\mathrm{NO}_3^-](n)\,V(n)}{V_{\mathrm{grain}}} + \phi_{\mathrm{H_2O}}\, k_{\mathrm{H}}^{\mathrm{eff}}\, [\mathrm{HNO}_{3\,(\mathrm{g})}] & \text{if} \quad T_e \leq T < T_m. \end{cases} \tag{18}$$

The term '$\frac{\sum[\mathrm{NO}_3^-](n)\,V(n)}{V_{\mathrm{grain}}}$' in Eq. 18 is representing the nitrate concentration in the ice-phase and is applied to all temperatures below the melting temperature, $T_m$. At $T < T_m$, $\mathrm{HNO}_3$ can be adsorbed/desorbed and co-condensed/co-sublimated from the ice surface as was the case in Model 1

when $T < T_o$ (Sect. 3.1.1). The adsorbed and co-condensed molecules on the ice surface then diffuse into or out of the bulk ice depending on the concentration gradient of nitrate as was the case in Model 1 (Sect. 3.1.3). The nitrate in the snow grain contributed by these processes is referred to as the ice-phase nitrate.

The term '$\phi_{\mathrm{H_2O}}\, k_{\mathrm{H}}^{\mathrm{eff}}\, [\mathrm{HNO_{3\,(g)}}]$' in Eq. 18 is representing the nitrate concentration in the liquid-phase when $T \geq T_e$. At $T \geq T_e$, liquid co-exists with ice, and the bulk mass of $\mathrm{NO_3^-}$ is contributed by $\mathrm{NO_3^-}$ located both within the ice and in the liquid micropocket. The volume of liquid can be calculated from the liquid water fraction, $\phi_{\mathrm{H_2O}}$ (Eq. 4). The liquid in the micropocket is assumed to be ideal and the partitioning between air and liquid micropocket is described by Henry's Law (Eq. 5). This implies instantaneous equilibrium between air and liquid micropocket, and is justified because; 1) the volume of the liquid solution is small which up to $10^{-7} - 10^{-6}\%$ of the total volume of the ice grain (as discussed below); 2) $\mathrm{HNO_3}$ is strongly soluble in solution; 3) the characteristic time of the interfacial mass transport across a liquid surface of a droplet with 70 $\mu\mathrm{m}$ diameter is only $\sim 10^{-7}$ s (Table 1); and 4) the diffusivity of $\mathrm{HNO_3}$ is faster in liquid-phase ($9.78 \times 10^{-10}\ \mathrm{m^2\,s^{-1}}$ at 0°C, Yuan-Hui and Gregory, 1974 ) than in ice ($3.8 \times 10^{-14}\ \mathrm{m^2\,s^{-1}}$ at 0°C). The characteristic time of liquid-phase diffusion within a 70 $\mu\mathrm{m}$ diameter water droplet is $\sim$1 s (Table 1).

Both the values of pH and $\Phi_{\mathrm{bulk}}^{\mathrm{aq}}$ (in Eq. 4) are updated at each model time step with values from the previous time step. At Dome C, the major anion in melted snow is $\mathrm{NO_3^-}$ (e.g. Udisti et al., 2004). Therefore, it is assumed that nitrate and hydrogen ions are the only ions present in the skin layer snow, i.e. $[\mathrm{Ion_{tot\,(bulk)}}]$ = 2×[$\mathrm{NO_3^-}$] in Eq. 4, and the eutectic temperature of a $\mathrm{H_2O}$-$\mathrm{HNO_3}$ system of 230.64 K (Beyer et al., 2002) is chosen as the threshold temperature for the existence of micropockets. In contrast, at Halley snowpack ion chemistry is dominated by $\mathrm{NaCl}$ (Wolff et al., 2008), contributing $\sim$70% to the total ion concentration in the 2004-05 Halley data set, due to the proximity of sea ice and open ocean. Surface snow at Halley also contains a significant amount of sulphate ion, $\mathrm{SO_4^-}$, from sea salt sulphate and sulphuric acid, together contributing $\sim 20\%$ of the total ion concentration. However, for simplicity, the only anions included in the calculation of $\phi_{\mathrm{H_2O}}$ at Halley are $\mathrm{NO_3^-}$ and $\mathrm{Cl^-}$, such that $[\mathrm{Ion_{tot\,(bulk)}}]$ = 2×( [$\mathrm{Cl^-}$] + [$\mathrm{NO_3^-}$]) in Eq. 4 and the value of $T_e$ used is that for a $\mathrm{H_2O}$-$\mathrm{NaCl}$ system of 251.95 K (Akinfiev et al., 2001).

### 3.3 Model BC1 by Bock et al. (2016)

Previously Bock et al. (2016) developed a model for air-ice exchange of nitrate in surface snow assuming only air-ice interaction and equilibrium with the surrounding air. They defined the concentration of nitrate in the outermost model shell of the snow grain in their Configuration 2 - BC1 by the thermodynamic equilibrium solubility parameterisation by Thibert et al. (1998):

$$[\mathrm{NO_3^-}](n = N) = 2.37 \times 10^{-12} \exp\left(\frac{3532.2}{T}\right) P_{\mathrm{HNO_3}}^{1/2.3}\, \frac{\rho_{ice}\, N_A}{\bar{m}_{\mathrm{H_2O}}} \tag{19}$$

where $N$ is the number of concentric shells in the snow grain, $T$ is the snow temperature (K), $P_{\mathrm{HNO_3}}$ is the partial pressure of $\mathrm{HNO_3}$ (Pa) and $\bar{m}_{\mathrm{H_2O}}$ is the molar mass of $\mathrm{H_2O}$. They concluded that the concentration of nitrate in surface snow at Dome C during winter is mainly governed by thermodynamic equilibrium solubility coupled to solid-state diffusion. (Bock et al., 2016)

The configuration after Bock et al. (2016) (referred to as 'Bock - BC1' from hereon) is compared with the non-equilibrium adsorption coupled to solid-state diffusion model presented in this paper ('Model 1 - BCice', Sect. 3.1.1). Note that co-condensation was excluded in these model runs to allow a direct comparison between the two different approaches. The two configurations are analysed and discussed in Sect. 6.1 based on data collection during winter at Dome C and Halley.

## 4 Model Validation

Model calculations are constrained and validated with existing observations of atmospheric $\mathrm{NO_3^-}$, skin layer snow $\mathrm{NO_3^-}$ concentration, and meteorology at Dome C and Halley, which are summarised below.

### 4.1 Observation at Dome C

Dome C is characterised by the following: 1) air temperatures are below the freezing point year round, and no snow melt occurs, with an annual mean of $-52°\mathrm{C}$, maximum of $-17°\mathrm{C}$ in summer (mid November until the end of January) and minimum temperature of $-80°\mathrm{C}$ in winter (April to mid September) as shown in Fig. 3a (Erbland et al., 2013). The diurnal temperature variation is $\sim$10 K in summer, spring (mid September until mid November) and autumn (February to March). 2) the air-snow chemistry of reactive nitrogen is relatively simple due to the remoteness of the site. In particular, concentrations of sea salt and other particles that may scavenge atmospheric $\mathrm{HNO_3}$ are low on the East Antarctica Plateau (Legrand et al., 2016). Hence, the main atmospheric nitrate is gaseous $\mathrm{HNO_3}$ that dissolves in or adsorbs onto snow grains (Traversi et al., 2014). 3) Furthermore, a low snow accumulation rate of 27 $\mathrm{kg\,m^{-2}\,yr^{-1}}$ (Röthlisberger et al., 2000) leads to significant post-depositional processing of nitrate driven by photolysis before the surface snow is buried by new snowfall (e.g. Röthlisberger et al., 2000; Frey et al., 2009).

Observations of skin layer snow nitrate concentration, atmospheric nitrate concentration, temperature, and pressure were carried out previously at Dome C during January 2009 to 2010 (Erbland et al., 2013) and are shown in Fig. 3. The snow samples were collected from the 'skin layer' snow, the top $4 \pm 2$ mm of the snowpack, approximately every 3 days (Erbland et al., 2013). The skin layer was assumed to be spatially heterogeneous with an uncertainty in thickness of about 20% due to the softness of the uppermost layer and sampling by different people. The nitrate concentration in the melted sample was measured by ion chromatography (Erbland et al., 2013).

The concentration of atmospheric nitrate, i.e. the sum of atmospheric particulate nitrate ($p-\mathrm{NO_3^-}$) and the concentration of gaseous nitric acid ($\mathrm{HNO_3}$), was collected on glass fibre filters with a high volume air sampler (HVAS) as described in Morin et al. (2008). Erbland et al. (2013) stated that the concentration of atmospheric nitrate shows good agreement with $\mathrm{HNO_3}$ gas-phase concentration measured by denuder tubes at Dome C over the same time period, therefore we equate the observed atmospheric nitrate with gaseous $\mathrm{HNO_3}$. The filter was positioned approximately 1 $\mathrm{m}$ above the snow surface and changed weekly. The atmospheric boundary layer is assumed to be well mixed so that the atmospheric nitrate at the snowpack surface would be the same at 1 $\mathrm{m}$. The characteristic transport time of $\mathrm{HNO_3}$ from the snowpack surface to the skin layer (4 $\mathrm{mm}$) is on the order of 1 $\mathrm{s}$, which is much shorter than the temporal resolution of the model (10 min, Table 1). Therefore, the concentration of gaseous $\mathrm{HNO_3}$ in the open pore space of the skin layer was assumed to be the same as in the air above the snow. The concentration of gaseous $\mathrm{HNO_3}$ was more than 2 orders of magnitude higher in the summer than in autumn/ early winter (Fig. 3b).

Continuous meteorological observation and snow science are carried out at Dome C under the 'Routine Meteorological Observations' of the Concordia Project by the Italian National Antarctic Research Programme, PNRA, and the French Polar Institute, IPEV (http://www.climantartide.it). Temperature and humidity were measured at 10 $\mathrm{s}$ resolution. Both the temperature and relative humidity were measured at 1.6 $\mathrm{m}$ above the snow surface with a platinum resistance thermometer (VAISALA PT100 DTS12) with a precision of $\pm$ 0.13 °C at $-15\,°\mathrm{C}$, and the humidity sensor (HUMICAP, VAISALA) had a precision of $\pm$ 2 %. Based on the assumption of a well mixed boundary layer, the RH above the snowpack surface was assumed to be the same as that at 1.6 $\mathrm{m}$. Atmospheric nitrate concentrations and meteorological data used as model input have been linearly interpolated to 10 minute resolution.

### 4.2 Observation at Halley

Halley is at a similar latitude as Dome C but in coastal Antarctica at sea level and with very different geographic features. Halley is on the Brunt Ice Shelf and is close to the Weddell Sea in three directions. Hence the temperature, relative humidity, and concentration of atmospheric aerosol are much larger at Halley than Dome C. The average surface temperature in summer is around $-10°\mathrm{C}$ and below $-20°\mathrm{C}$ in the winter. Occasionally, the temperature can rise above $0°\mathrm{C}$ (surface melt is possible) or drop to $-55°\mathrm{C}$ (See Fig. 4a). The annual mean snow accumulation rate at Halley is 480 $\mathrm{kg\,m^{-2}\,yr^{-1}}$ (Wolff et al., 2008), about one order of magnitude larger than at Dome C and therefore limiting post-depositional processes relative to Dome C.

Meteorological and chemical data were collected at Halley under the CHABLIS (Chemistry of the Antarctic Boundary Layer and the Interface with Snow) campaign at the Clean Air Sector Laboratory (CASLab), (details in Jones et al., 2008, 2011). The site description and data given in details elsewhere (Jones et al., 2008), below is a brief description. Measurement of atmospheric concentration

of $HNO_3$ were carried out at weekly resolution using annular denuders (URG corporation) mounted 7-8 $m$ above the snow surface with a collection efficiency of 91% (Fig. 4 B). The atmospheric boundary layer is assumed to be well-mixed so that the nitric acid concentration at the snowpack surface would be the same as at 7-8 $m$. Surface snow (the top 10 to 25 $mm$) was collected on a daily basis and the samples were analysed using ion chromatography (Fig. 4 B). Bulk concentrations of the major anions and cations were measured, including $Cl^-$, $SO_4^{2-}$ and $NO_3^-$ (Wolff et al., 2008). The concentrations were interpolated to the 10 minutes model resolution.

Other meteorological data included 10 minute averages of air temperature by Aspirated PRT, RH by Humidity probe (Vaisala Corp) and wind speed and direction by Propeller vane. All sensors were at 1 $m$ above the snow surface. All values were linearly interpolated to the model time step of 10 $min$.

### 4.3 Other Model Inputs

There are no available pH measurements of the snowpack, therefore, the pH of the DI in Model 1 and the initial pH in Model 2 is assumed to be 5.6 (Udisti et al., 2004, based on the pH of the completely melted samples) at both Dome C and Halley. There are no measurements of SSA recorded during 2009-2010 for skin layer snow. The SSA and effective grain radius in this study are estimated based on observations at Dome C from 2012 to 2015 by Picard et al. (2016) as well as the annual temperature variation, as shown in Fig. A4. To the author's knowledge there are no observations of SSA are available for Halley. Therefore the observations of SSA from Dome C were adjusted taking into account the shorter cold period, which tends to have a larger SSA (Fig. A4, dashed line).

### 4.4 Statistical Analysis

Three-day running means are calculated from all model outputs to better match the time resolution of the snow observations. The performance of the models is assessed by the coefficient of variation of RMSE, $C_v(RMSE)$, as a goodness of fit. The $C_v(RMSE)$ is defined as

$$C_v(RMSE) = \frac{\sqrt{\sum_{t=1}^{n}(obs(t) - model(t))^2 / n}}{\overline{obs}} \tag{20}$$

where $obs(t)$ and $model(t)$ are the observed value and modelled value at time $t$ respectively, $n$ is the number of observations, and $\overline{obs}$ is the observation mean.

## 5 Results

### 5.1 Dome C

The predicted concentration of nitrate in skin layer snow for Model 1 and Model 2 in Dome C (Fig. 5 and Table 2) are discussed by season - Winter to Spring (April - Mid November) and Summer (Mid November - January).

### 5.1.1 Winter to Spring

The average temperature ($\pm 1\sigma$) at Dome C between late autumn to late spring in 2009 is 213.7 ($\pm$7.9) K (Fig. 3 A), which is below the threshold temperature, $T_o$, for detection of DI (set at 238 K, purple shaded area in Fig. 5 A) for Model 1 and below the eutectic temperature, $T_e$, for a $H_2O$-$HNO_3$ mixture (230 K, yellow shaded area in Fig. 5 B) for Model 2. Therefore, in winter, the skin layer concentration of nitrate is well described by non-equilibrium kinetic surface adsorption and co-condensation coupled to solid-state diffusion within the snow grain in both models. The models combine both processes and agree very well with the observations of nitrate (Fig. 5 A & B) with a $\mathrm{C_v(RMSE)}$ = 0.73 (Table 2). Both models captured the small peak from mid April to early May and another peak from mid to end of August then a steady increase from middle September till the beginning of November, except for the peak in late February.

The results from 'Bock-BC1' and 'Model 1 - BCice' are shown in Fig. 6a. Both the configurations resulted in a very similar trend and variation until mid Sept. Despite the 'Model 1 - BCice' approach yielding a larger $\mathrm{C_v(RMSE)} = 0.65$ compared to the "Bock-BC1' approach $\mathrm{C_v(RMSE)} = 0.52$, (Table. 2), the 'Model 1 - BCice' approach captures the temporal pattern from mid September till early November but not in the 'Bock-BC1' approach.

### 5.1.2 Summer

The average temperature ($\pm 1\sigma$) from late spring to early autumn is 240.0 ($\pm$5.0) K (Fig. 3a) and the dominant process determining the snow nitrate concentration are solvation into the DI coupled with solid state diffusion in Model 1 and partitioning of nitrate to the liquid micropockets in Model 2.

Model 1 captures some trends observed in early spring and during the summer period, including the decrease in concentration of nitrate from the beginning of February, the rise between mid and late November, and the sharp increase in mid December (Fig. 5a). It also reproduced the steep decrease in concentration at the beginning of 2010 (Fig. 5a) . However, Model 1 (with $T_o$ = 238 K) did not capture the peak in early February and overestimated the concentration of nitrate by a factor of 1.5-5 in December (Fig. 5 A).

The results from Model 2 agreed reasonably well with the observation in these few months with $\mathrm{C_v(RMSE)}$ of 0.67. With the contribution from the partitioning of $HNO_3$ in the micropockets, the features in early February and the peaks between November and mid December were captured (Fig. 5 B). The model underestimates the the nitrate concentration from mid December until January 2010 by a factor of 3. During the summer period, the partitioning into the micropockets contributed $\sim$75% to the total $NO_3^-$ concentration.

### 5.2 Halley

Model results for Model 1 and Model 2 in Halley (Fig. 7 and Table. 3) are presented by the season - Late Autumn to Winter (April - Mid September) and Spring to Early Autumn (Mid September - February).

#### 5.2.1 Late Autumn to Winter

The mean temperature ($\pm 1\sigma$) during this period at Halley is 244.72($\pm$7.7) K (Fig. 4a). During this period, the temperature was mostly above the threshold temperature ($T_o$ = 238 K, purple shaded area in Fig. 7 A) used in Model 1 but below the eutectic temperature for a $H_2O$-NaCl mixture (252 K, yellow shaded area in Fig. 7 B ) used in at Halley in Model 2. Therefore, the main process controlling the concentration of $NO_3^-$ in Model 1 is solvation into the DI whereas in Model 2 the main controlling processes are the combination of non-equilibrium adsorption and co-condensation coupled with solid-state diffusion. Performance of Model 1 was poor ($C_v(RMSE)$ = 27.78), overestimating the concentration of $NO_3^-$ by two orders of magnitude (Fig. 7 A). However, some of the trends were reproduced during this cold period such as the two small peaks in mid April and early May, and the rise in mid September (Fig. 7 A).

The modelled results from Model 2 ($C_v(RMSE)$ = 1.08) were a much closer match to the observations compared to Model 1. It captured the first peak in mid April and the small peak in beginning of September (Fig. 7 B). However, it did not reproduce the peak in mid August and underestimated the $NO_3^-$ concentration for the majority of the time.

The results from 'Bock-BC1' and 'Model 1 - BCice' are shown in Fig. 6b. Similar to the Dome C site, the modelled results from both approaches are very similar in value and temporal variations and both the configurations failed to reproduce the peak in mid August.

#### 5.2.2 Spring to Early Autumn

Similar to the winter months, Model 1 overestimated the bulk $NO_3^-$ concentration at Halley by an order of magnitude and failed to capture any of the variability (Fig. 7 A) with $C_v(RMSE)$ = 89.28. Model 2, however, reproduced some features during the warmer months, such as the peak in late September followed by a steady rise in October, the spikes in mid December, beginning of and mid January and also the peak and trough in late January (Fig. 7 B). The partitioning to the micropockets contributed $\sim$80% of the total $NO_3^-$ concentration during this period. Results from Model 2 are within the same order of magnitude compared to the observations ($C_v(RMSE)$ = 0.65, Table. 3).

## 6 Discussion

The results from both Model 1 and 2 show that the bulk $NO_3^-$ concentration in surface snow can be reasonably well described by non-equilibrium adsorption and co-condensation coupled with solid-

state diffusion during autumn to spring at Dome C and in winter at Halley, i.e. when it is cold and the solar irradiance is small. In the summer months, the combination of warmer temperatures and a larger range of diurnal temperature causes the 'Air-Ice' only processes to no longer provide an accurate prediction. The concentration of $NO_3^-$ in the surface snow, during the warmer months, is mainly determined by solvation into DI in Model 1 or partitioning into micropockets in Model 2.

Overall, the results from Model 1 match reasonably well with the year-round observations at Dome C ($C_v(RMSE)$ = 1.34). However, for Halley, Model 1 overestimated the concentration by two order of magnitude ($C_v(RMSE)$ = 89.28). On the other hand, results from Model 2 agree well for both study sites year-round ($C_v(RMSE)$ = 0.84 for both Dome C and Halley). The mismatch between the models and observations can be separated into 2 categories - data limitations and model configurations, and will be discussed below.

The temporal resolution of the concentration of atmospheric nitrate at both study sites was roughly 5 to 10 days, therefore, any substantial changes in the atmospheric input within a short time scale might be missed and consequently the relative changes in concentration of nitrate in snow might not be observed. Secondly, the vertical snow pit profile of $NO_3^-$ at Dome C (and sites with a low accumulation rate) tended to have a maximum concentration of $NO_3^-$ at the surface of the snowpack (Röthlisberger et al., 2000), especially during the summer period, and the concentration of $NO_3^-$ decreases sharply with the depth in the snowpack. The skin layer is the most responsive layer of snow to the changes in the concentration of $HNO_3$ in the atmosphere above. The snow samples from Dome C were collected carefully from the top $4\pm2\ \mathrm{mm}$ while the snow samples from Halley were collected from the top 25 $\mathrm{mm}$. It is possible that the snow $NO_3^-$ concentrations measured at Halley may be 'diluted' from deeper snow, with a smaller nitrate concentration than the surface layer, leading to a positive model bias.

Thirdly, atmospheric nitrate can be found in the particulate forms of $NO_3^-$, i.e. associated with $Na^+$, $Ca^{2+}$ or $Mg^{2+}$ (Beine et al., 2003). An increase in sea salt aerosol concentration can shift gaseous $HNO_3$ to particle-phase (i.e. $NaNO_3$, Dasgupta et al., 2007), and therefore, decreases the ratio of gaseous $HNO_3$ and the total atmospheric nitrate. At Dome C, the atmospheric sea salt aerosol concentration in late winter or early spring can be up to a factor of 4 larger than the annual mean ($\sim$ 5 $\mathrm{ng\,m^{-3}}$, Legrand et al., 2016) due to the large sea ice extend (Jourdain et al., 2008). Therefore, using the total measured atmospheric nitrate as gaseous $HNO_3$ for constraining the models might lead to an overestimate of $[NO_3^-]$ in snow at Dome C, especially in early summer. At the coastal site of Halley, there is a strong influence from sea salt aerosol with corresponding larger concentration of nitrate containing aerosol, especially in spring time that the monthly mean $p{-}NO_3^-$ mixing ratio is $\sim$ 4.6 $\mathrm{pptv}$ (Rankin et al., 2003; Jones et al., 2011). Therefore, neglecting the dry deposition of nitrate aerosols might underestimate the concentration of nitrate in the surface snow in spring time. The concentration of $p{-}NO_3^-$ (data not show here, see Jones et al., 2008 for more information) is typically 2.6 and 3.0 times higher than the concentration of nitric acid in winter and summer,

respectively, but was up to 8.3 times higher in spring during 2004-2005 at Halley. This might explain the underestimation of concentration of nitrate in surface snow in winter and spring at Halley.

Lastly, no detailed information is available on timing and amount of snowfall events for the time periods in question at both study sites. Single snowfall events can increase the nitrate concentration in surface snow by up to a factor of 4 above the background (Wolff et al., 2008). The contribution of snow nitrate from fresh precipitation may be less important at low accumulation sites, such as Dome C compared to sites with large snow accumulation like Halley. Wolff et al. (2008) reports that the large concentration of $NO_3^-$ recorded from mid until end of August was due to new snowfall, which explains why both models failed to reproduce the peak. In the following sections, various processes included in Model 1 and 2 will be discussed.

### 6.1 Kinetic 'Model 1-BCice' Approach vs Equilibrium 'Bock-BC1' Approach

The 'Model 1-BCice' approach defines the snow grain boundary concentration of $NO_3^-$ by non-equilibrium, kinetic surface adsorption while the 'Bock-BC1' approach after Bock et al. (2016) defines the concentration of the outermost shell of the snow grain by thermodynamic equilibrium ice solubility. Both approaches describe the interaction between air and ice, therefore, only results from the winter period are compared. For both sites, the 'Model 1-BCice' and 'Bock-BC1' approach resulted in very similar trends except the peak in late October at Dome C (Fig. 6, Table 2 & 3), of which the 'Model 1-BCice' approach managed to reproduce but not the 'Bock-BC1' approach.

The peak of snow nitrate in late October at Dome C corresponds to an increase in atmospheric $HNO_3$ (Fig. 3 B). The grain surface concentration of the 'Bock-BC1' approach is a function of the partial pressure of $HNO_3$ with an exponent of 1/2.3 (Eq. 19), while the concentration of the grain boundary defined by the 'Model 1- BCice' approach is linearly related to the concentration of atmospheric nitrate (Eq. 8). Therefore, the 'Model 1- BCice' approach is more responsive to any changes in the atmospheric nitrate concentration compared to the 'Bock-BC1' approach. Other advantages of the former approach are, 1) dynamic characteristics of the grain surface due to changing temperature gradients are taken into consideration; 2) applicability even for sites with high accumulation rates where the skin layer is buried by subsequent snowfall before reaching equilibrium.

At Halley, in winter, the concentrations of $NO_3^-$ are underestimated by both approaches (Fig. 6 and Table 3). There are 2 possible explanations. First, the SSA values used may be underestimated and lead to an underestimation of adsorption or dissolution in the outermost shell of the snow grain, further field observations are required to verify this. Secondly, due to higher temperatures at Halley compared to Dome C, other processes might be involved in controlling the snow surface concentration of $NO_3^-$, such as snowfall (not included in the models) or partitioning into liquid micropockets in Model 2 (discussed in Sect. 6.4).

### 6.2 Co-Condensation - 'Air-Ice' Interaction

The process of co-condensation/sublimation is considered as part of the 'Air-Ice' interaction in both Models 1 and 2. It is driven by the difference in water vapour density across the skin layer snow and the overlying atmosphere. The water vapour density gradient depends exponentially on the temperature gradient. At Dome C the temperature is extremely low and relatively dry, especially in winter, and therefore it is not surprising that only 2% of the grain surface concentration of $\mathrm{NO_3^-}$ is from co-condensation during winter and spring (Fig. 6 A, difference between the light and dark blue line). In contrast, at Halley, where winter is warmer and it is relatively humid, $\sim$21% of the grain surface concentration is contributed by co-condensation during winter (Fig. 6 B, difference between the light and dark blue line). As shown in Table 3, the $\mathrm{C_v(RMSE)}$ decreased slightly in winter after including co-condensation as part of the 'Air-Ice' interaction. In the summer, the dominant process in Model 1 is solvation into the DI (See Sect. 6.3) while in Model 2 the dominant process is partitioning into the micropockets (See Sect. 6.4), hence the contribution from co-condensation to the skin nitrate concentration is insignificant.

There are a few possible sources of uncertainties in the calculation of co-condensation/sublimation processes. For example, the macro-scale gradients of water vapour pressure (across a few $\mathrm{mm}$) were used instead of micro-scale gradients (across a few $\mu\mathrm{m}$) and there were no precise measurements of skin layer snow density. Uncertainty in the density would lead to uncertainty in the modelled skin layer snow temperature (Eq. 12). Despite the potential errors in the calculation of co-condensation, the large $\mathrm{NO_3^-}$ concentrations in the skin layer in the summer are unlikely to be driven by co-condensation. An unrealistically large average rate of volume change, $\frac{dV}{dt}$, of 130 and 118 $\mu\mathrm{m^{-3}\,s^{-1}}$, equivalent to an average grain volume increases of 170% and 135% per day, would be required for Dome C and Halley respectively if the large concentration of $\mathrm{NO_3^-}$ in summer was contributed by co-condensation (Eq. 9 & 10). Assuming the RH in the open pore space of the skin layer snow to be 100% and RH of the overlying atmosphere to be the same as measured at 1 $\mathrm{m}$ above snowpack, a macro-temperature gradient as high as $2.7\times10^3\ \mathrm{K\,m^{-1}}$ would be required across the top 4 $\mathrm{mm}$ of the snowpack to match the large concentration of bulk $\mathrm{NO_3^-}$ in the summer at Dome C and in an average temperature gradient of 500 $\mathrm{K\,m^{-1}}$ would be required across the top 10 $\mathrm{mm}$ of the snowpack at Halley. Therefore, the required temperature gradients are 1- 2 orders of magnitude larger than indicated by observations or modelled result (Frey et al., 2013, and as listed in Sect. 3.1.1).

### 6.3 Disordered Interface - Model 1 (T > $T_o$ = 238 K)

In Model 1, the air-snow grain interface is described as 'Air-DI' at $T$> 238 $\mathrm{K}$. Therefore, at Dome C, the 'Air-DI' regime applies only during summer months due to the extremely cold temperatures in winter, whereas, at Halley most of the time the interface is considered as 'Air-DI'. Model

1 simulations suggest that an 'Air-DI' interfaceat $T$> 238 K leads to an overestimation of nitrate concentration in early December at Dome C and all year round at Halley. The poor performance of Model 1 at Halley and at Dome C in summer is attributed to uncertainties in physical and chemical properties of the DI.

Here, $T_o$ has been set to the lower end of the temperature range, where the onset of a DI is observed in the lab on a pure ice surface (Bartels-Rausch et al., 2014). The exact DI onset temperature is uncertain as reported values vary with different experimental setups, probing and sample preparation techniques (Bartels-Rausch et al., 2014). Furthermore, for a mixture of $H_2O$ and impurities it has been observed that already at 100 K below the melting point a small fraction of water molecules begins to leave the outermost crystalline layer of the ice with the number of mobile molecules increasing with temperature (Conde et al., 2008). When the temperature is within 10 K below the melting point, molecules might even begin to leave the deeper crystalline layer. Therefore, the chosen threshold temperature, $T_o$, might be substantially different from what would be found in natural snow or it might not be representative to be used as the threshold all year-round. The Model 1 sensitivities to $T_o$ are evaluated below (Sect. 6.5), and suggest that goodness of fit improves slightly at Dome C with a 2 K increase, but shows no significant improvement at Halley (Table 4).

The onset and thickness of the DI not only depend on temperature, but also the speciation and concentration of impurities present within the snow grain (McNeill et al., 2012; Dash et al., 2006). Different impurities have different impacts on the hydrogen bonding network at the ice surface and hence have a different impact on the thickness of the DI, leading in general to a thickening compared to pure ice (Bartels-Rausch et al., 2014). However no accepted model parameterisation is available. In this model imposing a seasonal cycle of SSA and therefore grain size causes the thickness of the outermost model shell to vary between 1.5 μm in summer and 0.5 μm in winter (Sect. 3.1), relatively large values and potentially contributing to the positive bias in Model 1. This is explained as follows: the bulk concentration of $NO_3^-$ is calculated as the sum of number of molecules in each model shell divided by the total volume of the snow grain (Eq. 17). At $T > T_o$ the outermost model shell is equivalent to a DI and its concentration is determined by Henry's Law (Eq. 13), which is independent of grain size and thus model shell thickness $\Delta r$. However, the absolute number of molecules in each model shell including the DI, increases with $\Delta r$ yielding a larger bulk concentration in summer. Choosing a thinner outermost model shell may reduce the Model 1 bias at Halley.

In summary, a combination of potential factors contribute to why Model 1 performs reasonably well at Dome C, but not at Halley: 1) at Dome C the chemical composition of surface snow is relatively simple, dominated by the nitrate anion, which would induce only insignificant changes to the hydrogen bonding network at the DI surface compared to a more complicated snow composition (Bartels-Rausch et al., 2014) and suggesting that the surface properties of snow at Dome C are likely to be comparable to pure ice; 2) at Halley temperatures occasionally rise above 0 °C potentially causing melting and significant changes in snow grain morphology at the surface especially; 3) as

temperature increases the DI may become more distinct from ice and more isolated from the bulk and may have less or even no interaction with the bulk. This is supported by previous laboratory experiments showing that physical properties, such as extinction coefficient and refractive index, of the ice surface gradually change from the measured value of ice to the measured value for water and the layer of disordered water molecules grows increasingly thicker as temperature approaches the melting point (Huthwelker et al., 2006).

### 6.4 Micro-Liquid Pocket - Model 2 ($T \geq T_e$ )

Model 2, which includes non-equilibrium surface adsorption and co-condensation coupled with solid diffusion within the grain and partitioning in liquid micropockets, successfully reproduces the concentration of $NO_3^-$ of the surface snow without any tuning parameters for both Dome C and Halley all year round. This is a crucial outcome as it indicates that Model 2 can be used for predicting the air-snow exchange of nitrate at the surface for a wide range of meteorological and depositional conditions that are typical for the entire Antarctic ice sheet.

The liquid water fraction is a function of the total ionic concentration (Eq. 4). Hence, neglecting the existence of other ions may lead to underestimation of the micropocket volume. The additional liquid would increase the dissolution capacity of $HNO_3$ and hence increase the estimated $NO_3^-$ concentration. As shown in Fig. 7 B, the estimated bulk $NO_3^-$ concentration followed a similar trend as the 'other ions concentration', which is the observed $Cl^-$ concentration. Despite $NO_3^-$ being the major anion in the surface snow in Dome C, other anions, such as $Cl^-$ and $SO_4^{2-}$, were also detected from the same samples (Udisti et al., 2004). Jones et al. (2008) also measured $SO_4^{2-}$ along with $Cl^-$ and $NO_3^-$ from the surface snow samples from Halley. The mismatch between modelled and observed nitrate concentration in the summer can be explained by assuming nitrate to be the only impurity at Dome C, or nitrate and sea salt as the only impurities at Halley. Nevertheless, the underestimation of the $NO_3^-$ concentration due to underestimating the liquid-water content may be compensated or even overwhelmed if atmospheric deposition of other acids such as $HCl$ or $H_2SO_4$ increases, which lowers the pH and reduces the solubility of $HNO_3$ in the micropocket.

Note that the micropockets only exist above the eutectic temperature. For simplification, the eutectic temperature was based on a system containing $H_2O$ and the most abundant solute within surface snow. However, in reality, the presence of other impurities might have an impact on the eutectic temperature. Moreover, the liquid in the micropocket is assumed to behave ideally and, therefore, Henry's coefficient is used to describe the partitioning between air and the micropocket. In reality, there may be some deviation from ideality as the concentration of solutes in the micropocket is likely to be too large to be considered as an ideal dilute solution. The non-ideality should be accounted for in terms of activity coefficient, $\gamma$. At equilibrium, the relationship between a solute $B$ and the solvent can be expressed as follow (Sander, 1999):

$$K_B = \frac{\gamma_B x_B}{P_B} \tag{21}$$

where $P_B$ is the vapour pressure of $B$, $\gamma_B$ is the activity coefficient of $B$ and $x_B$ is the mole fraction of $B$. The value of the activity coefficient approaches unity as the mole fraction of $B$ approaches zero ($\gamma_B \rightarrow 1$ as $x_B \rightarrow 0$) and, under such ideal-dilute condition, the equilibrium constant, $K_B$, is defined as Henry's law coefficient. Values of activity coefficient can be found experimentally. The available parameterisation of activity coefficient of $\mathrm{HNO_3}$(aq), $\mathrm{H^+}$ and $\mathrm{NO_3^-}$ is only accurate for concentration up to 28 $\mathrm{m}$ (Jacobson , 2005). When the molarity is higher than ~4-5 $\mathrm{m}$, depending on the temperature, the activity coefficient of $\mathrm{H^+}$ and $\mathrm{NO_3^-}$ increases as molarity increase. The concentration of the micropocket is estimated based on the parameterisation by Cho et al. (2002), which predicts a concentration a lot larger than the limit of activity coefficient parameterisation available at present. Hence, it is not possible to quantify the uncertainties caused by assuming the micropocket has ideal-solution behaviour. If the relationship between activity coefficient and molarity extend to molarity larger than 28 $\mathrm{m}$, the activity coefficient will be larger than 1 and hence reduces the value of the equilibrium constant, $K_B$, compared to the Henry's Law coefficient. By means, the assumption of ideal-solution behaviour of micropocket is likely to overestimate the concentration of the micropocket. The activity coefficient of highly concentrated solution is needed to be found by further experimental studies.

### 6.5 Sensitivity Analysis

In order to assess the robustness of the findings presented here they were analysed as a function of model sensitivities to constraints, parameterisations and measurement uncertainties. Parameters were varied one at a time by the given range while keeping all others constraints and parameterisation the same (Table. 4, Column 1). The coefficient of variation, $\mathrm{C_v(RMSE)}$, was calculated from each sensitivity test (Table. 4) and compared with the $\mathrm{C_v(RMSE)}$ of the 'Control', which uses the observed values and parameterisation listed in Sect. 4 and Table. A1.

Both Model 1 and 2 are sensitive to the concentration of $\mathrm{HNO_3}$ in the air and the concentration of $\mathrm{NO_3^-}$ in snow. Reducing concentration of $\mathrm{HNO_3}$ in the atmosphere by 20% or increasing the concentration of $\mathrm{NO_3^-}$ in snow by 20% improves the performance of both models. This supports the suggestion that the atmospheric nitrate observed at Dome C only represents the upper limit of nitric acid and it is likely to lead to an overestimation of the concentration of nitrate in snow (Sect. 6) while at Halley, the skin layer snow might well be 'diluted' by snow sample from the deeper layer (Sect. 6).

Both models are sensitive to the value of SSA as a smaller SSA implies a smaller surface area per unit volume of snow, and hence, less surface sites available for adsorption per unit volume of snow. It has a more notable impact in Model 1 and in the winter, when the grain boundary processes play an important role for the overall snow nitrate concentration due to the cold temperature. A similar explanation applies the value of the maximum number of adsorption site, $N_{\mathrm{max}}$. However, varying

the accommodation coefficient, $\alpha$, by $\pm$ 10% does not have a significant impact on the performance of the models (Table 4).

Model 1 is very sensitive to the threshold temperature, $T_o$. At Dome C, the best match (lowest $\mathrm{C_v(RMSE)}$) between modelled and observation is with a threshold temperature 2 K larger than the control $T_o$ = 238 K. However, increasing $T_o$ to 242 K worsens the model performance further (Fig. 5A, Green line & Table 4). When a larger value of $T_o$ is used, a larger in-snow temperature is required to assume the interface is 'Air-DI'. Nitrate concentrations at the grain boundary, $U(R_{\mathrm{eff}})$, have a much larger value when the interface between air and grain boundary is defined as 'Air-DI' (Eq. 13) than when it is defined as 'Air-Ice' (Eq. 7). At Dome C, a larger value of $T_o$ may have reduced the overestimation in late November due to a larger fraction of time falling below the threshold but compromised the good fit from mid December onward and yield a higher $\mathrm{C_v(RMSE)}$. At Halley, despite the improvement in $\mathrm{C_v(RMSE)}$ when a higher temperature threshold was used, the modelled [$\mathrm{NO_3^-}$] is still an order of magnitude larger than the observation (Fig. 7 B).

Model 1 is not sensitive to the pH of the DI. Even though the effective Henry's law coefficient increases by an order of magnitude when pH increases from 5 to 6.5 (Fig. A3), the $\mathrm{C_v(RMSE)}$ remains the same. This behaviour can be explained by the combination of the kinetic approach and slow diffusion rate of nitrate in ice that the rate of change in the grain boundary concentration remains small even if the boundary concentration increases.

Model 2 is sensitive to the eutectic temperature, $T_e$, but not as much as for $T_o$ in Model 1. Increasing $T_e$ in Model 2, only improves the performance at Dome C but not Halley. Higher $T_e$ implies that a larger temperature is required for the co-existence of liquid micropockets. For Dome C, increasing $T_e$ by 2-4 K reduces the overestimation in November without compromising the results from mid December onwards, as the average temperature during that period was higher than $T_e = 234\mathrm{K}$.

## 7 Conclusions

Two surface physical models were developed from existing sphysical parameterisations and laboratory data to estimate the bulk concentration of $\mathrm{NO_3^-}$ in the skin layer of snow constrained by observed atmospheric nitrate concentrations, temperature and humidity.

Model 1 assumes that below a threshold temperature, $T_o$, the outermost shell of a snow grain is pure ice, whereas above $T_o$ the outermost shell is a disordered interface (DI). The nitrate concentration at the air-ice boundary is defined by non-equilibrium kinetic adsorption and co-condensation whereas the nitrate concentration at the air-DI boundary is defined by non-equilibrium kinetics based on Henry's Law. A non-equilibrium grain boundary is assumed as the partial pressure of $\mathrm{HNO_3}$ is low in Antarctica and a large temperature gradient is expected across the snowpack surface which leads to redistribution of water molecule at the grain surface. The boundary of the grain is also assumed to be interacting with the bulk so that the mass transport is driven by the concentration

difference between the outermost model shell and centre of the grain and constrained by solid-state diffusion. The uncertainties of Model 1 are 1) the temperature threshold, $T_o$, that defines the emergence of the 'air-DI' interface; 2) the partitioning coefficient of $HNO_3$ into the DI; 3) the interaction between the grain boundary and the bulk ice; and 4) the thickness of the DI and its dependence on temperature and ion concentration. Assuming too large of a DI thickness results in an overestimate of the bulk concentration of nitrate. The modelled skin layer concentration of $NO_3^-$ from Model 1 agreed reasonably well with observations at Dome C but overestimated observations by an order of magnitude at the relatively warmer Halley site. The poor performance of Model 1 at the warmer site suggests that as the temperature increases the disordered interface is becoming more liquid-like and disconnected from the bulk ice.

Model 2 assumes that below melting temperature, $T_m$, the outermost model shell of a snow grain is pure ice and above eutectic temperature, $T_e$, liquid exists in grooves at grain boundaries and triple junctions as micropockets. The nitrate concentration at the air-ice boundary is defined by non-equilibrium kinetic adsorption and co-condensation. The boundary of the grain is also assumed to be interacting with the bulk and the mass transport between the surface and centre of the grain is driven by solid-state diffusion. The nitrate concentration of the liquid micropocket is defined by Henry's law. Equilibrium between air and liquid in micropockets is assumed because the liquid micropocket volume is small and $HNO_3$ is very soluble in water implying fast interfacial mass transport. The main uncertainties in Model 2 are three-fold, 1) dry and wet deposition of atmospheric nitrate are currently not included in the model, but lead to episodic increases of $NO_3^-$ in surface snow; 2) the liquid micropocket is likely not an ideal solution due to high ionic strength, which is likely leading to overestimation of solvation; and 3) third the eutectic temperature of natural snow is assumed to be that of a single major ion - water system but may be different because snow ionic composition is complex. However, Model 2 reproduced the skin layer concentration of $NO_3^-$ with good agreement at both Dome C and Halley without any tuning parameters.

Both Model 1 and 2 suggest that in the winter the interaction of nitrate between the air and skin layer snow can be described as a combination of non-equilibrium kinetic ice surface adsorption and co-condensation coupled with solid diffusion within the grain. Only Model 2 provides a reasonable estimate at both sites year-round, that suggests in the summer, the major interface between snow grain and surrounding air is still air-ice, but it is the equilibrium solvation into liquid micropockets that dominates the exchange of nitrate between air and snow. Despite the simplified parameterisation of processes in Model 2, it provided a new parameterisation to describe the interaction of nitrate between air and snow as 'air-ice' with a liquid formed by impurities present as micropockets as suggested by Domine et al. (2013) instead of an 'air-DI' interface assumed by most models developed previously. Moreover, the non-equilibrium boundary between air and snow grain allows the models to work at sites with high rate of accumulation that the snow layer might be buried by fresh snowfall before reaching equilibrium.

Additional modelling studies, e.g. including uptake of other chemical species and aerosols such as $H_2SO_4$ and nitrate aerosols, backed up by field observations from other locations with various meteorological conditions as well as laboratory studies on the eutectic point of a multi-ion - $H_2O$ system, uptake coefficient at a higher temperature, are needed to improve the performance of Model 2. Moreover, the models presented here are describing the exchange between air and the skin layer of snowpack as the uptake processes are much quicker than the photochemical loss, and therefore, can be modelled by 'physical-only' processes. Atmospheric nitrate can reach deeper than the skin layer via wind pumping and temperature gradient, however, the nitric acid concentration in snow interstitial air is expected to be small compared to the overlying atmosphere due to the high uptake of nitrate near the surface of the snowpack. A smaller concentration of $HNO_3$ in snow interstitial air implies a smaller uptake in deeper snow, and hence the photochemical loss cannot be assumed to be negligible in deeper snow. Therefore, a more complex multi-layer model including both physical and chemical processes is required to reproduce the nitrate concentration in deeper snow and to implement in regional and global atmospheric chemistry models.

*Acknowledgements.* HGC is funded by the Natural Environment Research Council through Doctoral Studentship NE/L501633/1. We are thankful to our colleagues (Anna Jones, Neil Brough and Xin Yang) for helpful discussion.

## 8 Notation

| Symbol | Description | units |
|---|---|---|
| $\alpha$ | Accommodation coefficient | dimensionless |
| $\mathrm{A_{ice}}$ | Surface area of ice per unit volume of snowpack | $\mathrm{m^2\,m^{-3}_{snowpack}}$ |
| $\mathrm{C_v(RMSE)}$ | Coefficient of variation | N/A |
| DI | Disordered Interface | N/A |
| $D_v$ | Water vapour diffusivity | $\mathrm{m^2\,s^{-1}}$ |
| $D'_s$ | Gas-phase diffusivity in snow | $\mathrm{m^2\,s^{-1}}$ |
| $\Delta H^0_f$ | enthalpy of fusion | $\mathrm{J\,mol^{-1}}$ |
| $[\mathrm{HNO_{3\,(ads)}}]$ | Nitric acid concentration contributed by surface adsorption | $\mathrm{molecule\,m^{-3}}$ |
| $[\mathrm{HNO_{3\,(cc)}}]$ | Nitric acid concentration contributed by co-condensation | $\mathrm{molecule\,m^{-3}}$ |
| $[\mathrm{HNO_{3\,(DI)}}]$ | Nitric acid concentration in the DI | $\mathrm{molecule\,m^{-3}}$ |
| $[\mathrm{HNO_{3\,(g)}}]$ | Nitric acid concentration in gas-phase | $\mathrm{molecule\,m^{-3}}$ |
| $[\mathrm{HNO_{3\,(ice)}}]$ | Nitric acid concentration in solid ice | $\mathrm{molecule\,m^{-3}}$ |
| $[\mathrm{HNO_{3\,(surf)}}]$ | Nitric acid concentration on surface of grain | $\mathrm{molecule\,m^{-3}}$ |
| $[\mathrm{Ion_{tot,bulk}}]$ | Total ionic concentration in melted snow sample | $\mathrm{molecule\,m^{-3}}$ |
| $k_{\mathrm{ads}}$ | Adsorption coefficient on ice | $\mathrm{m^3\,molecule^{-1}\,s^{-1}}$ |
| $k_{\mathrm{des}}$ | Desorption coefficient on ice | $\mathrm{s^{-1}}$ |
| $k_{\mathrm{H^{cc}}}$ | Henry's Law coefficient | dimensionless |
| $k^{\mathrm{eff}}_{\mathrm{H}}$ | Effective Henry's Law coefficient | dimensionless |
| $k_{\mathrm{diff}}$ | Diffusivity in ice | $\mathrm{m^2\,s^{-1}}$ |
| $k_w$ | Thermal conductivity of snowpack | $\mathrm{Wm^{-1}K^{-1}}$ |
| $\mathrm{K_a}$ | Acid dissociation constant | $\mathrm{molecule\,m^{-3}}$ |
| $\mathrm{K_{eq}}$ | Equilibrium constant for Langmuir adsorption | $\mathrm{m^3\,molecule^{-1}}$ |
| $m_{\bar{\mathrm{H_2O}}}$ | Molecular mass of water | $\mathrm{kg\,mol^{-1}}$ |
| $N_{max}$ | Maximum number of adsorption sites | $\mathrm{molecule\,m^{-2}}$ |
| $[\mathrm{NO^-_{3\,(bulk)}}]$ | Bulk nitrate concentration | $\mathrm{molecule\,m^{-3}}$ |
| $\phi_{\mathrm{H_2O}}$ | Liquid water fraction | dimensionless |
| $\Phi^{\mathrm{aq}}_{\mathrm{bulk}}$ | Fraction of the total amount of solute in aqueous phase | dimensionless |
| $R_{\mathrm{eff}}$ | Effective radius of snow grain derived from SSA data | m |
| $R$ | Ideal gas constant | $\mathrm{J\,mol^{-1}\,K^{-1}}$ |
| $\rho_{ice}$ | Density of ice | $\mathrm{kg\,m^{-3}}$ |
| $\rho_v$ | Water vapour density | $\mathrm{kg\,m^{-3}}$ |
| [S] | Number of available surface sites per unit volume of air | $\mathrm{molecule\,m^{-3}_{air}}$ |
| SSA | Specific surface area | $\mathrm{m^2\,kg^{-1}}$ |
| $T_e$ | Eutectic temperature | K |
| $T_f$ | Reference temperature | K |
| $T_o$ | Threshold temperature in Model 1 | K |
| $\theta$ | Fraction of surface sites being occupied | dimensionless |
| $\overline{v}$ | Mean molecular speed | $\mathrm{m\,s^{-1}}$ |
| $V_{air}$ | Volume of air per unit volume of snowpack | $\mathrm{m^3_{air}\,m^{-3}_{snowpack}}$ |
| $V_{grain}$ | Volume of a snow grain | $\mathrm{m^3}$ |

**Table 1.** Characteristic times associated with gas-phase diffusion, mass transport and uptake of gas into ice grain

| Process | Expression | Order of magnitude, s |
|---|---|---|
| Interfacial mass transport to a liquid surface[i] | $\frac{4R_{\mathrm{eff}}}{3\overline{v}\alpha_{aq}}$ | $10^{-7}$ |
| Gas-phase diffusion to the surface of a spherical droplet[ii] | $\frac{R_{\mathrm{eff}}^2}{3\,D_s'}$ | $10^{-4}$ |
| Molecular diffusion between snowpack and the atmosphere[iii] | $\frac{z^2}{D_s'}$ | $10^{0}$ |
| Liquid-phase diffusion within a water droplet[iv] | $\frac{4\,R_{\mathrm{eff}}^2}{\pi^2\,k_{\mathrm{diff(aq)}}}$ | $10^{0}$ |
| Surface adsorption on ice[v] | $\frac{1}{k_{\mathrm{des}}}$ | $10^{3}$ |
| Solid-state diffusion within a snow grain[vi] | $\frac{4\,R_{\mathrm{eff}}^2}{\pi^2\,k_{\mathrm{diff}}}$ | $10^{6}$ |
| Photolysis at a snowpack surface[vii] | $\frac{1}{J}$ | $> 10^{7}$ |

[i] Sander (1999), with an effective radius, $R_{\mathrm{eff}}$ = 70 µm, and accommodation coefficient on liquid water, $\alpha_{aq} = 7.5 \times 10^{-5} \exp(2100/\mathrm{Temp})$ (Ammann et al., 2013). [ii] Sander (1999), with an effective molecular diffusivity, $D_s' = D_a/\tau_g$, where the tortuosity, $\tau_g = 2$ and molecular diffusivity in free air at 296 K, $D_a(296\mathrm{K}) = 87\ \mathrm{Torr\,cm^2\,s^{-1}}$ (Tang et al., 2014). [iii] Waddington et al. (1996), with a snow layer thickness, $z$ = 4 mm. [iv] Finlayson-Pitts and Jr. (2000), with a diffusion coefficient in liquid water, $k_{\mathrm{diff(aq)}} = 1 \times 10^{-9}\ \mathrm{m^2\,s^{-1}}$ (Yuan-Hui and Gregory, 1974) . [v] Crowley et al. (2010), with an equilibrium constant for Langmuir adsorption, $K_{eq} = 2 \times 10^{-16}\ \mathrm{m^3\,molecule^{-1}}$ and adsorption coefficient, $k_{\mathrm{ads}} = 1.7 \times 10^{-19}\ \mathrm{m^3\,molecule^{-1}\,s^{-1}}$. [vi] Finlayson-Pitts and Jr. (2000), with a diffusion coefficient in ice, $k_{\mathrm{diff}} = 6 \times 10^{-16}\ \mathrm{m^2\,s^{-1}}$ (Thibert et al., 1998). [vii] Finlayson-Pitts and Jr. (2000), with a surface $\mathrm{NO_3^-}$ photolysis rate coefficient, $J$, = $10^{-7}\ \mathrm{s^{-1}}$ (Thomas et al., 2011).

**Table 2.** Summary of model performance at Dome C based on the coefficient of variation of RMSE, $\mathrm{C_v(RMSE)}$

| Model description | Short name | Whole year DOY 30 - 385 | Winter-Spring DOY 90 - 318 | Summer DOY 319 - 385 |
|---|---|---|---|---|
| Surface Adsorption & Solid Diffusion | Model1-BCice | - | 0.65 | - |
| Ice Solubility & Solid Diffusion | Bock-BC1 | - | 0.52 | - |
| Surface Adsorption-Co Condensation/DI Solvation & Solid Diffusion | | | | |
| No threshold (no Solvation) | Model 1-none | 1.07 | 0.65 | 0.88 |
| $T_o$= 238 K | Model 1-238K | 1.34 | 0.73 | 1.11 |
| Surface Adsorption-Co Condensation & Solid Diffusion + micropocket | Model 2 | 0.84 | 0.73 | 0.67 |

**Table 3.** Summary of model performance at Halley based on the coefficient of variation of RMSE, $\mathrm{C_v(RMSE)}$

| Model description | Short name | Whole year DOY 87 - 406 | Winter DOY 90 - 257 | Spring -Early Autumn DOY 258 - 406 |
|---|---|---|---|---|
| Surface Adsorption & Solid Diffusion | Model1-BCice | - | 1.13 | - |
| Ice Solubility & Solid Diffusion | Bock-BC1 | - | 1.12 | - |
| Surface Adsorption-Co Condensation/DI Solvation & Solid Diffusion | | | | |
| No threshold (no Solvation) | Model 1-none | 1.06 | 1.06 | 0.95 |
| $T_o$= 238 K | Model 1-238K | 89.28 | 27.78 | 87.15 |
| Surface Adsorption-Co Condensation & Solid Diffusion + micropocket | Model 2 | 0.84 | 1.08 | 0.65 |

**Table 4.** Sensitivity test for Model 1 and 2 based on the coefficient of variation of RMSE, $\mathrm{C_v(RMSE)}$, the metric was used to measure a goodness of fit. Note that column one is not fitted to the observation and the values are only varying to show the sensitivity of the models against inputs and parameterisation.

| Parameter | | Model 1 | | | | | | Model 2 | | | | | |
|---|---|---|---|---|---|---|---|---|---|---|---|---|---|
| | | Dome C | | | Halley | | | Dome C | | | Halley | | |
| | | Whole year | Winter-Spring | Summer | Whole year | Winter | Spring-Summer | Whole year | Winter-Spring | Summer | Whole year | Winter | Spring-Summer |
| Control | | 1.34 | 0.73 | 1.11 | 89.28 | 27.78 | 87.15 | 0.84 | 0.73 | 0.67 | 0.84 | 1.08 | 0.65 |
| $[\mathrm{HNO_3}]$ | $-20\%$ | 0.98 | 0.60 | 0.81 | 71.19 | 22.12 | 69.5 | 0.80 | 0.62 | 0.64 | 0.77 | 1.10 | 0.56 |
| | $+20\%$ | 1.73 | 0.90 | 1.45 | 107.36 | 33.43 | 104.80 | 0.95 | 0.88 | 0.76 | 0.92 | 1.07 | 0.75 |
| SSA | $-10\%$ | 1.06 | 0.63 | 0.88 | 79.35 | 24.79 | 77.46 | 0.83 | 0.67 | 0.67 | 0.84 | 1.10 | 0.65 |
| | $+10\%$ | 1.63 | 0.84 | 1.36 | 99.22 | 30.75 | 96.86 | 0.84 | 0.78 | 0.67 | 0.83 | 1.07 | 0.65 |
| $\alpha$ | $-10\%$ | 1.34 | 0.73 | 1.11 | 79.35 | 24.78 | 77.46 | 0.83 | 0.73 | 0.67 | 0.83 | 1.08 | 0.65 |
| | $+10\%$ | 1.34 | 0.73 | 1.11 | 79.35 | 24.80 | 77.46 | 0.83 | 0.73 | 0.67 | 0.83 | 1.08 | 0.65 |
| $N_{max}$ | $-10\%$ | 1.32 | 0.67 | 1.10 | 89.27 | 27.77 | 87.15 | 0.83 | 0.69 | 0.67 | 0.84 | 1.09 | 0.65 |
| | $+10\%$ | 1.36 | 0.80 | 1.13 | 89.29 | 27.78 | 87.15 | 0.84 | 0.77 | 0.67 | 0.84 | 1.07 | 0.65 |
| $T_o$ (Model 1) or | -2 K | 3.53 | 0.91 | 3.00 | 90.45 | 42.54 | 87.31 | 0.95 | 0.92 | 0.75 | 0.85 | 1.12 | 0.65 |
| $T_e$ (Model 2) | +2 K | 0.50 | 0.64 | 0.36 | 67.49 | 25.33 | 65.62 | 0.73 | 0.65 | 0.58 | 0.86 | 1.07 | 0.65 |
| | +4 K | 0.61 | 0.65 | 0.47 | 50.76 | 23.86 | 49.00 | 0.72 | 0.65 | 0.57 | 0.88 | 1.06 | 0.67 |
| pH | -0.4 | 1.34 | 0.73 | 1.11 | 89.28 | 27.78 | 87.15 | - | - | - | - | - | - |
| | +0.4 | 1.34 | 0.73 | 1.11 | 89.28 | 27.78 | 87.15 | - | - | - | - | - | - |
| | +0.8 | 1.34 | 0.73 | 1.11 | 89.28 | 27.78 | 87.15 | - | - | - | - | - | - |
| $[\mathrm{NO_3}^-]$ | $-20\%$ | 1.85 | 0.98 | 1.54 | 111.87 | 34.84 | 109.2 | 0.99 | 0.96 | 0.79 | 1.09 | 1.08 | 0.93 |
| | $+20\%$ | 1.04 | 0.61 | 0.86 | 74.22 | 23.07 | 72.45 | 0.80 | 0.64 | 0.64 | 0.74 | 1.10 | 0.51 |

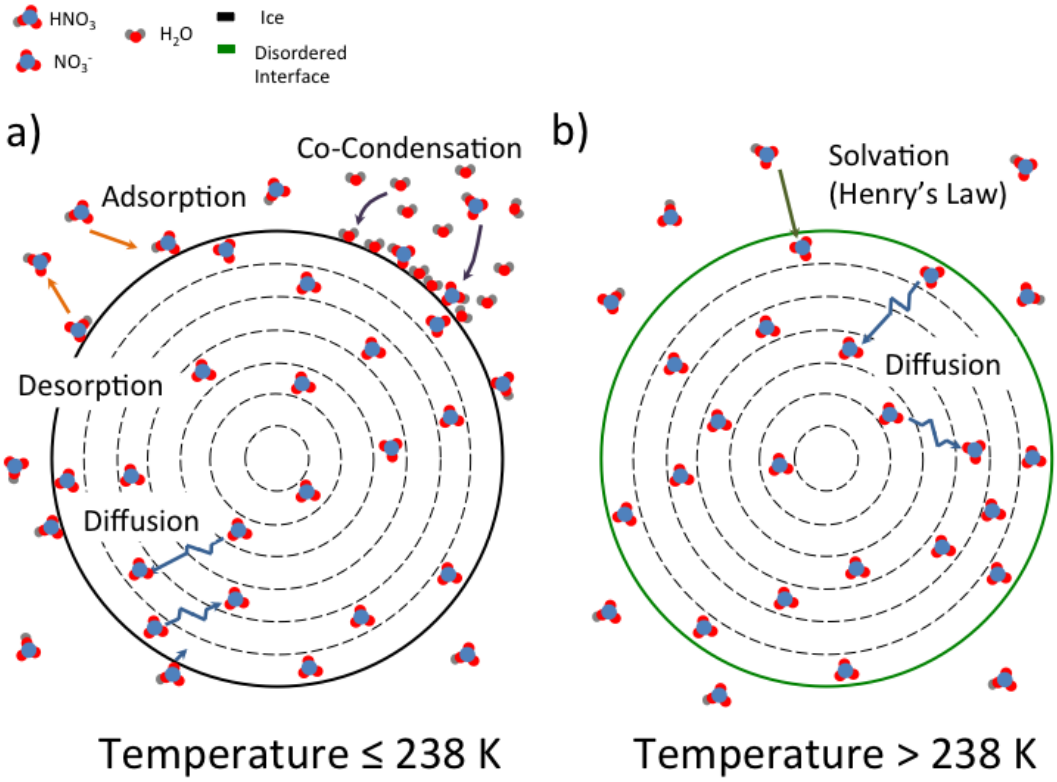


**Figure 1.** Schematic of Model 1. a) At T $\leq$ 238 K the concentration of $NO_3^-$ at the boundary of the snow grain is determined by Air-Ice processes, i.e. non-equilibrium adsorption and co-condensation. b) At T > 238 K the concentration of $NO_3^-$ at the boundary of the snow grain is determined by Air-DI processes, i.e. non-equilibrium solvation into DI.

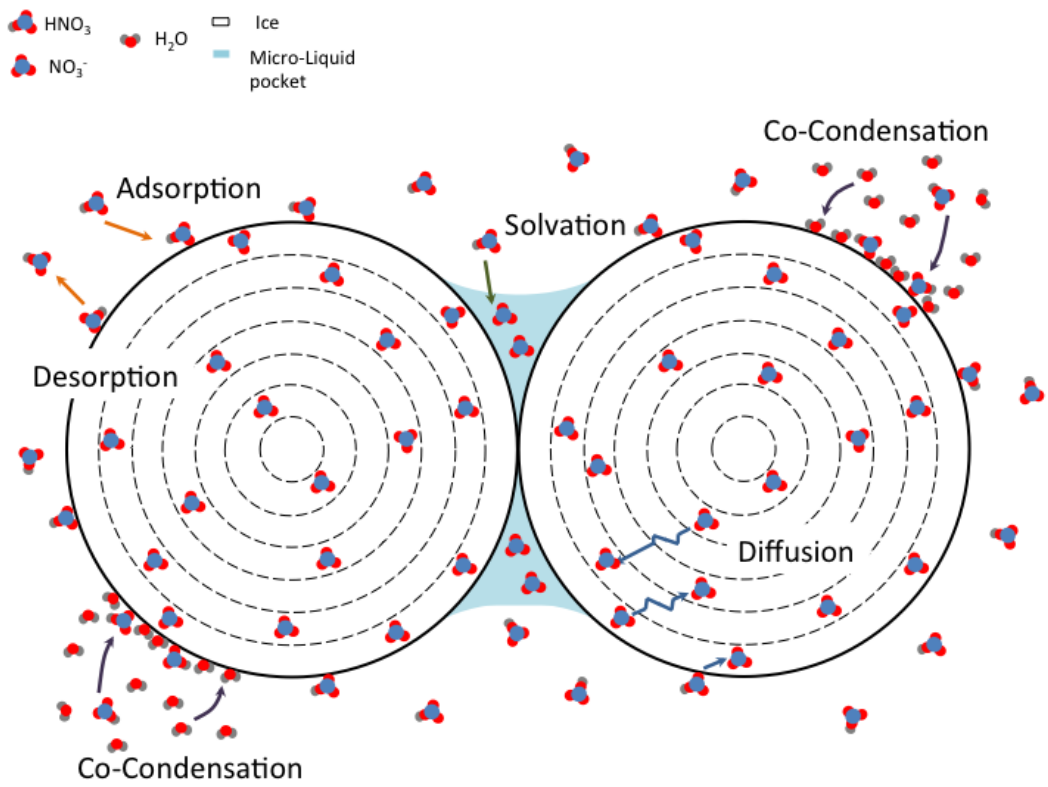


**Figure 2.** Schematic of Model 2. At T < $T_m$, the concentration of $NO_3^-$ at the boundary of the snow grain is determined by Air-Ice processes, i.e. non-equilibrium adsorption and co-condensation. At T $\geq T_e$, liquid is assumed to co-exist with ice and the liquid fraction is in the form of micropockets that are located at grain boundaries and triple junctions (Domine et al., 2013).

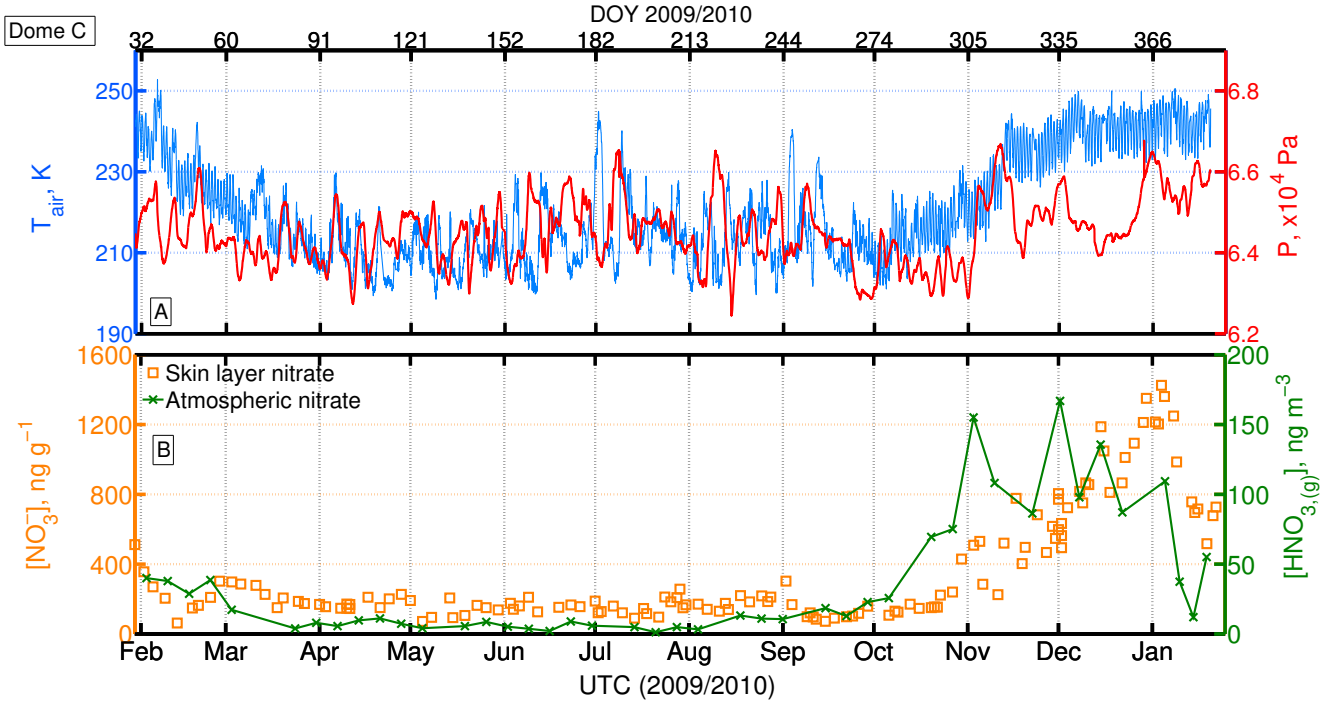


**Figure 3.** Atmospheric and snow observations from Dome C from Erbland et al. (2013)). (**A**) Air temperature (blue, left axis) and atmospheric pressure (red, right axis). (**B**) $NO_3^-$ in the snow skin layer (i.e. top $4 \pm 2$ mm, orange square, left axis) and atmospheric $NO_3^-$, i.e. sum of the atmospheric particulate $NO_3^-$ and $HNO_3$ (green, right axis).

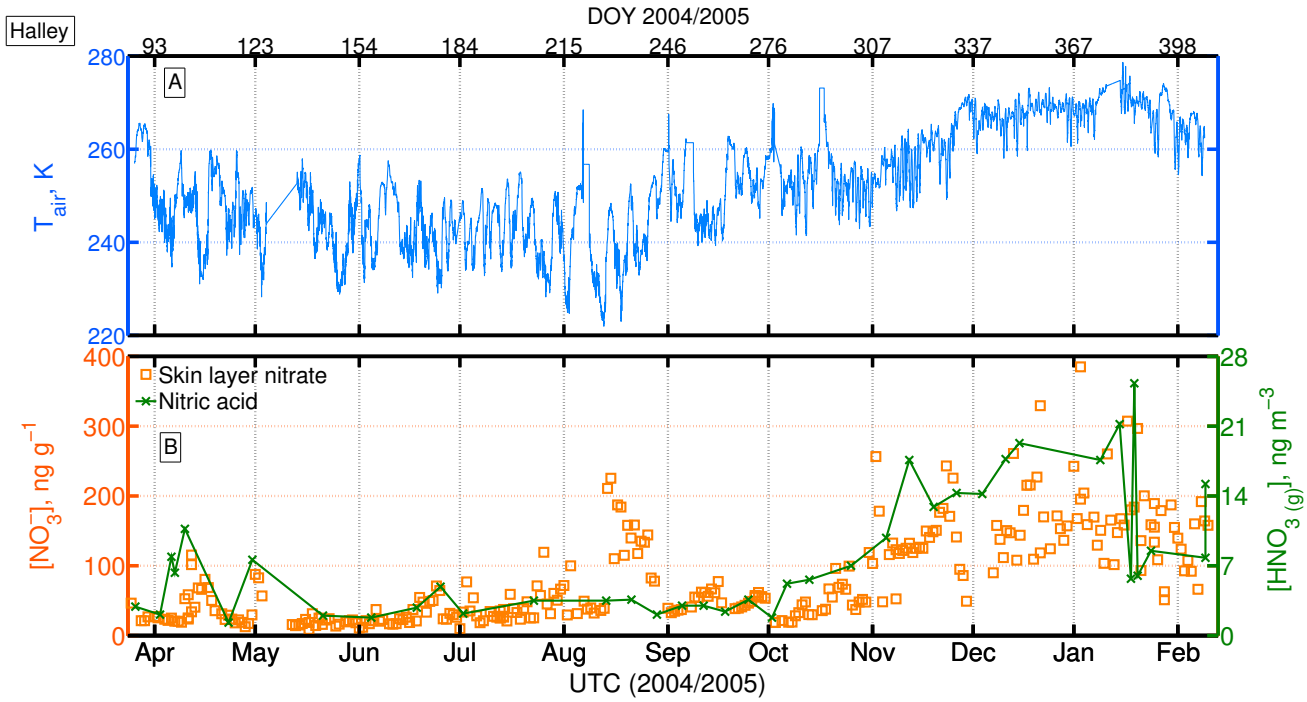


**Figure 4.** Atmospheric and snow observations at Halley between $27^{\mathrm{th}}$ March 2004 and $9^{\mathrm{th}}$ February 2005 from Jones et al. (2008). (**A**) Air temperature. (**B**) $NO_3^-$ in the surface snow (i.e. top $10 \pm 15$ mm, orange square, left axis) and gas-phase $HNO_3$ (green, right axis).

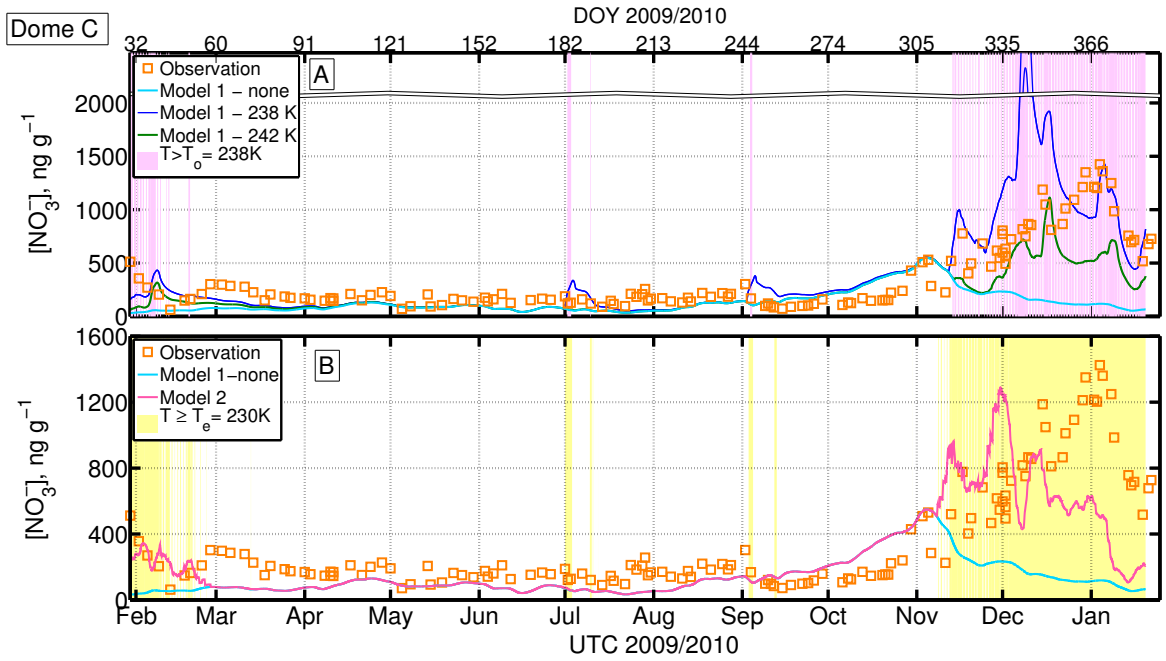


**Figure 5.** (**A**) Model 1 output of Dome C skin layer snow concentration of $NO_3^-$. At $T < T_o$ the interface between air and snow grain is assumed to be ice ('Air-Ice') and the $NO_3^-$ concentration is determined by a combination of non-equilibrium adsorption on ice and co-condensation coupled with solid-state diffusion. At $T > T_o$, the interface between air and snow grain is assumed to be a DI ('Air-DI'), i.e. the $NO_3^-$ concentration is determined by a combination of non-equilibrium solvation into the DI coupled with solid-state diffusion. Note that the y-axis is broken between 2000-3500 $\mathrm{ng\,g^{-1}}$. Orange squares: observation; Light blue: Model 1 with $T_o > T_m$, i.e. only air-ice interaction; Dark blue: Model 1 with $T_o$ = 238 K; Green: Model 1 with $T_o$ = 242 K; Purple shaded area indicate times when $T > T_o$ = 238 K; (**B**) Model 2 output of Dome C skin layer snow $NO_3^-$ concentration. The major interface between air and snow is assumed to be ice ('Air-Ice') at $T < T_m$ and the $NO_3^-$ concentration in ice is determined by a combination of non-equilibrium adsorption and co-condensation coupled with solid-state diffusion. Above $T > T_e$ =230 K, liquid co-exists with ice in the form of micropocket. The partition between air and micropocket is determined by Henry's law. Orange squares: observation; Light blue: Model 1 with $T_o > T_m$, i.e. air-ice only interaction; Pink: 'Model 2' - air-ice interaction plus micro-liquidpockets; Yellow shaded area indicates times when $T > T_e$ = 230 K ($T_e$ for $HNO_3$-$H_2O$ system).

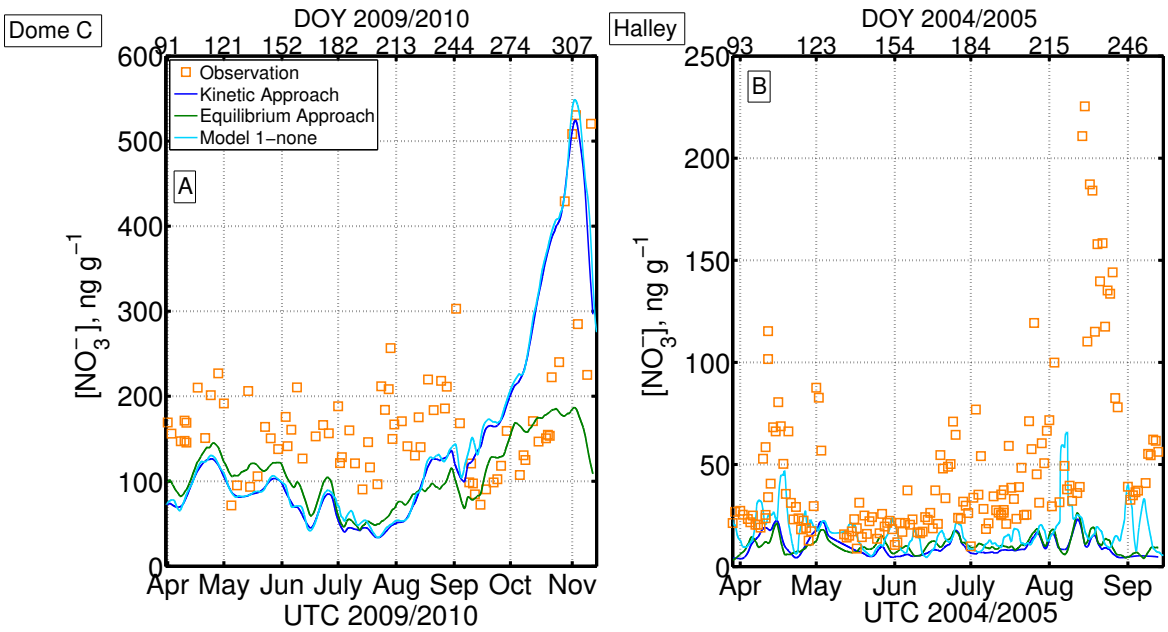


**Figure 6.** Comparison of the 'Kinetic' approach (this work, in dark blue) with the 'Equilibrium' approach (similar to Bock et al. (2016), in green), and the contribution from the co-condensation process (Results from Model 1- none, in light blue) in winter. The 'Kinetic' approach describes the air-snow interaction of nitrate as non-equilibrium kinetic surface adsorption coupled with solid diffusion inside the grain whereas the 'Equilibrium' approach describes the interaction as equilibrium solubility coupled with solid diffusion inside the grain. The 'Model 1-none' describes the interaction as co-condensation plus non-equilibrium kinetic surface adsorption coupled with solid diffusion within the grain. (**A**) Results at Dome C. (**B**) Results at Halley.

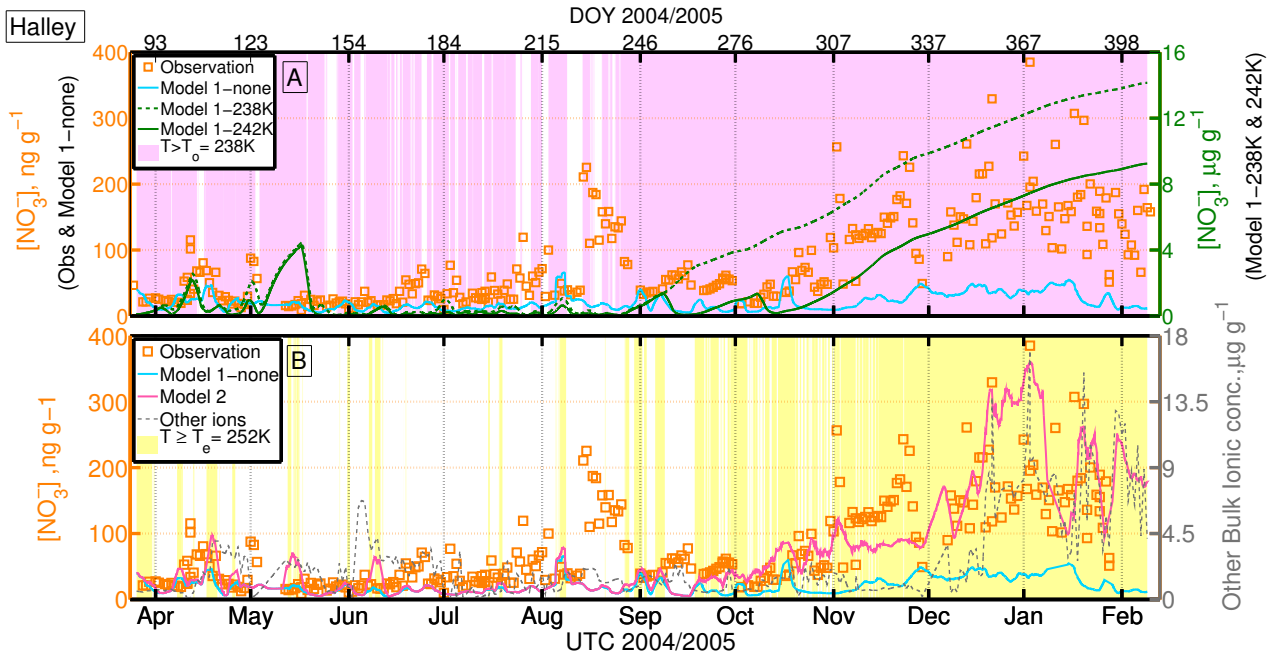


**Figure 7.** (**A**) Model 1 output of Halley skin layer snow concentration of $NO_3^-$. At $T < T_o$ the interface between air and snow grain is assumed to be ice ('Air-Ice') and the $NO_3^-$ concentration is determined by a combination of non-equilibrium adsorption on ice and co-condensation coupled with solid-state diffusion. At $T > T_o$, the interface between air and snow grain is assumed to be a DI ('Air-DI'), i.e. the $NO_3^-$ concentration is determined by a combination of non-equilibrium solvation into the DI coupled with solid-state diffusion. Orange squares: observation; Light blue: Model 1 with $T_o > T_m$, i.e. only air-ice interaction; Dark blue: Model 1 with $T_o$ = 238 K; Green: Model 1 with $T_o$ = 242 K; Purple shaded area indicate times when $T > T_o$ = 238 K; (**B**) Model 2 output of Dome C skin layer snow $NO_3^-$ concentration. The major interface between air and snow is assumed to be ice ('Air-Ice') at $T < T_m$ and the $NO_3^-$ concentration in ice is determined by a combination of non-equilibrium adsorption and co-condensation coupled with solid-state diffusion. Above $T > T_e$ =252 K, liquid co-exists with ice in the form of micropocket. The partition between air and micropocket is determined by Henry's law. Orange squares: observation; Light blue: Model 1 with $T_o > T_m$, i.e. air-ice only interaction; Pink: 'Model 2' - air-ice interaction plus micro-liquidpockets; Grey (Right axis) - measured bulk concentration of other ions, where other ions refers to the sum of $[Na^+]$ and $[Cl^-]$; Yellow shaded area indicates times when $T > T_e$ = 252 K ($T_e$ for NaCl-$H_2O$ system)

## Appendix A: Parameterisation

**Table A1.** Parameterisation for $HNO_3$

| Symbol | Parameter | Value/Parameterisation | units | Reference |
|---|---|---|---|---|
| $\alpha_0$ | Accommodation coefficient at reference temperature | $3 \times 10^{-3}$ [i] | Dimensionless | Hudson et al. (2002) |
| $k_{\mathrm{diff}}$ | Diffusion coefficient of nitrate in ice | $1.37 \times 10^{-2610/T}$ | $\mathrm{cm^2\,s^{-1}}$ | Thibert et al. (1998) |
| $k_w$ | Thermal conductivity of snow-pack | $k_w = k_{ice}\left(\frac{\rho}{\rho_{ice}}\right)^{2-0.5\frac{\rho}{\rho_{ice}}}$ | $\mathrm{Wm^{-1}K^{-1}}$ | Hutterli et al. (2003) therein |
| $k_{ice}$ | Thermal conductivity of ice | $k_{ice} = 9.828\exp(-0.0057T)$ | $\mathrm{Wm^{-1}K^{-1}}$ | Hutterli et al. (2003) therein |
| $\Delta_{\mathrm{sol}}H$ | Enthalpy of solution at standard temperature | -72.3 | $\mathrm{kJ\,mol^{-1}}$ | Brimblecombe and Clegg (1988) |
| $\Delta_{\mathrm{obs}}H$ | Enthalpy of uptake | -44 | $\mathrm{kJ\,mol^{-1}}$ | Thomas et al. (2011) |
| $k_{\mathrm{H}}^0$ | Henry constant at 298 K | $1.7 \times 10^5$ [ii] | $\mathrm{M\,atm^{-1}}$ | Brimblecombe and Clegg (1988) |
| $N_{max}$ | Maximum adsorption site | $2.7 \times 10^{18}$ | $\mathrm{molecules\,m^{-2}}$ | Crowley et al. (2010) |
| $\overline{v}$ | Mean molecular speed | $\sqrt{\frac{8R\,\mathrm{T}}{M_m\,\pi}}$ [iii] | $\mathrm{m\,s^{-1}}$ | Sander (1999) |
| $X^0_{\mathrm{HNO_3}}$ | Molar fraction of $HNO_3$ in ice | $X^0_{\mathrm{HNO_3}} = 2.37 \times 10^{-12}\exp(\frac{3532.2}{T})P^{1/2.3}_{\mathrm{HNO_3}}$ | $\mathrm{mol\,mol^{-1}}$ | Thibert et al. (1998) |
| $K_{eq}$ | Langmuir adsorption equilibrium constant | $-8.2 \times 10^{-18}\mathrm{T} + 2.01 \times 10^{-15}$ | $\mathrm{m^3 molecule^{-1}}$ | Burkholder and Wine (2015) |
| $D_v$ | Water vapour diffusivity | $D_v = 2.11 \times 10^{-5}(\frac{T}{T_o})^{1.94}\frac{P_o}{P}$ | $\mathrm{m^2\,s^{-1}}$ | Pruppacher and Klett (1997) |

[i] Temperature dependent accommodation coefficient, $\alpha = \frac{\exp\{\ln(\frac{\alpha_0}{1-\alpha_0})[-\frac{\Delta_{\mathrm{obs}}H}{R}(\frac{1}{T}-\frac{1}{T_f})]\}}{1-\exp\{\ln(\frac{\alpha_0}{1-\alpha_0})[-\frac{\Delta_{\mathrm{obs}}H}{R}(\frac{1}{T}-\frac{1}{T_f})]\}}$, (Thomas et al., 2011), where $R$ is the molar gas constant, $T$ is the temperature, $\mathrm{T_f}$ is the reference temperature (220 K) and $\alpha_0$ is the from Hudson et al. (2002) at 220 K

[ii] Temperature dependent dimensionless Henry's Law coefficient, $k_{\mathrm{H}}^{\mathrm{cc}} = k_{\mathrm{H}}^0 \times RT \times \exp\left(\frac{-\Delta_{\mathrm{sol}}H}{R}\left(\frac{1}{T}-\frac{1}{T^{\ominus}}\right)\right)$, where $T^{\ominus}$ is the standard temperature (298 K).

[iii] $M_m$ is the molar mass of the gas.

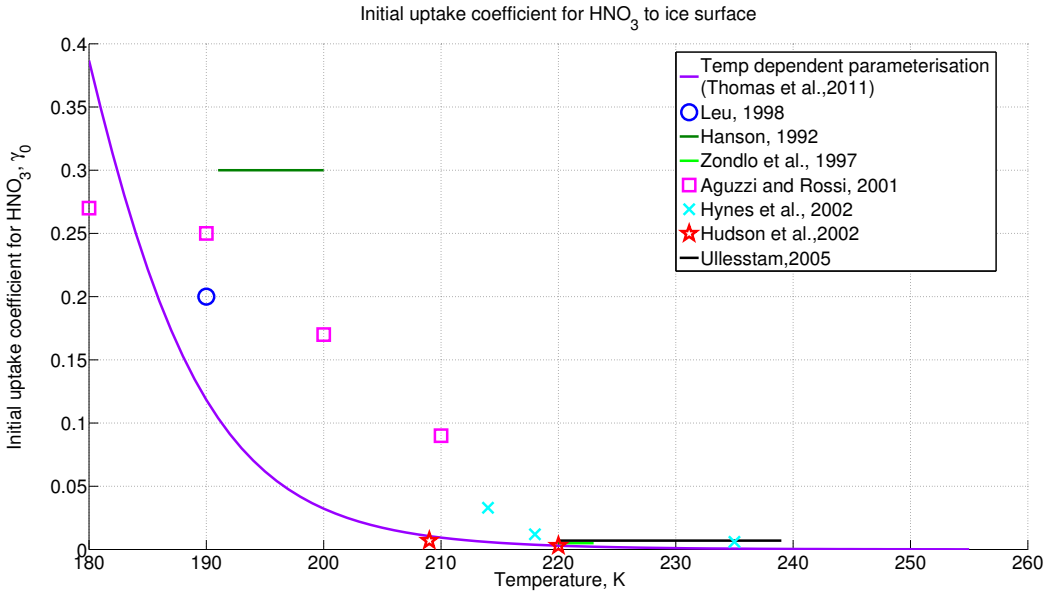


**Figure A1.** Initial uptake coefficient for $HNO_3$ as a function of temperature obtained from different studies. In this study the parameterisation of $\alpha(T)$ with $\alpha_0$ after Hudson et al. (2002) is used (Table A1, solid purple line) and is chosen to give the best representation of the dependency on temperature.

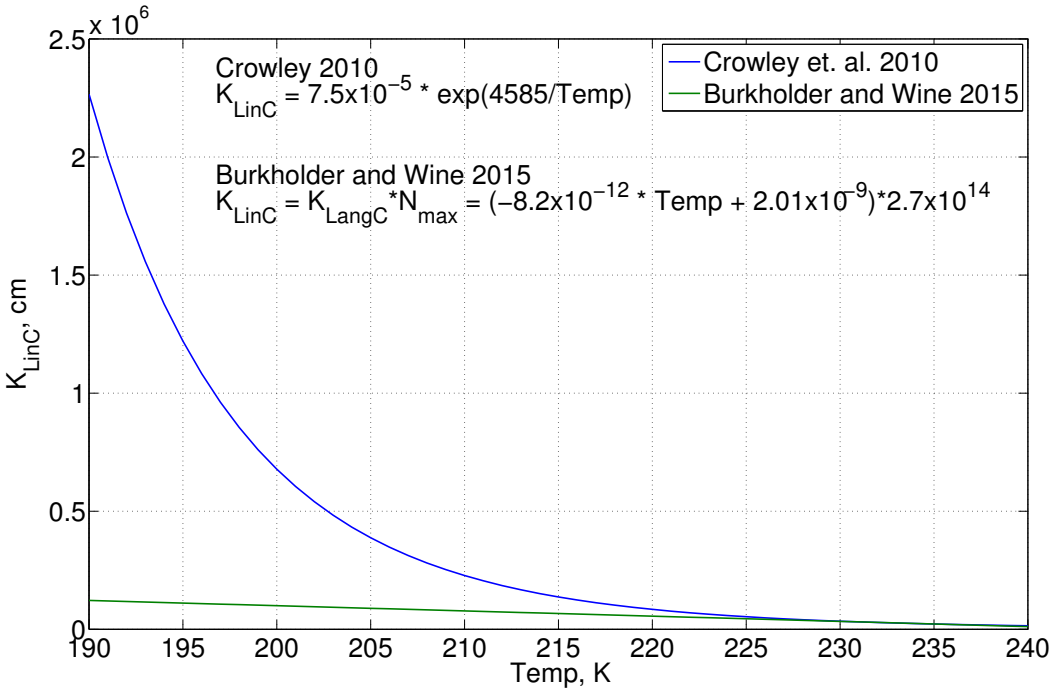


**Figure A2.** Langmuir adsorption equilibrium constant, $K_{\mathrm{LinC}} = K_{eq} \times N_{\max}$. The preferred temperature range for both parameterisation is 214-240 K and within this range the two parameterisations provide a comparable value. The Crowley et al. (2010) parameterisation deviate from the Burkholder and Wine (2015) parameterisation as temperature drop below 214 K due to the exponential temperature term. Here, the parameterisation from Burkholder and Wine (2015) was chosen based on the extreme cold temperature found in our validation sites (minimum winter temperature at Dome C is $\sim$ 199 K, Erbland et al., 2013).

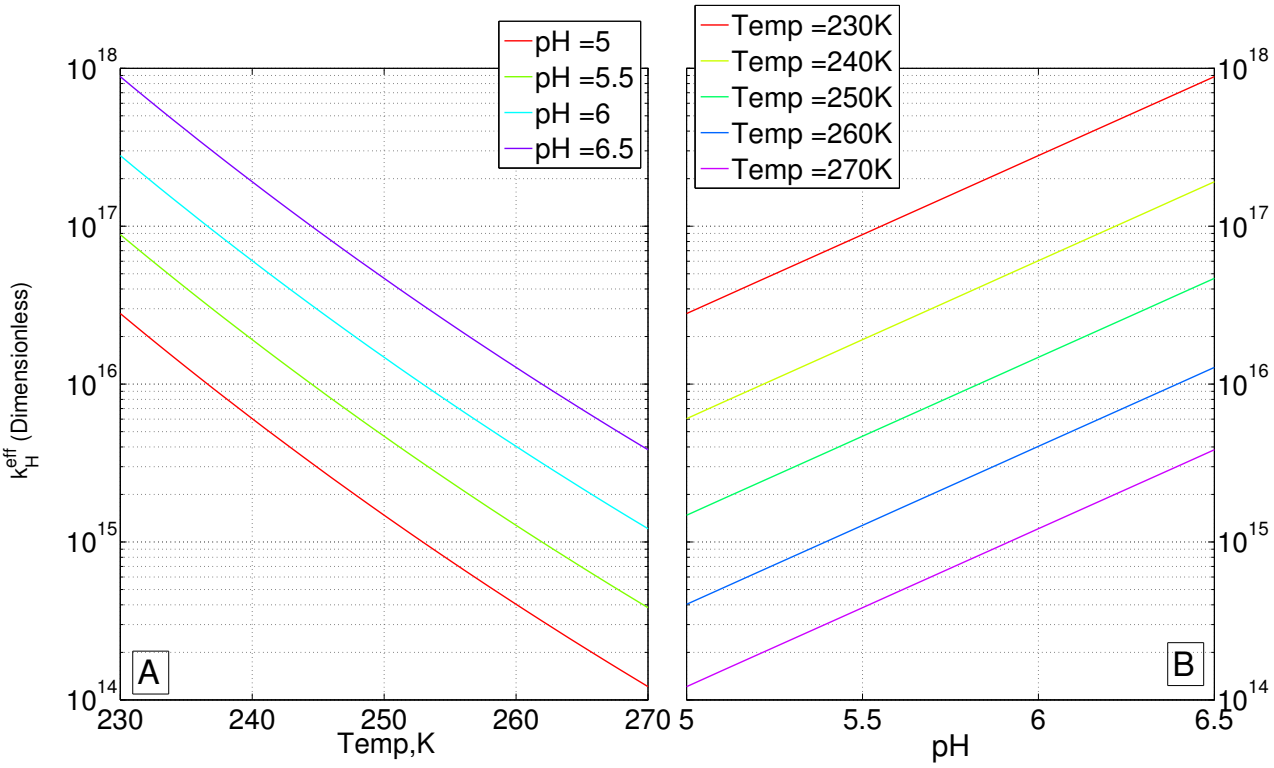


**Figure A3.** The dependence of the effective Henry's Law coefficient, $k_{\mathrm{H^{eff}}}$, of $\mathrm{HNO_3}$ on (A) temperature and (B) pH

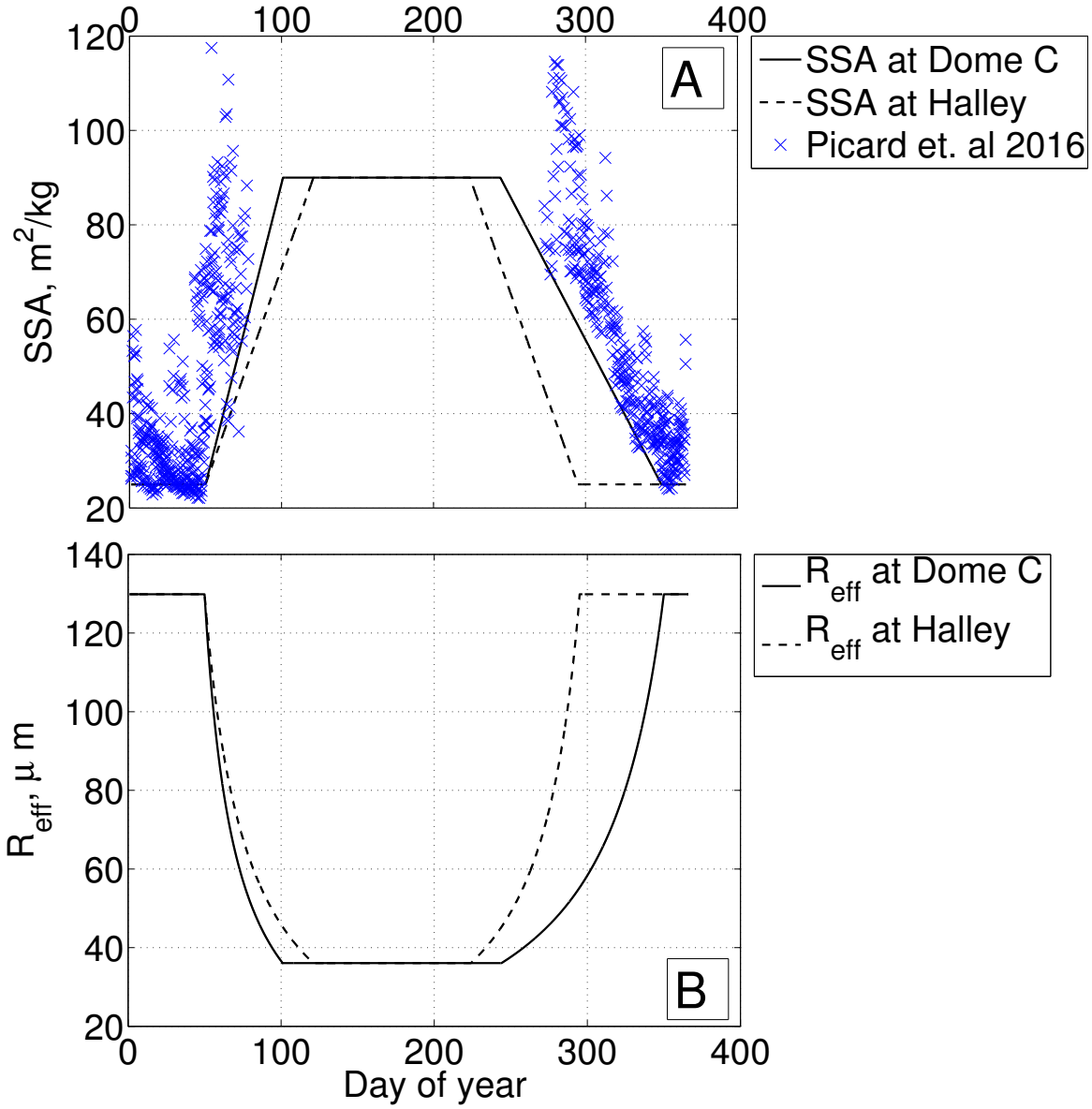


**Figure A4.** (**A**) Year-round estimates of the specific surface area (SSA) of snow at Dome C (−) and Halley (−−) were interpolated from observations at Dome C during 2012-2015 by Picard et al. (2016) (×). The SSA estimates for Halley take into account the shorter cold period compare to Dome C, which tends to have larger SSA. (**B**) Year-round estimates of effective grain radius ($R_{\mathrm{eff}}$) at Dome C (−) and Halley (−−) derived from Eq. 6.

## Appendix B: Derivation for non-equilibrium kinetics

The processes involved in the equilibrium of the gas-phase and the surface of a droplet (Fig. A5): 1) Gas-phase diffusion from far away (> μm) from the droplet to the surface of the droplet, which is likely to be driven by turbulence and molecular diffusion; 2) Interfacial mass transport; and 3) Condensed-phase diffusion and chemical reactions;

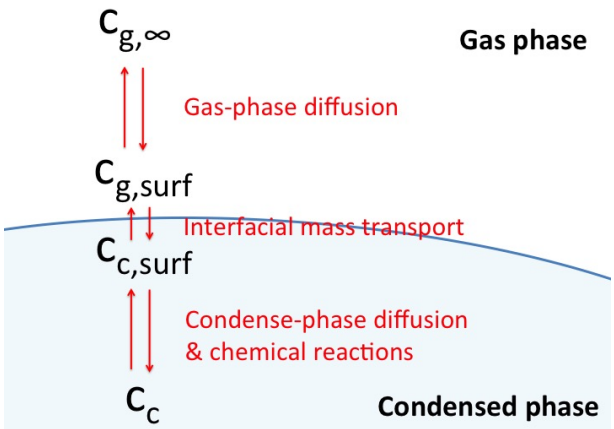


**Figure A5.** Processes involve in the equilibrium between gas-phase and condensed-phase, where $c_{g,\infty}$ is the gas-phase concentration in the snow interstitial air far away from the droplet, $c_{g,\mathrm{surf}}$ is the gas-phase concentration at the surface (outside the droplet), $c_{c,\mathrm{surf}}$ is the condensed-phase concentration at the surface (inside the droplet) and $c_c$ is the average condensed-phase concentration.

Transport of gas-phase species from the snow interstitial air to the surface of the droplet can be described using Fick's law as diffusion flux, $J_g$:

$$J_g = -D_g \frac{dc_g}{dx} \tag{B1}$$

where $D_g$ is the gas-phase diffusivity, and $\frac{dc}{dx}$ is the concentration gradient at the droplet surface that $\frac{dc_g}{dx} = \frac{c_{g,\infty} - c_{g,\mathrm{surf}}}{R_{\mathrm{eff}}}$ with $R_{\mathrm{eff}}$ as the radius of the droplet. The concentration change in the condense-phase can be expressed as

$$\frac{dc_c}{dt} = \frac{A\,J_g}{V} = -\frac{A}{V}\frac{D_g}{R_{\mathrm{eff}}}(c_{g,\infty} - c_{g,\mathrm{surf}}) \tag{B2}$$

where $A$ is the surface area of the droplet and $V$ is the volume of the droplet. The first-order rate coefficient for the gas-phase diffusion process can be defined as $k_{dg} = \frac{A}{V}\frac{D_g}{R_{\mathrm{eff}}}$ (Sander, 1999). For an example, a liquid droplet with a radius $R_{\mathrm{eff}}$ the gas-phase diffusion rate coefficient $k_{dg} = \frac{3D_g}{R_{\mathrm{eff}}^2}$.

The interfacial mass transport from gas-phase to condensed-phase can be expressed in terms of accommodation coefficient, $\alpha$. The flux through the phase boundary into the droplet, $J_b^{in}$, is defined as:

$$J_b^{in} = \frac{\alpha \bar{v}}{4} c_{g,\mathrm{surf}} \tag{B3}$$

where the subscript $b$ stands for 'boundary' and $\bar{v}$ is the mean molecular velocity. The opposite flux, $J_b^{out}$, through the phase boundary out of the droplet can be expressed in the similar form as Eq. B3 that $J_b^{out} = \frac{\alpha_a \bar{v_c}}{4} c_{a,\mathrm{surf}}$, where $\bar{v_c}$ is the mean molecular velocity in condensed-phase and $\alpha_c$ is the condensed-phase accommodation coefficient. The net flux through the grain boundary, $J_b$, is the difference between the in and out flux.

$$J_b = J_b^{in} - J_b^{out} = \frac{\alpha \bar{v}}{4} \left( \frac{c_{c,\mathrm{surf}}}{K} - c_{g,\mathrm{surf}} \right) \tag{B4}$$

where $K$ is the equilibrium constant, of which $K = c_{c,\mathrm{surf}}^{eq} / c_{g,\mathrm{surf}}^{eq}$. For example, for a gas-aqueous interface, the ratio of aqueous-phase concentration to gas-phase concentration at equilibrium can be described as $c_{a,\mathrm{surf}}^{eq} / c_{g,\mathrm{surf}}^{eq} = k_H^{cc}$, where $c_{a,\mathrm{surf}}$ is the aqueous-phase concentration at the surface and $k_H^{cc}$ is the Henry's constant. The concentration change in the condensed phase due to interfacial mass transport can be expressed as:

$$\frac{dc_c}{dt} = -\frac{A\,J_b}{V} = \frac{A}{V} \frac{\alpha \bar{v}}{4} \left( c_{g,\mathrm{surf}} - \frac{c_{c,\mathrm{surf}}}{K} \right) \tag{B5}$$

The first-order rate coefficient for the interfacial mass transport, $k_b$, to a droplet with a radius $R_{\mathrm{eff}}$ can then be defined as $k_b = \frac{3\alpha\bar{v}}{4} R_{\mathrm{eff}}$. By assuming the fluxes of gas-phase diffusion, $J_g$, is equal to the interfacial mass transport, $J_b$, the rate of change of concentration in the condensed phase can be expressed as

$$\frac{dc_c}{dt} = \frac{A}{V} \left( \frac{R_{\mathrm{eff}}}{D_g} + \frac{4}{\bar{v}\alpha} \right)^{-1} \left[ c_{g,\infty} - \frac{c_{c,\mathrm{surf}}}{K} \right] \tag{B6}$$

the term ' $\frac{A}{V} \left( \frac{R_{\mathrm{eff}}}{D_g} + \frac{4}{\bar{v}\alpha} \right)^{-1}$' is often referred as the mass transfer coefficient, $k_{mt}$, for a chemical species transfer from air to liquid/solid. The mass transfer coefficient for chemical into a spherical droplet with radius $R_{\mathrm{eff}}$ is $k_{mt} = (\frac{r^2}{3D_g} + \frac{4R_{\mathrm{eff}}}{3\bar{v}\alpha})^{-1}$ and if the surface of the droplet is described as DI then the concentration at the grain surface, $c_{c,\mathrm{surf}}$ = [$\mathrm{HNO_{3,DI}}$].

## References


Abbatt, Jonathan P. D.: Interaction of HNO3 with water-ice surfaces at temperatures of the free troposphere, Geophysical Research Letters, 24, 1479–1482, doi:10.1029/97GL01403, http://dx.doi.org/10.1029/97GL01403, 1997.

Akinfiev, N. N., Mironenko, M. V., and Grant, S. A.: Thermodynamic Properties of NaCl Solutions at Subzero Temperatures, Journal of Solution Chemistry, 30, 1065–1080, doi:10.1023/A:1014445917207, http://dx.doi.org/10.1023/A:1014445917207, 2001.

Ammann, M., Cox, R. A., Crowley, J. N., Jenkin, M. E., Mellouki, A., Rossi, M. J., Troe, J., and Wallington, T. J.: Evaluated kinetic and photochemical data for atmospheric chemistry: Volume VI ? heterogeneous reactions with liquid substrates, Atmospheric Chemistry and Physics, 13, 8045–8228, doi:10.5194/acp-13-8045-2013, http://www.atmos-chem-phys.net/13/8045/2013/, 2013.

Argentini, S., Pietroni, I., Mastrantonio, G., Viola, A. P., Dargaud, G., and Petenko, I.: Observations of near surface wind speed, temperature and radiative budget at Dome C, Antarctic Plateau during 2005, Antarctic Science, 26, 104–112, doi:10.1017/S0954102013000382, 2014.

Arthern, R. J., Winebrenner, D. P., and Vaughan, D. G.: Antarctic snow accumulation mapped using polarization of 4.3-cm wavelength microwave emission, Journal of Geophysical Research: Atmospheres, 111, n/a–n/a, doi:10.1029/2004JD005667, http://dx.doi.org/10.1029/2004JD005667, d06107, 2006.

Bartels-Rausch, T., Jacobi, H.-W., Kahan, T. F., Thomas, J. L., Thomson, E. S., Abbatt, J. P. D., Ammann, M., Blackford, J. R., Bluhm, H., Boxe, C., Domine, F., Frey, M. M., Gladich, I., Guzmán, M. I., Heger, D., Huthwelker, T., Klán, P., Kuhs, W. F., Kuo, M. H., Maus, S., Moussa, S. G., McNeill, V. F., Newberg, J. T., Pettersson, J. B. C., Roeselová, M., and Sodeau, J. R.: A review of air ice chemical and physical interactions (AICI): liquids, quasi-liquids, and solids in snow, Atmospheric Chemistry and Physics, 14, 1587–1633, doi:10.5194/acp-14-1587-2014, http://www.atmos-chem-phys.net/14/1587/2014/, 2014.

Beine, H. J., Honrath, R. E., DominÈ, F., Simpson, W. R., and Fuentes, J. D.: NOx during background and ozone depletion periods at Alert: Fluxes above the snow surface, Journal of Geophysical Research: Atmospheres, 107, ACH 7–1–ACH 7–12, doi:10.1029/2002JD002082, http://dx.doi.org/10.1029/2002JD002082, 4584, 2002.

Beine, H. J., DominÈ, F., Ianniello, A., Nardino, M., Allegrini, I., Teinilä, K., and Hillamo, R.: Fluxes of nitrates between snow surfaces and the atmosphere in the European high Arctic, Atmospheric Chemistry and Physics, 3, 335–346, doi:10.5194/acp-3-335-2003, http://www.atmos-chem-phys.net/3/335/2003/, 2003.

Beyer, K. D., , and Hansen, A. R.: Phase Diagram of the Nitric Acid/Water System: Implications for Polar Stratospheric Clouds, The Journal of Physical Chemistry A, 106, 10 275–10 284, doi:10.1021/jp025535o, http://dx.doi.org/10.1021/jp025535o, 2002.

Bock, J., Savarino, J., and Picard, G.: Air–snow exchange of nitrate: a modelling approach to investigate physicochemical processes in surface snow at Dome C, Antarctica, Atmospheric Chemistry and Physics, 16, 12 531–12 550, doi:10.5194/acp-16-12531-2016, http://www.atmos-chem-phys.net/16/12531/2016/, 2016.

Boxe, C. S. and Saiz-Lopez, A.: Multiphase modeling of nitrate photochemistry in the quasi-liquid layer (QLL): implications for $NO_x$ release from the Arctic and coastal Antarctic snowpack, Atmospheric Chemistry and Physics, 8, 4855–4864, doi:10.5194/acp-8-4855-2008, http://www.atmos-chem-phys.net/8/4855/2008/, 2008.

Brimblecombe, P. and Clegg, S. L.: The solubility and behaviour of acid gases in the marine aerosol, Journal of Atmospheric Chemistry, 7, 1–18, doi:10.1007/BF00048251, http://dx.doi.org/10.1007/BF00048251, 1988.

Burkholder,J. B. , Sander, S. P. , Abbatt, J. P., Barker, J. R., Huie, R. E., Kolb, C. E., Kurylo, M. J., Orkin, V. L., Wilmouth, D. M., Wine, P. H. : Chemical Kinetics and Photochemical Data for Use in Atmospheric Studies, Evaluation No. 18, JPL Publication 15-10, Jet Propulsion Laboratory, Pasadena, 2015.

Cho, H., Shepson, P. B., Barrie, L. A., Cowin, J. P., Zaveri, R.: NMR Investigation of the QuasiBrine Layer in Ice/Brine Mixtures, The Journal of Physical Chemistry B, 106, 11 226–11 232, doi:10.1021/jp020449, http://dx.doi.org/10.1021/jp020449+, 2002.

Conde, M. M., Vega, C., and Patrykiejew, A.: The thickness of a liquid layer on the free surface of ice as obtained from computer simulation, The Journal of Chemical Physics, 129, 014702, doi:http://dx.doi.org/10.1063/1.2940195, http://scitation.aip.org/content/aip/journal/jcp/129/1/10.1063/1.2940195, 2008.

Cox, R. A., Fernandez, M. A., Symington, A., Ullerstam, M., and Abbatt, J. P. D.: A kinetic model for uptake of HNO3 and HCl on ice in a coated wall flow system, Phys. Chem. Chem. Phys., 7, 3434–3442, doi:10.1039/B506683B, http://dx.doi.org/10.1039/B506683B, 2005.

Crowley, J. N., Ammann, M., Cox, R. A., Hynes, R. G., Jenkin, M. E., Mellouki, A., Rossi, M. J., Troe, J., and Wallington, T. J.: Evaluated kinetic and photochemical data for atmospheric chemistry: Volume V heterogeneous reactions on solid substrates, Atmospheric Chemistry and Physics, 10, 9059–9223, doi:10.5194/acp-10-9059-2010, http://www.atmos-chem-phys.net/10/9059/2010/, 2010.

Dash, J. G., Rempel, A. W. and Wettlaufer, J. S.:The physics of premelted ice and its geophysical consequences, Rev. Mod. Phys., 78, 695 – 741, doi:10.1103/RevModPhys.78.695, https://link.aps.org/doi/10.1103/RevModPhys.78.695, 2006.

Dasgupta, P. K., Campbell, S. W., Al-Horr, R. S., Ullah, S. R., Li, J., Amalfitano, C., and Poor, N. D.: Conversion of sea salt aerosol to NaNO3 and the production of HCl: Analysis of temporal behavior of aerosol chloride/nitrate and gaseous HCl/HNO3 concentrations with {AIM}, Atmospheric Environment, 41, 4242 – 4257, doi:http://dx.doi.org/10.1016/j.atmosenv.2006.09.054, http://www.sciencedirect.com/science/article/pii/S1352231006012921, (BRACE)Bay Region Atmospheric Chemistry Experiment, 2007.

Domine, F., Bock, J., Voisin, D., and Donaldson, D. J.: Can We Model Snow Photochemistry? Problems with the Current Approaches, The Journal of Physical Chemistry A, 117, 4733–4749, doi:10.1021/jp3123314, http://dx.doi.org/10.1021/jp3123314, pMID: 23597185, 2013.

Erbland, J., Vicars, W. C., Savarino, J.,Morin, S., Frey, M. M., Frosini, D., Vince, E., Martins, J. M. F.: Air snow transfer of nitrate on the East Antarctic Plateau Part 1: Isotopic evidence for a photolytically driven dynamic equilibrium in summer , Atmospheric Chemistry and Physics, 13, 6403–6419, doi:10.5194/acp-13-6403-2013, http://www.atmos-chem-phys.net/13/6403/2013/, 2013.

Finlayson-Pitts, B. J. and Jr., J. N. P.: {CHAPTER} 5 - Kinetics and Atmospheric Chemistry, in: Chemistry of the Upper and Lower Atmosphere, edited by Finlayson-Pitts, B. J. and Pitts, J. N., pp. 130 – 178, Academic Press, San Diego, doi:http://dx.doi.org/10.1016/B978-012257060-5/50007-1, http://www.sciencedirect.com/science/article/pii/B9780122570605500071, 2000.

Fowler, D., Amann, M., Anderson, F., Ashmore, M., Cox, P., Depledge, M., Derwent, D., Grennfelt, P., Hewitt, N., Hov, O., Jenkin, M., Kelly, F., Liss, P. S., Pilling, M., Pyle, J., Slingo, J. and Stevenson, D.: Ground-level

ozone in the 21st century: future trends, impacts and policy implications, vol. 15/08 of *Science Policy*, The Royal Society, London, http://nora.nerc.ac.uk/8577/, prof. David Fowler was Chair of the Working Group, 2008.

France, J. L., King, M. D., Frey, M. M., Erbland, J., Picard, G., Preunkert, S., MacArthur, A., and Savarino, J.: Snow optical properties at Dome C (Concordia), Antarctica; implications for snow emissions and snow chemistry of reactive nitrogen, Atmospheric Chemistry and Physics, 11, 9787–9801, doi:10.5194/acp-11-9787-2011, http://www.atmos-chem-phys.net/11/9787/2011/, 2011.

Frey, M. M., Savarino, J., Morin, S., Erbland, J., and Martins, J. M. F.: Photolysis imprint in the nitrate stable isotope signal in snow and atmosphere of East Antarctica and implications for reactive nitrogen cycling, Atmospheric Chemistry and Physics, 9, 8681–8696, doi:10.5194/acp-9-8681-2009, http://www.atmos-chem-phys.net/9/8681/2009/, 2009.

Frey, M. M., Brough, N., France, J. L., Anderson, P. S., Traulle, O., King, M. D., Jones, A. E., Wolff, E. W., and Savarino, J.: The diurnal variability of atmospheric nitrogen oxides (NO and $NO_2$) above the Antarctic Plateau driven by atmospheric stability and snow emissions, Atmospheric Chemistry and Physics, 13, 3045–3062, doi:10.5194/acp-13-3045-2013, http://www.atmos-chem-phys.net/13/3045/2013/, 2013.

Flanner, M. G. and Zender, C. S.: Linking snowpack microphysics and albedo evolution, Journal of Geophysical Research: Atmospheres, 111, n/a–n/a, doi:10.1029/2005JD006834, http://dx.doi.org/10.1029/2005JD006834, d12208, 2006.

Gligorovski, S., Strekowski, R., Barbati, S., and Vione, D.: Environmental Implications of Hydroxyl Radicals (OH), Chemical Reviews, 115, 13 051–13 092, doi:10.1021/cr500310b, http://dx.doi.org/10.1021/cr500310b, pMID: 26630000, 2015.

Grannas, A. M., Jones, A. E., Dibb, J., Ammann, M., Anastasio, C., Beine, H. J., Bergin, M., Bottenheim, J., Boxe, C. S., Carver, G., Chen, G., Crawford, J. H., Dominé, F., Frey, M. M., Guzmán, M. I., Heard, D. E., Helmig, D., Hoffmann, M. R., Honrath, R. E., Huey, L. G., Hutterli, M., Jacobi, H. W., Klán, P., Lefer, B., McConnell, J., Plane, J., Sander, R., Savarino, J., Shepson, P. B., Simpson, W. R., Sodeau, J. R., von Glasow, R., Weller, R., Wolff, E. W., and Zhu, T.: An overview of snow photochemistry: evidence, mechanisms and impacts, Atmospheric Chemistry and Physics, 7, 4329–4373, doi:10.5194/acp-7-4329-2007, http://www.atmos-chem-phys.net/7/4329/2007/, 2007.

Honrath, R. E., Peterson, M. C., Dziobak, M. P., Dibb, J. E., Arsenault, M. A., and Green, S. A.: Release of NOx from sunlight-irradiated midlatitude snow, Geophysical Research Letters, 27, 2237–2240, doi:10.1029/1999GL011286, http://dx.doi.org/10.1029/1999GL011286, 2000.

Hudson, P. K., Zondlo, M. A., , and Tolbert*, M. A.: The Interaction of Methanol, Acetone, and Acetaldehyde with Ice and Nitric Acid-Doped Ice: Implications for Cirrus Clouds, The Journal of Physical Chemistry A, 106, 2882–2888, doi:10.1021/jp012718m, http://dx.doi.org/10.1021/jp012718m, 2002.

Huthwelker, T. , Malmström, M. E., Helleis, F. , Moortgat, G. K. and Peter, T.: , Kinetics of HCl Uptake on Ice at 190 and 203 K: Implications for the Microphysics of the Uptake Process, The Journal of Physical Chemistry A, 30, 6302–6318, doi:10.1021/jp0309623, http://dx.doi.org/10.1021/jp0309623, 2004.

Huthwelker, T. and Ammann, M. and Peter, T.: , The Uptake of Acidic Gases on Ice, Chemical Reviews, 106, 1375-1444, doi:10.1021/cr020506v, http://dx.doi.org/10.1021/cr020506v, 2006.

Hutterli, M. A. and Röthlisberger, R.: Atmosphere-to-snow-to-firn transfer studies of HCHO at Summit, Greenland, GEOPHYSICAL RESEARCH LETTERS, 26, 1691–1694, 1999.

Hutterli, M. A., McConnell, J. R., Bales, R. C., and Stewart, R. W.: Sensitivity of hydrogen peroxide (H2O2) and formaldehyde (HCHO) preservation in snow to changing environmental conditions: Implications for ice core records, Journal of Geophysical Research: Atmospheres, 108, ACH 6–1–ACH 6–9, doi:10.1029/2002JD002528, http://dx.doi.org/10.1029/2002JD002528, 4023, 2003.

Jacobson, M. Z.: Fundamentals of Atmospheric Modeling, Cambridge University Press, https://books.google.co.uk/books?id=96wWzoyKRMoC, 2005.

Jones, A. E., Weller, R., Anderson, P. S., Jacobi, H.-W., Wolff, E. W., Schrems, O., and Miller, H.: Measurements of NOx emissions from the Antarctic snowpack, Geophysical Research Letters, 28, 1499–1502, doi:10.1029/2000GL011956, http://dx.doi.org/10.1029/2000GL011956, 2001.

Jones, A. E., Wolff, E. W., Salmon, R. A., Bauguitte, S. J.-B., Roscoe, H. K., Anderson, P. S., Ames, D., Clemitshaw, K. C., Fleming, Z. L., Bloss, W. J., Heard, D. E., Lee, J. D., Read, K. A., Hamer, P., Shallcross, D. E., Jackson, A. V., Walker, S. L., Lewis, A. C., Mills, G. P., Plane, J. M. C., Saiz-Lopez, A., Sturges, W. T., and Worton, D. R.: Chemistry of the Antarctic Boundary Layer and the Interface with Snow: an overview of the CHABLIS campaign, Atmospheric Chemistry and Physics, 8, 3789–3803, doi:10.5194/acp-8-3789-2008, http://www.atmos-chem-phys.net/8/3789/2008/, 2008.

Jones, A. E., Wolff, E. W., Ames, D., Bauguitte, S. J.-B., Clemitshaw, K. C., Fleming, Z., Mills, G. P., Saiz-Lopez, A., Salmon, R. A., Sturges, W. T., and Worton, D. R.: The multi-seasonal $NO_y$ budget in coastal Antarctica and its link with surface snow and ice core nitrate: results from the CHABLIS campaign, Atmospheric Chemistry and Physics, 11, 9271–9285, doi:10.5194/acp-11-9271-2011, http://www.atmos-chem-phys.net/11/9271/2011/, 2011.

Jourdain, B., Preunkert, S., Cerri, O., Castebrunet, H, Udisti, R. and Legrand, M.: Year-round record of size-segregated aerosol composition in central Antarctica (Concordia station): Implications for the degree of fractionation of sea-salt particles, Journal of Geophysical Research: Atmospheres, 113, D14308, doi:10.1029/2007JD009584 , http://dx.doi.org/10.1029/2007JD009584, 2008.

Kuo, M. H., Moussa, S. G., and McNeill, V. F.: Modeling interfacial liquid layers on environmental ices, Atmospheric Chemistry and Physics, 11, 9971–9982, doi:10.5194/acp-11-9971-2011, http://www.atmos-chem-phys.net/11/9971/2011/, 2011.

Legrand, M., Yang, X., Preunkert, S., and Theys, N.: Year-round records of sea salt, gaseous, and particulate inorganic bromine in the atmospheric boundary layer at coastal (Dumont d'Urville) and central (Concordia) East Antarctic sites, Journal of Geophysical Research: Atmospheres, 121, 997–1023, doi:10.1002/2015JD024066, http://dx.doi.org/10.1002/2015JD024066, 2015JD024066, 2016.

McConnell, J. R., Bales, R. C., Stewart, R. W., Thompson, A. M., Albert, M. R., and Ramos, R.: Physically based modeling of atmosphere-to-snow-to-firn transfer of H2O2 at South Pole, Journal of Geophysical Research: Atmospheres, 103, 10 561–10 570, doi:10.1029/98JD00460, http://dx.doi.org/10.1029/98JD00460, 1998.

McNeill, V. F., Grannas, A. M., Abbatt, J. P. D., Ammann, M., Ariya, P., Bartels-Rausch, T., Domine, F., Donaldson, D. J., Guzman, M. I., Heger, D., Kahan, T. F., Klán, P., Masclin, S., Toubin, C., and Voisin, D.:

Organics in environmental ices: sources, chemistry, and impacts, Atmospheric Chemistry and Physics, 12, 9653–9678, doi:10.5194/acp-12-9653-2012, http://www.atmos-chem-phys.net/12/9653/2012/, 2012.

Morin, S., Savarino, J., Frey, M. M., Yan, N., Bekki, S., Bottenheim, J. W., and Martins, J. M. F.: Tracing the Origin and Fate of NOx in the Arctic Atmosphere Using Stable Isotopes in Nitrate, Science, 322, 730–732, doi:10.1126/science.1161910, http://science.sciencemag.org/content/322/5902/730, 2008.

Murray, K. A., Kramer, L. J., Doskey, P. V., Ganzeveld, L., Seok, B., Dam, B. V., and Helmig, D.: Dynamics of ozone and nitrogen oxides at Summit, Greenland. II. Simulating snowpack chemistry during a spring high ozone event with a 1-D process-scale model, Atmospheric Environment, 117, 110 – 123, doi:http://dx.doi.org/10.1016/j.atmosenv.2015.07.004, http://www.sciencedirect.com/science/article/pii/S135223101530203X, 2015.

Picard, G., Libois, Q., Arnaud, L., Vérin, G., and Dumont, M.: Time-series of snow spectral albedo and superficial snow specific surface area at Dome C in Antarctica, 2012-2015, doi:10.1594/PANGAEA.860945, https://doi.pangaea.de/10.1594/PANGAEA.860945, supplement to: Picard, G et al. (2016): Development and calibration of an automatic spectral albedometer to estimate near-surface snow SSA time series. The Cryosphere, 10(3), 1297-1316, doi:10.5194/tc-10-1297-2016, 2016.

Pinzer, B. R., Schneebeli, M., and Kaempfer, T. U.: Vapor flux and recrystallization during dry snow metamorphism under a steady temperature gradient as observed by time-lapse micro-tomography, The Cryosphere, 6, 1141–1155, doi:10.5194/tc-6-1141-2012, http://www.the-cryosphere.net/6/1141/2012/, 2012.

Press, .W. H, Teukolsky, S. A., Vetterling, W. T., F.lannery, B. P.: Numerical Recipe in Fortran 90, Cambridge Univeristy Press, 2 edn., 1996.

Pruppacher, H. R. and Klett, James D., .: Microphysics of clouds and precipitation, Dordrecht ; Boston : Kluwer Academic Publishers, 2nd rev. and enl. ed edn., "With an introduction to cloud chemistry and cloud electricity.", 1997.

Rankin, A. M. and Wolff, E. W.: A year-long record of size-segregated aerosol composition at Halley, Antarctica, Journal of Geophysical Research: Atmospheres, 108, D24, 4775 doi:10.1029/2003JD003993, http://dx.doi.org/10.1029/2003JD003993, 2003.

Röthlisberger, R., Hutterli, M. A., Sommer, S., Wolff, E. W., and Mulvaney, R.: Factors controlling nitrate in ice cores: Evidence from the Dome C deep ice core, Journal of Geophysical Research: Atmospheres, 105, 20 565–20 572, doi:10.1029/2000JD900264, http://dx.doi.org/10.1029/2000JD900264, 2000.

Sander, R.: Modeling Atmospheric Chemistry: Interactions between Gas-Phase Species and Liquid Cloud/Aerosol Particles, Surveys in Geophysics, 20, 1–31, doi:10.1023/A:1006501706704, http://dx.doi.org/10.1023/A:1006501706704, 1999.

Sander, R.: Compilation of Henry's law constants (version 4.0) for water as solvent, Atmospheric Chemistry and Physics, 15, 4399–4981, doi:10.5194/acp-15-4399-2015, http://www.atmos-chem-phys.net/15/4399/2015/, 2015.

Sazaki, G, and Zepeda S, Nakatsubo S, Yokomine. M. Furukawa. Y.: Quasi-liquid layers on ice crystal surfaces are made up of two different phases, Proc Natl Acad Sci U S A., 4, 1052–1055, doi:10.1073/pnas.1116685109, 2012.

Tang, M. J., Cox, R. A., and Kalberer, M.: Compilation and evaluation of gas phase diffusion coefficients of reactive trace gases in the atmosphere: volume 1. Inorganic compounds, Atmospheric Chemistry and Physics, 14, 9233–9247, doi:10.5194/acp-14-9233-2014, http://www.atmos-chem-phys.net/14/9233/2014/, 2014.

Thibert, E., , and Dominé, F.: Thermodynamics and Kinetics of the Solid Solution of HNO3 in Ice, The Journal of Physical Chemistry B, 102, 4432–4439, doi:10.1021/jp980569a, http://dx.doi.org/10.1021/jp980569a, 1998.

Thomas, J. L., Stutz, J., Lefer, B., Huey, L. G., Toyota, K., Dibb, J. E., and von Glasow, R.: Modeling chemistry in and above snow at Summit, Greenland? Part 1: Model description and results, Atmospheric Chemistry and Physics, 11, 4899–4914, doi:10.5194/acp-11-4899-2011, http://www.atmos-chem-phys.net/11/4899/2011/, 2011.

Toyota, K., McConnell, J. C., Staebler, R. M., and Dastoor, A. P.: Air-snowpack exchange of bromine, ozone and mercury in the springtime Arctic simulated by the 1-D model PHANTAS - Part 1 In-snow bromine activation and its impact on ozone, Atmospheric Chemistry and Physics, 14, 4101–4133, doi:10.5194/acp-14-4101-2014, http://www.atmos-chem-phys.net/14/4101/2014/, 2014.

Traversi, R., Udisti, R., Frosini, D., Becagli, S., Ciardini, V., Funke, B., Lanconelli, C., Petkov, B., Scarchilli, C., Severi, M., and Vitale, V.: Insights on nitrate sources at Dome C (East Antarctic Plateau) from multi-year aerosol and snow records, Tellus B, 66, http://www.tellusb.net/index.php/tellusb/article/view/22550, 2014.

Waddington, E. D., Cunningham, J., and Harder, S. L.: The Effects Of Snow Ventilation on Chemical Concentrations, pp. 403–451, Springer Berlin Heidelberg, Berlin, Heidelberg, doi:10.1007/978-3-642-61171-1_18, http://dx.doi.org/10.1007/978-3-642-61171-1_18, 1996.

Wolff, E. W., Jones, A. E., Bauguitte, S. J.-B., and Salmon, R. A.: The interpretation of spikes and trends in concentration of nitrate in polar ice cores, based on evidence from snow and atmospheric measurements, Atmospheric Chemistry and Physics, 8, 5627–5634, doi:10.5194/acp-8-5627-2008, http://www.atmos-chem-phys.net/8/5627/2008/, 2008.

Udisti, R., Becagli, S., Benassai, S., Castellano, E., Fattori, I., Innocenti, M., Migliori, A., and Traversi, R.: Atmospheresnow interaction by a comparison between aerosol and uppermost snow-layers composition at Dome C, East Antarctica, Annals of Glaciology, 39, 53–61, doi:doi:10.3189/172756404781814474, http://www.ingentaconnect.com/content/igsoc/agl/2004/00000039/00000001/art00010, 2004.

Ullerstam, M. and Abbatt, J. P. D.: Burial of gas-phase HNO3 by growing ice surfaces under tropospheric conditions, Phys. Chem. Chem. Phys., 7, 3596–3600, doi:10.1039/B507797D, http://dx.doi.org/10.1039/B507797D, 2005a.

Ullerstam, M., Thornberry, T., and Abbatt, J. P. D.: Uptake of gas-phase nitric acid to ice at low partial pressures: evidence for unsaturated surface coverage, Faraday Discuss., 130, 211–226, doi:10.1039/B417418F, http://dx.doi.org/10.1039/B417418F, 2005b.

Yuan-Hui, L. and Gregory, S.: Diffusion of ions in sea water and in deep-sea sediments, Geochimica et Cosmochimica Acta, 38, 703 – 714, doi:http://dx.doi.org/10.1016/0016-7037(74)90145-8, http://www.sciencedirect.com/science/article/pii/0016703774901458, 1974.

# Chapter 5

# Towards a multi-phase 1-D model of air-snow exchange of nitrogen oxides at Dome C, Antarctica

## 5.1 Introduction

Production of nitrogen oxides, $NO_x$ (= NO + $NO_2$) from sunlit snow have been observed in the polar and mid-latitudes as a result of photolysis of nitrate, $NO_3^-$, in snow (Dibb et al., 1998; Honrath et al., 2000; Jones et al., 2001; Beine et al., 2002; Jacobi et al., 2004). The emission of $NO_x$ have a significant impacts on the oxidising capacity, such as the concentration of $O_3$ or OH, in the atmospheric boundary layer, especially in remote high latitude area, such as the polar regions where pollution is less. The interconversion of the $NO_x$, $HO_x$ (= OH + $HO_2$ + $H_2O_2$) and $O_x$ (= $O(^1D)$ + $O(^3P)$ + $O_2$ + $O_3$) are closely linked as shown in Fig. 5.1. The photolysis of $NO_2$ to NO is the major precursor of $O_3$ in the troposphere and, at the same time, NO can reacts with $O_3$ to form back as $NO_2$. The interconversion of $NO_x$ also involves reactions with $HO_x$, which shift the partitioning $HO_x$ radical towards OH via reaction NO + $HO_2$ $\rightarrow$ $NO_2$ + OH. The $NO_x$ cycle determinate when $NO_2$ reacts with OH to form nitric acid ($HNO_3$).

There is a great need to understand more about the interaction of nitrogen species between the atmosphere and snowpack, not only to predict the regional and global chemical transport and climate, but also crucial for interpreting the $NO_3^-$, one of the most preserved chemicals, record in polar ice cores. The physical and chemical depositional and post-depositional processes have a strong influence on the preserved concentrations in snow (Rothlisberger et al., 2000; Frey et al., 2013), therefore, to reconstruct the past

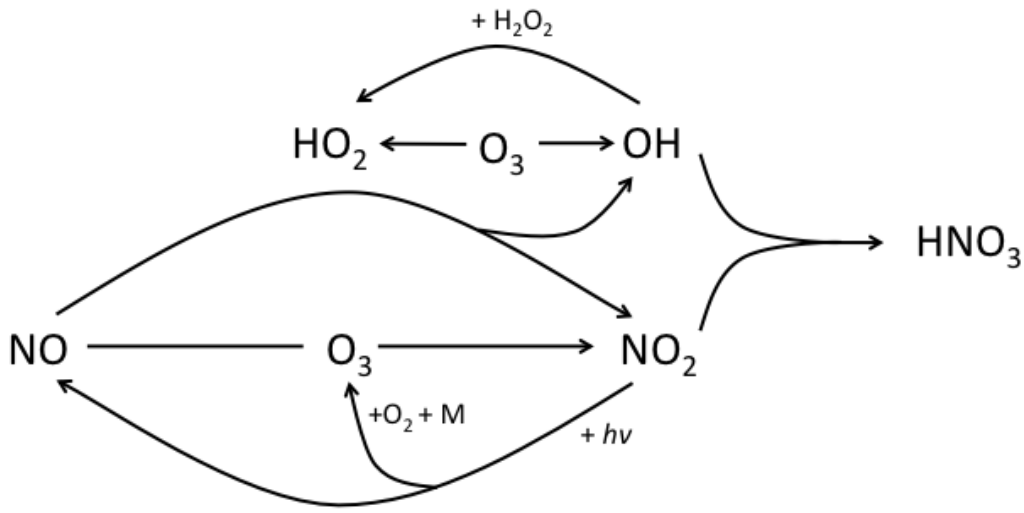


FIGURE 5.1: Reactions involving the cycling of $NO_x$, $HO_x$ and $O_3$.

atmospheric composition from ice core data these processes need to be understood.

The main sources of $NO_x$ in the boundary layer above snow covered remote regions includes long-range transport in the troposphere, downwelling from the stratosphere and recycled from photolysis of $NO_3^-$ in snow as mentioned in Ch. 1. The major pathways for $NO_3^-$ photolysis in snow is to produce $NO_2$ (C1 on Table. 5.4) and the minor pathways is to produce $O(^3P)$ and $NO_2^-$ (C2 on Table. 5.4). The photochemically produced $NO_2^-$ can be further photolysed to produce NO and OH (C3 on Table. 5.4) . The photolysis rate coefficient, $J$, in the snowpack depends on the 1) actinic flux, which is a function of solar zenith angle, depth and optical properties of the snowpack; 2) quantum yield of the photolysis reaction, which is a function of temperature and possibly the location of the $NO_3^-$ molecules within the snow grain; and 3) absorption cross-section. The photochemically produced $NO_x$ can escape the snow grain and released to the snow interstitial air (SIA), and subsequently be transported out of the snowpack to the overlying atmosphere by molecular diffusion and wind pumping (Zatko et al., 2016b).

However, due to the lack of observational constraints, the snow models developed to estimate emission flux and seasonal and diurnal variability are still simplistic in their description of the multiphase physical and chemical processes in the snowpack. Most of the current snow chemistry models have different simplifications and assumptions, such as 1) simplifying the air-snow interface to either 'Air-Ice' (e.g. Hutterli and Rothlisberger, 1999; McConnell et al., 1998; Bock et al., 2016) or 'Air-Liquid' or 'Air-Disordered Interface,

DI' (e.g. Thomas et al., 2011; Toyota et al., 2014); 2) poor constraints on the location/distribution of the solutes within the snow grain, of which have significant impact on the interaction between snow grain and SIA and 3) uncertainties in the quantum yield for photolysis reactions of snow (Honrath et al., 1999; Jones et al., 2000; Beine et al., 2002). These models often require tuning parameters, for example fitting the ion partitioning coefficients (Hutterli and Rothlisberger, 1999), the fraction of solute in DI (Thomas et al., 2011), or the co-condensation parameters (Bock et al., 2016), to match the model output with the observation.

Chan et al. (2016) (Ch. 4 in this thesis) presented a box multi-phase air-snow exchange model of nitrate that was developed from physically-based parameterisations and reproduced with good agreement to observation without requiring any tuning parameters. The temperature-dependent multi-phase exchange model (Model 2 from Chan et al., 2016 ) is based on a hypothesis suggested by Domine et al. (2008) that the air-snow interface is mainly air and ice, and, if liquid co-existed with ice, it will be in the form of liquid-micropocket that located between grain boundaries and triple junctions. They suggested the interaction of nitrate between the air and snow can be described as equilibrium solvation into liquid-micropockets in the summer in Antarctica.

The purpose of this study is to test the hypothesis that $NO_x$ flux out of the snowpack in summer can be attributed to a temperature-dependent exchange of nitrate between micropocket and surrounding air, as presented by Chan et al. (2016). A 1-D air-snowpack model incorporated the multi-phase physical exchange between air and snow grain, heterogeneous chemical mechanism, and vertical mass transport is developed to quantify the emission of $NO_x$ and the dynamic of $NO_x$ and $O_3$ within the snowpack in the summer at the Antarctica. The model is validated with available observation from Dome C, Antarctica.

## 5.2 Modelling Approach

### 5.2.1 Overview

The 1-D model presenting here is to describe the multi-phase air-snow exchange and the vertical transport of trace gases through the porous snowpack to the overlying atmosphere. The focus of this paper is to investigate if the air-snow exchange model of skin-layer snow developed by Chan et al. (2016) can be extended to deeper snow when including photochemistry. The model is constrained by the observed atmospheric concentration of $HNO_3$, skin layer temperature, atmospheric pressure and wind speed. The estimated

emission flux of $NO_x$ is compared to available observed values from Dome C, Antarctica. The model consists of 21 layers representing the top 1 $\mathrm{m}$ of the snowpack. The photolysis rates and the nitrate concentration decreases rapidly with depth, therefore, the top layer has a thickness of 4 $\mathrm{mm}$, then 1 $\mathrm{cm}$ interval until 10 $\mathrm{cm}$ and 10 $\mathrm{cm}$ intervals up to 1 $\mathrm{m}$. The model solves a set of partial differential equation describing the temporal and vertical spatial changes of trace gases concentration in the SIA as well as the condensed phase concentration in the snow:

$$\frac{\partial C_g}{\partial t} = \frac{\partial}{\partial z}\left(D_{\mathrm{eff},z}\frac{\partial C_g}{\partial z}\right) + S_{g,\,z} \tag{5.1}$$

where $C_g$ is the concentration of the gas-phase chemical species of interest, z is the depth of the snowpack, $D_{\mathrm{eff},z}$ is the effective diffusion constant, and $S_{g,\,z}$ is the chemical or physical source or sink term for the gaseous species of each vertical grid, which can be expressed as follows:

$$S_{g,\,z} = P_g - L_g - \phi_{\mathrm{air}}^{\mathrm{H_2O}}\frac{\partial C_{c,mt}}{\partial t} \tag{5.2}$$

where $P_g$ is the gas-phase chemical production at each time step, $L_g$ is the gas-phase chemical loss term at each time step, and the last term '$\phi_{\mathrm{air}}^{\mathrm{H_2O}}\frac{\partial C_{c,mt}}{\partial t}$' is the change in the gas-phase concentration correspond to the physical mass transfer to condensed-phase, i.e. into or out of the snow grain. The volume ratio of water (ice+liquid) to air per unit volume of snowpack, $\phi_{\mathrm{air}}^{\mathrm{H_2O}}$, with units of $\mathrm{m}^3_{\mathrm{H_2O}}\mathrm{m}^{-3}_{\mathrm{air}}$ and is defined as

$$\phi_{\mathrm{air}}^{\mathrm{H_2O}} = \frac{V_{\mathrm{H_2O}}}{V_{\mathrm{air}}} = \frac{\rho_{snow}}{\rho_{ice} - \rho_{snow}} \tag{5.3}$$

where $V_{\mathrm{H_2O}}$ is the volume of water (ice+liquid) per unit volume of snowpack, $V_{\mathrm{air}}$ is the volume of air per unit volume of snowpack, $\rho_{snow}$ and $\rho_{ice}$ is the density of snow and ice respectively. Here, for simplicity, the rate of change in condensed-phase concentration as a result of mass transfer, $\frac{\partial C_{c,mt}}{\partial t}$, is only applicable to $HNO_3$ due to its high solubility in ice (Details in Sect. 5.2.3).

### 5.2.2 Gas Transport in SIA

The effective diffusion constant, $D_{\mathrm{eff},z}$, is to describe the turbulent diffusion of trace gases within the snowpack, which is defined as the sum of both molecular diffusion and wind pumping as follow (Thomas et al., 2011):

$$D_{\mathrm{eff},z} = \tau D_g + U_{\mathrm{firn}}\Delta z \tag{5.4}$$

where $D_g$ is the gas phase diffusion constant in free air ( values of $D_g$ in free air at 296 K for various species are listed in Table. 5.1), $\tau$ is the tortuosity, $\Delta z$ is the vertical grid spacing, and $U_{\text{firn}}$ is the vertical pumping speed, which defines as Cunningham and Waddington (1993)

$$U_{\text{firn}} = \frac{6k\rho_{\text{air}}}{\pi\mu\lambda_{\text{surf}}} \frac{h}{\lambda_{\text{surf}}} \frac{\sqrt{\alpha^2+1}}{\alpha} u_{10}^2 e^{-\frac{z}{\delta}} \tag{5.5}$$

where $k$ is the permeability, $\rho_{\text{air}}$ is the density of air, $\mu$ is the dynamic viscosity of air, $\lambda_{\text{surf}}$ is the relief wavelength, $h$ is the relief amplitude, $\alpha$ is the horizontal aspect ratio of the relief relative to wind direction, $u_{10}$ is the horizontal wind speed at 10 m above the snow surface, and $\delta$ defines as

$$\delta = \frac{1}{2} \frac{\alpha}{\sqrt{\alpha^2+1}} \frac{\lambda_{\text{surf}}}{\pi} \tag{5.6}$$

The values of $\tau$, $\lambda_{\text{surf}}$, $h$, $\alpha$ and parameterisations for $k$ and $\mu$ are listed in Table 5.2.

TABLE 5.1: The gas phase diffusion constant, $D_g$, at 296 K in Torr cm$^2$ s$^{-1}$

| Species | $D_g$ | Reference | Species | $D_g$ | Reference |
|---|---|---|---|---|---|
| NO | 176 | Tang et al. (2014) | OH | 178 | Tang et al. (2014) |
| $NO_2$ | 106 | Tang et al. (2014) | $HO_2$ | 107 | Ivanov et al. (2007) |
| $NO_3$ | 92 | Tang et al. (2014) | $H_2O_2$ | 116 | Tang et al. (2014) |
| $HNO_3$ | 87 | Tang et al. (2014) | $O_3$ | 96.3 | Ivanov et al. (2007) |
| $N_2O_5$ | 65 | Tang et al. (2014) | | | |

### 5.2.3 Exchange Between Air and Snow Grain

Both the chemical and physical processes can change the concentration of condensed-phase species, for example, the rate of change nitrate, $\frac{\partial[\text{NO}_3^-]}{\partial t}$, in a snow grain can be expressed as

$$\frac{\partial[\text{NO}_3^-]}{\partial t} = P_{\text{NO}_3^-} - L_{\text{NO}_3^-} + \frac{\partial[\text{NO}_{3,mt}^-]}{\partial t} \tag{5.7}$$

where $P_{\text{NO}_3^-}$ and $L_{\text{NO}_3^-}$ is the chemical production and loss of $NO_3^-$ at each time step, and $\frac{\partial[\text{NO}_{3,mt}^-]}{\partial t}$ is the rate of change of concentration of $NO_3^-$ as a result of mass transfer to or from gas-phase $HNO_3$. The temperature dependent multi-phase air-snow interaction model, Model 2, in Chan et al. (2016) is incorporated into the 1-D model, which determines the concentration of $NO_3^-$ in snow by non-equilibrium kinetic adsorption on ice and co-condensation

TABLE 5.2: Summary of the performance from different model runs for Dome C along with $C_v$(RMSD)

| Parameter | Symbol | Value/Parameterisation | Units |
|---|---|---|---|
| Tortuosity | $\tau$ | $0.5^{I}$ | - |
| Relief wavelength | $\lambda_{\text{surf}}$ | $3 \times 10^{-2\ II}$ | m |
| Relief amplitude | $h$ | $1.5 \times 10^{-2\ III}$ | m |
| Horizontal Aspect ratio of relief | $\alpha$ | $1^{IV}$ | - |
| Permeability | $k$ | $k = 3R_{\text{eff}}^2\, e^{-0.013\rho_{snow}\ *\ V}$ | $\text{m}^2$ |
| Dynamic viscosity of air | $\mu$ | $\mu = 1.8325 \times 10^{-5}(\frac{416.16}{T+120})(\frac{T}{296.16})^{1.5\ **\ VI}$ | Pa s |

$^{I}$ Albert and Shultz (2002), $^{II}$ Thomas et al. (2011), $^{III}$ Thomas et al. (2011), $^{IV}$ Thomas et al. (2011), $^{V}$ Domine et al. (2013a), $^{VI}$ Jacobson (2005)
$^{*}$ $R_{\text{eff}}$ is the effective radius of the snow grain in m, and $\rho_{snow}$ is the density of the snowpack in $\text{kg m}^{-3}$.
$^{**}$ $T$ is the temperature in K.

couple with solid-state diffusion in ice at all temperatures below the melting temperature. For temperatures higher than the eutectic temperature, $T_e$, liquid co-exists with ice as micropocket, which concentration defined by Henry's Law. The bulk concentration of $NO_3^-$, the concentration of $NO_3^-$ in the melted snow sample, can be expressed as (Chan et al., 2016):

$$[\text{NO}_3^-(t)] = \begin{cases} \frac{\sum[\text{NO}_3^-(r,t)]\,V(r)}{V_{\text{grain}}} & \text{if} \quad T < T_e. \\ \frac{\sum[\text{NO}_3^-(r,t)]\,V(r)}{V_{\text{grain}}} + \phi_{\text{H}_2\text{O}}\, k_{\text{H}}^{\text{eff}}\, [\text{HNO}_{3(\text{g})}(t)] & \text{if} \quad T_e \leq T < T_m. \end{cases} \tag{5.8}$$

where the first term '$\frac{\sum[\text{NO}_3^-(r,t)]\,V(r)}{V_{\text{grain}}}$' is the bulk concentration contributed by the ice-phase $NO_3^-$, of which $[NO_3^-(r,t)]$ is the nitrate concentration of the $r^{th}$ concentric shell of the spherical snow grain at time $t$, $V(r)$ is the volume of each concentric shell of the spherical snow grain, $V_{grain}$ is the total volume of the snow grain. The second term '$\phi_{\text{H}_2\text{O}}\, k_{\text{H}}^{\text{eff}}\, [\text{HNO}_{3(\text{g})}(t)]$' is the bulk concentration contributed by the liquid-phase $NO_3^-$ presented in the micropocket, of which $\phi_{\text{H}_2\text{O}}$ is the liquid water content (volume ratio of liquid water and the snow grain), $k_{\text{H}}^{\text{eff}}$ is the effective Henry's law, $T_e$ is the eutectic temperature of the $H_2O$-$HNO_3$ mixture (230.64 K Beyer et al., 2002), and $T_m$ is the melting temperature.

The snow grain is assumed to be a radially symmetrical sphere with radius, $\mathrm{R_{eff}}$, which is estimated from the specific surface area, SSA, as the follows (Domine et al., 2008):

$$\mathrm{R_{eff}} = \frac{3}{\rho_{ice}\,\mathrm{SSA}} \tag{5.9}$$

of which the volume of snow grain can be calculated as $V_{grain} = \frac{3}{4}\pi \mathrm{R_{eff}}^3$, and the snow grain is divided as 85 evenly spread concentric shells. The liquid water content, $\phi_{\mathrm{H_2O}}$, is a function of bulk ionic concentration ([$H^+$] + [$NO_3{}^-$]) and temperature as follows (Cho et al., 2002):

$$\phi_{\mathrm{H_2O}}(T) = \frac{\overline{m}_{\mathrm{H_2O}} R T_f}{1000 \Delta H_f^0} \left(\frac{T}{T_f - T}\right) \Phi_{\mathrm{bulk}}^{\mathrm{aq}} \left([\mathrm{H^+}] + [\mathrm{NO_3}^-]\right) \tag{5.10}$$

where $\phi_{\mathrm{H_2O}}(T)$ has a unit of $\mathrm{m}^3_{\mathrm{liquid}}\,\mathrm{m}^{-3}_{\mathrm{liquid+solid}}$, $\overline{m}_{\mathrm{H_2O}}$ is the molecular weight of water, $R$ is the ideal gas constant, $T_f$ is the freezing temperature of pure water in K, $\Delta H_f^0$ is the enthalpy of fusion in $\mathrm{J\,mol^{-1}}$ and $\Phi_{\mathrm{bulk}}^{\mathrm{aq}}$ is the fraction of the total solute in the aqueous phase.

### 5.2.4 Chemical Mechanism

A simplified multi-phase chemistry of the $NO_x$-$HO_x$-$O_x$ system is used as the cycle of $NO_x$, $HO_x$, $O_x$ are closely linked (See Introduction). The temperature dependent rate of the gas-phase reactions used are recommended by the 'The Master Chemical Mechanism' website (MCM v3.2, http://mcm.leeds.ac.uk/MCM). The parameterisation of photolysis by MCM is based on calculation at an altitude of 0.5 km and latitude of 45 °N, therefore, not relevant to this application that the photolysis rate constant in the model is computed offline by radiative transfer model TUV (Lee-Taylor and Madronich, 2002). A chemical kinetics solver Kinetic PreProcessor (KPP-2.2, Sandu and Sander, 2006) is used for solving the chemical ordinary differential equations. A full list of reactions included in the model can be found in Table 5.4.

Chan et al. (2015) concluded the photolysis rates within the snowpack in the polar region can be well estimated by the $e$-folding depth, $z_e$. Therefore, the photolysis rate coefficient within the snowpack is parameterised as:

$$J(z) = J(z_0)\exp(-\frac{z - z_0}{z_e}) \tag{5.11}$$

where $J(z)$ is the photolysis rate constant at depth $z$ and $J(z_0)$ is the photolysis rate constant at the surface of the snowpack, i.e. $z_0 = 0\,\mathrm{m}$. The $e$-folding depth for various chemical species are listed in Table 5.3. For chemical species, that are not listed in Table 5.3, the $z_e$ were set to a default value of

10 cm based on values reported by France et al. (2011).

TABLE 5.3: Vales of $e$-folding depth, $z_e$, for chemical species, in cm.

| Species | $z_e$ (cm) | Reference |
|---|---|---|
| $O_3$ | 15 | Murray et al. (2015) |
| $H_2O_2$ | 13.3 | Murray et al. (2015) therein |
| $NO_2$ | 25 | Murray et al. (2015) |
| $NO_3^-$ | 10 | Thomas et al. (2011) |
| $NO_2^-$ | 16.3 | Murray et al. (2015) therein |

The reference photolysis rate constants, $J(z_0)$, at the surface of the snowpack are calculated offline by a radiative transfer model TUV (Lee-Taylor and Madronich, 2002), using an 8-steam DISORT model. The TUV model consists of 72 layers with 1 m spacing for the first 10 m above the snowpack surface and then 10 m intervals until 100 m, 100m intervals up to 1 km, 1 km intervals up to 10 km and 2 km intervals up to 80 km with clear sky, and typical aerosol optical depth found at Dome C, AOD(500 nm) = 0.02 (Tomasi et al., 2007), and Angstrom's parameter, $\alpha$ = 1.6 (Tomasi et al., 2007) are used. Lookup tables of photolysis rate coefficient at the snowpack surface are created for various ozone column values ranging from 200-400 DU with an increment of 50 DU and range of solar zenith angles from 0°-90° with an interval of 1°. The photolysis rate constants above the snowpack are a function of absorption cross-section of the reactant ($\sigma_{\text{abs}}$), the quantum yield of the reaction ($\phi$) and the actinic flux ($I$), which is a function of solar zenith angle ($\theta$):

$$J(z_0) = \int \sigma_{\text{abs}}(\lambda, T)\, \phi(\lambda, T)\, I(\lambda, \theta, z_0) d\lambda \tag{5.12}$$

where $\lambda$ is the wavelength and $T$ is the temperature. The absorption cross-section, $\sigma_{\text{abs}}$, and the values of quantum yield, $\phi$, used are same as referenced in Chan et al. (2015). In this study, it is assumed that all $NO_x$ formed from photolysis of $NO_3^-$ in snow is transferred to SIA as the quantum yield used has taken the recombination chemistry (the cage effect) into account.

TABLE 5.4: List of chemical reactions included in the 1D model

| # | Reactions | n | Rate constants ($(\mathrm{cm^3 molecule^{-1}})^{1-n}\mathrm{s^{-1}}$) | Refs |
|---|---|---|---|---|
| $O_x$ | & $HO_x$ | | | |
| G1 | $O(^1D)^+ O_2 \rightarrow O(^3P) + O_2$ | 2 | $3.2 \times 10^{-11}\exp(67/T)$ | Atkinson et al. (2004) |
| G2 | $O(^1D) + N_2 \rightarrow O(^3P) + N_2$ | 2 | $2 \times 10^{-11}\exp(130/T)$ | Streit et al. (1976) |
| G3 | $O(^1D) + H_2O \rightarrow 2\,OH$ | 2 | $2.14 \times 10^{-10}$ | Atkinson et al. (2004) |
| G4 | $O(^3P) + O_2 + M \rightarrow O_3$ | 2 | $6.0 \times 10^{-34}(T/300)^{-2.6}[O_2]$ | Atkinson et al. (2004) |
| | | 2 | $5.6 \times 10^{-34}(T/300)^{-2.6}[N_2]$ | Atkinson et al. (2004) |
| G5 | $OH + O_3 \rightarrow HO_2$ | 2 | $1.70 \times 10^{-12}\exp(-940/T)$ | Atkinson et al. (2004) |
| G6 | $OH + HO_2 \rightarrow H_2O + O_2$ | 2 | $4.8 \times 10^{-11}\exp(250/T)$ | Atkinson et al. (2004) |
| G7 | $OH + H_2O_2 \rightarrow HO_2 + H_2O$ | 2 | $2.9 \times 10^{-12}\exp(-160/T)$ | Atkinson et al. (2004) |
| G8 | $HO_2 + O_3 \rightarrow OH + 2\,O_2$ | 2 | $2.03 \times 10^{-16}(T/300)^{4.57}\exp(693/T)$ | Atkinson et al. (2004) |
| G9 | $HO_2 + HO_2 \rightarrow H_2O_2 + O_2$ | 2 | $2.20 \times 10^{-13}\exp(600/T)\mathrm{KMT}^a_{06}$ | Atkinson et al., 2004 |
| G10 | $O_3 + h\nu \rightarrow O(^1D)$ | 1 | b | |
| G11 | $O_3 + h\nu \rightarrow O$ | 1 | b | |
| G12 | $H_2O_2 + h\nu \rightarrow 2\,OH$ | 1 | b | |
| $NO_x$ | | | | |
| G13 | $NO + HO_2 \rightarrow NO_2 + OH$ | 2 | $3.45 \times 10^{-12}\exp(270/T)$ | Atkinson et al. (2004) |
| G14 | $NO + O_3 \rightarrow NO_2 + O_2$ | 2 | $1.4 \times 10^{-12}\exp(-1310/T)$ | Atkinson et al. (2004) |
| G15 | $NO + NO_3 \rightarrow NO_2 + NO_2$ | 2 | $1.8 \times 10^{-11}\exp(110/T)$ | Atkinson et al. (2004) |
| G16 | $NO_2 + OH \rightarrow HNO_3$ | 2 | $\mathrm{KMT}^a_{08}$ | |
| G17 | $NO_2 + O_3 \rightarrow NO_3 + O_2$ | 2 | $1.4 \times 10^{-13}\exp(-2470/T)$ | Atkinson et al. (2004) |
| G18 | $NO_2 + NO_3 \rightarrow N_2O_5$ | 2 | $\mathrm{KMT}^a_{03}$ | |
| G19 | $N_2O_5 \rightarrow NO_2 + NO_3$ | 1 | $\mathrm{KMT}^a_{04}$ | |
| G20 | $N_2O_5 + H_2O \rightarrow HNO_3 + HNO_3$ | 2 | $2.6 \times 10^{-22}$ | Atkinson et al. (2004) |
| G21 | $HNO_3 + OH \rightarrow NO_3 + H_2O$ | 2 | $\mathrm{KMT}^a_{11}$ | |
| G22 | $NO_2 + h\nu \rightarrow NO + O$ | 1 | b | |
| G23 | $NO_3 + h\nu \rightarrow NO + O_2$ | 1 | b | |
| G24 | $NO_3 + h\nu \rightarrow NO_2 + O$ | 1 | b | |
| G25 | $HNO_3 + h\nu \rightarrow NO_2 + OH$ | 1 | b | |
| C1 | $NO_3^- (^+H^+) + h\nu \rightarrow NO_2 + OH$ | 1 | b | |
| C2 | $NO_3^- (^+H^+) + h\nu \rightarrow NO_2^- + O$ | 1 | b | |
| C3 | $NO_2^- (^+H^+) + h\nu \rightarrow NO + OH$ | 1 | b | |

a - Adopted from (MCM, http://mcm.leeds.ac.uk/MCM/); b- Photolysis reaction rate at the snowpack surface computed from TUV and as a function depth of snow;

### 5.2.5 Heat Transport

The measured surface temperature of the snowpack is used to estimate the variations of temperature within the snowpack by the heat transport equation (Hutterli et al., 2003) as follow:

$$\frac{\partial T}{\partial t} = \frac{\partial}{\partial z}\left(\frac{k_{snow}}{\rho_{snow}\, c}\right)\frac{\partial T}{\partial z} \tag{5.13}$$

where $T$ is the temperature, $z$ is depth, $t$ is time, $c$ is the specific heat capacity, which parameterised as $c\,(\mathrm{J\,kg^{-1}\,K^{-1}}) = 152.2 + 7.122T$ (Paterson, 1994), and $k_{snow}$ is the thermal conductivity, which defined as:

$$k_{snow} = k_{ice}\left(\frac{\rho_{snow}}{\rho_{ice}}\right)^{2-0.5\frac{\rho_{snow}}{\rho_{ice}}} \tag{5.14}$$

where $k_{ice}$ is the thermal conductivity of ice, of which parameterised as $k_{ice} = 9.828e^{-0.0057T}$ (Paterson, 1994). The heat transfer model is allowed to spin up 300 days to the period of the model experiment to ensure pseudo-equilibrium state as the thermal conductivity of the snowpack is low.

### 5.2.6 $NO_x$ Flux Estimation

The diffusive flux, $F$, of $NO_x$ from the snowpack to the overlying atmosphere is calculated by the Fick's law as

$$F = -K_c\frac{\partial C_g}{\partial z} \tag{5.15}$$

where $K_c$ is the diffusion coefficient in the atmosphere, which mainly driven by the turbulence, and the concentration gradient, $\frac{\partial C_g}{\partial z}$, is the concentration difference between the modelled value at the surface of the snowpack and the observed value in the atmosphere (See Sect. 5.3).

It is not the aim of this study to investigate the dynamic of the atmosphere, therefore, values of $K_c$ from Frey et al. (2013), which calculated for the same period at Dome C, is adopted. They found that the values of $K_c$ have a strong diurnal variability, due to the diurnal variability in temperature as well as wind speed and wind direction. They calculated the average local noon value of $K_c$ = 0.9 $\mathrm{m^2s^{-1}}$ and a nighttime value of $K_c$ = 0.03 $\mathrm{m^2s^{-1}}$.

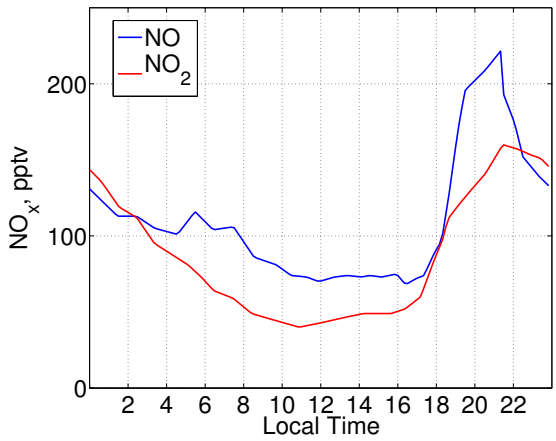


FIGURE 5.2: Observed mixing ratio of NO (Blue) and $NO_2$ (Red) at at 0.01 m above the surface of snowpack at Dome C, December 2009 (Frey et al., 2013).

## 5.3 Data

### 5.3.1 Observation at Dome C

Observation of atmospheric nitrogen oxides (NO + $NO_2$), temperature, wind speed and direction, and snow nitrate at the snow surface were observed at Dome C, East Antarctica (75.1°S, 123.3°E, 3233 m) from 22 December 2009 to 28 January 2009 (details in Frey et al., 2013). The atmospheric $NO_x$ was measured at 0.01, 1.00 and 4.00 m above the natural snowpack with a 2-channel chemiluminescence detector (CLD). An hourly bin during the entire period of the atmospheric $NO_x$ at 0.01 m is calculated (Fig. 5.2) and uses as the constraints of the model and for calculating the diffusive flux (Eq. 5.15).

The atmospheric nitrate, the sum of atmospheric particulate nitrate ($p-NO_3^-$) and gaseous nitric acid ($HNO_3$), was collected on glass fibre filter by high volume air sampler (HVAS) as described in Morin et al. (2008). Erbland et al. (2013) stated that the particulate nitrate data shows good agreement with $HNO_3$ gas-phase concentration measured by denuder tubes at Dome C over the same time period, therefore we equate the observed atmospheric nitrate with gaseous $HNO_3$. The filter was positioned approximately 1 m above the snow surface and was being changed on a weekly base. The atmospheric boundary layer is assumed to be well mixed so that the atmospheric nitrate at the snowpack surface would be the same at 1 m. Maximum atmospheric $HNO_3$ of 167 $\mathrm{ng\,m^{-3}}$ was observed during the summer period, while the minimum concentration of 1.2 $\mathrm{ng\,m^{-3}}$ was recorded during autumn and early winter period.

The standard meteorological data, including wind speed and direction at 3.3 m were measured (Fig. 5.4A shows wind speed measured on the 26 December 2009). Snow surface temperature was also recorded with an infrared radiometer (Fig. 5.4B shows the surface temperature of the snowpack measured on the 26 December 2009). Atmospheric nitrate concentrations and meteorological data used as model input have been interpolated to 3 seconds resolution.

### 5.3.2 Model Initialisation

The model time steps is set to 3 seconds to satisfy model stability between chemical production and destruction rate and the dispersion rate. The initial bulk concentration of $NO_3^-$ in snow is shown in Fig. 5.3A (Erbland et al., 2013) and the initial concentration of $HNO_3$ is as shown in Fig. 5.3B, by assuming the fraction of the total solute in the aqueous phase, $\Phi^{aq}_{bulk}$, to be 0.8; and the liquid-micropocket is in equilibrium with the SIA. The initial concentration of various gas-phase species is listed in Table 5.5.

TABLE 5.5: Initial concentration in SIA and the atmospheric boundary concentration for gas-phase species.

| Species | Initial | Reference |
|---|---|---|
| $O_3$ | 50 ppbv | Kukui et al., 2014 |
| $OH_2$ | 4 pptv | Kukui et al., 2014 |
| NO | 150 pptv | Frey et al., 2013 |
| $NO_2$ | 150 pptv | Frey et al., 2013 |

### 5.3.3 Other Model Inputs

There were no density of snow, $\rho_{snow}$, and the specific surface area, SSA, recorded at Dome C during the Austral summer 2009-2010. The values of density and SSA profile observed by Gallet et al. (2011) at Dome C during the Austral summer 2008-2009 are being used in this study (Fig. 5.3C & D).

## 5.4 Results and discussion

### 5.4.1 Effect of wind speed on chemistry in snowpack

Dome C is located at the highest point for several hundred kilometres that it does not affect by katabatic winds (Aristidi, E. et al., 2005), and hence, the wind speed is low. The ground level average ($\pm\sigma$) wind speed observed at Dome C in late December 2009 is 2.1 $ms^{-1}$ at 3.3 m above the surface of the

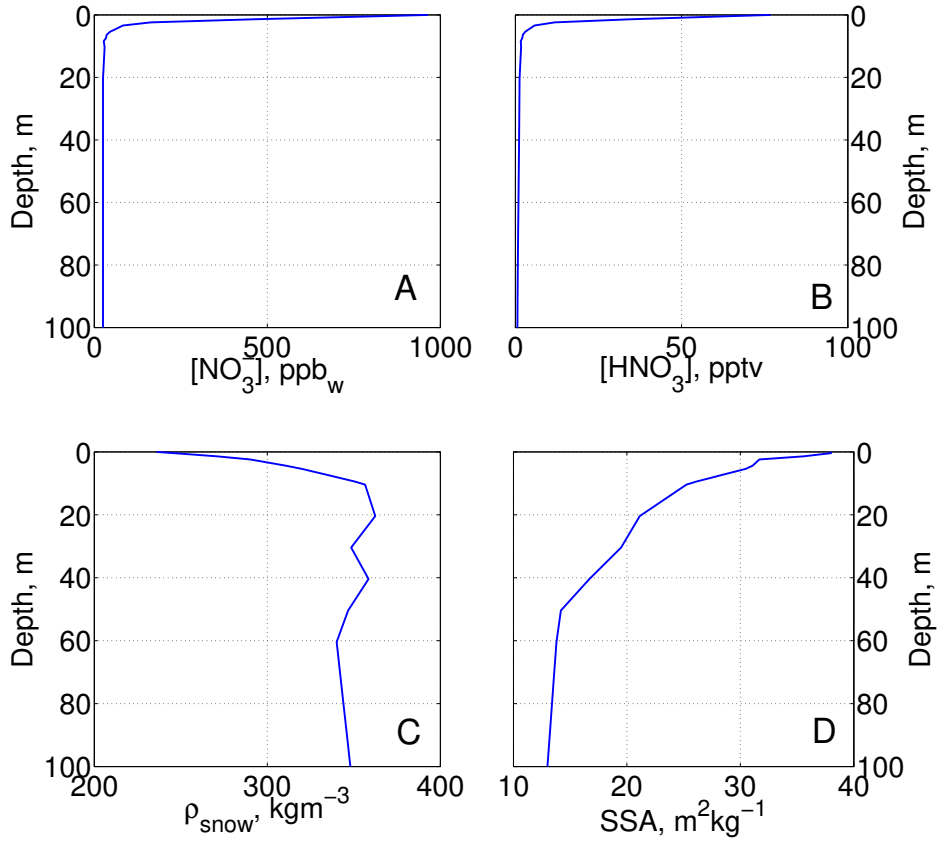


FIGURE 5.3: **A.** Initial profile of the concentration of nitrate in snow, (Erbland et al., 2013); **B.** The initial profile of concentration of nitric acid in SIA; **C.** The vertical profile of snow density, $\rho_{snow}$, (Gallée et al., 2015); **D.** The vertical profile of specific snow area, SSA, (Gallée et al., 2015).

snowpack (Fig. 5.4A in blue). There is a rather small diurnal amplitude of $\sim$1.5 $\mathrm{ms}^{-1}$, with maximum wind speed around noon which decrease sharply around 18:00 LT and picks up again during nighttime. Due to the low wind speed, the chemical mass transport caused by wind pumping at Dome C only has an impact on the top few $\mathrm{cm}$. For example, the effective diffusion constant for $NO_2$, $D_{\mathrm{eff,NO_2}}$, has increase by $\sim$ 0.006-8.3 times at the 0-3 few $\mathrm{cm}$ when wind pumping is included (Fig. 5.4C).

However, the effect of wind pumping is also dependent on the surface topography, as no information available for the topography at Dome C, the vertical mass transport contributed by wind pumping can be under- or over-estimated and, consequently, under or over-estimated the overall gas transport within the snowpack. If the relief wavelength, $\lambda_{\mathrm{surf}}$, and relief amplitude, $h$, is halved of the values listed inTable 5.2, the diffusivity caused by

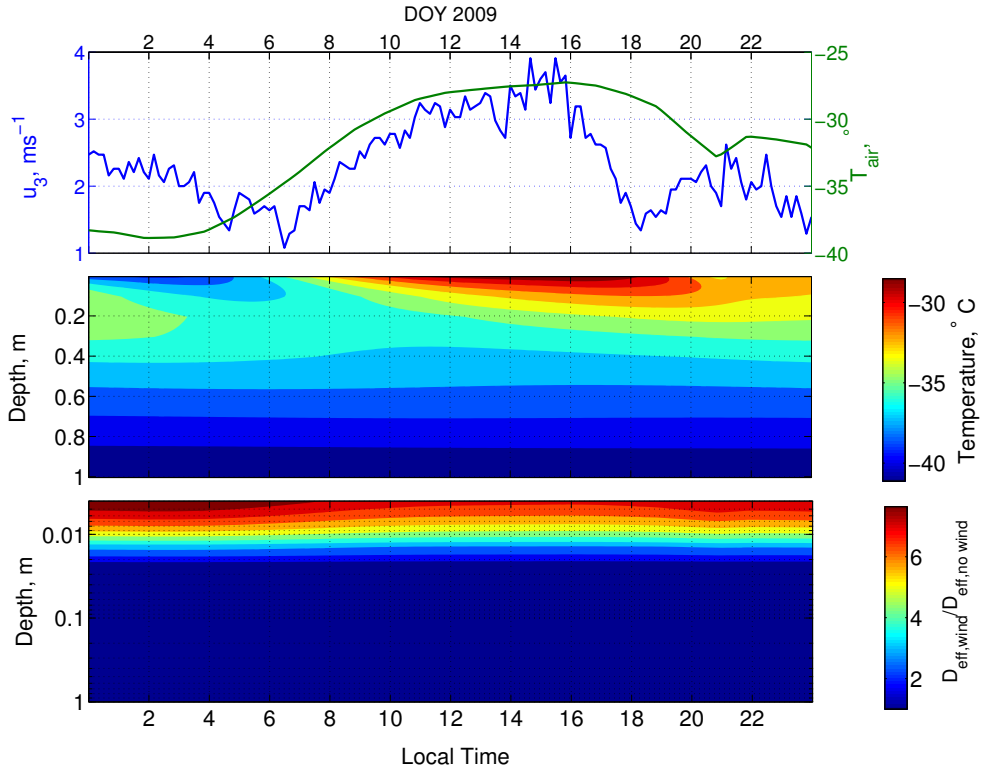


FIGURE 5.4: **A.** Observed Wind speed at 3.3 m above surface of the snowpack in $\mathrm{m\,s^{-1}}$ with an average ($\pm\sigma$) = 2.5 $\pm$ 1.4 (Green, right axis) and the observed temperature of the surface of the snowpack in °C on 26 December 2009; **B.** Modelled temperature profile within the snowpack in °C; **C.** The ratio of effective diffusion constant with wind, $D_{\mathrm{eff,wind}}$, to the effective diffusion constant without wind, $D_{\mathrm{eff,nowind}}$, for $NO_2$ within the snowpack (Eq. 5.4). Note: Depth in **C** is plotted logarithmically.

wind pumping (the term'$U_{\mathrm{firn}}\Delta z$' in Eq. 5.5) increases by 200% and reduces by 55%, respectively. Future field observations on the surface topography are required to improve the estimation of the effective diffusion coefficient.

### 5.4.2 Diurnal Cycle

#### Snow Temperature

The average maximum daytime surface temperature is $\sim$ -27°C occur between 11:00 -14:30 LT and the average minimum temperature is $\sim$ -40°C occur between 2:00-3:30 LT (Fig. 5.4A). The daily fluctuations in the atmosphere temperature is $\sim$ 13°C and it is reflected in the near-surface snowpack. The diurnal variability at the top 20 cm of the snowpack is a lot stronger compared to below 50 cm deep in the snowpack (Fig. 5.4B). In general, there is a

7-9 hours lag between the surface and 20 cm deep in the snowpack and 12-14 hours lag at 35 cm depth, which leads to a positive temperature gradient during the day and a negative temperature gradient in the evening.

The heat transport within the snowpack is dominated by the conduction through snow crystal, yet the conduction through SIA, latent heat exchange and convection by wind can also have an impact of the heat transport. The thermal conductivity (Eq. 5.14) only taken account of the conduction through snow crystal but not the others. This assumption is acceptable at Dome C, as the air temperature is always below melting, of which the latent heat exchange is insignificant, and, secondly, the annual mean wind speed is low, and hence, the heat transport via convection is negligible. However, the future model should include other factors that can impact the heat transport within the snowpack to be applicable for area outside the polar regions.

**Photolysis Rate Coefficient**

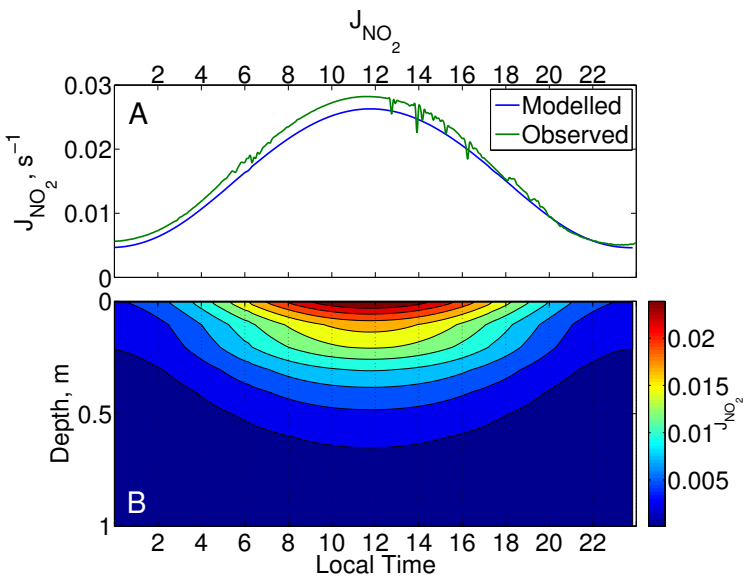


FIGURE 5.5: **A.** Photolysis rate coefficient for gas-phase $NO_2$ (G11 on Table 5.4), at the surface of the snowpack. Green - observation by Frey et al. (2013); Blue - modelled results from TUV. **B.** Estimated vertical profile of photolysis rate coefficient for gas-phase $NO_2$ (within a 1 m snowpack with Eq. 5.11.

The offline surface photolysis rate coefficients, $J(z_0)$, calculated by the radiative transfer model - TUV (Sect. 5.2.4) shows excellent agreement with the observation for gas-phase $NO_2$ (Fig. 5.5) and $O_3$ (Fig. 5.6) at Dome C in late December 2009. The good agreement between the two indicates that the rate of $NO_2$ and $O_3$ loss at the surface of the snowpack is correctly represented in

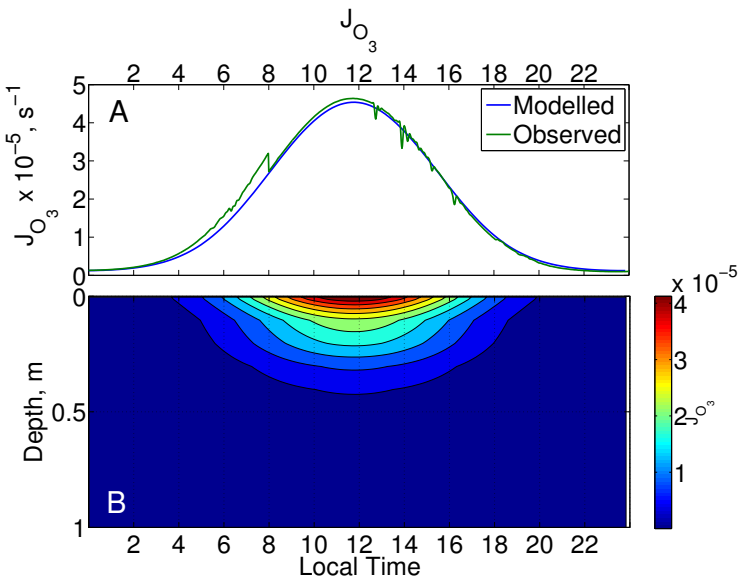


FIGURE 5.6: **A.** Photolysis rate coefficient for gas-phase $O_3$ (G11 on Table 5.4), at the surface of the snowpack. Green - observation by Frey et al. (2013); Blue - modelled results from TUV. **B.** Estimated vertical profile of photolysis rate coefficient for gas-phase $O_3$ (within a 1 m snowpack with Eq. 5.11.

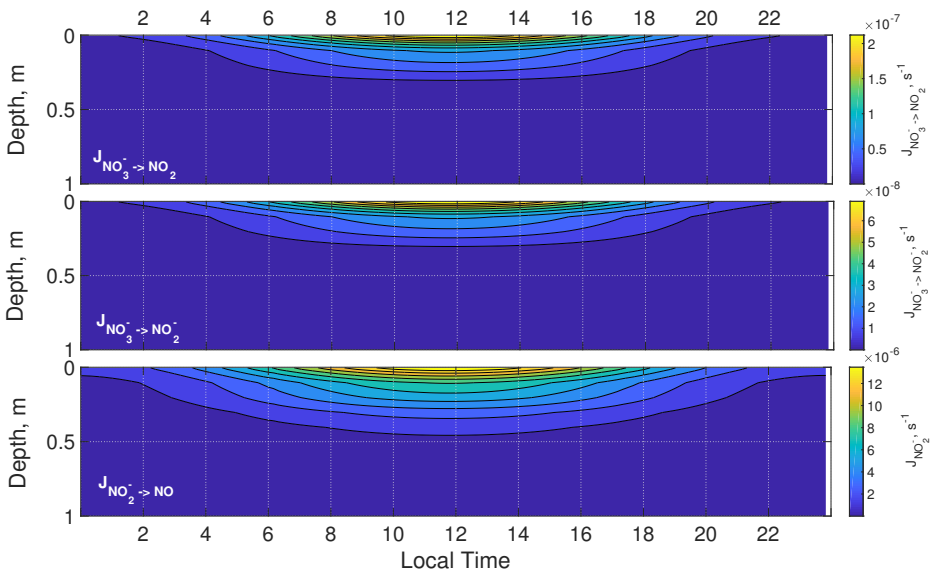


FIGURE 5.7: Modelled vertical profile of photolysis rate coefficient of **A.** $NO_3^-$ to $NO_2$, $J_{C1}$ (C1 on Table 5.4); **B.** condensed-phase $NO_3^-$ to $NO_2^-$, $J_{C2}$ (C2 on Table 5.4); and **C.** condensed-phase $NO_2^-$ to NO, $J_{C3}$ (C3 on Table 5.4).

the model, despite a cloud-free condition was assumed when generating the photolysis rate coefficient lookup table. However, the cloud-free assumption

is a potential shortcomings of the model, which can overestimate the surface photolysis rate coefficient for cloudy regions, such as the coastal Antarctica.

The surface photolysis rate coefficient for $NO_3^-$ (C1, Table. 5.4) have a maximum value of $\sim 2 \times 10^{-7} s^{-1}$ at local noon (Fig. 5.7A). The use wavelength dependent $e$-folding depth (Table 5.3) leads to slightly different photolysis rate coefficient profile for $NO_2$, $O_3$, $NO_3^-$ and $NO_2^-$ (Fig. 5.5, 5.6, and 5.7, respectively). The attenuation of photolysis rate coefficient for $NO_3^-$ is a lot more rapid compared to the photolysis rate coefficient for $NO_2$ as the $e$-folding depth for $NO_3^-$ is set as 10 cm while the $e$-folding depth is set as 25 cm (Table 5.3).

### Nitrogen Oxides & Ozone

The diurnal profile of NO, $NO_2$, and $O_3$ predicted by this model (Fig. 5.8) is contradicting to the observations in the polar regions (e.g. Dam et al., 2015; Frey et al., 2015) or previous model studies (e.g. Thomas et al., 2011; Murray et al., 2015). The modelled level of NO at the near-surface layer of the snowpack ($\sim$ top 30 cm) is driven by the concentration gradient of NO between the overlying atmosphere and near-surface layer of the snowpack (Fig. 5.2A), and hence, followed the same trend as the NO in the overlying atmosphere, which the maximum NO occurs in the evening when solar radiation is minimum. The level of NO in the SIA is also modelled to be lower than the level in

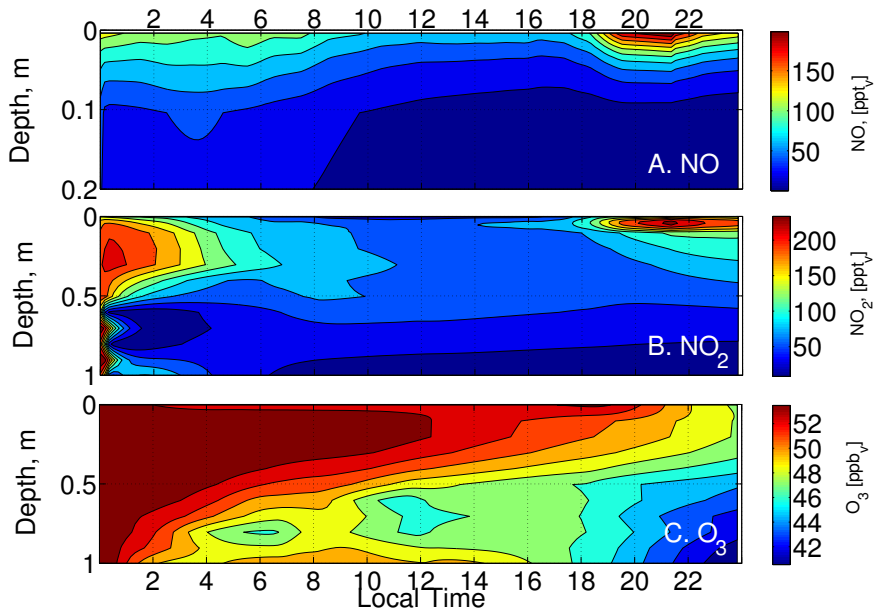


FIGURE 5.8: Modelled vertical profile of **A.** NO ; **B.** $NO_2$; and **C.** $O_3$ within the snowpack.

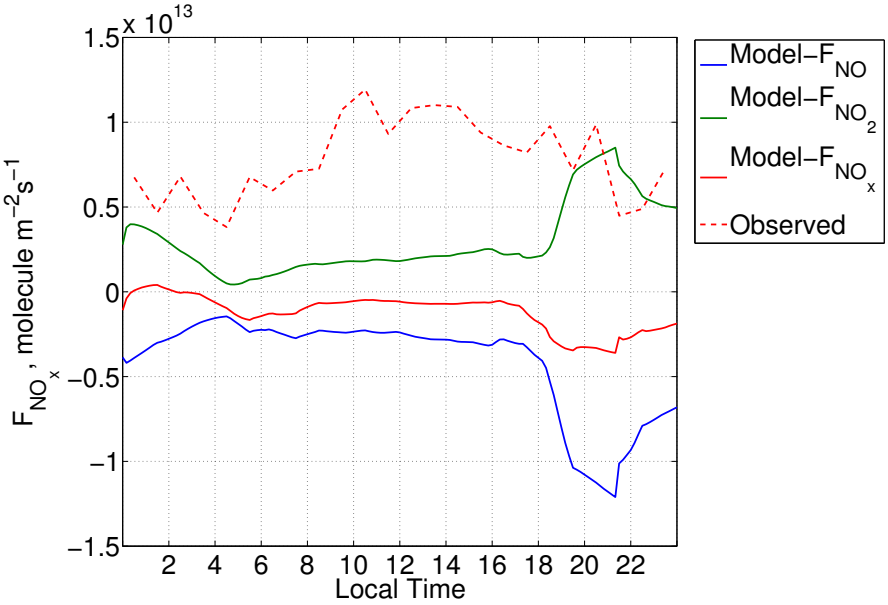


FIGURE 5.9: Observed flux of $NO_x$ (red-dash), $F_{NO_x}$, by Frey et al. (2009); and modelled flux of NO (blue), $NO_2$ (green), and $NO_x$ (red-solid) flux of $NO_x$, at Dome C in December 2009.

the overlying atmosphere, and as a result, a downward flux of NO (Fig. 5.9) from the atmosphere to the snowpack is estimated. From field measurements and other modeling studies (e.g. Dam et al., 2015; Frey et al., 2015; Thomas et al., 2011; Murray et al., 2015), the SIA profile of NO at the near-surface layer is expected to be closely followed the diurnal cycle of the solar radiation due to its instantaneous production and short lifetime and the values are expected to be higher than the atmospheric value, and hence, a upward flux (release) of NO from the snowpack to the overlying atmosphere. Photolysis of $NO_2$ is the dominant source of NO during the day and the maximum production of NO from photolysis of $NO_2$ should be at local noon with a production rate $\sim 10^{14}$ molec $m^{-3}$ $s^{-1}$ ($\sim$ 1-10 pptv $s^{-1}$). Another minor source of NO during the day is the photolysis of $NO_2^-$ in snow with a production rate $\sim 10^8$ molec $m^{-3}$ $s^{-1}$.

This 1-D air-snow model reproduced the maximum $NO_2$ beneath the photic zone (> $\sim$ 30 cm) in the evening when the solar radiation is minimum, which agreed with observations from the field and other modeling studies. The production of $NO_2$ in the deep layer is suggested to be dominated by dark chemical reactions of the $NO_x$ reservoir species (Dam et al., 2015), such as

$N_2O_5$ (R25) and $HO_2NO_2$ (R26).

$$N_2O_5 \longleftrightarrow NO_2 + NO_3 \tag{R25}$$

$$HO_2NO_2 \longleftrightarrow NO_2 + HO_2 \tag{R26}$$

The dark chemical reaction of $N_2O_5$ is included as one of the chemical reactions in this model, which explains the enhancement of $NO_2$ below the near-surface layer (Fig. 5.8) and the modelled flux of $NO_2$ matches with the observation when the solar radiation is low (Fig. 5.9). However, the reaction of $HO_2NO_2$ is not yet included in the model, which is suggested to be an important source of $NO_2$ production in the layer below the photic zone. Therefore, the production of $NO_2$ via the dark chemistry is likely to be underestimated.

Moreover, the model failed to reproduce the diurnal variation of $NO_2$ at the near-surface layer too, which is expected to follow the diurnal pattern of the solar radiation as the main source of $NO_2$ at the near-surface layer is suggested to be the photolysis of $NO_3^-$. The maximum production rate of $NO_2$ via photolysis of $NO_3^-$ in the near-surface layer is $\sim 10^{14}\,\mathrm{molec\,m^{-3}\,s^{-1}}$ ($\sim$ 1-10 $\mathrm{pptv\,s^{-1}}$).

The consumption of $O_3$ at the near-surface layer is related to the solar radiation, which correspond to the photolysis of $O_3$. However, the $O_3$ at the near-surface layer continued to deplete in the evening when the solar radiation is low, which indicated the sources of $O_3$ are missing in the model. Below the photic zone, the depletion of $O_3$ is due to reaction with $NO_x$ (G14, 17 & 18 in Table 5.4) or $HO_x$ (G5 & 8 in Table 5.4). However, the maximum depletion is expected to be occurred deep in the snowpack while the maximum $O_3$ level is below the photic zone. The level of $O_3$ is also expected to be lower than the overlying atmosphere that the snowpack would be a sink of $O_3$, however, the depletion mechanism is still not fully understood (Dam et al., 2015). It has been suggested that the reactions between $O_3$ with other species, such as the halogen and condensed-phase reaction with formic acid (HCOOH) or $NO_2^-$ (Murray et al., 2015). These reactions are needed to be included in the chemical mechanism to improve the estimation of $O_3$ profile within the snow.

The poor performance of the model presented here, which did not capture the temporal variation at the near-surface layer as well as the vertical spatial variation of of NO and $NO_2$ within the snowpack, is explained by a bug within the model. The customised KPP has failed to include the photochemically produced $NO_2$ and NO from the photolysis of $NO_3^-$ in the system. Therefore, the level of $NO_x$ shows in Fig. 5.8 is from the initial SIA or downward transported from the overlying atmosphere. The initial value of $NO_2$ plus the $NO_2$ produces by the dark chemistry is higher than the level of $NO_2$

in the overlying atmosphere, and therefore, resulted an upward flux from the snowpack into the atmosphere. While for initial NO minus the losses of NO via reaction with $HO_2$, $O_3$ and $NO_3$ is lower than the level of NO as there are no production of NO from photolysis of $NO_3^-$ is included in the system. Both the upward flux of $NO_2$ and downward flux of NO (Fig. 5.9) reduces when solar radiation increases as the photolysis of $NO_2$ (G22) in the near-surface layer reduces the level of $NO_2$ but increases the level of NO, and hence, decreases the concentration gradient of $NO_2$ as well as NO between between air and snowpack. Moreover, $NO_2$ is the precursor of $O_3$, therefore, the lack of photochemically produced $NO_2$ in the system leads to a net consumption of $O_3$ within the snowpack. The bug in the KPP code has to be fixed to be able to evaluate the hypothesis of the multi-phase air-snow exchange as presented in Ch. 4 (Chan et al., 2016).

## 5.5 Conclusions

A 1-D air-snow exchange model is developed to study the dynamics of $NO_x$ and $O_3$ within snow to evaluate the emission flux of $NO_x$ to the overlying atmosphere during summer at Dome C, East Antarctic. A temperature dependent multi-phase air-snow mass exchange between air and snow grain has been incorporated into the framework of previously developed air-snow models (Thomas et al., 2011; Toyota et al., 2014), which include gas-phase and condensed-phase chemical reactions, vertical heat transport and vertical mass transport. The important features of this 1-D air-snow exchange model include the following: 1) vertical transport of gas-phase species within the snowpack is constrained by the observed gas-phase concentration in the overlying atmosphere and controlled by wind pumping and molecular diffusion; 2) attenuation of actinic flux, and hence, photolysis rate coefficient, within the snowpack is parameterised by the $e$-folding depth; 3) a temperature dependent multi-phase mass transfer between air and snow grain, of which air-ice mass only transfer at temperatures below eutectic temperature and at temperatures above the eutectic temperature the mass transfer is the combination of both air-ice and air-liquid; 4) a single photolysis rate coefficient is applied to the total concentration of $NO_3^-$ in snow (sum of the $NO_3^-$ in solid-solution and liquid micropocket) and the photochemically produced $NO_x$ is transferred directly to the SIA.

The aim of this modeling study is to address the multi-phase mass transfer between SIA and snow grain, which has not been addressed explicitly in the past. This initial study of incorporating a temperature dependent multi-phase interaction model into a 1-D air-snow model failed to reproduce the

emission flux of $NO_x$ and the vertical spatial profile of NO, $NO_2$ and $O_3$ due to a bug in the KPP code, which fails to include the condensed-phase photochemical products. The code correspond for solving the chemical reactions needs to be fixed in order to access the applicability of multi-phase mass transfer between air-snow at all depth. Beside, there are numbers of issues need to be addressed in the new 1-D model to further improve our understanding of the impacts of snow photochemistry on the chemistry of the boundary layer and the preserved $NO_3^-$ in ice core. In terms of model developments, a relatively simple chemistry scheme is used here, future development should include halogen and organic radicals chemistry, which are closely linked to the depletion of tropospheric $O_3$ and the partitioning of $HO_x$ and $NO_x$. The model development should focus on the including mass transfer between SIA and snow of other chemical species, especially those have a high solubility such as $HO_x$ and $HO_2NO_2$. Moreover, an atmospheric boundary layer model should be coupled with the new 1-D model to describe the interactive processes between boundary layer and snowpack.. In terms of observations, there is lack of data on the surface topography, which causes uncertainties in the emission flux from snow to the atmosphere.

Last but not least, the current 1-D air-snow model is developed in MATLAB. The current version of the model requires a long computational time due to the complexity of the model, which involves solving a large number of ordinary differential equations (for chemical kinetics, mass transport within the snow grain and snowpack). Therefore, the results presented here did not have a long enough spin-up time to ensure pseudo-equilibrium state was reached. To improve the performance of the model in terms of computation time, it needs to be re-written in another programming languages that are more efficient in technical calculations, such as Fortran.

1

# Chapter 6

# Discussion

The description of snow in existing air-snow models is highly simplified even though snow is known to be a highly dynamic environment and the air-snow grain interface is complex. The idea of a temperature dependent multi-phase air-snow exchange model for nitrogen oxide has been implemented for the first time. A 1-D air-snow exchange model for reactive nitrogen is developed to estimate the $NO_x$ flux emitted from the snow and the impacts of the emission to the oxidising capacity of the atmospheric boundary layer, i.e. concentration of $O_3$ and OH radicals. The findings presented Ch. 3 provides essential information for incorporating the $e$-folding depth parameterisation to estimate the attenuation of actinic flux in the snowpack. It shows adopting the $e$-folding depth parameterisation for snow radiative transfer can reduce the computation cost of in the larger model (i.e. 1-D model in this case) but without compromising much of the accuracy comparing to a radiative transfer model. The 1-D model also incorporated the newly developed air-snow interaction model (Model 2 presented in Ch. 4), which provided a reasonably estimation of concentration of $NO_3^-$ in skin layer snow by assuming the major interface between air and snow grain is air-ice and any liquid present above the eutectic temperature is concentrated in micropockets as suggested by Domine et al. (2013b).

However, there are still uncertainties and deficiency in the newly developed 1-D air-snow exchange model, which might be able to identify and resolve with future field, laboratory and modeling studies. The uncertainties in the models are identified into three main categories: 1) description of snow, i.e. the size of the snow grain, the air-snow interface and location of impurities; 2) physical processes ; 3) chemical processes and 4) description of the atmosphere.

## 6.1 Description of Snow

One simplification that made in the air-snow exchange model presented here, and in most of the snow models, is that the snow grains are spherical with an

effective radius, $R_{\text{eff}}$. This simplification is very unlikely to be true as various shapes of snow grain can be found within the snowpack. The $R_{\text{eff}}$ is an important parameter for quantifying the uptake of impurities into snow grain and can be estimated from the specific surface area, SSA (Eq. 2.16 Bartels-Rausch et al., 2014). However, there is no SSA data recorded together with the validation datasets and that estimation had to be made based partly on observations by other studies (See Ch. 2.6.4 for details). At Dome C, the interannual variability in SSA of the surface snow is small (Picard et al., 2016) but the spatial variability in the vertical SSA profile, especially in the top 15 $\text{cm}$ of the snowpack, is significant (Gallet et al., 2011). The vertical profile of SSA is related to the stratification of the snowpack, i.e. small rounded grain and surface hoar have a SSA ~23-53 $\text{m}^2\text{kg}^{-1}$, wind crust snow has a SSA ~20-40 $\text{m}^2\text{kg}^{-1}$, faceted crystal has a SSA ~13-24 $\text{m}^2\text{kg}^{-1}$, and depth hoar has a SSA ~10-18 $\text{m}^2\text{kg}^{-1}$ (Gallet et al., 2011). The SSA profiles of the top 70 $\text{cm}$ of the snowpack at Dome C has a maximum coefficient of variation (standard deviation divided by mean) of 35 % (Gallet et al., 2011). Even though the sensitivity test performed in Ch. 4, Sect. 6.5 suggests the air-snow interaction model is not that sensitive to the value of SSA, the range of SSA being tested ($\pm 10\%$) is a lot smaller than the natural variability of the snowpack. Therefore, to reduce the uncertainties in the uptake of chemical species, SSA profile should be measured in future field studies.

Nonetheless, the two major uncertainties in snow photochemistry are still remain as the lack of understanding in the physical and chemical properties of the interface between air and snow grain and the location of impurities in snow, which both have an impact on the mass transfer of chemical species between air and snow as well as the reaction rate in snow (Ch. 1). Therefore, the focus of this study is on improving our understandings in the air-snow interaction and the location of impurities via modeling studies. The air-snow interaction models presented in Ch. 4 suggests at low temperature, the air-snow interface is ice and $NO_3^-$ can be found in both at the surface of the snow grain and within the bulk. The concentration of $NO_3^-$ in the 'ice-phase' is defined by non-equilibrium surface adsorption on ice and co-condensation coupled with solid-state diffusion within the bulk ice. However, there are few physically-based parameterisations that adopted in the models can be improved by future laboratory experiments to reduce the model uncertainties, such as the Langmuir adsorption equilibrium constant on ice, $K_{eq}$, maximum number of adsorption sites, $N_{max}$, and solid-state diffusion coefficient, $k_{\text{diff}}$.

The parameterisations of $K_{eq}$ and the value of $N_{max}$ recommended by Burkholder et al. (2015) and Crowley et al. (2010) only valid between 214-240

K. In the models, the parameterisation of $K_{eq}$ by Burkholder et al. (2015) is extended to colder temperatures (T<214 K, Fig. 2.13). It has been suggested that at T < 210 K, the uptake via adsorption is continuous and irreversible and cannot be described by Langmuir model (Crowley et al., 2010, and references therein). Therefore, the extending the parameterisation to lower temperature likely leads to underestimation of the number of molecules adsorbed onto the ice surface. On the other hand, the value of $K_{eq}$ was fixed to the value of $K_{eq}$ at 240 K for T > 240 K, which is likely to overestimate the number of adsorbed molecules at the ice surface. The adsorption mechanism at T < 210 and T > 240 K needs to be examined further to have a more accurate parameterisation at these temperatures. Improving the parameterisation at a lower temperature is not only beneficial to estimate the air-ice interaction in Antarctica in the winter time, that is below 241 K in general, but also useful for the air- cloud droplet interaction in the stratosphere. However, parameterising the adsorption mechanism at T>240 K might be challenging as the surface structure of ice is likely to become more disorganised as temperature increases.

Moreover, the air-snow interaction models, Model 2, presented in Ch. 4, assume that the adsorbed nitrate molecules can diffuse into the bulk ice as suggested by other studies (Abbatt, 1997; Huthwelker et al., 2004; Cox et al., 2005). Here, the diffusion of nitrate into the bulk is controlled by the concentration gradient between the surface and the centre of the snow grain and the solid-state diffusion coefficient. However, the exact diffusion kinetic of the adsorbed species is still unclear, further investigation in the laboratory is required in the future to better parameterised the diffusion process of the adsorbed molecules into the bulk.

The air-snow interaction models, Model 1 & 2, presented in Ch. 4 both have a temperature dependent multi-phase interaction. For Model 1 in Ch. 4, when the temperature is above a certain threshold, the air-snow interface is a disordered interface (DI). The DI is assumed to have a hybrid physical properties between liquid water and ice, i.e. the partitioning coefficient of DI is assumed to be the same as that measured in liquid, yet, the diffusivity of DI is assumed to be that measured in solid ice, and to have an infinitesimal thickness (Ch. 4, Sect.3.1.2). Model 1 only provide a good estimation of the concentration of $NO_3^-$ in surface snow at cold Dome C but not at the relatively warm site Halley (Ch. 4, Sect. 5) suggesting the partitioning and diffusivity of DI might be similar to that measured in ice at low temperature and relatively low impurities concentration and as the temperature and/or concentration of impurities increases the physical properties of the DI change towards to those measured in liquid.

Therefore, the poor performance of Model 1 at the relatively warm site, Halley, might down to the poor parameterisations of the properties of the DI at warmer temperatures. It has been observed in laboratory experiments that the crystal structure at the air-ice interface becomes more and more disordered as the temperature approaches melting temperature. The observed thickness of this disorder surface structure varies from a monolayer to a few hundreds $\mathrm{nm}$ depending on the temperature and the measuring technique (BartelsRausch et al., 2014). It is also suggested that the impurities concentration in the snow can affect the thickness of the DI. Future laboratory experiments need to focus on how the physical properties, such as partitioning, diffusivity, and thickness, of the interface between air and snow changes with temperature, as well as the concentration of impurities, in order to parameterise the DI more accurately.

Another temperature dependent multi-phase air-snows interaction model, Model 2, presented in Ch. 4, assumes majority of the air-snow interface is air-ice and only when the temperature is above the eutectic temperature that liquid co-existed with ice in the form of micropockets located between grain boundaries and grooves. The modelled results from Model 2 agreed well with the observed $NO_3^-$ concentration in snow for both of the validation sites without requiring any tuning parameters to fit the model results with observations. It suggests, in the warmer months, the concentration of $NO_3^-$ in snow is mainly governed by equilibrium solvation into the liquid micropocket (Ch. 4-Fig. 5B & 6B). There are various assumptions made regarding the existence and the physical properties of the liquid micropocket in this study, such as the micropocket is 1) only co-exist with ice when temperature is above eutectic temperature; 2) located between grain boundaries or triple junctions that the grain surface area they cover is negligible; and 3) treated as ideal-solution that Henry's Law is used to describe the partitioning between air and micropocket.

For simplification, the eutectic temperature, $T_e$, was based on a system containing most abundant solute within snow such as $HNO_3$ at Dome C or NaCl at Halley and $H_2O$. Including other ionic components is likely to lower the eutectic temperature compared to a two-component system, i.e.$T_e$ of $H_2SO_4$-$H_2O$ binary system is $\sim 200\ \mathrm{K}$ (Zeleznik, 1991), depending on the mixing ratio of each ionic components. Thermal analysis is required of detecting the eutectic temperature of various multi-components system. Moreover, as mentioned in Ch. 2.5.1, the liquid micropockets are treated as an ideal solution, which is not likely to be the case in reality. The impacts of the non-ideality in the concentrated liquid micropocket should also be examined by laboratory experiments.

## 6.2 Physical Processes

There are a lot of different physical processes included in the 1-D air-snow model, such as radiative transfer, heat transport, vertical mass transport and exchange between air and snow. In this study, the uncertainties caused by applying the $e$-folding depth parameterisation for radiative transfer on the photochemical production of $NO_x$ in snow were assessed (Ch. 3). Different snowpack types, i.e. cold polar, windpacked, and melting snow, with various concentration of light-absorbing impurities, i.e black carbon (BC) and humic like substances (HULIS), were investigated. The $e$-folding depth parameterisation found to be sufficient for estimating the attenuation of actinic flux within typical cold polar snowpack and that the $e$-folding depth parameterisation is recommended to be incorporated into larger-scale models for estimating photolysis reactions in snow to reduce computation cost.

The range of BC and HULIS concentrations used in Ch. 3 were limited to the typical concentration that found in polar snow. However, snow from the high Asian glaciers and mountains, which has more influence from the anthropogenic sources, can have a BC mass ratio up to 1000 $\mathrm{ng\,g^{-1}}$ (Schmale et al., 2017), an order of magnitude larger than the maximum BC concentration used in the study. Moreover, for the $e$-folding depth parameterisation to be incorporated into global models, other light-absorbers that found in snow, such as mineral dust, that have different spectral dependencies should be examined too. Mineral dust is a collective term referring to minerals containing aerosols, such as sand from the desert or soil that generated naturally or anthropogenically though agriculture or deforestation etc. North Africa, including the Saharan desert, contribute 62-73 % of the mineral dust in the atmosphere, other major contributors of mineral dust are Central Asia ($\sim 15\%$), and Arabian Peninsula ($\sim 11\%$) (Tanaka and Chiba, 2006). Mineral dust with diameters smaller than 10 $\mu\mathrm{m}$ can be transported long distances via dust storms and deposit on snow surface by both dry and wet deposition (Merrill et al., 1989). The mineral dust has been found to be the dominant light absorber for snow in the mountains of Colorado (Painter et al., 2007) and in the Qilian Mountains (Wang et al., 2014).

The absorption coefficient of mineral dust is determined by the relative abundance of each mineral and how the minerals are mixed in aerosols and that the absorption of mineral dust can have a large variation depending on it originate locations, i.e. mineral dust entrained in the Sahelian region in Africa has a high-Fe/Al ratio due to the abundance of ferralitic soil (Sokolik and Toon, 1999). The composition of soils vary from region to region, for example, the clay fraction of soils from the arid and semiarid region of China and Mongolia are mainly composed of illite, kaolinite, and smectite,

and the silt fraction is rich in quartz and feldspars with smaller amounts of calcite, iron oxides, i.e. hematite ($Fe_2O_3$) and goethite (FeO(OH)), and gypsum (Wang et al., 2014). Quartz, calcite and gypsum were found to have insignificant absorption at UV and visible wavelength, therefore, their concentration is possibly less important in this content as the photochemical active wavelength is in the UV region. On the other hand, hematite has strong absorption bands in the UV and visible wavelengths of all the major minerals studied (Lafon et al., 2006) that the absorption coefficient of mineral dust, especially in the UV, is sensitive to the content in iron oxides, despite their low concentration in the dust aerosol (Linke et al., 2006). Therefore, for a complete assessment of the impact of parameterising the attenuation of actinic flux into snow on the photochemical production of $NO_x$ and OH radicals in snow, further modeling exercises that include a larger range of BC concentration and other light-absorbing impurities, i.e. Hematite and goethite, are needed.

The heat transport in the snowpack had been well characterised and parameterised from previous studies, e.g. Albert, 1996, and it has been reconfirmed in this study that the heat transport model successfully captured the variabilities observed in measured data at the different depth of the snowpack (Fig. 2.5). The temperature profile also shown a temperature gradient exerts in the snowpack, especially across the top few $\mathrm{cm}$, due to the diurnal cycle. The air and the surface of the snowpack are warmed during the day from the sun and cooled radiatively at night. Temperature gradient causes morphological changes to size and shape of the snow grain. Pinzer et al. (2012) observed a redistribution of ice mass up to 60% within natural snow under an alternating temperature gradient of 50 $\mathrm{K\,m^{-1}}$ during a 12 $\mathrm{hour}$ period. However, the redistribution of impurities under temperature gradient is still unclear. Laboratory experiments are required to investigate how temperature gradient can affect the redistribution of impurities within the grain and, hence, the quantum yield of the photolysis reaction.

Another physical process based uncertainty would be the lack of physical exchange of chemical reactive nitrogen species other than $HNO_3$ between air and snow. The models presented in Ch. 4 are specially developed to model the interaction of $HNO_3$ between air and snow, as $HNO_3$ is thought to contribute to $NO_3^-$ deposited in the Antarctic snow (Michalski et al., 2005). Thus the models did not include deposition of particulate nitrate or nitrate aerosol. However, other forms of atmospheric nitrate, attributed to sea-spray or mineral dust, had been measured in the polar regions. It has been suggested that the sea salt (NaCl) can react with $HNO_3$ to form sodium nitrate ($NaNO_3$, R27). This modification of sea salt can happen in the atmosphere

during transport from coast to inland (Iizuka et al., 2016).

$$\mathrm{NaCl} + \mathrm{HNO_3} \longrightarrow \mathrm{NaNO_3} + \mathrm{HCl} \tag{R27}$$

This modification of sea salt and $HNO_3$ by reaction R27 mainly happens around the coastal area (70-74°S) and at an altitude below 3000 m a.s.l. that almost no sea salt left for the reaction at high altitudes and further inland (Iizuka et al., 2016).

Furthermore, mineral dust does not only alter the optical properties of the snow, in fact, mineral dust also plays a major role in the chemistry of the atmosphere. More than 40 % of the total nitrate in the atmosphere is coupled with mineral dust (Usher et al., 2003). The major source of mineral dust to East Antartica is in the southern South America region, where the fine dust particles are transported by Westerlies wind. The dust from the southern South America region contains calcic-rich plagioclase and calcite minerals, i.e. calcite ($CaCO_3$) and dolomite ($CaMg(CO_3)_2$) (Zárate, 2003), which can react with $HNO_3$ or $N_2O_5$ in the atmosphere to form calcium nitrate ($Ca(NO_3)_2$) and magnesium nitrate ($Mg(NO_3)_2$), respectively, as follow (Mahalinganathan and Thamban, 2016; Bjorkman et al., 2014):

$$\mathrm{CaCO_3} + 2\,\mathrm{HNO_3} \xrightarrow{\%\mathrm{RH}} \mathrm{Ca(NO_3)_2} + \mathrm{CO_2} + \mathrm{H_2O} \tag{R28}$$

$$\mathrm{CaCO_3} + \mathrm{N_2O_5} \xrightarrow{\%\mathrm{RH}} \mathrm{Ca(NO_3)_2} + \mathrm{CO_2} \tag{R29}$$

$$\mathrm{CaMg(CO_3)_2} + 4\,\mathrm{HNO_3} \xrightarrow{\%\mathrm{RH}} \mathrm{Ca(NO_3)_2} + \mathrm{Mg(NO_3)_2} + 2\,\mathrm{CO_2} + 2\,\mathrm{H_2O} \tag{R30}$$

$$\mathrm{CaMg(CO_3)_2} + 2\,\mathrm{N_2O_5} \xrightarrow{\%\mathrm{RH}} \mathrm{Ca(NO_3)_2} + \mathrm{Mg(NO_3)_2} + 2\,\mathrm{CO_2} \tag{R31}$$

The reaction between mineral dust and $HNO_3$ or $N_2O_5$ is enhanced under humid condition (Goodman et al., 2000). The formation of $Ca(NO_3)_2$ is likely to form in the atmosphere during the transport of mineral dust from southern South America to the Antarctic region (Mahalinganathan and Thamban, 2016). Majority of the $Ca(NO_3)_2$ aerosols deposited in the near-coastal regions (Mahalinganathan and Thamban, 2016). Therefore, neglecting the dry deposition of nitrate aerosol such as $NaNO_3$ or $Ca(NO_3)_2$, especially near the coastal regions, is likely lead to underestimation of the concentration of $NO_3^-$ in snow.

Furthermore, the concentration of nitrate in the surface snow that contribute from wet deposition is also missing from the models. The snow droplet

scavenges reactive nitrogen from the atmosphere that produced either naturally, i.e. solar activity, and lightening or anthropogenically, i.e. biofuel burning. It has been suggested that $NO_x$ are formed by ionising nitrogen in the middle stratosphere ($\sim 30$ km) and above during high-intensity solar proton events (SPEs) (Melott et al., 2016). The $NO_x$ produced in the stratosphere is most likely transported to the ground by large-scale downwelling of air in polar winter. This transportation is a slow process that could take months to years, of which the $NO_x$ would be broad and diffuse or diluted by other sources (Wolff et al., 2016). However, it has also been suggested during hard-spectrum SPEs, the protons would have high enough energy to ionise nitrogen in the lowermost stratosphere and upper troposphere (below $\sim 20$ km) to form $NO_x$ (Melott et al., 2016; Duderstadt et al., 2016). The $NO_x$ produced by SPEs is often assumed to be converted to $HNO_3$, which then deposited onto cloud droplets and transported downward to ground level as rain or snow (Melott et al., 2016). Hence, a significant and sharp enhancement in snow precipitation might be detected subsequent to a hard-spectrum SPEs.

Whereas anthropogenically produced $NO_x$ can have a strong influence on the wet deposition of $NO_3^-$ in the mid-latitude regions. A snow $NO_3^-$ concentration up to 2-10 times higher than those measured in the polar region had been measured in Tianshan, China (Zhang and Edwards, 2011). Therefore, the future version of the skin layer exchange model should include wet deposition and coupled with chemical transport model, i.e. Whole Atmosphere Community Climate Model, WACCM, that includes ionisation by SPEs, to provide a better estimation of $NO_3^-$ in skin layer snow.

To summarise, the future laboratory studies should focus on the redistribution of $NO_3^-$ in snow under temperature gradient and the future air-snow modeling development should include dry deposition of nitrate aerosol and wet deposition by coupling with chemical transport model.

## 6.3 Chemical Processes

The emission of $NO_x$ from snowpack to the overlying atmosphere is driven by the photolysis of $NO_3^-$ in snow, yet, the quantum yield for the photolysis of $NO_3^-$ is still remained as the one of the main uncertainties when estimating the emission flux of $NO_x$. In this study the quantum yield for the photolysis of $NO_3^-$ is parameterised as a function of temperature and wavelength (Chu and Anastasio, 2003). However, the quantum yield for the photolysis of $NO_3^-$ has also been suggested to be strongly dependent on the location of $NO_3^-$ within the snow grain (See Ch.1.2.5). Meusinger et al. (2014) recorded

that the quantum yield for loss of $NO_3^-$ by photolysis reaction, $\Phi_{R1+R2}$, reduced to only ~7 % of its original value after exposing to UV radiation at -15 °C for ~17-33 Antarctic sunny day equivalents ($N_{asd}$, of which $N_{asd}$ = 1 corresponds to the number of photons absorbed by nitrate in one sunny day at Dome C). They parameterised the quantum yield as an exponential function that depends on $N_{asd}$.

Despite the study of Meusinger et al. (2014) suggests the quantum yield reaches minimum ($\Phi_{R1+R2}$ = 0.003) after $N_{asd}$ =17-33, some parts of the Antarctica the $NO_3^-$ in snow can remains in the photic zone (the top ~ 30- 60 cm of the snowpack, France et al., 2011) up to 6.5 years due to the low accumulation rate. To access the applicability of the parameterisation for the entire snow column in the photic zone, especially for sites with low accumulation rate, the experiment should be repeated with snow samples collected at the various depth of the snowpack to examine if the quantum yield reduces further after even longer exposure of radiation. Meusinger et al. (2014) also suggested the quantum yield for loss of nitrate might be influenced by other factors, such as the chloride concentration and the snow type (wind-blown or wind-packed). Future laboratory studies should investigate how the presence of other impurities and size of the snow grain might have an impact on the quantum yield for loss of nitrate.

In the 1-D model presented in Ch. **??**, the interaction between air and snow is assumed to be multi-phased, which included an air-ice and/or an air-liquid micropocket interactions depending on the temperature. The only condensed-phase reactions (in ice and in liquid micropocket) are the photolysis of $NO_3^-$ and $NO_2^-$. The photochemically produced $NO_x$ and OH radical are transferred from the snow grain to the snow interstitial air (SIA) by assuming the quantum yield for photolysis of $NO_3^-$ has taken the cage effect into account. The partition of other species, such as $O_x$ and $HO_x$, between air and snow and the subsequence dissociation and condensed-phase reactions are not included in the newly developed air-snow model. The partitioning between air and ice, solubility in ice as well as the chemical reaction rates of those species are not clear and future studies should focus on parameterising the air-ice partitioning of different chemical species.

Neglecting the mass transfer into the liquid-micropocket, the subsequence aqueous-phase photolysis reactions and dissociation are also neglected, such as the photolysis of aqueous-phase $O_3$ to form $H_2O_2$ (R32), which can be further photolysed as OH (R33 ) or dissociated into hydrogen ion ($H^+$) and hydroperoxyl anion ($HO_2^-$, R35), and dissociation of $HO_2$ to $H^+$ and $O_2^-$ (R35)

as follow:

$$O_3 + hv\,(^{+}H_2O) \longrightarrow H_2O_2 + O_2 \tag{R32}$$

$$H_2O_2 + hv \longrightarrow 2\,OH \tag{R33}$$

$$H_2O_2 \rightleftharpoons H^+ + HO_2{}^- \tag{R34}$$

$$HO_2 \rightleftharpoons H^+ + O_2{}^- \tag{R35}$$

The dissociated ions could react with other species in the aqueous-phase, for example (a complete list of aqueous-phase photolysis reactions and reactions are described in details in Toyota et al., 2014):

$$OH + OH \longrightarrow H_2O_2 \tag{R36}$$

$$OH + HO_2 \longrightarrow H_2O + O_2 \tag{R37}$$

$$OH + O_2{}^- \longrightarrow OH^- + O_2 \tag{R38}$$

$$H_2O_2 + OH \longrightarrow HO_2 + H_2O \tag{R39}$$

$$HO_2 + HO_2 \longrightarrow H_2O_2 + O_2 \tag{R40}$$

$$HO_2 + O_2{}^- \longrightarrow HO_2{}^- + O_2 \tag{R41}$$

Therefore, neglecting the mass transfer of $HO_x$, $H_2O_2$ and $O_3$ between the liquid-micropocket and SIA might have an impact on there mixing ratio and the distribution within the SIA, especially the highly soluble $HO_x$ and $H_2O_2$. The future development should include these mass transfer and the subsequence dissociation and aqueous-phase reactions.

Besides the aqueous-phase reactions, the 1-D model is missing the snow chemistry of halogen, which been suggested to be important in polar boundary layer chemistry, especially for coastal sites or over sea ice that has the most deposition of sea salt aerosols onto the snow grain and sea ice (e.g. Saiz-Lopez et al., 2007; Simpson et al., 2007; Grannas et al., 2007). For example, the bromide (in the form of $Br^-$) contained in sea ice and snowpack can turn into reactive bromine (BrO and Br) via a series of heterogeneous and photochemical reactions (R42 & R43) then emit to the atmosphere. The reaction between reactive bromide and with $O_3$, which is one of the major pathways for $O_3$ destruction in the troposphere in polar region in spring time (Grannas et al.,

2007), can leads to a series of chain reactions, known as the bromine explosion, which included the following reactions (Simpson et al., 2007):

$$\mathrm{HOBr} + \mathrm{Br}^- + \mathrm{H}^+ \longrightarrow \mathrm{H_2O} + \mathrm{Br_2} \tag{R42}$$

$$\mathrm{Br_2} + \mathrm{hv} \longrightarrow 2\,\mathrm{Br} \tag{R43}$$

$$\mathrm{Br} + \mathrm{O_3} \longrightarrow \mathrm{BrO} + \mathrm{O_2} \tag{R44}$$

$$\mathrm{BrO} + \mathrm{HO_2} \longrightarrow \mathrm{HOBr} + \mathrm{O_2} \tag{R45}$$

$$\text{———————————} \tag{R46}$$

$$\mathrm{Net:}\,\mathrm{Br}^- + \mathrm{H}^+ + \mathrm{HO_2} + \mathrm{O_3} \longrightarrow \mathrm{Br} + \mathrm{H_2O} + 2\,\mathrm{O_2}$$

Note that the reaction R42 is a multi-phase reaction. It has been suggested that reaction R42 happens in the liquid brine solution co-exiting with ice, which might consist of 3 sub-step: 1) uptake of gas phase HOBr; 2) reaction in brine solution; and 3) releasing the dissolved $Br_2$ gas (Simpson et al., 2007). The 'Bromine explosion' or the halogen chemistry can significantly alter the concentration of tropospheric $O_3$, especially during springtime in polar regions when sunlight returns yet temperature remind low (< -20°C), which often referred as the "ozone depletion events" (ODEs).

The presence of halogen oxides (XO) can shorten the lifetime of $NO_x$ as well, via halogen oxidation process (Bauguitte et al., 2012).

$$\mathrm{NO} + \mathrm{XO} \longrightarrow \mathrm{X} + \mathrm{NO_2} \tag{R47}$$

$$\mathrm{NO_2} + \mathrm{XO} \xrightarrow{\mathrm{M}} \mathrm{XNO_3} \tag{R48}$$

Reaction R47 is a rapid reaction that the presence of halogen oxides can significantly decrease the ratio of $NO/NO_2$. Therefore, the chemistry of halogen and uptake of halogen nitrate should be included in the $NO_x$ cycle model, especially the site of interest is near the coast which has more influence from halogen compounds (Saiz-Lopez et al., 2007).

To summarise, the future laboratory studies should focus on the improving our knowledge on the quantum yield of the nitrate photolysis in snow as well as the partitioning of various species between air and snow and the future modeling development should includes the condensed-phase reactions and halogen chemistry .

## 6.4 Description of the Atmosphere

The model presented in Ch. **??** is constrained by the concentration of $HNO_3$ and $NO_x$ observed in the atmospheric boundary layer, ABL, above the snowpack with an assumption that the ABL is well mixed. However, the next generation models should include both chemical and physical processes in the ABL in order to describe the interactive processes between ABL and snowpack. Field studies have found the concentration of gas-phase species emitted from the snowpack to the overlying atmosphere is controlled mainly by the dynamic of the ABL, such as the height of the ABL and the turbulence diffusivity (King et al., 2006; Anderson and Neff, 2008; Frey et al., 2013).

The height of the ABL and the turbulence diffusivity both depends on the wind speed and temperature at the surface. The height of the ABL increases as surface wind speed and temperature increases. At low wind speed, the height of the ABL is mainly controlled by the surface temperature and would have a clear diurnal pattern, i.e. maximum ABL height is expected to occur at local noon concurrent the maximum surface temperature and minimum ABL height in the evening correspond to nighttime radiative cooling (Toyota et al., 2014). At high wind speed, the height of the ABL is mainly controlled by the surface wind speed rather than the temperature, i.e. the diurnal variation of the ABL height is insignificant at wind speed above 8 $\mathrm{ms}^{-1}$. Toyota et al. (2014) shown the maximum ABL height increased from 44 $\mathrm{m}$ to 268 $\mathrm{m}$ when the wind speed at 2 $\mathrm{m}$ above the surface increased from 2 $\mathrm{ms}^{-1}$ to 8 $\mathrm{ms}^{-1}$. The height of the ABL have an impact on the rate of accumulation of chemical species that emitted from the snow, i.e. a stable shallow ABL allows chemical species to accumulate a lot more rapidly than an unstable and turbulence ABL and hence resulted a high concentration in the ABL.

The vertical mixing in the ABL is through the action of buoyancy turbulence (free convection) and shear-driven turbulence (forced convection). The efficiency of the turbulent mixing can be described as the diffusion coefficient, $K_c$, which can be used to calculate the diffusive flux, $F$, of a trace gas by Fick's Law (Anderson and Neff, 2008):

$$F = K_c \frac{\partial C}{\partial z} \tag{6.1}$$

where $\frac{\partial C}{z}$ is the concentration gradient across two different heights. The diffusion coefficient, $K_c$, increase as temperature, wind speed, and ABL height increases. From Eq. 6.1, for a given concentration gradient, increase in $K_c$ would increase the flux.

Thus, increase in temperature and wind speed increases the ABL height and the diffusion coefficient, $K_c$, and, hence, the vertical mixing, which causes

the atmospheric concentration of the chemical species emitted by the snowpack to dilute. Therefore, a fully coupled atmosphere-snow model with an accurate description of the atmospheric boundary layer dynamics is required to predict the impact of snow emission to the overlying atmosphere. Future air-snow model development should be based on the existing air-snow chemistry models, such as MISTRA-SNOW (Thomas et al., 2011) or PHANTAS (Toyota et al., 2014), that coupled to the 1-D atmospheric boundary layer model describing the gas, aerosol and cloud droplet chemistry as well as dynamics and thermodynamics of the ABL.

Besides model development, as shown in Table 4 in Ch. 4, the air-snow interaction models are sensitive to the observed atmospheric concentration of $HNO_3$ and the measured concentration of $NO_3^-$ in the skin layer snow. In order to reduce model uncertainties, the snow samples of the skin layer should be collected more carefully and strictly restricted to from the top few mm rather than the top few cm. Moreover, both atmospheric concentration of $HNO_3$ and particulate nitrate (p-$NO_3^-$) should be measured simultaneously, such that the uptake of $HNO_3$ or p-$NO_3^-$ can be modelled separately.

## 6.5 Outlook

### 6.5.1 Validation Sites

It is the first time that two sets of year-round observations from two Antarctic sites, Dome C and Halley, are available for validating an air-snow interaction model. This is significant as the two sites have a very different atmospheric composition and significant meteorological differences (See Ch. 2.6.1). However, it will be beneficial to validate the models with long-time series obtained from other locations that might have a warmer temperature (occasionally above freezing) or larger daily temperature variation or has larger influence by anthropogenic pollutants, i.e the Arctic or Asian mountains. Moreover, the future field campaign should measure the concentration of atmospheric nitric acid and particulate nitrate, the concentration of $NO_3^-$ and the ionic strength from the snow at the top few mm of the snowpack as well as record the SSA and precipitation events to reduce the uncertainties in the model.

### 6.5.2 Air-Ice Interaction of Species Other than $HNO_3$

As mentioned in Ch. 1 that most current air-snow chemistry models assumed all the chemical reactions in snow take place in the DI, which has the same chemical properties as the aqueous solution, and hence, the rate of reactions are adopted from aqueous-phase and the partitioning between air and snow

is described by Henry's Law (e.g. Toyota et al., 2014). This work, as described in Ch. 4, suggests that liquid can co-exist with ice when the temperature is above the eutectic temperature and the liquid is in the form of micropocket located within grain boundaries or triple junction as suggested by Domine et al. (2013b). Under such conditions, the air-snow interaction is dominated by the partitioning between air and the liquid micropockets of which the partitioning of species between air and liquid micropocket can be expressed by Henry's Law. However, for temperatures below the eutectic temperature, the air-snow interaction is driven by the interaction (adsorption + solid-state diffusion) between air and ice. Therefore, the air-ice interaction of other species should not be neglected, especially at sites that experience low temperature. Future laboratory studies need to focus on gaining a better understanding of the thermodynamic and chemical properties, such as the air-ice partitioning, adsorption equilibrium, maximum adsorption site and solid-state diffusion coefficient, of various species in ice.

### 6.5.3 Modeling the Air-Snow Interaction of Other Acidic Gases

The partition of acidic gases and ice is not only important for understanding the $NO_x$ emission from snow but also for understanding the role of acidic hydrate in atmospheric chemistry. Acidic gas, such as hydrochloric acid (HCl), can be produced by volcanic eruptions, which is then removed from the troposphere by precipitation due to its high solubility. In the stratosphere, the anthropogenically produced chlorofluorocarbon (CFCs) can be broken down by the solar radiation to from active chlorine, i.e. chlorine radicals (Cl) and chlorine monoxide (ClO), which leads to a direct destruction of $O_3$ (Seinfeld and Pandis, 2012). The chlorine radical (Cl) can also react with methane ($CH_4$) to form HCl, which can be taken up by polar stratospheric cloud (PSC). Heterogeneous reactions of HCl with chlorine nitrate ($ClONO_2$) or hypochlorous acid (HOCl) can occur on PSC surface as follow (Huthwelker et al., 2006)

$$\mathrm{HCl} \longrightarrow \mathrm{H^+} + \mathrm{Cl^-} \tag{R49}$$

$$\mathrm{Cl^-} + \mathrm{ClONO_2} \longrightarrow \mathrm{Cl_2} + \mathrm{NO_3^-} \tag{R50}$$

$$\mathrm{Cl^-} + \mathrm{HOCl} \longrightarrow \mathrm{Cl_2} + \mathrm{OH^-} \tag{R51}$$

The molecular chlorine ($Cl_2$) that form on the PSC surface can then leave the surface to the gas phase. These are the reactions that responsible for the build up of high $Cl_2$ concentration in polar winter, which leads to significant $O_3$ destruction when the sun rises again in spring time in Antarctica. A phenomenon is known as the $O_3$ hole.

The interaction between HCl and ice has been studied intensely on ice clouds but ont on surface snow. The uptake mechanisms of HCl is found to be similar to the uptake of $HNO_3$, of which the adsorption of HCl molecules on ice is reversible and HCl can form solid-solution with ice. The air-ice interaction models presented in Ch. 4 should be modified for uptake of HCl and validated against field data.

### 6.5.4 Global Model

Box and 1-D exchange models are developed to describe the nitrogen cycle in the snowpack and the overlying atmosphere in the Antarctica and Arctic. Zatko et al. (2016a) also incorporate an idealised snowpack along with radiative transfer model into global transport model to estimate investigate the recycling and redistribution of reactive nitrogen and its spatial variability in Antartica and Greenland. However, up to 40 % of the land on Earth is snow-covered at given time that the photochemistry in snow might have a wider impact to the boundary layer chemistry elsewhere, such as high mountains in Asia or seasonal snowpack in urban area (Grannas et al., 2007).

The emission of $NO_x$ from snow in the urban area is expected to have a small contribution to the mixing ratios of total $NO_x$, OH and $O_3$ in the boundary layer as its proximity to pollution sources from heavy traffic, dense population and a lot of factories. Nevertheless, $NO_x$ flux from snow still requires a better understanding to evaluate the natural background levels of chemical species as well as the extent of anthropogenic pollution effect on the chemistry of the atmosphere, especially on the tropospheric $O_3$. Future model studies should focus incorporates a realistic snowpack with photochemistry and air-snow interaction into a global model to investigate the impacts of snow $NO_3^-$ photolysis and $NO_x$ recycling on boundary layer chemistry and radiative forcing in all snow covered area.

Moreover, this study found that the $e$-folding depth parameterisation can provide a reasonable estimation of photolysis rate coefficient profile in cold polar or heavily polluted snow, which is commonly found in urban area or high Asia mountains (Wang et al., 2014; Schmale et al., 2017, e.g.). In regions or area that those criteria do not meet, then a chemical species specific correction factor, $C$, can be applied to minimise the errors. Therefore, in the future, it is not necessary to incorporate a radiative transfer model to the global transport model when studying impacts of snow photochemistry, instead, uses the $e$-folding depth parameterisation to reduce the computational cost.

# Chapter 7

# Conclusion

The main aim of this study is to improve the parameterisation for quantifying the emission of $NO_x$ from snow to the overlying atmosphere and the findings of this study can be summarised as to four main points.

1) Radiative transfer models that contain a snow module, such as TUV by Lee-Taylor and Madronich (2002), can model the complex relationship between actinic flux, and hence the photolysis rate coefficient, and depth at the top few $\mathrm{cm}$ of the snowpack caused by the rapid changing contributions of direct and diffuse radiation, but it is computational costly when incorporated into larger scaled models. In this study, the impact of using a simple $e$-folding depth parameterisation to estimate the attenuation of actinic flux in the snowpack on the photochemical production rate compared to TUV was being assessed. It is concluded in the UV-A region (320-400 $\mathrm{nm}$), which is the wavelength range correspond to the photolysis reaction of $NO_3^-$, $NO_2^-$, $NO_2$ and $H_2O_2$, the simple $e$-folding depth parameterisation provides a comparable results to TUV for typical cold polar and wind-packed snowpack. The $e$-folding depth parameterisation causes underestimation (up to 30 % smaller) of photochemical production for melting or clean snowpack at solar zenith angles or effective solar zenith angle (e.g. on a slope) smaller than 37° due to the enhancement of actinic flux in the near-surface layer. The $e$-folding depth parameterisation for the photochemical production under those circumstances can be improved by applying the solar zenith angle dependent and chemical species specific correction factor, $C(\theta)$, and the computation cost can be reduced without compromising the accuracy.

2) The location of the reactive chemical species and the interactions between air and snow grain still remains as the major uncertainty in snow photochemistry. The modelling study presented here suggested the interface between air and snow is dominated by air-ice at all temperatures below melting of ice and that liquid co-exists as micropocket located between grain boundaries at temperature above eutectic temperature. The concentration of nitrate in snow can be described as non-equilibrium adsorption on ice and co-condensation couple with solid-state diffusion into the bulk, plus equilibrium

solvation into the liquid micropocket at temperatures above the eutectic. A non-equilibrium air-ice interaction is taken as the typical gas-phase concentration of $HNO_3$ in the Antarctica is low and the surface of the snow grain is likely to be dynamic due to the constantly existing temperature gradient that causes redistribution of water molecules. On the other hand, the volume of the co-existing liquid at temperatures above eutectic temperatures is likely to be small so that instantaneous equilibrium is possible. The air-snow grain exchange model developed based on these physical processes above has successfully reproduced the concentration of nitrate in surface snow at Dome C and Halley without requiring any tuning parameters.

3) The air-snow grain exchange modelling study also suggests the physical properties of the air-snow grain interface might change from those observed in solid ice to those observed in liquid water as the temperature increase towards the melting temperature and as the concentration of chemical impurities increases. Future laboratory experiments should focus on establishing a relationship between temperature and the physical properties of the air-snow grain interface.

4) An 1-D air-snow photochemical model incorporated a temperature dependent multi-phase interaction model, based on non-equilibrium adsorption on ice and co-condensation couple with solid-state diffusion into the bulk, plus equilibrium solvation into the liquid micropocket at temperatures above the eutectic, does not manage to reproduce the diurnal profile of $NO_x$ due to the poor model constraints and instability. The 1-D air-snow model has to be further developed to access if the temperature dependent multi-phase interaction model can represent the mass transfer of chemical species between SIA and snow grain. At it stand, the model predict an average emission flux of $NO_2$, $F_{NO_2}$, $3 \times 10^{12}\ \mathrm{molecule\,m^{-2}\,s^{-1}}$, which is almost half of the observed emission flux of $NO_x$ (Frey et al., 2013).

# Appendix A

# Maths Derviation

## A.1 Deviation of Mass Transfer Coefficient, $k_{mt}$

The mass transfer coefficient, $k_{mt}$, for transfer mass to and from gas-phase to condensed phase is deviated by assuming the fluxes of gas-phase diffusion, $J_g$ (Eq. 2.23), and interfacial mass transport, $J_b$ (Eq. 2.24), is equal:

$$\begin{aligned}
J_g &= J_b \\
-\frac{D_g}{r}(c_{g,\infty} - c_{g,\text{surf}}) &= \frac{\alpha\bar{v}}{4}\left(\frac{c_{c,\text{surf}}}{K} - c_{g,\text{surf}}\right) \\
\left(\frac{\alpha\bar{v}}{4} + \frac{D_g}{r}\right) c_{g,\text{surf}} &= \frac{\alpha\bar{v}}{4}\frac{c_{c,\text{surf}}}{K} + \frac{D_g}{r}c_{g,\infty} \\
c_{g,\text{surf}} &= \left(\frac{\alpha\bar{v}}{4} + \frac{D_g}{r}\right)^{-1}\left(\frac{\alpha\bar{v}}{4}\frac{c_{c,\text{surf}}}{K} + \frac{D_g}{r}c_{g,\infty}\right) \qquad \text{(A.1)}
\end{aligned}$$

Substituting Eq. A.1 to Eq. 2.22

$$\begin{aligned}
\frac{dc_c}{dt} &= \frac{A}{V}\frac{D_g}{r}(c_{g,\infty} - c_{g,\text{surf}}) \\
&= \frac{A}{V}\frac{D_g}{r}\left[c_{g,\infty} - \left(\frac{\alpha\bar{v}}{4} + \frac{D_g}{r}\right)^{-1}\frac{D_g}{r}c_{g,\infty} - \left(\frac{\alpha\bar{v}}{4} + \frac{D_g}{r}\right)^{-1}\left(\frac{\alpha\bar{v}}{4}\frac{c_{c,\text{surf}}}{K}\right)\right] \\
&= \frac{A}{V}\frac{D_g}{r}\left[\frac{\alpha\bar{v}r}{\alpha\bar{v}r + 4D_g}c_{g,\infty} - \frac{\alpha\bar{v}r}{\alpha\bar{v}r + 4D_g}\frac{c_{c,\text{surf}}}{K}\right] \\
&= \frac{A}{V}\left(\frac{\alpha\bar{v}r + 4D_g}{D_g\alpha\bar{v}}\right)^{-1}\left[c_{g,\infty} - \frac{c_{c,\text{surf}}}{K}\right] \\
&= \frac{A}{V}\left(\frac{r}{D_g} + \frac{4}{\bar{v}\alpha}\right)^{-1}\left[c_{g,\infty} - \frac{c_{c,\text{surf}}}{K}\right] \qquad \text{(A.2)}
\end{aligned}$$

For a liquid droplet with a radius $r$, Eq. A.2 is written as

$$\begin{aligned}
\frac{dc_a}{dt} &= \frac{4\pi r^2}{3/4\pi r^3}\left(\frac{r}{D_g} + \frac{4}{\bar{v}\alpha}\right)^{-1}\left[c_{g,\infty} - \frac{c_{a,\text{surf}}}{k_H^{cc}}\right] \\
&= \left(\frac{r^2}{3D_g} + \frac{4r}{3\bar{v}\alpha}\right)^{-1}\left[c_{g,\infty} - \frac{c_{a,\text{surf}}}{k_H^{cc}}\right] \qquad \text{(A.3)}
\end{aligned}$$

# Appendix B

# Reproduction of Fig. 6 in Ch. 2

For better readability the Fig. 6 in Ch. 2, “The impact of parameterising light penetration into snow on the photochemical production of $NO_x$ and OH radicals in snow", is reproduced below.

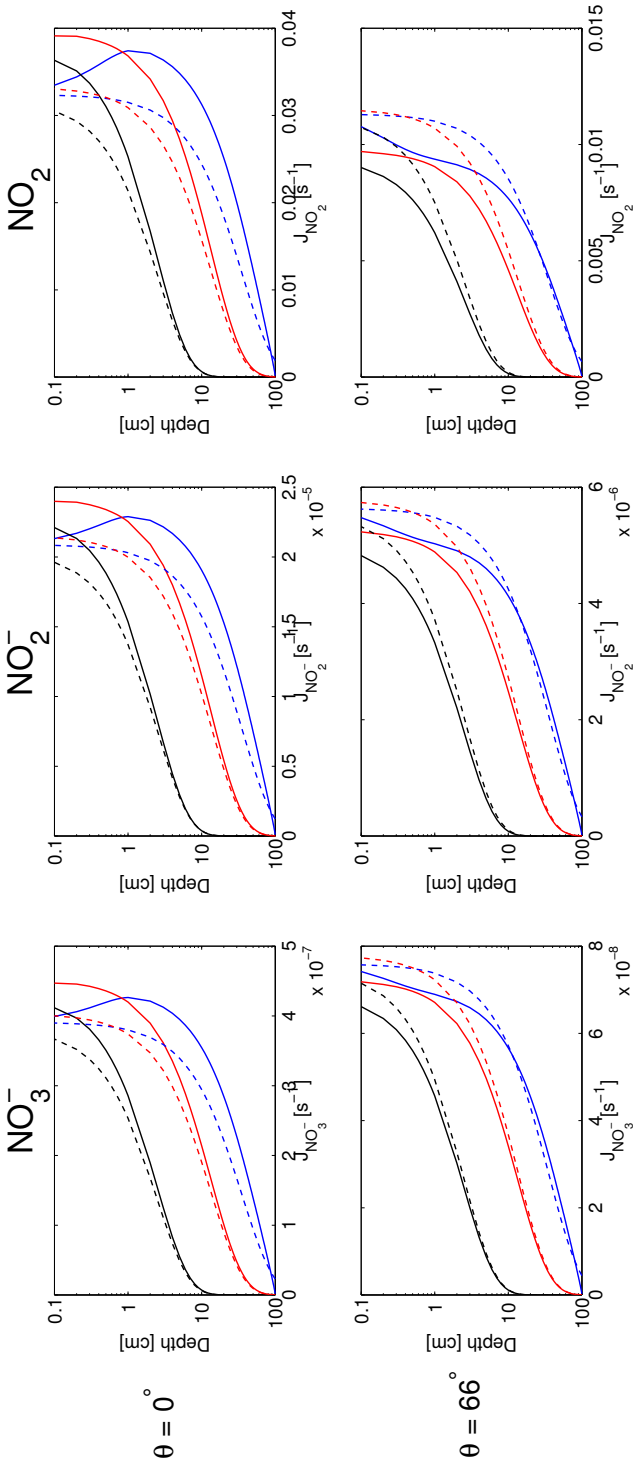


FIGURE B.1: Photolysis rate coefficient for the $NO_3^-$ anion (LH panels), the $NO_2^-$ anion (middle panels) and $NO_2$ (RH panels) computed by TUV (solid line) and $z_e$ method (dashed line) at two different solar zenith angles, $\theta$, at 0° (top row) and 66° (bottom row). At $\theta = 0°$ the transfer velocity ratio is maximum while minimum transfer velocity ratio when $\theta = \sim 66°$. Blue is the "melting snow", Scatt2, ($\rho = 0.4\,\mathrm{g\,cm^{-3}}$, $[BC] = 4\,\mathrm{ng(C)\,g^{-1}}$ and $\sigma_{scatt} = 2\,\mathrm{m^2\,kg^{-1}}$); red is the "standard snow", Standard, ($\rho = 0.4\,\mathrm{g\,cm^{-3}}$, $[BC] = 4\,\mathrm{ng(C)\,g^{-1}}$ and $\sigma_{scatt} = 25\,\mathrm{m^2\,kg^{-1}}$); and black is the "heavily polluted snow", BC128, ($\rho = 0.4\,\mathrm{g\,cm^{-3}}$, $[BC] = 128\,\mathrm{ng(C)\,g^{-1}}$ and $\sigma_{scatt} = 25\,\mathrm{m^2\,kg^{-1}}$). Surface (depth $= 0\,\mathrm{cm}$) values of photolysis rate coefficient from "RT method" and "$z_e$ method" are the same (see Eq. (??) for calculation of $J_{TUV}$). The deviation between the two methods was the largest for "melting snowpack", especially for small solar zenith angles, and the the $z_e$ method provided the best estimation compare with RT method with the "heavily polluted" snowpack.

# Bibliography


Abbatt, Jonathan P. D. (1997). In: *Geophysical Research Letters* 24.12, pp. 1479–1482. ISSN: 1944-8007. DOI: 10.1029/97GL01403. URL: http://dx.doi.org/10.1029/97GL01403.

— (2003). In: *Chemical Reviews* 103.12. PMID: 14664633, pp. 4783–4800. DOI: 10.1021/cr0206418. eprint: http://dx.doi.org/10.1021/cr0206418. URL: http://dx.doi.org/10.1021/cr0206418.

Ackermann, M. et al. (2006). "Optical properties of deep glacial ice at the South Pole". In: *Journal of Geophysical Research: Atmospheres* 111.D13. D13203, n/a–n/a. ISSN: 2156-2202. DOI: 10.1029/2005JD006687. URL: http://dx.doi.org/10.1029/2005JD006687.

Aguzzi, Arnaud, Benoit Fluckiger, and Michel J. Rossi (2003). "The nature of the interface and the diffusion coefficient of HCl/ice and HBr/ice in the temperature range 190-205 K". In: *Phys. Chem. Chem. Phys.* 5 (19), pp. 4157–4169. DOI: 10.1039/B308422C. URL: http://dx.doi.org/10.1039/B308422C.

Akinfiev, Nikolai N., Mikhail V. Mironenko, and Steven A. Grant (2001). "Thermodynamic Properties of NaCl Solutions at Subzero Temperatures". In: *Journal of Solution Chemistry* 30.12, pp. 1065–1080. ISSN: 1572-8927. DOI: 10.1023/A:1014445917207. URL: http://dx.doi.org/10.1023/A:1014445917207.

Albert, Mary R. (1996). "MOdeling heat, mass and species transport in polar firn". In: *International Glaciological Society* 23, pp. 138–143.

Albert, Mary R and Edward F Shultz (2002). "Snow and firn properties and air–snow transport processes at Summit, Greenland". In: *Atmospheric Environment* 36.15–16. Air/Snow/Ice Interactions in the Arctic: Results from {ALERT} 2000 and {SUMMIT} 2000, pp. 2789 –2797. ISSN: 1352-2310. DOI: https://doi.org/10.1016/S1352-2310(02)00119-X. URL: http://www.sciencedirect.com/science/article/pii/S135223100200119X.

Anderson, P. S. and W. D. Neff (2008). "Boundary layer physics over snow and ice". In: *Atmospheric Chemistry and Physics* 8.13, pp. 3563–3582. DOI: 10.5194/acp-8-3563-2008. URL: https://www.atmos-chem-phys.net/8/3563/2008/.

Appel, B.R. et al. (1984). "Artifact particulate sulfate and nitrate formation on filter media". In: *Atmospheric Environment (1967)* 18.2, pp. 409 –416. ISSN: 0004-6981. DOI: http://dx.doi.org/10.1016/0004-6981(84)90116-1. URL: http://www.sciencedirect.com/science/article/pii/0004698184901161.

Aristidi, E. et al. (2005). "An analysis of temperatures and wind speeds above Dome C, Antarctica". In: *AA* 430.2, pp. 739–746. DOI: 10.1051/0004-6361:20041876. URL: https://doi.org/10.1051/0004-6361:20041876.

Atkins, P. and J. de Paula (2010). *Atkins' Physical Chemistry*. OUP Oxford. ISBN: 9780199543373. URL: https://books.google.co.uk/books?id=BV6cAQAAQBAJ.

Atkinson, R. et al. (2004). "Evaluated kinetic and photochemical data for atmospheric chemistry: Volume I - gas phase reactions of $O_x$, $HO_x$, $NO_x$ and $SO_x$ species". In: *Atmospheric Chemistry and Physics* 4.6, pp. 1461–1738. DOI: 10.5194/acp-4-1461-2004. URL: https://www.atmos-chem-phys.net/4/1461/2004/.

BartelsRausch, T. et al. (2014). "A review of air- ice chemical and physical interactions (AICI) liquids, quasi-liquids, and solids in snow". In: *Atmospheric Chemistry and Physics* 14.3, pp. 1587–1633. DOI: 10.5194/acp-14-1587-2014. URL: http://www.atmos-chem-phys.net/14/1587/2014/.

Bauguitte, S. J.-B. et al. (2012). "Summertime $NO_x$ measurements during the CHABLIS campaign: can source and sink estimates unravel observed diurnal cycles?" In: *Atmospheric Chemistry and Physics* 12.2, pp. 989–1002. DOI: 10.5194/acp-12-989-2012. URL: https://www.atmos-chem-phys.net/12/989/2012/.

Beine, Harald J. et al. (2002). "NOx during background and ozone depletion periods at Alert: Fluxes above the snow surface". In: *Journal of Geophysical Research: Atmospheres* 107.D21. 4584, ACH 7–1–ACH 7–12. ISSN: 2156-2202. DOI: 10.1029/2002JD002082. URL: http://dx.doi.org/10.1029/2002JD002082.

Beyer, Keith D., and Anne R. Hansen (2002). "Phase Diagram of the Nitric Acid/Water System Implications for Polar Stratospheric Clouds". In: *The Journal of Physical Chemistry A* 106.43, pp. 10275–10284. DOI: 10.1021/jp025535o. eprint: http://dx.doi.org/10.1021/jp025535o. URL: http://dx.doi.org/10.1021/jp025535o.

Bjorkman, Mats P. et al. (2014). "Nitrate postdeposition processes in Svalbard surface snow". In: *Journal of Geophysical Research: Atmospheres* 119.22.

2013JD021234, pp. 12,953–12,976. ISSN: 2169-8996. DOI: 10.1002/2013JD021234. URL: http://dx.doi.org/10.1002/2013JD021234.

Blunier, Thomas et al. (2005). "Isotopic view on nitrate loss in Antarctic surface snow". In: *Geophysical Research Letters* 32.13. L13501, n/a–n/a. ISSN: 1944-8007. DOI: 10.1029/2005GL023011. URL: http://dx.doi.org/10.1029/2005GL023011.

Bock, J., J. Savarino, and G. Picard (2016). "Air–snow exchange of nitrate: a modelling approach to investigate physicochemical processes in surface snow at Dome C, Antarctica". In: *Atmospheric Chemistry and Physics* 16.19, pp. 12531–12550. DOI: 10.5194/acp-16-12531-2016. URL: http://www.atmos-chem-phys.net/16/12531/2016/.

Burkholder, J. B. et al. (2015). "Chemical Kinetics and Photochemical Data for Use in Atmospheric Studies, Evaluation No. 18". In: *JPL Publication 15-10, Jet Propulsion Laboratory, Pasadena*.

Chan, H. G., M. D. King, and M. M. Frey (2015). "The impact of parameterising light penetration into snow on the photochemical production of $NO_x$ and OH radicals in snow". In: *Atmospheric Chemistry and Physics* 15.14, pp. 7913–7927. DOI: 10.5194/acp-15-7913-2015. URL: http://www.atmos-chem-phys.net/15/7913/2015/.

Chan, H. G., M. M. Frey, and M. D. King (2016). "Modeling the Physical Multi-Phase Interactions of HNO3 Between Snow and Air on the Antarctic Plateau (Dome C) and coast (Halley)". In: *Atmospheric Chemistry and Physics Discussions* 2016, pp. 1–40. DOI: 10.5194/acp-2016-1069. URL: http://www.atmos-chem-phys-discuss.net/acp-2016-1069/.

Chen, G. et al. (2001). "An investigation of South Pole HOx chemistry: Comparison of model results with ISCAT observations". In: *Geophysical Research Letters* 28.19, pp. 3633–3636. ISSN: 1944-8007. DOI: 10.1029/2001GL013158. URL: http://dx.doi.org/10.1029/2001GL013158.

Cho, H. et al. (2002). "NMR Investigation of the Quasi-Brine Layer in Ice/Brine Mixtures". In: *The Journal of Physical Chemistry B* 106.43, pp. 11226–11232. DOI: 10.1021/jp020449. eprint: http://dx.doi.org/10.1021/jp020449+. URL: http://dx.doi.org/10.1021/jp020449+.

Chu, Liang and Cort Anastasio (2003). "Quantum Yields of Hydroxyl Radical and Nitrogen Dioxide from the Photolysis of Nitrate on Ice". In: *The Journal of Physical Chemistry A* 107.45, pp. 9594–9602. DOI: 10.1021/jp0349132. eprint: http://pubs.acs.org/doi/pdf/10.1021/jp0349132. URL: http://pubs.acs.org/doi/abs/10.1021/jp0349132.

Chu, Liang and Cort Anastasio (2005). "Formation of Hydroxyl Radical from the Photolysis of Frozen Hydrogen Peroxide". In: *The Journal of Physical Chemistry A* 109.28, pp. 6264–6271. DOI: 10.1021/jp051415f. eprint: http://pubs.acs.org/doi/pdf/10.1021/jp051415f. URL: http://pubs.acs.org/doi/abs/10.1021/jp051415f.

— (2007). "Temperature and Wavelength Dependence of Nitrite Photolysis in Frozen and Aqueous Solutions". In: *Environmental Science Technology* 41.10, pp. 3626–3632. DOI: 10.1021/es062731q. eprint: http://pubs.acs.org/doi/pdf/10.1021/es062731q. URL: http://pubs.acs.org/doi/abs/10.1021/es062731q.

Colbeck, S. C. (1982). "An overview of seasonal snow metamorphism". In: *Reviews of Geophysics* 20.1, pp. 45–61. ISSN: 1944-9208. DOI: 10.1029/RG020i001p00045. URL: http://dx.doi.org/10.1029/RG020i001p00045.

Courville, Z. R. et al. (2007). "Impacts of an accumulation hiatus on the physical properties of firn at a low-accumulation polar site". In: *Journal of Geophysical Research: Earth Surface* 112.F2. F02030, n/a–n/a. ISSN: 2156-2202. DOI: 10.1029/2005JF000429. URL: http://dx.doi.org/10.1029/2005JF000429.

Cox, R. A. et al. (2005). "A kinetic model for uptake of HNO3 and HCl on ice in a coated wall flow system". In: *Phys. Chem. Chem. Phys.* 7 (19), pp. 3434–3442. DOI: 10.1039/B506683B. URL: http://dx.doi.org/10.1039/B506683B.

Crowley, J. N. et al. (2010). "Evaluated kinetic and photochemical data for atmospheric chemistry: Volume V ,§? heterogeneous reactions on solid substrates". In: *Atmospheric Chemistry and Physics* 10.18, pp. 9059–9223. DOI: 10.5194/acp-10-9059-2010. URL: http://www.atmos-chem-phys.net/10/9059/2010/.

Cunningham, J. and E.D. Waddington (1993). "Air flow and dry deposition of non-sea salt sulfate in polar firn: Paleoclimatic implications". In: *Atmospheric Environment. Part A. General Topics* 27.17, pp. 2943 –2956. ISSN: 0960-1686. DOI: http://dx.doi.org/10.1016/0960-1686(93)90327-U. URL: http://www.sciencedirect.com/science/article/pii/096016869390327U.

Dam, Brie Van et al. (2015). "Dynamics of ozone and nitrogen oxides at Summit, Greenland: I. Multi-year observations in the snowpack". In: *Atmospheric Environment* 123, Part A, pp. 268 –284. ISSN: 1352-2310. DOI: https://doi.org/10.1016/j.atmosenv.2015.09.060. URL: http://www.sciencedirect.com/science/article/pii/S1352231015304027.

Davis, Douglas D. et al. (2008). "A reassessment of Antarctic plateau reactive nitrogen based on {ANTCI} 2003 airborne and ground based measurements". In: *Atmospheric Environment* 42.12. Antarctic Tropospheric Chemistry Investigation (ANTCI) 2003, pp. 2831 –2848. ISSN: 1352-2310. DOI: http://dx.doi.org/10.1016/j.atmosenv.2007.07.039. URL: http://www.sciencedirect.com/science/article/pii/S1352231007006425.

Dibb, Jack E. et al. (1998). "Air-Snow Exchange of HNO3 and NOy at Summit, Greenland." In: *Journal of Geophysical Research: Atmospheres* 103.D3. 3475. ISSN: 3475-3486. DOI: 10.1029/97jd03132. URL: http://nrs.harvard.edu/urn-3:HUL.InstRepos:14121848.

Domine, F. et al. (2008). "Snow physics as relevant to snow photochemistry". In: *Atmospheric Chemistry and Physics* 8.2, pp. 171–208. DOI: 10.5194/acp-8-171-2008. URL: http://www.atmos-chem-phys.net/8/171/2008/.

Domine, F. et al. (2013a). "Seasonal evolution of snow permeability under equi-temperature and temperature-gradient conditions". In: *The Cryosphere* 7.6, pp. 1915–1929. DOI: 10.5194/tc-7-1915-2013. URL: https://www.the-cryosphere.net/7/1915/2013/.

Dominé, Florent and Emmanuel Thibert (1996). "Mechanism of incorporation of trace gases in ice grown from the gas phase". In: *Geophysical Research Letters* 23.24, pp. 3627–3630. ISSN: 1944-8007. DOI: 10.1029/96GL03290. URL: http://dx.doi.org/10.1029/96GL03290.

Domine, Florent et al. (1995). "Determining past atmospheric HCl mixing ratios from ice core analyses". In: *Journal of Atmospheric Chemistry* 21.2, pp. 165–186. ISSN: 1573-0662. DOI: 10.1007/BF00696579. URL: http://dx.doi.org/10.1007/BF00696579.

Domine, Florent et al. (2013b). "Can We Model Snow Photochemistry? Problems with the Current Approaches". In: *The Journal of Physical Chemistry A* 117.23. PMID: 23597185, pp. 4733–4749. DOI: 10.1021/jp3123314. eprint: http://dx.doi.org/10.1021/jp3123314. URL: http://dx.doi.org/10.1021/jp3123314.

Duderstadt, Katharine A. et al. (2016). "Nitrate ion spikes in ice cores not suitable as proxies for solar proton events". In: *Journal of Geophysical Research: Atmospheres* 121.6. 2015JD023805, pp. 2994–3016. ISSN: 2169-8996. DOI: 10.1002/2015JD023805. URL: http://dx.doi.org/10.1002/2015JD023805.

Erbland, J. et al. (2013). "Air-snow transfer of nitrate on the East Antarctic Plateau-Part 1: Isotopic evidence for a photolytically driven dynamic equilibrium in summer". In: *Atmospheric Chemistry and Physics* 13.13, pp. 6403–

6419. DOI: 10.5194/acp-13-6403-2013. URL: http://www.atmos-chem-phys.net/13/6403/2013/.

Eyring, Henry (1962). "Photochemistry of Air Pollution." In: *Science* 135.3502, pp. 427–428. ISSN: 0036-8075. DOI: 10.1126/science.135.3502.427-b. eprint: http://science.sciencemag.org/content/135/3502/427.3.full.pdf. URL: http://science.sciencemag.org/content/135/3502/427.3.

Fahidy, Thomas Z. (1993). "Activity coefficients in electrolyte solutions (second edition), edited by Kenneth S. Pitzer, 1991, 542 + vi pages, CRC Press, Boca Raton, FL; ISBN 0-8493-5415-3. Price: US$ 195.00". In: *The Canadian Journal of Chemical Engineering* 71.3, pp. 494–494. DOI: 10.1002/cjce.5450710328. URL: http://dx.doi.org/10.1002/cjce.5450710328.

Fitz, Dennis R. (2002). *Evaluation of Diffusion Denuder Coatings for Removing Acid Gases from Ambient Air*. Tech. rep. EPA-454R-02-011. United States Environmental Protection Agency.

Flanner, Mark G. and Charles S. Zender (2006). "Linking snowpack microphysics and albedo evolution". In: *Journal of Geophysical Research: Atmospheres* 111.D12. D12208, n/a–n/a. ISSN: 2156-2202. DOI: 10.1029/2005JD006834. URL: http://dx.doi.org/10.1029/2005JD006834.

Fowler, D. et al. (2008). *Ground-level ozone in the 21st century: future trends, impacts and policy implications*. Vol. 15/08. Science Policy. Prof. David Fowler was Chair of the Working Group. London: The Royal Society. URL: http://nora.nerc.ac.uk/8577/.

France, J. L. et al. (2011). "Snow optical properties at Dome C (Concordia), Antarctica implications for snow emissions and snow chemistry of reactive nitrogen". In: *Atmospheric Chemistry and Physics* 11.18, pp. 9787–9801. DOI: 10.5194/acp-11-9787-2011. URL: http://www.atmos-chem-phys.net/11/9787/2011/.

Frey, M. M. et al. (2009). "Photolysis imprint in the nitrate stable isotope signal in snow and atmosphere of East Antarctica and implications for reactive nitrogen cycling". In: *Atmospheric Chemistry and Physics* 9.22, pp. 8681–8696. DOI: 10.5194/acp-9-8681-2009. URL: http://www.atmos-chem-phys.net/9/8681/2009/.

Frey, M. M. et al. (2013). "The diurnal variability of atmospheric nitrogen oxides (NO and $NO_2$) above the Antarctic Plateau driven by atmospheric stability and snow emissions". In: *Atmospheric Chemistry and Physics* 13.6, pp. 3045–3062. DOI: 10.5194/acp-13-3045-2013. URL: http://www.atmos-chem-phys.net/13/3045/2013/.

Frey, M. M. et al. (2015). "Atmospheric nitrogen oxides (NO and $NO_2$) at Dome C, East Antarctica, during the OPALE campaign". In: *Atmospheric*

*Chemistry and Physics* 15.14, pp. 7859–7875. DOI: 10.5194/acp-15-7859-2015. URL: https://www.atmos-chem-phys.net/15/7859/2015/.

Fu, Fengfu et al. (2008). "Difference between low-volume and high-volume Andersen samplers in measuring atmospheric aerosols". In: *Particuology* 6.3, pp. 218 –222. ISSN: 1674-2001. DOI: https://doi.org/10.1016/j.partic.2008.01.005. URL: http://www.sciencedirect.com/science/article/pii/S1674200108000473.

Gallée, H. et al. (2015). "Characterization of the boundary layer at Dome C (East Antarctica) during the OPALE summer campaign". In: *Atmospheric Chemistry and Physics* 15.11, pp. 6225–6236. DOI: 10.5194/acp-15-6225-2015. URL: http://www.atmos-chem-phys.net/15/6225/2015/.

Gallet, J.-C. et al. (2011). "Vertical profile of the specific surface area and density of the snow at Dome C and on a transect to Dumont D'Urville, Antarctica - albedo calculations and comparison to remote sensing products". In: *The Cryosphere* 5.3, pp. 631–649. DOI: 10.5194/tc-5-631-2011. URL: http://www.the-cryosphere.net/5/631/2011/.

Goodman, A. L., G. M. Underwood, and V. H. Grassian (2000). "A laboratory study of the heterogeneous reaction of nitric acid on calcium carbonate particles". In: *Journal of Geophysical Research: Atmospheres* 105.D23, pp. 29053–29064. ISSN: 2156-2202. DOI: 10.1029/2000JD900396. URL: http://dx.doi.org/10.1029/2000JD900396.

Grannas, A. M. et al. (2007). "An overview of snow photochemistry: evidence, mechanisms and impacts". In: *Atmospheric Chemistry and Physics* 7.16, pp. 4329–4373. DOI: 10.5194/acp-7-4329-2007. URL: http://www.atmos-chem-phys.net/7/4329/2007/.

Hamer, Walter J. and Yung Chi Wu (1972). "Osmotic Coefficients and Mean Activity Coefficients of Uni-univalent Electrolytes in Water at 25 °C". In: *Journal of Physical and Chemical Reference Data* 1.4, pp. 1047–1100. DOI: 10.1063/1.3253108. eprint: http://dx.doi.org/10.1063/1.3253108. URL: http://dx.doi.org/10.1063/1.3253108.

Haynes, W.M. (2016). *CRC Handbook of Chemistry and Physics, 97th Edition*. CRC Press. ISBN: 9781498754293. URL: https://books.google.co.uk/books?id=VVezDAAAQBAJ.

Hobbs, P.V. (1974). *Ice Physics*. Clarendon Press. ISBN: 9780198519362. URL: https://books.google.co.uk/books?id=2o8JAQAAIAAJ.

Honrath, R. E. et al. (1999). "Evidence of NOx production within or upon ice particles in the Greenland snowpack". In: *Geophysical Research Letters*

26.6, pp. 695–698. ISSN: 1944-8007. DOI: 10.1029/1999GL900077. URL: http://dx.doi.org/10.1029/1999GL900077.

Honrath, R. E. et al. (2000). "Release of NOx from sunlight-irradiated mid-latitude snow". In: *Geophysical Research Letters* 27.15, pp. 2237–2240. ISSN: 1944-8007. DOI: 10.1029/1999GL011286. URL: http://dx.doi.org/10.1029/1999GL011286.

Hudson, Paula K. et al. (2002). "Uptake of Nitric Acid on Ice at Tropospheric Temperatures: Implications for Cirrus Clouds". In: *The Journal of Physical Chemistry A* 106.42, pp. 9874–9882. DOI: 10.1021/jp020508jÃĎÃź. eprint: http://dx.doi.org/10.1021/jp020508j. URL: http://dx.doi.org/10.1021/jp020508j.

Huthwelker, Thomas et al. (2004). In: *The Journal of Physical Chemistry A* 108.30, pp. 6302–6318. DOI: 10.1021/jp0309623. eprint: http://dx.doi.org/10.1021/jp0309623. URL: http://dx.doi.org/10.1021/jp0309623.

Huthwelker, Thomas, Markus Ammann, and Thomas Peter (2006). "The Uptake of Acidic Gases on Ice". In: *Chemical Reviews* 106.4. PMID: 16608185, pp. 1375–1444. DOI: 10.1021/cr020506v. eprint: http://dx.doi.org/10.1021/cr020506v. URL: http://dx.doi.org/10.1021/cr020506v.

Hutterli, Manuel A. and Regine Rothlisberger (1999). "Atmosphere-to-snow-to-firn transfer studies of HCHO at Summit, Greenland". In: *GEOPHYSICAL RESEARCH LETTERS* 26.12, pp. 1691–1694.

Hutterli, Manuel A. et al. (2003). "Sensitivity of hydrogen peroxide (H2O2) and formaldehyde (HCHO) preservation in snow to changing environmental conditions: Implications for ice core records". In: *Journal of Geophysical Research: Atmospheres* 108.D1. 4023, ACH 6–1–ACH 6–9. ISSN: 2156-2202. DOI: 10.1029/2002JD002528. URL: http://dx.doi.org/10.1029/2002JD002528.

Iizuka, Yoshinori et al. (2016). "Spatial distributions of soluble salts in surface snow of East Antarctica". In: *Tellus B: Chemical and Physical Meteorology* 68.1, p. 29285. DOI: 10.3402/tellusb.v68.29285. eprint: http://dx.doi.org/10.3402/tellusb.v68.29285. URL: http://dx.doi.org/10.3402/tellusb.v68.29285.

Ivanov, Andrey V. et al. (2007). "OH, HO2, and Ozone Gaseous Diffusion Coefficients". In: *The Journal of Physical Chemistry A* 111.9. PMID: 17298040, pp. 1632–1637. DOI: 10.1021/jp066558w. eprint: http://dx.doi.org/10.1021/jp066558w. URL: http://dx.doi.org/10.1021/jp066558w.

Jacobi, Hans-Werner et al. (2004). "Reactive trace gases measured in the interstitial air of surface snow at Summit, Greenland". In: *Atmospheric Environment* 38.12, pp. 1687 –1697. ISSN: 1352-2310. DOI: http://dx.doi.org/10.1016/j.atmosenv.2004.01.004. URL: http://www.sciencedirect.com/science/article/pii/S1352231004000561.

Jacobson, Mark Z. (1999). *Fundamentals of Atmospheric Modeling*. 2nd ed. Cambridge University Press, p. 828. ISBN: 9780521548656. URL: http://www.cambridge.org/us/academic/subjects/earth-and-environmental-science/atmospheric-science-and-meteorology/fundamentals-atmospheric-modeling-2nd-edition.

Jacobson, M.Z. (2005). *Fundamentals of Atmospheric Modeling*. Cambridge University Press. ISBN: 9780521548656. URL: https://books.google.co.uk/books?id=96wWzoyKRMoC.

Jones, A. E. et al. (2000). "Speciation and rate of photochemical NO and NO2 production in Antarctic snow". In: *Geophysical Research Letters* 27.3, pp. 345–348. ISSN: 1944-8007. DOI: 10.1029/1999GL010885. URL: http://dx.doi.org/10.1029/1999GL010885.

Jones, A. E. et al. (2001). "Measurements of NOx emissions from the Antarctic snowpack". In: *Geophysical Research Letters* 28.8, pp. 1499–1502. ISSN: 1944-8007. DOI: 10.1029/2000GL011956. URL: http://dx.doi.org/10.1029/2000GL011956.

Jones, A. E. et al. (2008). "Chemistry of the Antarctic Boundary Layer and the Interface with Snow: an overview of the CHABLIS campaign". In: *Atmospheric Chemistry and Physics* 8.14, pp. 3789–3803. DOI: 10.5194/acp-8-3789-2008. URL: http://www.atmos-chem-phys.net/8/3789/2008/.

Ketcham, W. M. and P. V. Hobbs (1969). "An experimental determination of the surface energies of ice". In: *Philosophical Magazine* 19.162, pp. 1161–1173. DOI: 10.1080/14786436908228641. eprint: http://dx.doi.org/10.1080/14786436908228641. URL: http://dx.doi.org/10.1080/14786436908228641.

King, J. C., S. A. Argentini, and P. S. Anderson (2006). "Contrasts between the summertime surface energy balance and boundary layer structure at Dome C and Halley stations, Antarctica". In: *Journal of Geophysical Research: Atmospheres* 111.D2. D02105, n/a–n/a. ISSN: 2156-2202. DOI: 10.1029/2005JD006130. URL: http://dx.doi.org/10.1029/2005JD006130.

Krepelova, Adela et al. (2010). "The nature of nitrate at the ice surface studied by XPS and NEXAFS". In: *Phys. Chem. Chem. Phys.* 12 (31), pp. 8870–8880. DOI: 10.1039/C0CP00359J. URL: http://dx.doi.org/10.1039/C0CP00359J.

Kukui, A. et al. (2014). "Measurements of OH and $RO_2$ radicals at Dome C, East Antarctica". In: *Atmospheric Chemistry and Physics* 14.22, pp. 12373–12392. DOI: 10.5194/acp-14-12373-2014. URL: https://www.atmos-chem-phys.net/14/12373/2014/.

Lafon, Sandra et al. (2006). "Characterization of iron oxides in mineral dust aerosols: Implications for light absorption". In: *Journal of Geophysical Research: Atmospheres* 111.D21. D21207, n/a–n/a. ISSN: 2156-2202. DOI: 10.1029/2005JD007016. URL: http://dx.doi.org/10.1029/2005JD007016.

Lee-Taylor, Julia and Sasha Madronich (2002). "Calculation of actinic fluxes with a coupled atmosphere–snow radiative transfer model". In: *JOURNAL OF GEOPHYSICAL RESEARCH* 107.D24, p. 4796.

Liao, W. and D. Tan (2008). "1-D Air-snowpack modeling of atmospheric nitrous acid at South Pole during ANTCI 2003". In: *Atmospheric Chemistry and Physics* 8.23, pp. 7087–7099. DOI: 10.5194/acp-8-7087-2008. URL: http://www.atmos-chem-phys.net/8/7087/2008/.

Libois, Q. et al. (2014). "Experimental determination of the absorption enhancement parameter of snow". In: *Journal of Glaciology* 60, pp. 714–724.

Linke, C. et al. (2006). "Optical properties and mineralogical composition of different Saharan mineral dust samples: a laboratory study". In: *Atmospheric Chemistry and Physics* 6.11, pp. 3315–3323. DOI: 10.5194/acp-6-3315-2006. URL: https://www.atmos-chem-phys.net/6/3315/2006/.

Lodge Jr, James (1989). "ES&T Books: Methods of Air Sampling and Analysis, 3rd ed." In: *Environmental Science & Technology* 23.8, pp. 938–938. DOI: 10.1021/es00066a606. eprint: http://dx.doi.org/10.1021/es00066a606. URL: http://dx.doi.org/10.1021/es00066a606.

Mahalinganathan, K. and M. Thamban (2016). "Potential genesis and implications of calcium nitrate in Antarctic snow". In: *The Cryosphere* 10.2, pp. 825–836. DOI: 10.5194/tc-10-825-2016. URL: https://www.the-cryosphere.net/10/825/2016/.

McCabe, Justin R., Mark H. Thiemens, and Joel Savarino (2007). "A record of ozone variability in South Pole Antarctic snow: Role of nitrate oxygen isotopes". In: *Journal of Geophysical Research: Atmospheres* 112.D12. D12303, n/a–n/a. ISSN: 2156-2202. DOI: 10.1029/2006JD007822. URL: http://dx.doi.org/10.1029/2006JD007822.

McConnell, Joseph R. et al. (1997). "Physically based inversion of surface snow concentrations of H2O2 to atmospheric concentrations at South Pole". In: *Geophysical Research Letters* 24.4, pp. 441–444. ISSN: 1944-8007. DOI:

10.1029/97GL00183. URL: http://dx.doi.org/10.1029/97GL00183.

McConnell, Joseph R. et al. (1998). "Physically based modeling of atmosphere-to-snow-to-firn transfer of H2O2 at South Pole". In: *Journal of Geophysical Research: Atmospheres* 103.D9, pp. 10561–10570. ISSN: 2156-2202. DOI: 10.1029/98JD00460. URL: http://dx.doi.org/10.1029/98JD00460.

Melott, Adrian L. et al. (2016). "Atmospheric ionization by high-fluence, hard-spectrum solar proton events and their probable appearance in the ice core archive". In: *Journal of Geophysical Research: Atmospheres* 121.6, pp. 3017–3033. ISSN: 2169-8996. DOI: 10.1002/2015JD024064. URL: http://dx.doi.org/10.1002/2015JD024064.

Merrill, John T., Mitsuo Uematsu, and Rainer Bleck (1989). "Meteorological analysis of long range transport of mineral aerosols over the North Pacific". In: *Journal of Geophysical Research: Atmospheres* 94.D6, pp. 8584–8598. ISSN: 2156-2202. DOI: 10.1029/JD094iD06p08584. URL: http://dx.doi.org/10.1029/JD094iD06p08584.

Meusinger, Carl et al. (2014). "Laboratory study of nitrate photolysis in Antarctic snow. I. Observed quantum yield, domain of photolysis, and secondary chemistry". In: *The Journal of Chemical Physics* 140.24, p. 244305. DOI: 10.1063/1.4882898. eprint: http://dx.doi.org/10.1063/1.4882898. URL: http://dx.doi.org/10.1063/1.4882898.

Michalski, G. et al. (2005). "Isotopic composition of Antarctic Dry Valley nitrate: Implications for NOy sources and cycling in Antarctica". In: *Geophysical Research Letters* 32.13. L13817, n/a–n/a. ISSN: 1944-8007. DOI: 10.1029/2004GL022121. URL: http://dx.doi.org/10.1029/2004GL022121.

Morin, Samuel et al. (2008). "Tracing the Origin and Fate of NOx in the Arctic Atmosphere Using Stable Isotopes in Nitrate". In: *Science* 322.5902, pp. 730–732. ISSN: 0036-8075. DOI: 10.1126/science.1161910. eprint: http://science.sciencemag.org/content/322/5902/730.full.pdf. URL: http://science.sciencemag.org/content/322/5902/730.

Murray, Keenan A. et al. (2015). "Dynamics of ozone and nitrogen oxides at Summit, Greenland. II. Simulating snowpack chemistry during a spring high ozone event with a 1-D process-scale model". In: *Atmospheric Environment* 117, pp. 110 –123. ISSN: 1352-2310. DOI: http://dx.doi.org/10.1016/j.atmosenv.2015.07.004. URL: http://www.sciencedirect.com/science/article/pii/S135223101530203X.

Painter, Thomas H. et al. (2007). "Impact of disturbed desert soils on duration of mountain snow cover". In: *Geophysical Research Letters* 34.12. L12502,

n/a–n/a. ISSN: 1944-8007. DOI: 10.1029/2007GL030284. URL: http://dx.doi.org/10.1029/2007GL030284.

Paterson, W.S.B. (1994). *The Physics of Glaciers*. Ed. by W.S.B. Paterson. 3rd ed. Birlington, USA: Butterworth Heinemann.

Picard, G. et al. (2016). "Development and calibration of an automatic spectral albedometer to estimate near-surface snow SSA time series". In: *The Cryosphere* 10.3, pp. 1297–1316. DOI: 10.5194/tc-10-1297-2016. URL: http://www.the-cryosphere.net/10/1297/2016/.

Picard, Ghislain et al. (2016). *Time-series of snow spectral albedo and superficial snow specific surface area at Dome C in Antarctica, 2012-2015*. data set. Supplement to: Picard, G et al. (2016): Development and calibration of an automatic spectral albedometer to estimate near-surface snow SSA time series. The Cryosphere, 10(3), 1297-1316, doi:10.5194/tc-10-1297-2016. DOI: 10.1594/PANGAEA.860945. URL: https://doi.pangaea.de/10.1594/PANGAEA.860945.

Pietroni, Ilaria, Stefania Argentini, and Igor Petenko (2014). "One Year of Surface-Based Temperature Inversions at Dome C, Antarctica". In: *Boundary-Layer Meteorology* 150.1, pp. 131–151. ISSN: 1573-1472. DOI: 10.1007/s10546-013-9861-7. URL: http://dx.doi.org/10.1007/s10546-013-9861-7.

Pinzer, B. R., M. Schneebeli, and T. U. Kaempfer (2012). "Vapor flux and recrystallization during dry snow metamorphism under a steady temperature gradient as observed by time-lapse micro-tomography". In: *The Cryosphere* 6.5, pp. 1141–1155. DOI: 10.5194/tc-6-1141-2012. URL: http://www.the-cryosphere.net/6/1141/2012/.

Press, W. H. et al. (1996). *Numerical Recipe in Fortran 90, Second Edition*. 2nd ed. Cambridge Univeristy Press.

Rothlisberger, Regine et al. (2000). "Factors controlling nitrate in ice cores: Evidence from the Dome C deep ice core". In: *Journal of Geophysical Research: Atmospheres* 105.D16, pp. 20565–20572. ISSN: 2156-2202. DOI: 10.1029/2000JD900264. URL: http://dx.doi.org/10.1029/2000JD900264.

Saiz-Lopez, Alfonso et al. (2007). "Boundary Layer Halogens in Coastal Antarctica". In: *Science* 317.5836, pp. 348–351. ISSN: 0036-8075. DOI: 10.1126/science.1141408. eprint: http://science.sciencemag.org/content/317/5836/348.full.pdf. URL: http://science.sciencemag.org/content/317/5836/348.

Sander, Rolf (1999). "Modeling Atmospheric Chemistry: Interactions between Gas-Phase Species and Liquid Cloud/Aerosol Particles". In: *Surveys in Geophysics* 20.1, pp. 1–31. ISSN: 1573-0956. DOI: 10.1023/A:1006501706704. URL: http://dx.doi.org/10.1023/A:1006501706704.

Sandu, A. and R. Sander (2006). "Technical note: Simulating chemical systems in Fortran90 and Matlab with the Kinetic PreProcessor KPP-2.1". In: *Atmospheric Chemistry and Physics* 6.1, pp. 187–195. DOI: 10.5194/acp-6-187-2006. URL: https://www.atmos-chem-phys.net/6/187/2006/.

Sazaki, Gen et al. (2012). "Quasi-liquid layers on ice crystal surfaces are made up of two different phases". In: *Proceedings of the National Academy of Sciences* 109.4, pp. 1052–1055. DOI: 10.1073/pnas.1116685109. eprint: http://www.pnas.org/content/109/4/1052.full.pdf. URL: http://www.pnas.org/content/109/4/1052.abstract.

Schmale, Julia et al. (2017). "Modulation of snow reflectance and snowmelt from Central Asian glaciers by anthropogenic black carbon". In: 7, 40501 EP –. URL: http://dx.doi.org/10.1038/srep40501.

Seinfeld, J.H. and S.N. Pandis (2012). *Atmospheric Chemistry and Physics: From Air Pollution to Climate Change*. Wiley. ISBN: 9781118591505. URL: https://books.google.co.uk/books?id=J3s30hwn_K0C.

Simpson, W. R. et al. (2007). "Halogens and their role in polar boundary-layer ozone depletion". In: *Atmospheric Chemistry and Physics* 7.16, pp. 4375–4418. DOI: 10.5194/acp-7-4375-2007. URL: https://www.atmos-chem-phys.net/7/4375/2007/.

Sokolik, Irina N. and Owen B. Toon (1999). "Incorporation of mineralogical composition into models of the radiative properties of mineral aerosol from UV to IR wavelengths". In: *Journal of Geophysical Research: Atmospheres* 104.D8, pp. 9423–9444. ISSN: 2156-2202. DOI: 10.1029/1998JD200048. URL: http://dx.doi.org/10.1029/1998JD200048.

Sommerfeld, R. A. and E. LaChapelle (1970). "The Classification of Snow Metamorphism". In: *Journal of Glaciology* 9.55, 3?18. DOI: 10.1017/S0022143000026757.

Streit, G. E. et al. (1976). "Temperature dependence of O(1D) rate constants for reactions with O2, N2, CO2, O3, and H2O". In: *The Journal of Chemical Physics* 65.11, pp. 4761–4764. DOI: 10.1063/1.432930. eprint: http://dx.doi.org/10.1063/1.432930. URL: http://dx.doi.org/10.1063/1.432930.

Sturm, Matthew and Carl S. Benson (1997). "Vapor transport, grain growth and depth-hoar development in the subarctic snow". In: *Journal of Glaciology* 43.143, pp. 42–59. ISSN: 0022-1430. DOI: doi:10.3198/1997JoG43-143-42-59. URL: http://www.ingentaconnect.com/content/igsoc/jog/1997/00000043/00000143/art00004.

Tanaka, Taichu Y. and Masaru Chiba (2006). "A numerical study of the contributions of dust source regions to the global dust budget". In: *Global and Planetary Change* 52.1–4. Monitoring and Modelling of Asian Dust Storms,

pp. 88 –104. ISSN: 0921-8181. DOI: https://doi.org/10.1016/j.gloplacha.2006.02.002. URL: http://www.sciencedirect.com/science/article/pii/S0921818106000312.

Tang, M. J., R. A. Cox, and M. Kalberer (2014). "Compilation and evaluation of gas phase diffusion coefficients of reactive trace gases in the atmosphere volume 1. Inorganic compounds". In: *Atmospheric Chemistry and Physics* 14.17, pp. 9233–9247. DOI: 10.5194/acp-14-9233-2014. URL: http://www.atmos-chem-phys.net/14/9233/2014/.

Thibert, Emmanuel, and Florent Dominé* (1998). "Thermodynamics and Kinetics of the Solid Solution of HNO3 in Ice". In: *The Journal of Physical Chemistry B* 102.22, pp. 4432–4439. DOI: 10.1021/jp980569a. eprint: http://dx.doi.org/10.1021/jp980569a. URL: http://dx.doi.org/10.1021/jp980569a.

Thomas, J. L. et al. (2011). "Modeling chemistry in and above snow at Summit, Greenland ,§? Part 1: Model description and results". In: *Atmospheric Chemistry and Physics* 11.10, pp. 4899–4914. DOI: 10.5194/acp-11-4899-2011. URL: http://www.atmos-chem-phys.net/11/4899/2011/.

Tomasi, C. et al. (2007). "Aerosols in polar regions: A historical overview based on optical depth and in situ observations". In: *Journal of Geophysical Research: Atmospheres* 112.D16. D16205, n/a–n/a. ISSN: 2156-2202. DOI: 10.1029/2007JD008432. URL: http://dx.doi.org/10.1029/2007JD008432.

Toyota, K. et al. (2014). "Air-snowpack exchange of bromine, ozone and mercury in the springtime Arctic simulated by the 1-D model PHANTAS - Part 1 In-snow bromine activation and its impact on ozone". In: *Atmospheric Chemistry and Physics* 14.8, pp. 4101–4133. DOI: 10.5194/acp-14-4101-2014. URL: http://www.atmos-chem-phys.net/14/4101/2014/.

Udisti, Roberto et al. (2004). "Atmosphere snow interaction by a comparison between aerosol and uppermost snow-layers composition at Dome C, East Antarctica". In: *Annals of Glaciology* 39.1, pp. 53–61. ISSN: 0260-3055. DOI: doi:10.3189/172756404781814474. URL: http://www.ingentaconnect.com/content/igsoc/agl/2004/00000039/00000001/art00010.

Ullerstam, Maria and Jonathan P. D. Abbatt (2005). "Burial of gas-phase HNO3 by growing ice surfaces under tropospheric conditions". In: *Phys. Chem. Chem. Phys.* 7 (20), pp. 3596–3600. DOI: 10.1039/B507797D. URL: http://dx.doi.org/10.1039/B507797D.

Ullerstam, Maria, Troy Thornberry, and Jonathan P. D. Abbatt (2005). "Uptake of gas-phase nitric acid to ice at low partial pressures: evidence for unsaturated surface coverage". In: *Faraday Discuss.* 130 (0), pp. 211–226. DOI: 10.1039/B417418F. URL: http://dx.doi.org/10.1039/B417418F.

Usher, Courtney R., Amy E. Michel, and Vicki H. Grassian (2003). "Reactions on Mineral Dust". In: *Chemical Reviews* 103.12. PMID: 14664636, pp. 4883–4940. DOI: 10.1021/cr020657y. eprint: http://dx.doi.org/10.1021/cr020657y. URL: http://dx.doi.org/10.1021/cr020657y.

Waddington, E. D., J. Cunningham, and S. L. Harder (1996). "The Effects Of Snow Ventilation on Chemical Concentrations". In: *Chemical Exchange Between the Atmosphere and Polar Snow*. Ed. by Eric W. Wolff and Roger C. Bales. Berlin, Heidelberg: Springer Berlin Heidelberg, pp. 403–451. ISBN: 978-3-642-61171-1. DOI: 10.1007/978-3-642-61171-1_18. URL: http://dx.doi.org/10.1007/978-3-642-61171-1_18.

Wang, Xin, Baiqing Xu, and Jing Ming (2014). "An overview of the studies on black carbon and mineral dust deposition in snow and ice cores in East Asia". In: *Journal of Meteorological Research* 28.3, pp. 354–370. ISSN: 2198-0934. DOI: 10.1007/s13351-014-4005-7. URL: https://doi.org/10.1007/s13351-014-4005-7.

Warren, Stephen G. (1984). "Optical constants of ice from the ultraviolet to the microwave". In: *Appl. Opt.* 23.8, pp. 1206–1225. DOI: 10.1364/AO.23.001206. URL: http://ao.osa.org/abstract.cfm?URI=ao-23-8-1206.

Warren, Stephen G. and Richard E. Brandt (2008). "Optical constants of ice from the ultraviolet to the microwave: A revised compilation". In: *Journal of Geophysical Research: Atmospheres* 113.D14, n/a–n/a. ISSN: 2156-2202. DOI: 10.1029/2007JD009744. URL: http://dx.doi.org/10.1029/2007JD009744.

Wolff, E. W. et al. (2008). "The interpretation of spikes and trends in concentration of nitrate in polar ice cores, based on evidence from snow and atmospheric measurements". In: *Atmospheric Chemistry and Physics* 8.18, pp. 5627–5634. DOI: 10.5194/acp-8-5627-2008. URL: http://www.atmos-chem-phys.net/8/5627/2008/.

Wolff, E. W. et al. (2016). "Comment on "Low time resolution analysis of polar ice cores cannot detect impulsive nitrate events" by D.F. Smart et al." In: *Journal of Geophysical Research: Space Physics* 121.3. 2015JA021570, pp. 1920–1924. ISSN: 2169-9402. DOI: 10.1002/2015JA021570. URL: http://dx.doi.org/10.1002/2015JA021570.

Wolff, Eric W. et al. (2002). "Modelling photochemical NOX production and nitrate loss in the upper snowpack of Antarctica". In: *Geophysical Research Letters* 29.20. 1944, pp. 5–1–5–4. ISSN: 1944-8007. DOI: 10.1029/2002GL015823. URL: http://dx.doi.org/10.1029/2002GL015823.

Zárate, Marcelo A (2003). "Loess of southern South America". In: *Quaternary Science Reviews* 22.18. Loess and the Dust Indicators and Records of Terrestrial and Marine Palaeoenvironments (DIRTMAP) database, pp. 1987–2006. ISSN: 0277-3791. DOI: http://dx.doi.org/10.1016/S0277-3791(03)00165-3. URL: http://www.sciencedirect.com/science/article/pii/S0277379103001653.

Zatko, M. et al. (2016a). "The impact of snow nitrate photolysis on boundary layer chemistry and the recycling and redistribution of reactive nitrogen across Antarctica and Greenland in a global chemical transport model". In: *Atmospheric Chemistry and Physics* 16.5, pp. 2819–2842. DOI: 10.5194/acp-16-2819-2016. URL: https://www.atmos-chem-phys.net/16/2819/2016/.

Zatko, Maria et al. (2016b). "The magnitude of the snow-sourced reactive nitrogen flux to the boundary layer in the Uintah Basin, Utah, USA". In: 16, pp. 13837–13851.

Zeleznik, Frank J. (1991). "Thermodynamic Properties of the Aqueous Sulfuric Acid System to 350 K". In: *Journal of Physical and Chemical Reference Data* 20.6, pp. 1157–1200. DOI: 10.1063/1.555899. eprint: http://dx.doi.org/10.1063/1.555899. URL: http://dx.doi.org/10.1063/1.555899.

Zhang, Xiaoyu and Ross Edwards (2011). "Anthropogenic sulfate and nitrate signals in snow from Bogda Glacier, eastern Tianshan". In: *Journal of Earth Science* 22.4, pp. 490–502. ISSN: 1867-111X. DOI: 10.1007/s12583-011-0196-3. URL: https://doi.org/10.1007/s12583-011-0196-3.

Zhu, Chengzhu et al. (2010). "308 nm Photolysis of Nitric Acid in the Gas Phase, on Aluminum Surfaces, and on Ice Films". In: *The Journal of Physical Chemistry A* 114.7. PMID: 20121260, pp. 2561–2568. DOI: 10.1021/jp909867a. eprint: http://dx.doi.org/10.1021/jp909867a. URL: http://dx.doi.org/10.1021/jp909867a.